# Semiconductor Quantum-well Nanowire Lasers: Analysis, Modeling, and Dynamics

by **Parya Reyhanian**

Thesis submitted in fulfilment of the requirements for the degree of
*Doctor of Philosophy*
under the supervision of
Dr. Arti Agrawal
Prof. Charlene Lobo
Prof. Christopher G. Poulton

School of Electrical and Data Engineering
Faculty of Engineering and IT
University of Technology Sydney
August 21, 2024

# Certificate of Authorship / Originality

I, Parya Reyhanian, declare that this thesis is submitted in fulfilment of the requirements for the award of Doctor of Philosophy, in the School of Electrical and Data Engineering at the University of Technology Sydney.

This thesis is wholly my own work unless otherwise referenced or acknowledged. In addition, I certify that all information sources and literature used are indicated in the thesis. This document has not been submitted for qualifications at any other academic institution.

This research is supported by the Australian Government Research Training Program.

Signature: Production Note: Signature removed prior to publication.

Date: August 21, 2024

# Abstract

Semiconductor nanowire lasers represent a promising frontier in optoelectronics, with greater potential when coupled with embedded quantum wells. Their small dimensions enable efficient light confinement and amplification, resulting in reduced threshold currents and the possibility of on-chip integration. Integrating quantum wells within nanowires enables precise control over emission wavelength and spectral characteristics due to the step-like density of states.

However, existing theoretical models struggle to incorporate both quantum confinement effects and the nanowire cavity effects, hindering predictions of the nanowire laser behavior. Also, the spontaneous emission coupling factor is often treated as a fitting parameter, limiting nanowire laser optimization. This thesis addresses the challenges in the theoretical analysis of quantum well nanowire lasers. We present a comprehensive laser model with three main components: cavity simulations, dynamics of the optical processes, and laser rate equation analysis.

The primary contribution of this thesis revolves around the development of a formalism to describe absorption and emission processes within quantum well nanowires. We start from equations originally intended for bulk semiconductors and we further adapt them for quantum wells. Our modifications not only consider the quantum confinement effect within quantum wells but also encompass the integration of the effect of the nanowire cavity on absorption, gain, and spontaneous emission rates. Furthermore, this thesis derives the equations to calculate the spontaneous emission factor and the Purcell effect for quantum well nanowire lasers. One of the advantages of our model is the absence of curve-fitting to experimental data to determine the spontaneous emission factor. Instead, we employ $\beta$ and the gain derived from our formulations to solve the laser rate equations.

We implement our laser model to simulate a ten $In_{0.2}Ga_{0.8}As/GaAs$ multiple quantum well nanowire laser. Simulation results reveal that spontaneous emission is not a constant parameter and it depends on carrier densities. As more carriers are excited into the conduction band, the spontaneous emission factor increases. After reaching a maximum, it starts to decrease when stimulated emissions take over. We also discuss the effect of the quantum well thickness and the temperature on the spontaneous emission emission factor.

In summary, our simulations and theoretical framework comprehensively capture the dynamics of nanowire lasers, shedding light on the complex interplay between absorption, gain, and spontaneous emission rates. This thesis significantly advances our fundamental understanding of MQW-nanowire lasers, offering a novel contribution to the theoretical groundwork necessary to harness their unique properties across a wide array of applications.

# Dedication

To my parents and my brother,

Your unwavering support, encouragement, and love have been the driving forces behind the completion of this thesis. Through every challenge and triumph, you stood by my side, providing the strength and motivation I needed to persevere. This work is a testament to your belief in me, and I dedicate it to you with heartfelt gratitude.

With love and appreciation,
Parya

# Acknowledgements

I would like to express my heartfelt gratitude to my supervisors, Dr. Arti Agrawal, Professor Charlene Lobo, and Professor Christopher Poulton. Your guidance, unwavering support, and dedication in my PhD journey have been truly invaluable. Throughout the highs and lows of my research, you have not only offered your expertise but have also extended your kindness and patience, which I deeply appreciate. Your willingness to invest your valuable time in mentoring me, even during the most challenging moments, has made all the difference in my academic pursuits.

Beyond the realm of academia, I have learned immeasurable life lessons from each of you. Your dedication to your work and your commitment to excellence continue to inspire me daily. I am very grateful to have had the opportunity to learn from you, and I carry the lessons and inspiration you've provided with me as I move forward in my academic and personal journey. Thank you for being exceptional mentors and role models.

Parya Reyhanian
August 21, 2024
Sydney, Australia

# Contents

# List of Figures

# List of Tables

# Chapter 1

# Introduction

A laser, which stands for "Light Amplification by Stimulated Emission of Radiation," is a device that produces an intense, highly focused beam of coherent light through the process of stimulated emission. Lasers are indispensable in the field of medicine and modern communication technologies. Among different types of lasers, semiconductor lasers have become a cornerstone of modern technology due to their numerous advantages, including compact size, energy efficiency, and precise wavelength control. The high demand for semiconductor lasers has mainly been driven by their use in fields like telecommunications, medicine, and optical data storage.

In recent years a notable shift has been towards even smaller and more efficient laser designs, such as Vertical-Cavity Surface-Emitting Lasers (VCSELs), microdisk lasers, photonic crystal cavities, and nanowire lasers. These micro and nanostructured lasers offer exceptional levels of miniaturization and integration, making them ideal for emerging applications in optical computing, on-chip data communication, and biosensing. They promise to further revolutionize industries by enabling compact, high-performance devices that were previously unimaginable with conventional semiconductor lasers.

Among semiconductor lasers, nanowire lasers display a variety of advantages for optoelectronic devices, including low threshold, significant light absorption/extraction efficiency, and less temperature sensitivity. By tailoring the nanowires' shape, material, or dimensions, their properties can be custom-fit to align with a range of applications. This has led to nanowires attracting considerable research attention due to their capacity to minimize device size, enhance performance, and provide unique capabilities [1]–[5].

Embedding quantum wells inside semiconductor nanowire lasers brings about several changes in their characteristics, leading to improved performance and novel applications. One of the key benefits is a reduction in the threshold current. This is the minimum current required to initiate lasing action. Confining the carriers (electrons and holes) in quantum wells increases carrier density and enhances recombination probability, which results in a lower threshold current for lasing in quantum well nanowires [6], [7].

Moreover, quantum structures enable bandgap engineering, allowing for the tuning of emission wavelengths in nanowire laser. By adjusting the quantum well thickness and composition, the effective bandgap can be tailored to achieve desired emission wavelengths, making these lasers highly versatile for various applications. Temperature stability is also enhanced when quantum wells are embedded in the nanowire lasers [8]–[11].

Optical gain is also increased in quantum well nanowire lasers compared to single nanowire lasers. The quantum confinement effect leads to a step-like energy-independent density of states, resulting in a higher optical gain. This characteristic can be beneficial in applications requiring strong optical signals or amplification. In addition, embedding quantum wells within a nanowire allows for the integration of compact, nanoscale semiconductor lasers in photonic circuits and devices, which is particularly important for applications such as on-chip communication and sensing [12]–[14].

Although semiconductor nanowire lasers are promising as ultrasmall and highly efficient coherent light emitters, modeling nanolasers with quantum confinement is challenging because even a slight change in the size of the gain medium, cavity dimensions, and where the gain material placed inside the cavity can noticeably change the laser behavior.

Currently, theoretical models available for quantum well nanowire lasers don't fully encapsulate their laser attributes and clarify the complex optical processes occurring within these laser systems. A full analysis of nanowire geometry is necessary to analyze quantum well nanowire lasers effectively. Additionally, accurately describing absorption, gain, and spontaneous emission rates in quantum wells demands a profound understanding of the dynamics seen in bulk semiconductors. This understanding is essential for adapting equations to suit quantum well nanowires.

Moreover, laser models fall short in capturing both the quantum confinement effect, resulting from the thin quantum well layers, and the optical cavity effect, which arises from placing these quantum wells inside the nanowires. The spontaneous emission factor ($\beta$) is one of the unknown parameters in laser analysis. Parameter $\beta$ determines the rate of spontaneous emissions into the lasing mode divided by the total spontaneous emission rates. Calculating $\beta$ requires complex calculations of the optical processes within the laser. Therefore, $\beta$ is typically treated as a fitting parameter, by using experimental data in the simulations. However, this approach is less than ideal because optimizing $\beta$ can lead to lower thresholds and highly efficient lasers, bringing us closer to achieving the ideal thresholdless laser.

Additionally, the Purcell factor, which measures the effect of the cavity on the spontaneous emission lifetime, is one of the key parameters in designing nanoscale lasers. However, conventional methods for calculating the Purcell factor may not yield accurate results in lower dimensional nanowire lasers due to the fact that the gain medium only exists in a small fraction of the nanowire cavity. Lastly, laser rate equations, primarily designed for analyzing conventional bulk semiconductors, need modification for lower-dimensional lasers, especially when the gain material exists in a small fraction within the cavity.

This thesis aims to address these challenges in the theoretical analysis of multiple quantum well (MQW)-nanowire lasers by developing a comprehensive laser model comprising laser cavity simulations, modeling of laser gain and spontaneous emission dynamics, and rate equation analysis. This thesis contributes to a deeper understanding of quantum well nanowire lasers and lays the theoretical groundwork for leveraging their unique properties in various innovative applications. In the next section, we will present a brief overview of each chapter along with the research objectives.

## 1.1 Research Objectives and Overview

The objectives of this thesis are outlined as:

- Develop the formalism to describe the absorption, gain, and spontaneous emissions within the quantum well nanowire laser
- Incorporates the nanowire photonic density of states in the calculations of the gain and the spontaneous emission rates
- Derive a theoretical framework to calculate the spontaneous emission factor
- Derive a theoretical approach to calculate the Purcell factor
- Investigate change in the laser characteristics when transitioning from the conventional bulk semiconductor lasers to the quantum well nanowire lasers
- Investigate the behavior of the spontaneous emission factor with carrier density and time in quantum well nanowire lasers
- Investigate the dependency of the Purcell factor on carrier density in quantum well nanowire lasers
- Compare and validate our developed model with the experimental data.

**Chapter 2** starts with an overview of lasers focusing on the semiconductor lasers. Then we will delve into the fundamentals of lasers to build the groundwork understanding of laser operation. Moreover, We discuss the advantages of incorporating lower-dimensional structures as gain media within laser systems encompassing quantum wells, quantum wire, and quantum dots. Additionally, we provide a brief overview of the current state of the art in the realm of lower-dimensional semiconductor research.

Moving forward, we focus on the domain of nanowire lasers, where we examine the advantages and challenges in the nanowire laser field. We also briefly explore the various fabrication techniques. Moreover, we discuss the integration of lower-dimensional gain media within nanowires leading to exceptionally low thresholds and high-efficiency lasers that can be tailored for specific applications. This chapter concludes with our investigations on different laser rate equations commonly employed to describe nanowire lasers, highlighting the associated challenges. Finally, we introduce our modified laser rate equations for analyzing quantum well nanowire lasers, paving the way for a deeper exploration of their unique properties and applications.

**Chapter 3** presents a set of formulations that we developed for modeling the intricate dynamics of optical processes within a quantum well nanowire laser. First, we provide a detailed analysis of absorption, gain, and spontaneous emissions occurring within a bulk semiconductor. Then we will adapt these equations for quantum wells within a nanowire cavity. Our model goes beyond the conventional consideration of quantum confinement effects on absorption, gain, and stimulated emission rates; it also takes into account the impact of the optical cavity by calculating the photonic density of states within the nanowire. This comprehensive approach enables us to establish a mathematical framework capable of precisely determining the complex dynamics of the optical processes within quantum well nanowire lasers. Furthermore, we derive the equations to accurately compute the spontaneous emission coupling efficiency and the Purcell factor in quantum well nanowire lasers. Our theoretical approach enhances our ability to predict and optimize the performance of these nanoscale laser devices, ultimately contributing to advancements in the field of nanophotonics.

**Chapter 4** describes the computational methods and the numerical approaches that we use to model the quantum well nanowire laser. We will present a comprehensive overview of the implementation of the Finite Element Method (FEM), to simulate a nanowire laser cavity. By

applying FEM, we aim to derive the eigenfrequencies of the nanowire and obtain its cavity-related properties. We will discuss both two-dimensional (2D) and three-dimensional (3D) cavity simulations. The 2D simulations will be used in studying the transverse modes of the cavity and determining their corresponding effective mode indices. Concurrently, we use 3D simulations to accurately visualize the longitudinal modes within the nanowire. These 3D simulations enable us to calculate essential cavity parameters such as the confinement factor ($\Gamma$), cavity quality factor ($Q$), and photon lifetime ($\tau_p$). These parameters are used as inputs to solve the laser rate equations.

Moreover, in Chapter 4 we will discuss how to use the fourth-order Runge-Kutta numerical method to solve the laser rate equations. Laser rate equations describe the rate of change in the carrier density and the number of photons with time and help us predict the laser's behavior. Furthermore, in this chapter, we validate our choice of computational methods and numerical techniques by comparing our simulation results with experimental data. Comparison of our simulations with real-world observations ensures the accuracy and reliability of our model.

**In Chapter 5**, we will use the theoretical framework developed in this thesis and presented in Chapter 3 to investigate the dynamics of absorption, gain, and spontaneous emissions within ten 19nm thick $In_{0.2}Ga_{0.8}As/GaAs$ quantum wells nanowire laser reported in [7].

Our approach involves consideration of the photonic density of states within the nanowire, enabling us to accurately predict the rates of stimulated emission and spontaneous emissions within the quantum wells embedded within the nanowire. Our analysis extends to the calculation of the spontaneous emission factor and the Purcell factor. A central objective of this chapter is to unveil the behavior of the spontaneous emission factor with carrier density and time, a facet that has not been previously explored in the context of quantum well nanowires. This distinction arises from the recognition that $\beta$ is not a constant parameter in a laser; instead, it undergoes changes over time and in response to carrier density variations, a phenomenon not previously reported within quantum well nanowires.

Furthermore, we will apply the outcomes from our nanowire simulations and the optical processes occurring within the quantum wells to solve the laser rate equations. Our ultimate goal is to rigorously compare our results with existing models employed for solving these equations and validate our findings by aligning them with experimental data. The outcomes of this chapter advance our understanding of quantum well nanowire lasers and contribute to the refinement of their theoretical framework, ensuring greater accuracy and applicability in practical laser applications.

**Chapter 6** summarises the key results and contributions of this thesis. Furthermore, it extends its scope by delineating recommended avenues for the continuation and expansion of this work in the foreseeable future, thereby providing valuable guidance to researchers in the field.

## 1.2 List of Publications

This thesis resulted in the following publications:

- Arti Agrawal, Parya Reyhanian, Charlene J. Lobo, and Christopher G. Poulton, "Computational methods," in On-Chip Photonics: Principles, Technology and Applications, 1st ed., A. Lakhtakia, A. Karabchevsky, and A. Choudhary, Eds. Elsevier, 2024, ch. 3.
- Parya Reyhanian, Charlene Lobo, Christopher. G. Poulton, and Arti Agrawal, "Impact

of the Purcell and Spontaneous Emission Factors in Nanowire Lasers" in Conference on Optoelectronic and Microelectronic Materials and Devices (COMMAD) 2022.

- Parya Reyhanian, Charlene Lobo, Christopher. G. Poulton, and Arti Agrawal, "A Numerical Study on the impact of Purcell Effect and Spontaneous Emission Factor in Lower-Dimension Semiconductor Nanolasers" in Conference on Optics, Photonics Quantum Optics (COPaQ) 2022.
- Parya Reyhanian, Charlene Lobo, Christopher. G. Poulton, and Arti Agrawal, "A Theoretical Model to Analyse Multiple Quantum-disks Nanowire Lasers" in the 6th workshop on Optics and Photonics: Theory and Computational Techniques (OPTCT) 2022.

# Chapter 2

# Fundamentals of Semiconductor Lasers and State of the Art

In 1917, Albert Einstein introduced the basics of amplifying radiation through stimulated emission [15]. However, the practical application of this concept didn't occur until 1952 when Joseph Weber started developing an optical maser. An "optical maser" is a term for "microwave amplification by stimulated emission of radiation," which was an earlier version of the same concept as laser but applied to microwaves instead of visible light. The first successful maser was built in 1953 by the teams of Charles Townes, Nikolay Basov, and Aleksandr Prokhorov [16]–[20].

"LASER" stands for the Light Amplification by Stimulated Emission of Radiation. Theodore Harold Maiman was the first one to demonstrate the first functional ruby laser in 1960 [21]–[23]. Maiman's accomplishment triggered a series of advances in laser technology. The development of lasers is considered one of the most significant breakthroughs of the century, playing crucial roles in various industries such as optoelectronics, engineering, information technology, medicine, and numerous scientific fields [24]–[31].

Stimulated emission is the fundamental phenomenon that lies at the heart of laser operation, distinguishing lasers from other light sources. In this remarkable process, atoms or molecules in an excited state interact with incoming photons, resulting in the emission of additional photons that match in frequency and phase with the incident photons. This process creates a positive feedback loop of photon stimulation and emission, with the end facets of the cavity ensuring that only the photons matching the exact frequency and phase are allowed to propagate. The photons amplify and build up, resulting in a coherent, intense laser beam that emerges through the partially reflective end facets [32], [33].

At the core of the laser's operation usually, there are three essential elements: the cavity, gain medium, and the pump. As illustrated in Figure 2.1, the cavity consists of two partially reflective facets, facing each other. This arrangement creates a confined space where light is trapped and bounces back and forth. The gain medium lies between these reflective facets. When an external energy source (the pump) is supplied to the gain medium, its atoms or molecules are excited to higher energy states [33], [34].

Population inversion occurs when a higher number of atoms or molecules reside in higher energy states than there are in lower energy states. A state of population inversion in the gain medium is often achieved through the pump [33], [34].

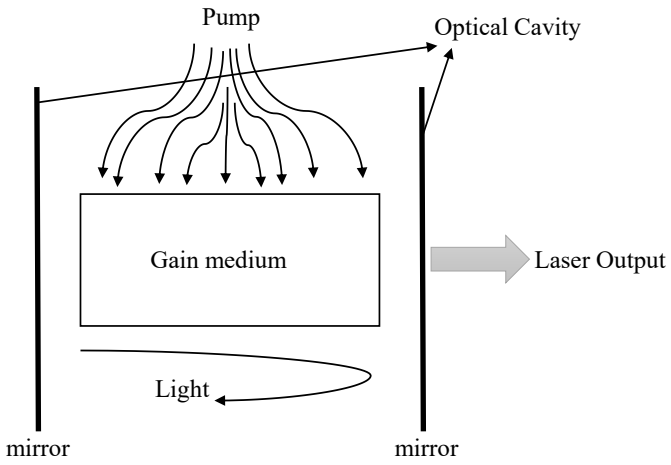


Figure 2.1: Schematic representation of a simple laser structure consisting of the optical cavity, gain medium, and pump.

## 2.1 Fundamentals of Semiconductor Lasers

A semiconductor laser is a type of diode laser that uses a semiconductor material as the gain medium. Semiconductor lasers play a significant role in optoelectronics. They are used in various applications, from optical communications to optical memory storage systems, due to their advantages over solid-state lasers, such as low cost, high efficiency, compact size, and compatibility with modern electronics [34]–[36]. Semiconductor lasers are designed to operate over a wide range of frequencies and they are mostly used in communications and control applications to produce the input information signals transmitted through the optical fibers [34], [37]–[39].

Semiconductor lasers are most popular due to their simple structure. As illustrated in Figure 2.2, layers of n-type and p-type semiconductor materials are carefully placed in a way that the active layer, presented with a black color, is sandwiched between them. Conventional semiconductor laser dimensions are typically in the order of a few hundred micrometers as presented in Figure 2.2 [34].

When a forward bias voltage is applied across the p-n junction via the electrodes, shown with blue color, electrons from the conduction band recombine with holes in the valence band. This recombination releases energy in the form of photons, creating coherent light. This light is then amplified as it bounces back and forth between cleaved end facets of the laser cavity, leading to a powerful, focused laser beam [34].

Within a semiconductor, the electrons are distributed throughout the entire volume of the crystal. Consequently, the wavefunctions of the electrons overlap, but due to the Pauli exclusion principle, they are unable to occupy the same quantum state. Thus, each electron within the crystal must be linked to a unique quantum state. In its isolated state, the atoms in the semiconductor display similar electron configurations and electrons from different atoms could potentially have the same energy states. When these atoms form a solid structure, interatomic interactions come into play and split the energy levels leading to the formation of the conduction and valence energy bands. As shown in Figure 2.3, these bands are separated by a bandgap ($E_g$) where electron presence is prohibited [33].

Due to the large number of atoms with different energy levels, each band offers a nearly continuous range of energy states. We show this continuous energy range with the gray color in Figure 2.3. The highest energy band in the semiconductor, where electrons are completely filled at 0 Kelvin, is called the "valence band". The higher band immediately above it, which is either partially occupied or completely vacant, is called the "conduction band". [33].

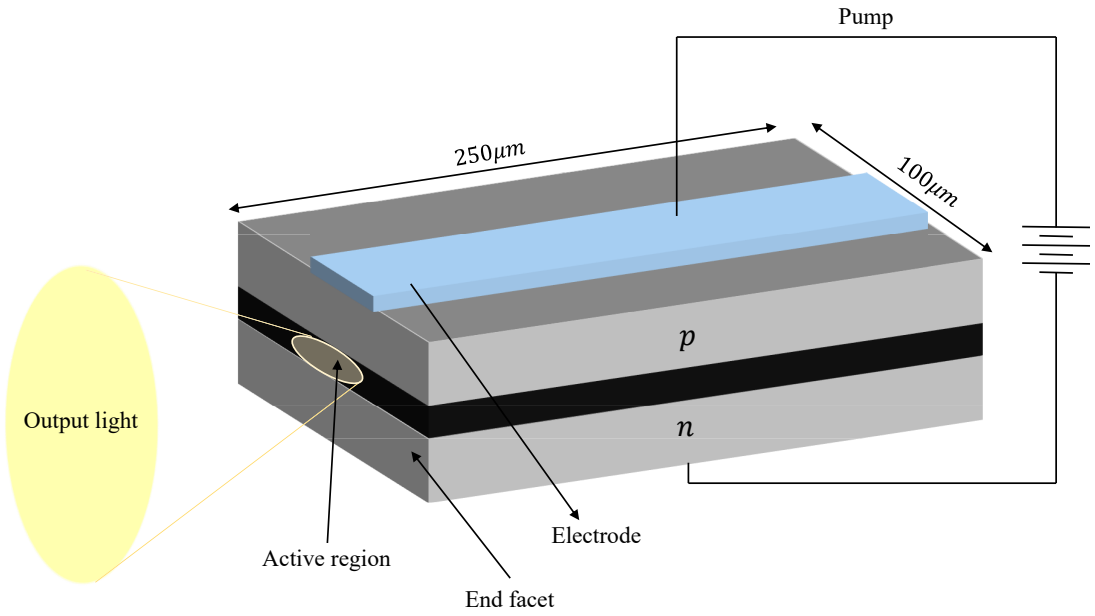


Figure 2.2: Schematic representation of a semiconductor laser structure. The active region depicted as the black layer is located at the intersection of the p-type and n-type regions where the current is flowing. The end facets form the resonant cavity and two electrodes are attached to the top and the bottom of the structure to provide pumping.

The gain coefficient in the semiconductor lasers is quite large in comparison to the gas and solid-state lasers and they are capable of operating at more than 50% efficiency [34]. the gain coefficient in a typical semiconductor laser is in the order of 1000 per centimeter. In contrast, the gain coefficient of a solid-state laser, such as a Neodymium-doped Yttrium Aluminum Garnet (Nd: YAG) laser, is in the range of 0.1 to 10 per centimeter [40].

Semiconductor lasers also face a few challenges. For example, they don't simply operate with fundamental transverse electromagnetic mode ($TEM_{00}$) and the field spot size is roughly in the order of the free space wavelength. Given their limited dimensions, the emitted beam diverges at angles of a few degrees, and owing to the uneven dimensions, the beam disperses unevenly in two directions which leads to a broad linewidth.

Moreover, the range of optical frequencies over which oscillation can occur is exceptionally wide when compared to solid-state lasers, leading to multimode oscillation. Such lasers require large input currents and their operation generates heat, which can affect the efficiency and lifespan. Therefore, cooling systems are needed to lower the device temperature [41], [42]. In the following sections, we will discuss different components of the laser, starting with the pump.

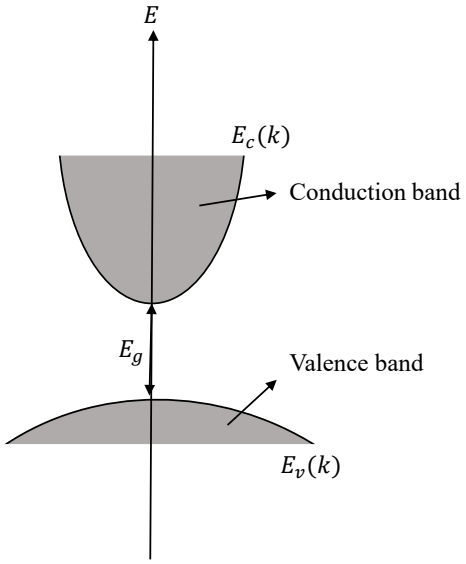


Figure 2.3: Schematic image of the conduction and the valence band in a bulk semiconductor. The bandgap is presented as $E_g$.

### 2.1.1 Pump

In a semiconductor, the number of electrons that exist in the valence band is usually more than the number of electrons in the conduction band. Thus, to start lasing, an external power supply is used to excite the electrons from the valence band into the conduction band. The electrons in the valence band absorb the incident energy and move to the conduction band. When the number of excited electrons in the conduction band exceeds the number of electrons in the valence band, population inversion is achieved. Electrons with higher energy levels eventually lose their energy and drop to the valence band either via spontaneous or stimulated photon emission. The wave passing through a collection of atoms in the state of population inversion causes more stimulated photon emissions, and it is amplified.

There are two primary pumping mechanisms in semiconductor lasers: electrical pumping and optical pumping. Each method has advantages and limitations, and the choice between them depends on the desired laser application and performance requirements [43]–[45].

Electrical pumping is the technique employed in conventional semiconductor lasers, where current is injected into the gain medium, resulting in the recombination of electron-hole pairs, which contribute to the stimulated emission process. The efficiency of electrical pumping which represents the percentage of the pump power that is able to interact with the gain medium is near 100% [46].

In contrast, optical pumping involves the excitation of electrons in the semiconductor using an external light source, such as another laser or a light-emitting diode (LED). When an external light source is shined on the gain medium, the electrons in the valence band absorb the energy of the incident photons and are excited into the conduction band. Optical pumping is often used in more specialized lasers.

The efficiency of the optical pump is significantly low compared to electrical pumping. The optical pump efficiency in a typical semiconductor laser is around 2-5% [47]. Improving the absorption efficiencies is essential to increase the pumping efficiency and reduce the required

pump power to achieve population inversion (threshold). Factors such as the pump light's polarization, wavelength, and spot size can affect absorption efficiency. The beam profile is also a vital factor in ensuring that carriers are uniformly pumped throughout the active region [48], [49]

### 2.1.2 Resonant Cavity

The cavity, often called the optical resonator, typically consists of two reflective surfaces at both ends of the gain medium. Its primary purpose is to reflect and confine the light waves between the end facets, allowing them to oscillate and gradually increase the intensity. The end facets are partially transparent, enabling a portion of the amplified light to exit and form the output laser beam [34].

The cavity design determines the emission wavelength by defining the allowed oscillation modes within the resonator. Controlling the laser's output wavelength, mode selection, and spectral linewidth is possible by thoughtfully designing the cavity [50]. Efficient coupling between the cavity and the gain medium is essential for optimal amplification and minimal losses. The cavity's geometry, size, and material composition influence the coupling efficiency [51].

Additionally, the end facets of the cavity must achieve the desired reflectivity and transmittivity at the intended wavelength. The significance of the cavity design becomes increasingly evident in the context of stabilizing compact and ultrafast lasers [52]–[56].

Optical parameters associated with the cavity are instrumental in laser behavior, such as the confinement factor ($\Gamma$), mode volume ($V_m$), and the quality factor ($Q$). These factors are essential for understanding the performance and behavior of laser systems and are crucial for designing effective lasers tailored to specific uses, as will be discussed in the following sections.

### 2.1.3 Gain Medium

Gain is the amplification of optical power that the gain medium provides per unit length and depends on the carrier density within the active region. The gain medium consists of a direct bandgap semiconductor material, such as Gallium Arsenide (GaAs), Indium Phosphide (InP), or their alloys such as InGaAs which facilitates the efficient recombination of electrons and holes, resulting in light emission.

The properties of the gain medium determine key laser characteristics such as its threshold current, output power, and spectral linewidth. Several parameters related to the gain medium are used to analyze the performance of semiconductor lasers, such as the gain ($g$), transparency carrier density ($N_{tr}$), and differential gain. The laser emits light when the carrier density exceeds the transparency carrier density. The differential gain is the rate at which the gain increases as more carriers are injected, $dg/dN$, and it is an essential parameter for understanding the modulation properties and dynamics of semiconductor lasers [57], [58].

### 2.1.4 Optical Processes in Semiconductors

Interactions between incident photons and electrons within the conduction band, as well as holes in the valence band, can occur through three distinct mechanisms:

**Absorption:** When a photon is absorbed by an electron in the valence band, the electron gains energy and jumps to the conduction band as presented with a dash-dotted line in Figure

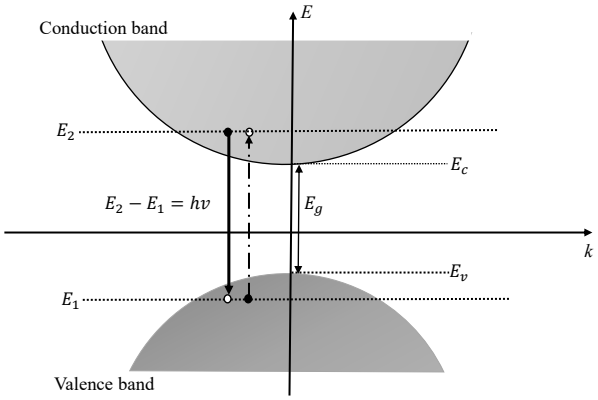


Figure 2.4: The energy band diagram of the conduction and valence bands according to the momentum (k) of electrons in a bulk semiconductor. $E_c$ represents the energy at the bottom of the conduction band, while $E_v$ indicates the energy level at the top of the valence band. An electron sitting in the $E_2$ energy level in the conduction band can recombine with a hole in the valence band at $E_1$ energy level via spontaneous or stimulated emission and emit a photon with energy equal to $hv = E_2 - E_1$, which is shown by the downward transition with the solid line. Also, an electron in the valence band can absorb the energy equal to $hv$ and move to the conduction band as shown by the upward transition with a dashed-dotted line.

2.4. As there are no energy levels within the energy gap, the minimum energy required for this transition should be larger than the energy of the bandgap $E_g < hv$.

The downward transition in Figure 2.4, happens when the electron in the conduction band loses its energy and drops to the valence band by emitting a photon. The downward transition can occur via either spontaneous or stimulated emission.

**Spontaneous Emission:** In quantum mechanics, spontaneous emission describes the process wherein an electron drops from a higher energy level to a lower energy level and, in doing so, emits a photon. The phenomenon is labeled as "spontaneous" because it occurs without any external intervention, exclusively due to the natural instability of the excited state. The emitted photon carries away the energy difference between the two levels ($E_1$ and $E_2$), which corresponds to its frequency ($v$), as given by the Planck-Einstein relation

$$E_2 - E_1 = hv. \tag{2.1}$$

The photons resulting from the spontaneous emission within a material, are emitted in different directions and wavelengths. The spontaneous emission lifetime is an important parameter associated with this process. Spontaneous emission lifetime ($\tau_{sp}$) is the average time that an electron spends in the conduction band before it decays due to spontaneous emission. We will discuss the spontaneous emission in great detail in section 2.2.5.

**Stimulated Emission:** The presence of an incident photon can prompt the de-excitation of an electron from the conduction band to the valence band, resulting in electron-hole recombination. The emitted photon maintains coherence with the incident photon.

Conservation of energy and momentum must be satisfied to enable these three processes. Conservation of energy states that in photon absorption, there should be an available electron in the valence band, while an unoccupied state must exist in the conduction band with the energy difference equivalent to the photon's energy as given in Equation 2.1. This should also be true in the case of stimulated and spontaneous emissions when an electron in the conduction band drops into a hole in the valence band.

The conditions governing absorption and emission processes also involve considerations of the electron's wave vector before and after the transition. The probability of the transition is determined by a momentum matrix element. If $\vec{k}_2$ and $\vec{k}_1$ represent the wave vector of the electron in the conduction band and in the valence band respectively, momentum conservation dictates that [33]

$$\hbar k_2 - \hbar k_1 = \hbar k_p, \tag{2.2}$$

Where $k_p$ is the momentum of the emitted photon.

Electrons in the conduction and valence bands exhibit much larger momentum than photons. Typically, if $a$ denotes the lattice constant of a semiconductor, then $a$ is substantially smaller than the wavelength ($a << \lambda$). Therefore, electrons possess significantly larger momentum than photons. This condition essentially indicates that the electron's momentum remains nearly constant before and after the transition ($k_1 \approx k_2$). This is referred to as the k-selection which implies that the transition of the electrons between the conduction and the valence bands in the k-space which is presented in Figure 2.4, should be a vertical transition [33].

In the following sections, we discuss the number of available electronic states in the conduction and valence bands.

#### 2.1.4.1 Electronic Density of States (DOS)

The joint electronic density of states (DOS) indicates the number of available states for an interaction (absorption or emission) involving a photon of energy $hv$. From the conservation of momentum, in the electron-hole recombination, the wave vectors $k_1$ and $k_2$ are almost equal to each other. However, as presented in Figure 2.4, for the transition from $E_2$ to $E_1$, the electron can have different values of $k$ at energy level $E_2$ and similarly a hole at energy level $E_1$ can have different $k$ values. Therefore we can write the energy levels by considering their position in the $k$ axis as

$$E_2(k) = E_c + \frac{\hbar^2 k^2}{2m_e^*}, \tag{2.3}$$

and

$$E_1(k) = E_v - \frac{\hbar^2 k^2}{2m_h^*}, \tag{2.4}$$

where $\hbar$ is the reduced Planck's constant, and $k$ is the wavenumber of the electron/hole. The parameters $m_e^*$ and $m_h^*$ represent the effective mass of electrons in the conduction band and the effective mass of holes in the valence band, respectively. The effective mass of electrons and holes in a semiconductor describes how they behave within the crystal lattice of the semiconductor. It represents the mass of these carriers as if they were free particles moving in a vacuum, taking into account their interaction with the surrounding crystal structure. The effective mass is a crucial parameter for understanding and predicting the electronic properties and mobility of charge carriers in semiconductors. Using Equations 2.3-4,

$$hv = E_2 - E_1 = (E_c - E_v) + \frac{\hbar^2 k^2}{2}(\frac{1}{m_e^*} + \frac{1}{m_h^*}) = E_g + \frac{\hbar^2 k^2}{2m_r^*}, \tag{2.5}$$

where $m_r^*$ is the reduced mass of the electron and it is calculated as

$$\frac{1}{m_r^*} = \frac{1}{m_e^*} + \frac{1}{m_h^*}. \tag{2.6}$$

Equation 2.5 can be rewritten as

$$k^2 = \frac{2m_r^*}{\hbar^2}(hv - E_g). \tag{2.7}$$

By substituting $k^2$ in Equations 2.3 and 2.4, we obtain

$$E_2 = E_c + \frac{m_r^*}{m_e^*}(hv - E_g), \tag{2.8}$$

and

$$E_1 = E_v - \frac{m_r^*}{m_h^*}(hv - E_g). \tag{2.9}$$

It is obvious that there is a direct relationship between a photon with frequency $v$ (or with Energy ($hv = E_{12} = E_2 - E_1$)) in Equations 2.8-9.

The electronic density of states (DOS) is the parameter that counts all the possible pairs of energy states per unit volume that exist in both the conduction band and the valence band. The DOS in bulk semiconductors is obtained as [57]

$$\rho_r(E)dE = \frac{1}{2\pi^2}(\frac{2m_r^*}{\hbar^2})^{3/2}(E - E_g)^{1/2}dE, \tag{2.10}$$

which can be written specifically as the density of electrons in the conduction band $\rho_c$ and the density of holes in the valence band $\rho_v$ as

$$\rho_c(E_2)dE_2 = \rho_v(E_1)dE_1 = \rho_r(E)dE. \tag{2.11}$$

The expression $\rho_r(E)dE$ covers all the available pairs of energy states per unit volume that exist in both the conduction band and the valence band within the energy range between $E$ and $E + dE$ that can participate in an electron-hole recombination. However, the probability of these states being empty or occupied is calculated by the Fermi functions.

#### 2.1.4.2 Occupancy probability

The Fermi-Dirac function determines the probability of electrons occupying energy states at level E as

$$f(E) = \frac{1}{1 + e^{(E-E_f)/k_BT}}, \tag{2.12}$$

where $E_f$ is the quasi-Fermi level, $T$ is the temperature and $k_B$ is the Boltzmann constant.

When the temperature is around zero (T = 0 K), energy levels below $E_f$ are fully occupied, while those above it remain unoccupied. As temperature rises, the probability of electrons occupying states above the Fermi level increases. Figure 2.5 presents the Fermi function distribution. At the energy level $E_f$ the occupancy probability is equal to 0.5.

Figure 2.5 shows that at absolute zero, the distribution behaves like a step function, with a value of 1 for energies below the quasi-Fermi energy and 0 for energies above it. As the temperature

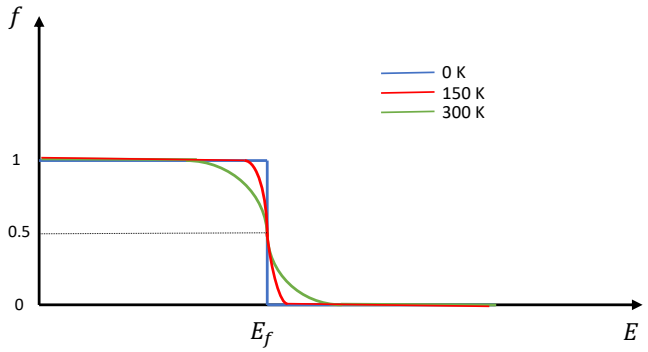


Figure 2.5: Fermi-dirac function distribution with respect to the energy at temperature 0 Kelvin, 150 K, and 300 K. At temperature increases the Fermi function behaves smoother. At temperatures near 0 K, the Fermi function is assumed to be a step function.

rises, the distribution becomes more smooth, compared to the sharp edges of the step function. At thermal equilibrium, Equation 2.12 determines the likelihood of electrons occupying both the conduction and valence bands, and as shown in Figure 2.6, the quasi-Fermi level $E_f$ lies in the middle of the bandgap.

When the gain medium is under the pump, the quasi-Fermi level $E_f$ splits into two separate quasi-Fermi levels as $F_c$ and $F_v$ describing the probabilities of electron and hole occupancy within the conduction and valence bands, respectively. From Figure 2.6, you can see that as we pump the gain medium, more and more electrons are excited. Therefore, $F_c$ and $F_v$ are pushed further up in the conduction band and down into the valence band.

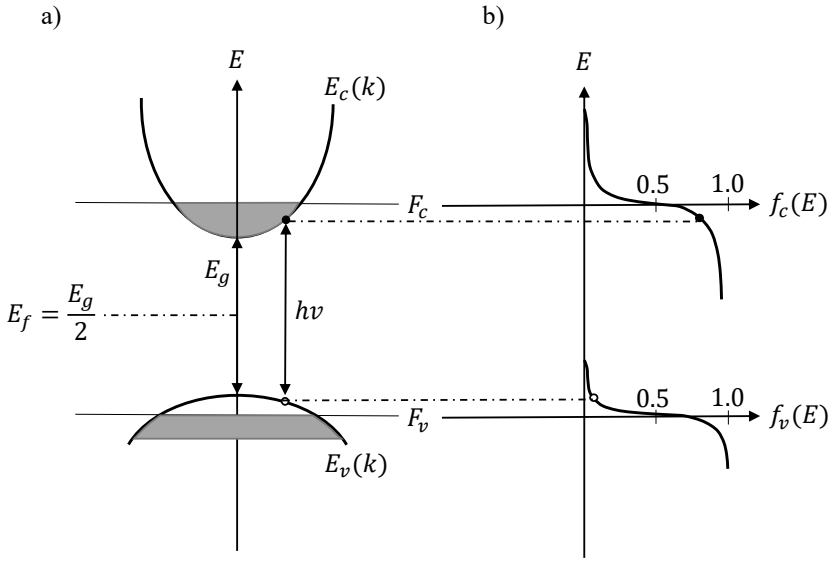


Figure 2.6: Quasi-Fermi levels in both the conduction $F_c$ and valence bands $F_v$ for a semiconductor under the pump. At thermal equilibrium, the quasi-fermi levels lie in the middle of the bandgap $E_f = F_c = F_v = E_g/2$.

We can then write the Fermi functions of the conduction and valence bands separately as

$$f_c(E) = \frac{1}{1 + e^{(E-F_c)/k_BT}}, \tag{2.13}$$

$$f_v(E) = \frac{1}{1 + e^{(E-F_v)/k_BT}}, \tag{2.14}$$

### 2.1.5 Absorption, Spontaneous and Stimulated Emissions

#### 2.1.5.1 Einstein A and B coefficients

Interactions between the incident photons and electrons within the conduction band, as well as holes in the valence band, can occur through three distinct mechanisms: absorption, spontaneous, and stimulated emission. In order to describe the rates of these optical processes within a semiconductor, we start with the Einstein A and B coefficients and we first consider transitions between discrete energy levels $E_1$ and $E_2$ as shown in Figure 2.7:

The rate of absorption transitions per unit volume is proportional to

1. The probability of a state at energy $E_1$ being occupied ($f_1$)
2. The probability of a state at energy $E_2$ being empty ($1 - f_2$)
3. $P(E_{21})$ which is is the number of photons per unit volume per unit energy at the transition frequency $v_{21} = E_{21}/h$

where $f_1$ and $f_2$ are the Fermi functions introduced in Equations 2.13-14. We note that $P(E_{21})$ is related to the Photonic Density of States (PDOS), $N_{ph}(E_{21})$, per unit volume via

$$P(E_{21}) = N_{ph}(E_{21})n_{ph}, \tag{2.15}$$

where $n_{ph}$ is the average number of existing photons at thermal Equilibrium according to Boson statistics and it is obtained as [57]

$$n_{ph} = \frac{1}{e^{\hbar\omega/k_BT} - 1}. \tag{2.16}$$

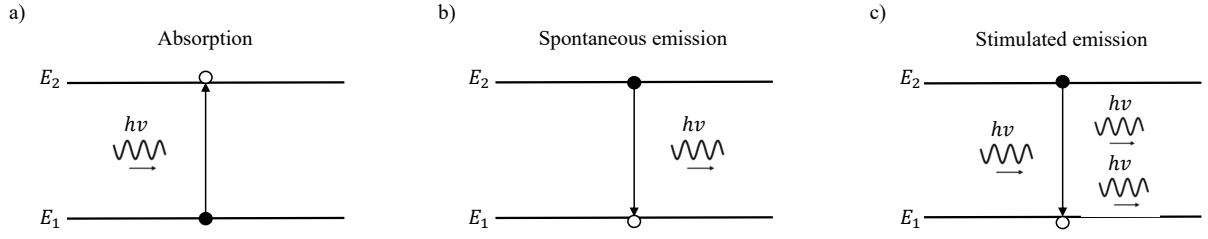


Figure 2.7: Simple representations of a) absorption, b) spontaneous emission, and c) stimulated emission of a photon between discrete energy levels 1 and 2.

The rate of transitions from level 1 to level 2 per unit volume is given by [57]

$$R_{12}^{abs} = B_{12}P(E_{12})f_1(1 - f_2), \tag{2.17}$$

where $B_{12}$ is one of the Einstein coefficients.

The downward transitions can happen through two separate mechanisms, the stimulated and spontaneous emission processes as presented in Figure 2.7. The stimulated emission depends on the photon density $P(E)$, and the spontaneous emission process does not. Therefore, we introduce two rates as

$$R_{21}^{stim} = B_{21}P(E_{21})f_2(1-f_1), \tag{2.18}$$

$$R_{21}^{spon} = A_{21}f_2(1-f_1), \tag{2.19}$$

where $B_{21}$, and $A_{21}$ is the Einstein A and B coefficients.

When the system is at thermal equilibrium, the rate of change in the number of electrons in level 2 is zero. Therefore the absorption rate is equal to the sum of the spontaneous and stimulated emission rates as

$$R_{12}^{abs} = R_{21}^{stim} + R_{21}^{spon}, \tag{2.20}$$

$$B_{12}P(E_{12})f_1(1-f_2) = B_{21}P(E_{21})f_2(1-f_1) + A_{21}f_2(1-f_1) \tag{2.21}$$

If we rewrite Equation 2.21 according to $A_{21}$, we obtain

$$A_{21} = [B_{12}\frac{f_1(1-f_2)}{f_2(1-f_1)} - B_{21}]P(E_{21}). \tag{2.22}$$

We now use Fermi-Dirac statistics for the energy levels 1 and 2 as

$$f_1(E_1) = \frac{1}{1+e^{(E_1-E_f)/k_BT}}, \tag{2.23}$$

$$f_2(E_2) = \frac{1}{1+e^{(E_2-E_f)/k_BT}}, \tag{2.24}$$

where $E_f$ is the quasi-Fermi level and $K_BT$ is the Boltzmann energy. We then have

$$\frac{f_1(1-f_2)}{f_2(1-f_1)} = \frac{1+e^{(E_2-E_f)/k_BT}}{1+e^{(E_1-E_f)/k_BT}} = e^{(E_2-E_1)/k_BT}. \tag{2.25}$$

So from Equation 2.22, we obtain

$$A_{21} = (B_{12}e^{(E_2-E_1)/k_BT} - B_{21})P(E_{21}). \tag{2.26}$$

now we can rewrite $P(E_{21})$ as

$$P(E_{21}) = N_{ph}(E_{21})n_{ph} = N_{ph}(E_{21})\frac{1}{e^{(E_2-E_1)/k_BT}-1}. \tag{2.27}$$

From Equations 2.26 and 2.27, we get

$$\frac{A_{21}}{B_{12}e^{E_{21}/K_BT} - B_{21}} = P(E_{21}) = N_{ph}(E_{21})\frac{1}{e^{E_{21}/k_BT}-1}. \tag{2.28}$$

The only way this can be true for all values of T is if

$$B_{12} = B_{21}, \tag{2.29}$$

and

$$\frac{A_{21}}{B_{21}} = N_{ph}(E_{21}). \tag{2.30}$$

From Equation 2.30, we can see that the A and B coefficients in the spontaneous and stimulated emission rates are related to the available number of photonic densities of states.

#### 2.1.5.2 Absorption, stimulated and Spontaneous Emission Rates

In a semiconductor material instead of having a single discrete state, we are dealing with a continuum of states in the conduction and valence bands. Also, the incident photons do not have just a single energy and they spread over a certain energy range. The absorption rate per unit volume is given by Equation 2.17. The net absorption independent of spontaneous emission is

$$R_{12}^{abs-net} = R_{12}^{abs} - R_{21}^{stim} = B_{21}N_{ph}(E_{21})(f_1 - f_2)n_{ph}. \tag{2.31}$$

By integrating over the incident energy range, we obtain the net absorption as

$$R_{21}^{abs-net} = \int B_{21}N_{ph}(E_{21})(f_1 - f_2)\delta(E_{21} - E)n_{ph}dE, \tag{2.32}$$

Where the delta function is added to describe only the transitions with energies equal to $E_{21}$.e spontaneous emission rate per unit volume for a discrete state is given by Equation 2.19 as

$$R_{21}^{spon} = A_{21}f_2(1 - f_1). \tag{2.33}$$

Using Equation 2.30, we can rewrite the spontaneous emission rate as

$$R_{21}^{spon} = N_{ph}B_{21}(E_{21})f_2(1 - f_1). \tag{2.34}$$

Similar to the net absorption, by integrating over the energies, we can rewrite the spontaneous emission rate as

$$R_{21}^{spon} = \int N_{ph}B_{21}(E_{21})f_2(1 - f_1)\delta(E_{21} - E)dE. \tag{2.35}$$

Similarly, the rate of stimulated emission is obtained by assuming that the stimulated emission rate is equal to the net absorption rate when spontaneous emission is neglected.

$$R_{21}^{stim} = \int B_{21}N_{ph}(E_{21})(f_2 - f_1)\delta(E_{21} - E)n_{ph}dE. \tag{2.36}$$

In Chapter 3, we will provide an in-depth exploration of optical processes in quantum-well semiconductors. We will delve into detailed explanations of how to calculate the photonic density of states $N_{ph}$, coefficient $B_{21}$, and how to incorporate the spontaneous emission linewidth into the equations. Ultimately, we will derive a comprehensive expression for gain, absorption, and the rate of spontaneous emission.

In the next section, we will discuss how semiconductor materials with different dimensions have various optical characteristics. We also investigate the impact of using lower-dimension semiconductors on the laser behavior when they are used as the gain medium.

## 2.2 Lower-dimensional Gain Media

With recent developments in the field of nanofabrication, we have witnessed a paradigm shift towards favoring small-sized lasers. As technology advances, the demand for compact and integrated solutions intensifies. Small lasers enable the creation of intricate and densely packed optoelectronic circuits, where multiple components can coexist on a single chip.

Simultaneously, it was realized that achieving superior device performance such as lower threshold and higher coupling efficiency could be accomplished by reducing the size of the gain medium to nanometer-scale in one or more directions. This discovery marked the inception of the field of lower-dimensional semiconductor lasers, including innovations such as quantum-well (QW), quantum-wire (QWR), and quantum-dot (QD) lasers.

When the thickness of the active medium is reduced to the order of the carrier de Broglie wavelength ($\lambda = h/p$, $p$ is the momentum), the motion of the carriers is confined in one or more directions. The geometrical constraints impose boundaries on the motion of electrons, causing them to adjust their energy levels in response to these constraints. This phenomenon is known as the quantum confinement effect which plays a crucial role in defining the unique properties of quantum wells, quantum wires, and quantum dot lasers [59].

As illustrated in Figure 2.8, a quantum well arises when the active medium is confined in a single direction. This arrangement restricts the electrons and holes motion to a thin layer. On the other hand, a quantum wire is referred to as a gain media with confinement in two dimensions. Here, electron and hole movement is constrained to a narrow wire-like region. The most intricate confinement scenario exists in the formation of quantum dots when the active region is confined in all three dimensions. In a quantum dot, electrons and holes are confined within tiny, isolated regions, yielding discrete atom-like energy levels.

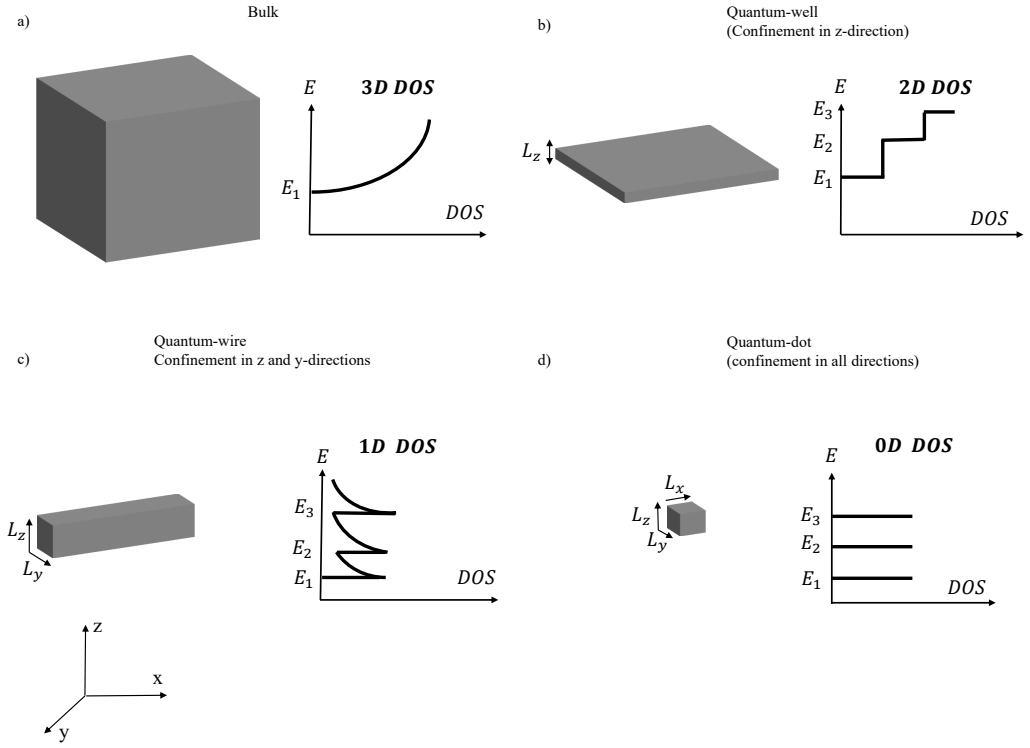


Figure 2.8: Schematic representation of a) bulk, b) quantum-well, c) quantum wire, and d) quantum dot gain media

As we reduce the size of the gain media from bulk to quantum well, quantum wire, or quantum dot, the properties of the gain medium change significantly. In bulk semiconductors, the gain media is a relatively thick layer of direct bandgap material with a 3D continuous parabolic

DOS as presented in Figure 2.8a [57] and it is defined as

$$\rho_r^{3D}(E)dE = \frac{1}{2\pi^2}(\frac{2m_r^*}{\hbar^2})^{3/2}(E - E_g)^{1/2}dE, \tag{2.37}$$

In a quantum well structure, the continuous energy states in the conduction and the valence bands are altered, transforming into discrete energy levels. Each energy level has a 2D density of states equal to $\frac{m_r^*}{\pi\hbar^2}$, which leads to a step-like DOS as illustrated in Figure 2.8b. The electronic density of states in a quantum well is defined as

$$\rho_r^{2D}(E)dE = \frac{m_r^*}{\pi\hbar^2 L_z}dE, \tag{2.38}$$

where $m_r^*$ is the reduced mass of the electron, $L_z$ is the thickness of the quantum well, and $\hbar$ is the reduced Planck's constant.

In a quantum wire, carriers are confined in two dimensions and the carriers are free to move only in one direction (1D) as shown in Figure 2.8c. Due to the confinement in two directions, the electronic density of states in quantum wires lies between the continuous energy states of bulk and the discrete energy states of quantum wells, and it is obtained as

$$\rho_r^{1D}dE = \frac{1}{\pi L_z L_y}(\frac{2m_r^*}{\hbar^2})^{1/2}\frac{1}{\sqrt{E}}dE, \tag{2.39}$$

where $L_z$ and $L_y$ are the confined lengths of the quantum wire, $m_r^*$ is the reduced mass of the electron, and $\hbar$ is the reduced Planck's constant.

Finally, in a quantum dot, due to the confinement in all directions (0D), a quantum dot density of states is similar to individual atoms or molecules, as shown in Figure 2.8d, and it is defined as

$$\rho_r^{0D}dE = 2\delta(E)dE \tag{2.40}$$

where $\delta(E)$ is the Dirac delta function.

Regarding material properties, bulk gain media have a continuous energy state distribution, therefore carriers are able to interact within a broad range of frequencies which can result in less control over the emission wavelength and broad emission linewidth. Quantum wells, quantum wires, and quantum dots offer more control over the emission wavelength and improved performance because of their modified DOS [60], [61].

## 2.3 Lower-dimensional Semiconductor Lasers

When such lower-dimensional gain media are embedded into a laser structure, they result in superior lasing properties such as having a lower threshold and being less temperature sensitive. This enhanced efficiency is mainly attributed to the higher concentration of carriers at the band edges due to the quantum confinement effect in the gain medium. However, there are several challenges in developing such lasers due to the complex physics and fabrication techniques involved in the growth of uniform and homogeneous nanoscale gain media [59], [62]–[65].

### 2.3.1 Quantum-well Semiconductor Lasers

A schematic image of a quantum wells laser is shown in Figure 2.9a. In the quantum well laser, a very thin (typically around 10-20nm) lower-bandgap active medium (well) is sandwiched

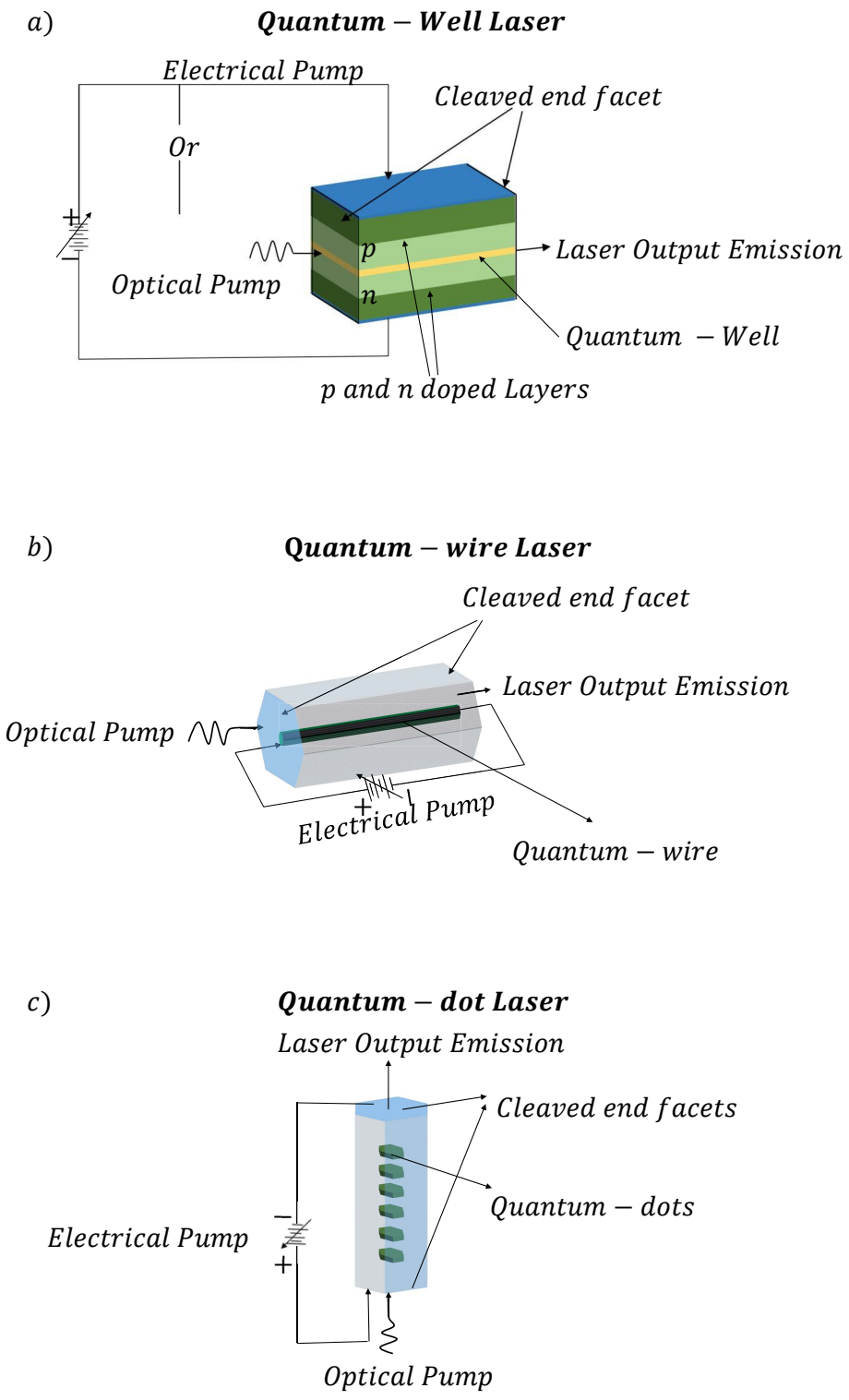


Figure 2.9: Schematic representations of typical a) quantum-well, b) Quantum-wire or nanowire, and c) quantum-dot Lasers.

between two lattice-matched cladding layers (barriers) of higher-bandgap material, which are n-doped and p-doped.

By sandwiching the active region between higher bandgap barriers, both electrons and holes are confined along the z-direction, resulting in discrete energy levels. As shown in Figure 2.10, the difference in the bandgap of cladding layers (barriers) and the active medium (well) creates a potential well that traps the charge carrier in the well region. The cladding layers are p-doped and n-doped to form a p-n junction, which allows the injection of electrons and holes into the active medium. Moreover, the resonant cavity is formed by cleaving the end facets at the ends of the structure perpendicular to the direction of propagation.

When the quantum well laser is under the pump, the p-n junction allows the injection of electrons and holes in the active medium. Here an optical gain is achieved via a series of stimulated emissions. this process is maximized when a high flux of photons sweeps an optical cavity with a high carrier density.

Optical confinement is necessary to take place both in lateral and transverse directions (parallel and normal to the junction). The dielectric constants of the layers are designed to confine the electromagnetic field in the well. The refractive index of the well is larger than the refractive index of the barriers and the cladding layers. This creates a structure similar to a slab waveguide which confines the field in the lateral direction while the cavity provides the optical confinement in the transverse direction.

The electromagnetic field partially leaks out and partially reflects back to the active medium at the interfaces. The quantum confinement of the charge carriers combined with the optical field confinement increases the probability of the interaction of the electrons and holes with the photons, thus substantially decreasing the threshold current to the order of around tens of milli-ampers enabling the laser to operate at room temperature.

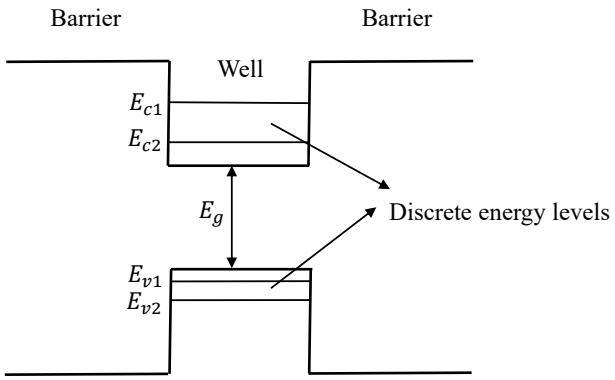


Figure 2.10: Schematic representation of a quantum well structure including the barriers and the well. The nanoscale thickness of the well, results in the quantum confinement effect resulting in discrete energy levels.

#### 2.3.1.1 State of the Art

Quantum well laser was proposed by Esaki and R. Tsu in 1969 [66], [67]. Quantum well lasers with a sole active region are referred to as single quantum well (SQW) lasers, while those

comprising multiple active regions are recognized as multiple-quantum-well (MQW) lasers. By using the MQW structure, a higher proportion of carriers can be trapped in the active layers. Therefore, the MQW laser has a lower threshold current and higher carrier density than the SQW laser, which leads to better performance [68]

The most common semiconductor materials that are used to fabricate single/multiple quantum well lasers are direct bandgap III-V semiconductors such as GaAs, InP, InGaAsP, AlGaAs, GaInN, and GaN. Significant shifts in optical properties, presenting opportunities to enhance laser design are achieved with different combinations and various strains within the band structure. Such semiconductors exhibit higher differential quantum efficiency as compared to regular Double Heterostructure (DHS) lasers [68].

Multiple quantum well lasers (MQWL) were introduced when Fuji reported a low threshold current density of 175 A/cm$^2$ with a 480 µm cavity length in a GaAs/AlGaAs graded refractive index-separate confinement heterostructure (GRIN-SCH) laser [69]. Threshold currents as low as 170 $A/cm^2$ at 45K is achieved with InGaAsP/InP multiple quantum wells laser, which is exceptionally smaller than the DHS lasers with threshold values around 1200 A/cm$^2$ [59].

Extensive research is done to effectively manage strain within the band structure which shows significant shifts in optical properties. This presents more opportunities to further enhance laser design. Such nanolasers incorporate gain mediums like $In_xGa_{1-x}As$ with compressive strain, while the barriers usually consist of GaAs [7].

Quantum well lasers are essential tools in telecommunications, optical networking, and spectroscopy. Furthermore, quantum well lasers drive advancements in emerging fields like quantum information processing and on-chip photonics, highlighting their significance across an array of applications that rely on efficient, tunable, and compact light sources.

However, the intricate process of material quality control presents its own set of challenges. The fabrication of quantum well material laser structures necessitates precise control over epitaxial growth and layer thickness to ensure uniformity and consistent material properties. Any deviations or defects during growth can lead to non-uniformities in the active region, impacting gain and emission characteristics. Achieving high-quality material growth on a consistent basis demands advanced techniques and robust quality control procedures, which often entail complex and meticulous processes. These will be discussed further in section 2.9.2.

### 2.3.2 Quantum-wire Semiconductor Lasers

Figure 2.9b represents a schematic of a hexagonal semiconductor laser with a quantum wire within a nanowire cavity The quantum wire laser is characterized by a transverse hexagonal cross-section, with dimensions in the nanometer range along both y and z-directions. This introduces the confinement of electrons and holes in two directions, contributing to the device's unique properties. The photons produced by electron-hole recombination bounce back and forth between the two end facets of the nanowire, inducing the emission of additional photons from the semiconductor material and amplifying the light intensity into a coherent, monochromatic light beam.

A key point worth mentioning here is that regardless of their similar structures, a quantum wire should not be mistaken for a nanowire. Quantum wires must have transverse dimensions of less than 30nm for quantum confinement to appear. While even the smallest nanowires have transverse dimensions of around 200nm [7]. One can consider the quantum wire as a special

type of nanowire with transverse dimensions small enough that quantum confinement occurs.

The larger density of states within the quasi-one-dimensional (1D) quantum wire subbands results in a higher differential gain and narrower line widths compared to the quantum well lasers [70]. Furthermore, the smaller size of the quantum wire lasers along with increased gain leads to the remarkably low threshold currents in the microampere current spectrum [71], [72].

#### 2.3.2.1 State of the Art

The first demonstration of an ultra-low-threshold AlGaAs/GaAs quantum Wire-like laser was presented by Hasegawa in 1994 [73] which had a threshold at around 10-16 mA. However, with the advances in the field of design and fabrication, thresholds as low as 0.6 mA are also achieved at room temperatures [74].

Quantum wire lasers benefit from their small dimensions, leading to reduced threshold currents and enhanced energy efficiency. The confined geometry also aids in efficient carrier transport, contributing to lower threshold currents [75]. However, the fabrication of quantum wire lasers can be challenging due to the need for well-controlled and uniform wire-like structures. Techniques such as selective-area growth or self-assembled growth can be employed [76].

### 2.3.3 Quantum-dot Semiconductor Lasers

Figure 2.9c is a schematic of a multiple quantum-dot laser in which quantum dots are embedded inside a hexagonal nanowire cavity. The size of the quantum dots is usually from 2 to 10 nanometers in all directions. Due to their small dimensions, 3D confinement of electrons and holes is achieved, leading to discrete energy levels and size-tunable emission spectra.

As shown in Figure 2.8c, in a quantum-dot laser, the quantum dots are embedded within another semiconductor material (cladding layers). Cladding layers have a higher band gap compared to quantum dots, and they play a critical role in the confinement of carriers (electrons and holes) and optical modes. They act as a barrier preventing the carriers from escaping, increasing their probability of recombining in the quantum dots and enhancing light emission efficiency.

#### 2.3.3.1 State of the Art

Quantum dot lasers were originally proposed by Arakawa and Sakaki in 1982 [77], and later validated in 1994 by Kirstaedter [78] and Mirin [79]. However, the first demonstrations of the quantum dot laser required a large threshold power near $7.6kA/cm^2$ at 77K [80] which is even higher than the threshold required for quantum well lasers.

The most common quantum dots are fabricated with In(Ga)As deposited on GaAs or InP substrates and their operating range of frequency is between 1 $\mu m$ to 1.8 $\mu m$ [81]. However, moving toward long wavelengths is quite challenging due to the crystal quality degrading and the phase separation in quantum dot lasers. Thermal broadening is also one of the challenges in the design and fabrication of quantum dot lasers.

With the advances in fabrication techniques, highly uniform quantum dots with high crystal quality were grown that unlocked the possibilities for the exploration of the low threshold quantum dot lasers (around 120 $A/cm^2$ [78]) for near-infrared semiconductor lasers towards the optical communication applications. These advantages manifest as ultralow threshold currents [82], capability to operate in high-temperature [83], and higher gain suitable for applications such as semiconductor optical amplifiers and mode-locked lasers [84].

Furthermore, the inherent insensitivity of quantum dot lasers to crystalline defects enhances their reliability and resilience, making them less susceptible to performance degradation caused by imperfections in the material [85]. Quantum dot lasers are compatible with silicon integration. Their resilience to defects permits epitaxial integration on silicon substrates, which holds great promise for the integration of lasers in silicon photonics integrated circuits (PICs). Each of these characteristics stems from the distinct three-dimensional confinement of carriers within quantum dots, leading to a delta-function-like density of states and inhomogeneously broadened gain spectra [81].

The size, shape, and strain profile of a quantum dot can be altered mostly with material selection, and growth conditions. Such modifications can result in significant changes in the energy of band level, transition energies, and the available number of states in quantum dots [86], [87]. This tunability allows for precise control over the emission wavelength, enabling the lasers to emit light at specific frequencies within a wide spectral range.

One of the pivotal areas of exploration within this context revolves around the integration of lower-dimensional gain media into nanowire structures. This endeavor represents a significant advance, as it takes advantage of the unique properties of nanowires, such as their high surface-to-volume ratio and enhanced carrier confinement, to create highly efficient and compact laser sources. In section 2.7, we will delve into the exploration of incorporating lower-dimensional gain media into nanowire structures, unraveling the potential benefits and technological advancements that this convergence can bring to the forefront of laser technology.

In the following section, we will delve into essential concepts that provide a foundation for understanding laser behavior. We will address cavity-related parameters and those associated with the gain medium. Moreover, we will investigate each of the parameters used to evaluate laser characteristics.

## 2.4 Key Laser Properties

### 2.4.1 Threshold Condition

As discussed in section 2.2, for a gain medium to amplify the incident radiation via stimulated emission, population inversion should be created. Such a medium acts as an amplifier for frequencies falling within its linewidth when it is pumped. To generate stimulated emission, the gain medium is placed within an optical cavity. A cavity in its simplest form consists of a pair of reflective surfaces facing each other, forming a Fabry–Perot resonator as illustrated in Figure 2.11.

Radiation that reflects back and forth between the reflective surfaces undergoes both amplification from the active medium and losses due to mirror reflectivity and other scattering effects. To maintain sustained oscillations within the cavity, the losses should be equal to the gain. Thus, a minimum population inversion density is needed to overcome the losses, known as the threshold population inversion.

To formulate an expression for the threshold condition, we consider a Fabry-Perot cavity with lengths $d$, $R_1$, and $R_2$ being the reflectivities of the end facets as presented in Figure 2.11. Here, $\alpha$ represents the overall loss mechanisms, including the scattering and diffraction loss due to the finite size of the end facet, and the gain coefficient $\gamma$ represents the amplification. When a radiation beam with an initial intensity of $I_0$ at the facet $R_1$ propagates through the medium

and reaches the second mirror, it experiences both amplification and attenuation by $I_0 e^{(\gamma-\alpha)d}$.

The intensity of the beam upon reflection at the second mirror can be expressed as $R_2 I_0 e^{(\gamma-\alpha)d}$. After a second passage through the resonator and reflection at the first mirror, the radiation's intensity following one complete round trip is given by $R_1 R_2 I_0 e^{2(\gamma-\alpha)d}$. Lasing is achieved when

$$R_1 R_2 I_0 e^{2(\gamma-\alpha)d} \geq 1 \tag{2.41}$$

The equality sign represents the threshold condition of the laser when the gain is equal to the loss. The carrier density corresponding to this condition is called the threshold population inversion [88].

It is worth mentioning that before threshold, spontaneous emission and absorption are the dominant optical processes within the laser. However, when the threshold condition is satisfied the stimulated emission will take over, and lasing is achieved [88].

Another threshold definition given by Yamamoto [89] is where the rate of stimulated emission equals the rate of spontaneous emission. The idea behind this approach lies in the fact that, at this particular pump level, half of the emitted photons within the mode will produce a coherent emission, while the other half will contribute noncoherently. As pumping intensity increases, both coherence and quantum efficiency will experience swift enhancement due to the substantial growth of stimulated emission. This definition of the threshold implies that the average number of photons inside the cavity reaches unity at the threshold.

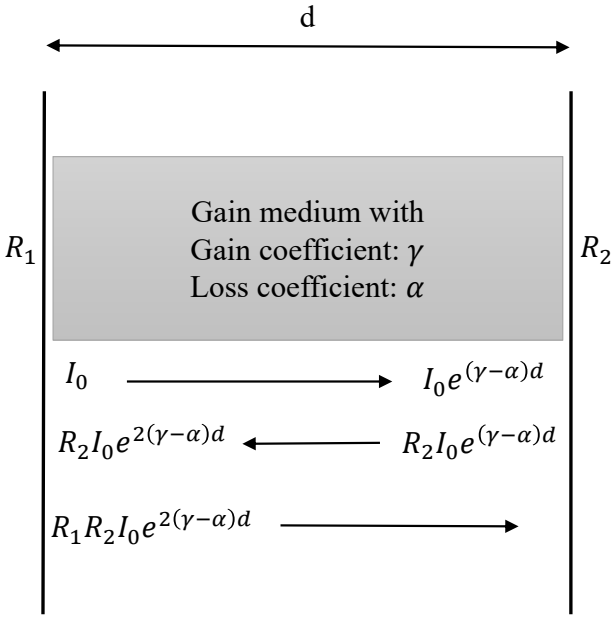


Figure 2.11: A typical Fabry-Perot cavity consisting of a pair of mirrors facing each other. The active medium is placed inside the cavity (shown with grey color).

### 2.4.2 Quality Factor ($Q$) and Photon Lifetime ($\tau_p$)

The quality factor ($Q$-factor) is a unitless parameter that describes the relationship between the energy stored, and energy dissipated from the optical cavity. A higher $Q$ value indicates a lower rate of energy loss in relation to the energy stored within the resonator. Consequently, a high-$Q$ cavity can retain light for an extended duration before it escapes, providing more opportunities for light to interact with the gain medium, leading to enhanced laser performance.

The quality factor is defined as [88]

$$Q = \omega \frac{W(t)}{-dW/dt}, \tag{2.42}$$

where $\omega$ represents the angular frequency of the resonant mode of the cavity, $W(t)$ is the energy stored in the mode, and $-dW/dt$ determines the rate of energy loss from the cavity.

The $Q$ factor associated with the resonant mode's linewidth is

$$Q = \frac{v}{\Delta v}, \tag{2.43}$$

where $v$ is the resonant frequency and $\Delta v$ is the emission linewidth.

High-Q cavities can produce laser beams with narrower line widths, which is particularly beneficial in applications requiring precise spectral control. When designing laser cavities, it is crucial to consider the quality factor as a parameter having a considerable impact on the laser threshold.

Photon lifetime,$\tau_p$, is a parameter directly linked to the quality factor. This measures the average time a photon spends inside the laser cavity before it is emitted. It is fundamentally related to the laser cavity's loss mechanisms, including transmission losses through the laser mirrors and scattering, and is calculated as [34]

$$\tau_p = \frac{Q}{\omega}. \tag{2.44}$$

A short photon lifetime means that photons are quickly emitted from the cavity after their creation. This can result in lower laser efficiency due to the fact that the cavity is not able to properly store energy. Conversely, a long photon lifetime provides more time for the energy to build up inside the cavity, resulting in a higher interaction between the photons and the active medium, and potentially increasing the laser's output power.

### 2.4.3 Linewidth

A key property of lasers is their ability to produce light in a narrow spectral frequency range. The finite spectral range observed in a laser operating continuously within a single mode can be attributed to two primary mechanisms. Firstly, external factors like temperature fluctuations and vibrations can disturb the laser cavity, causing frequency changes in the oscillations and leading to a limited spectral range [88]. The second, more fundamental mechanism governing the laser's ultimate spectral range is linked to the inherent occurrence of random spontaneous emissions within the cavity [88].

The linewidth of the cavity corresponds to the frequency of the resonant mode divided by the quality factor as [88]

$$\delta v = \frac{v}{Q}. \tag{2.45}$$

When the laser operates below the threshold, due to the dominance of the spontaneous emission process, the output light of the laser is relatively broad. As the laser approaches the threshold, the linewidth gradually becomes narrower as stimulated emissions take over. Once the threshold is achieved, the laser's output light coherence from stimulated emitted photons results in a

considerably narrower linewidth compared to its operation below the threshold. However, the Schawlow-Townes limit offers a boundary for the minimum achievable linewidth of a laser's output. This limit defines the narrowest range of frequencies that a laser can emit while maintaining a coherent and monochromatic beam as [40]

$$\delta v = \frac{4\pi h v (\delta_c)^2}{P_{out}}, \tag{2.46}$$

where $\delta_c$ is the FWHM of the linewidth in the passive cavity, $v$ is the resonant frequency, and $P_{out}$ is the output power.

### 2.4.4 Confinement Factor ($\Gamma$)

The confinement factor,$\Gamma$, describes how much of the optical field is confined within the gain medium. The confinement factor varies from zero to unity. A higher confinement factor indicates a stronger interaction between the electromagnetic field and the gain medium, which leads to enhanced performance in terms of the lasing threshold, modulation bandwidth, and overall efficiency.

The confinement factor of the cavity is defined as the ratio of the electric field that overlaps with the gain medium to the field in the entire geometry [34]

$$\Gamma = \frac{\int_{active-medium} ||\vec{E}||^2 dV}{\int_{All-domains} ||\vec{E}||^2 dV} \tag{2.47}$$

The confinement factor is primarily determined by the refractive index contrast between the active region and the surrounding cladding layers. The larger the refractive index contrast, the tighter the mode confinement and the higher the confinement factor. In a conventional bulk semiconductor laser, the value of the confinement factor is typically equal to 1. However, in lower-dimensional semiconductor lasers, the value of $\Gamma$ is decreased to the order of 1-2% due to the reduced size of the active region [6].

### 2.4.5 Transparency Carrier Density ($N_{tr}$)

Transparency carrier density determines the density of charge carriers within a semiconductor material which leads to the material becoming optically transparent. This specific carrier density signifies the point where the gain and loss mechanisms within the semiconductor are almost equal to each other, resulting in reduced absorption and the initiation of laser emission.

It is worth mentioning that the transparency carrier density is not the same as the threshold carrier density. While the two values are very close to each other, the transparency carrier density is usually a bit smaller than the value of the threshold carrier density.

### 2.4.6 Spontaneous Emission Lifetime ($\tau_{sp}$)

As discussed in section 2.2.4, spontaneous emission describes the process wherein an electron spontaneously loses its energy in the form of a photon and drops from the conduction band into the valence band.

The photons resulting from spontaneous emission within a material, are often emitted in different directions and wavelengths. Spontaneous emission lifetime ($\tau_{sp}$) is the average time that an excited electron spends at a higher energy level before it decays due to spontaneous emission.

According to the Purcell effect, spontaneous emission lifetime can be significantly affected when the atom or molecule is placed within a cavity [90]. Therefore, the spontaneous emission lifetime is described as the inverse of the sum of the spontaneous emission rates into the different modes of the cavity ($A_i$) as [46], [89]

$$\tau_{sp} = \frac{1}{\Sigma_i A_i} \tag{2.48}$$

Spontaneous emission rates into the different modes of the cavity are related to the photonic density of states in Equation 2.30. By considering all the resonant modes of the cavity and all the available energy states within the conduction and valence band one is able to obtain the spontaneous emission lifetime. We will discuss this further in Chapter 3.

The spontaneous emission lifetime is a crucial parameter in understanding the decay behavior of excited states in various systems. It is directly related to the quantum mechanical probabilities of transitions between energy levels and provides insights into the overall dynamics of the system. In Chapter 3, we will discuss the spontaneous emission lifetime in lower-dimensional lasers in great detail.

### 2.4.7 Spontaneous Emission Factor ($\beta$)

The spontaneous emission factor $\beta$ is the spontaneous emission rate ratio into the lasing mode ($A_0$) divided by the total spontaneous emission rates [46]

$$\beta = \frac{A_0}{\sum_i A_i} \tag{2.49}$$

The parameter $\beta$ provides an estimation of how much of the total spontaneous emissions couple to the lasing mode. The spontaneous emission factor directly affects the coupling efficiency of the laser and the pump power required to reach the lasing threshold. The value of the parameter $\beta$ varies from zero to unity. As the value of $\beta$ gets closer to the unity, it means that more spontaneous emissions couple to the lasing mode.

Although $\beta$ equal to unity is not achievable, increasing the value of $\beta$ brings us one step closer to the ideal thresholdless laser, implying that less energy is required for the laser to begin operating. The parameter $\beta$ is particularly significant for lasers on the micro and nanoscale, where managing energy efficiently is a high priority, and even a slight change in a parameter leads to a noticeable change in the laser behavior. Moreover, the spontaneous emission factor also shapes the laser's noise profile, influencing aspects like the linewidth (FWHM) of the laser emission.

For a bulk semiconductor laser, $\beta$ can be calculated as [89]

$$\beta = \frac{\lambda^4}{4\pi^2 V \Delta\lambda \epsilon^{3/2}}, \tag{2.50}$$

where $\lambda$ is the emission wavelength, $V$ is the volume of the active medium, $\Delta\lambda$ is the linewidth, and $\epsilon$ is the permittivity in the active medium.

Free space photonic density of states is assumed to estimate $\beta$ in Equation 2.50. However, when a lower dimensional gain media is embedded inside the cavity, the effect of the cavity manifests as an increase in the number of available photonic density of states, making it challenging to express $\beta$ as a straightforward equation.

As a result, in most laser analyses, $\beta$ is treated as a fitting parameter which is determined after the laser is fabricated and characterized. This approach restricts the opportunity for laser optimization. Complex mathematical calculations are required to estimate $\beta$ for lower dimensional semiconductor lasers. We will propose an equation to calculate $\beta$ in Chapter 3.

### 2.4.8 Purcell Factor $F_p$

The Purcell factor $F_p$ quantifies the enhancement of a light-emitting system's spontaneous emission rate due to the presence of a resonant cavity. The Purcell factor $F_p$, is defined as the ratio of the spontaneous emission rate inside the cavity to the rate in the absence of the cavity. The conventional form of the Purcell factor is given by [90] as

$$F_p = \frac{3}{4\pi^2}\frac{Q}{V_m}(\frac{\lambda}{n})^3 \tag{2.51}$$

where $Q$ is the quality factor, $V_m$ is the mode volume, $\lambda$ is the resonant wavelength, and $n$ is the refractive index of the cavity.

In bulk semiconductor lasers, the Purcell factor is relatively small, and in most cases, is close to unity. The spontaneous emission rate in bulk lasers is primarily determined by the radiative recombination of electron-hole pairs within the active region, which can be relatively slow due to extended carrier lifetimes.

However, Equation 2.50 is not valid in the case of lower-dimensional semiconductor lasers. This is firstly due to the fact that the spontaneous emission lifetime in lower dimensional gain media is affected by the size of the gain medium as will be discussed in Chapter 3. Secondly, the spontaneous emission lifetime can be significantly decreased when the active region is located inside a cavity that is smaller in size when compared to the cavity of the bulk semiconductor lasers. In Chapter 3, we will investigate the effect of the Purcell factor in lower-dimensional lasers.

### 2.4.9 Non-radiative Lifetime ($\tau_{nr}$)

Non-radiative recombination processes refer to process where electrons and holes recombine without emitting photons. This contrasts with radiative recombination, where electron-hole recombination leads to photon emission [91].

Non-radiative processes are essentially energy losses since the energy from the recombination is transferred to other forms, such as lattice vibrations or heat, rather than useful light output. Non-radiative recombination can be categorized into different types, such as Auger recombination and Shockley-Read-Hall (SRH) recombination [92], [93]. Auger recombination is a three-particle process involving two carriers of one type (either two electrons or two holes) and a single carrier of the opposite type. When an electron and hole recombine, the excess energy is transferred to the third carrier, exciting it without emitting a photon [94], [95].

In SRH recombination, recombination occurs via defect states in the semiconductor's bandgap. A defect state first traps the electron or hole and then recombines with a carrier of the opposite

type, releasing the energy as heat [96]–[99].

The non-radiative lifetime $\tau_{nr}$ is defined as the average time carriers exist before recombining non-radiatively through non-radiative processes [34], [57]. A longer non-radiative lifetime implies carriers have more time to participate in radiative recombination, improving device efficiency. Several factors, including material defects, contaminants, and temperature, can affect the non-radiative lifetime. It's important to suppress the non-radiative recombination (by having large $\tau_{nr}$) in order to boost laser performance. One approach to achieve this is through careful material selection and semiconductor growth processes. Certain materials are inherently less prone to non-radiative processes, while high-quality semiconductor growth techniques can minimize defect states that facilitate SRH recombination.

Apart from material properties, the operation temperature can remarkably influence the non-radiative recombination because non-radiative recombination processes often produce heat. In lasers operating at cryogenic temperature, non-radiative recombinations are suppressed. In the theoretical models, when the non-radiative lifetime is roughly a hundred times larger than the spontaneous emission lifetime, it can be assumed that the non-radiative processes are neglected.

With a grasp of the fundamental principles behind semiconductor lasers and their operational physics, the next section will delve into the latest developments in the field of semiconductor lasers with low-dimension gain media.

## 2.5 State of the Art of Semiconductor Lasers

In this section, we will discuss the latest developments in the field of semiconductor lasers. Since this thesis focuses on the behavior of nanowire lasers, we will present an extensive review of the nanowire lasers and the challenges associated with them.

The first semiconductor laser was introduced in the 1960s, as a form of slab waveguide [100], [101]. Since then, advances in the semiconductor laser field aimed at creating higher output powers, more temperature stability, and compact sizes on the order of micro and nanometer scales. In the field of optoelectronics, semiconductor lasers have an undeniable role in communication technology, serving as the light source for optical fiber communication systems [51]. Additionally, semiconductor lasers are also used in applications like laser printers [102], laser TV [103], and medical applications such as plastic surgery, ophthalmology, and physical therapy [104].

However, like any other technology, semiconductor lasers come with challenges. These lasers require large input currents and their operation generates heat, which can affect their efficiency and the lifetime of the laser. Achieving integrated photonics using Si as the substrate has always been a challenge. The mismatch in crystal structure between standard III-V semiconductors (such as GaAs, InP) and Si has hindered the direct growth of high-quality III-V semiconductor films on Si using various growth methods [105]. Additionally, issues related to beam quality, divergence, and coherence can limit their use in certain applications. Sensitivity to external factors, such as temperature fluctuations and current variations, necessitates careful design and control of the laser system [64].

The reduction in size has been achieved through the continuous introduction of new laser cavities.[64], [105]. This resulted in the emergence of innovative device types like vertical-cavity surface-emitting lasers (VCSEL) [106], [107], microdisk lasers [108], [109], photonic crystal lasers

[110], [111], and semiconductor nanowire lasers [112], [113]. The schematic representations of these lasers are presented in Figure 2.12.

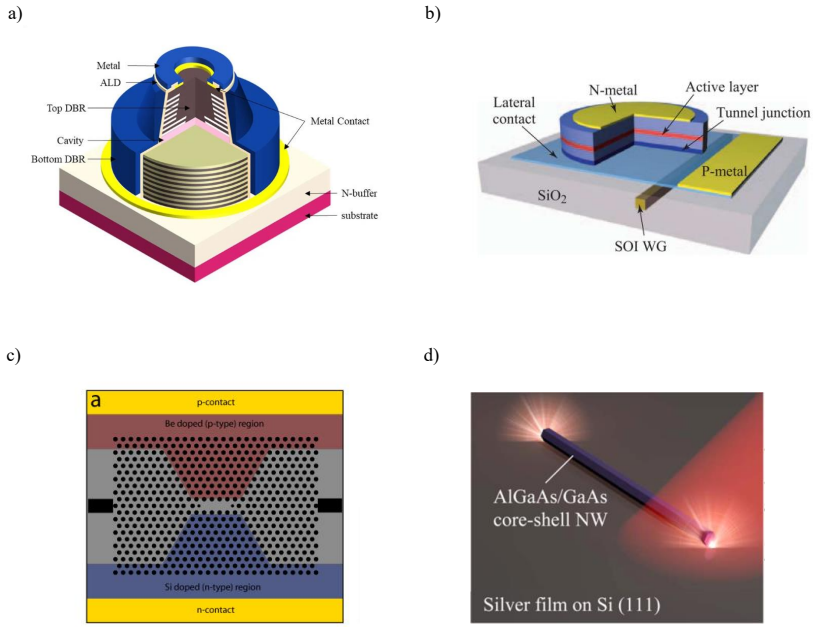


Figure 2.12: Schematic representation of a) VCSEL [114], b) microdisk [115], c) photonic crystal cavity [116], and d) nanowire lasers [117].

VCSELs bring about a significant size reduction, reducing the overall device volume by at least a factor of ten compared to conventional semiconductor lasers and they are one of the most energy-efficient types of semiconductor lasers [105]. VCSELs typically have diameters ranging from $2\mu m$ to $10\mu m$ and a combined thickness of Distributed Bragg Reflectors (DBRs) spanning $5\mu m$ to $10\mu m$ [105]. However, due to the limitations in effectively dissipating heat through the thick DBR mirrors and the confined lateral confinement within VCSEL structures, VCSELs face difficulties in meeting the persistent demands for on-chip applications [118]–[120].

Microdisk lasers originated from using a self-supporting piece of semiconductor material that harnessed whispering-gallery modes [121]. The large difference in refractive indices between the semiconductor and air allows optimal mode confinement without needing DBRs [122]. Microdisk devices typically have diameters ranging from $3\mu m$ to $5\mu m$ and are about one-micron thick [105].

Photonic crystal lasers are energy-efficient due to their small optical mode volumes. The distinct feature of photonic crystal lasers is having a very low threshold [123]. The overall dimensions of photonic crystal structures are around $10\mu m$ in diameter or side length [124], [125].

Semiconductor nanowires provide notably enhanced mode confinement compared to typical double-heterostructure designs [126]. When both ends of these nanowires are exposed to air, a unique configuration emerges that combines a formation of the laser cavity and the gain medium simultaneously which is an ideal combination for shrinking the laser size [127]. Nanowire laser dimensions are usually between 200-500nm in diameter and a few microns in length [112]. An additional advantage of nanowire lasers lies in their material and bandgap flexibility, enabling

lasing at wavelengths that are hard to achieve using either the microdisk or photonic crystal methods [105].

Achieving size reduction while maintaining a high energy efficiency requires a comprehensive strategy that encompasses design of the cavity and gain medium. Decreasing the dimensionality of the active region from bulk to quantum wells, quantum wires, and quantum dots enhances the population of electrons and holes within a specific energy range. The combination of nanoscale cavities such as nanowires with lower-dimensional gain media creates the smallest and most efficient lasers.

## 2.6 Semiconductor Nanowire Lasers

### 2.6.1 Advantages and Challenges

The field of semiconductor nanowire lasers began to take shape when room-temperature ultraviolet lasing was demonstrated in self-organized Zinc oxide (ZnO) nanowire arrays [127]. The study of semiconductor nanowire lasers has expanded significantly since its beginning in 2001 [128], with researchers exploring various material systems and cavity configurations. A key goal has been to develop the tiniest photonic lasers, pushing the limits of laser miniaturization.

Additionally, scientific exploration is being directed toward improving nanowire lasers by lowering their lasing threshold, thus increasing their operational efficiency and stability. An important goal is the ability to merge nanowire lasers with silicon platforms, facilitating easy integration with current semiconductor technologies and setting the stage for creating sophisticated optoelectronic devices [112], [129].

Semiconductor nanowire lasers have been explored across various material systems, with early demonstrations employing III-V and II-VI semiconductor nanowires [130]–[132]. Room-temperature lasing via optical pumping has been achieved in GaN, CdS, and ZnO nanowires due to their strong exciton binding energy and high material gain at room temperature [133]–[135]. These innovative efforts, spearheaded by researchers from the chemistry and materials fields, inspired optoelectronics and semiconductor laser experts to develop nanowire lasers using III-V semiconductors [115], [133], [136]–[138]. The nanowire field advancements in time is presented in Figure 2.13.

However, realizing room-temperature lasing in III-V semiconductor nanowire lasers presented challenges, primarily because of material quality issues and competing nonradiative recombination processes such as Auger recombination. Overcoming these obstacles demanded persistent research and development, ultimately taking several years to achieve room-temperature III-V semiconductor nanowire lasers successfully by the combination of quantum confinement effects, improved heat dissipation, and precise material engineering [6], [139]–[141].

Since then, advances in material synthesis and fabrication techniques have significantly improved the performance of these nanowire lasers, leading to broader applicability and potential integration with existing optoelectronic devices and systems [47], [139], [142]–[146].

The experimental successes in the early days of nanowire lasers spurred interest in developing lasers capable of covering a more extensive range of wavelengths. By utilizing ternary and quaternary alloys in the construction of nanowires, the laser emission wavelength can be adjusted simply by altering the alloy composition, thus expanding the range of applications. In recent

studies, scientists have demonstrated nanowire lasers capable of emitting red and green light by modifying the alloy composition within a single nanowire [147], [148].

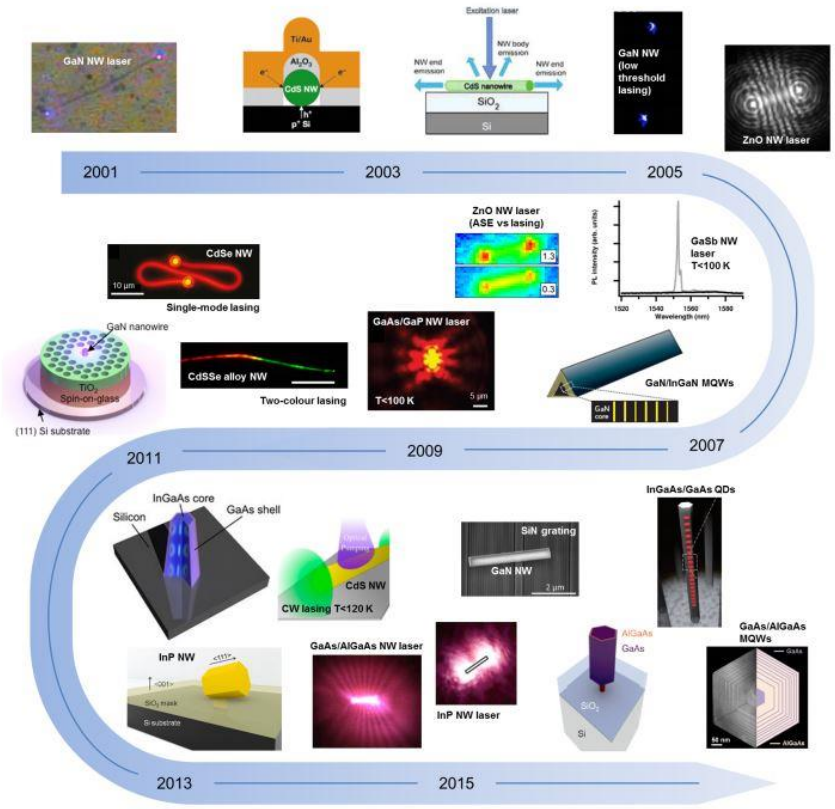


Figure 2.13: Timeline featuring several significant instances of lasing in single semiconductor nanowires. Reprinted from [149]

The successful lasing experiments in single-phase semiconductor nanowires encouraged researchers to investigate more advanced nanowire structures, which led to a significant development in this field: embedding single quantum-well (SQW)/quantum-dot (SQD) or multiple quantum-wells (MQW)/quantum-dots (MQD) inside the nanowires. These include core-shell, radial, and axial heterostructures, which enable the creation of nanowire lasers with quantum-confined active regions [64], [150]–[152]. Early quantum-well and quantum-dot nanowire laser demonstrations were realized using III-N heterostructure nanowires.

MQW/MQD nanowire lasers offer several advantages over their SQW/SQD counterparts beyond the increased density of available energy states for electron-hole recombination, which results in more efficient lasing [153]–[155]. MQW/MQD nanowire lasers also display enhanced gain and a broader gain spectrum compared to SQW/SQD lasers. This allows for better wavelength tunability, which is crucial for applications in wavelength-division multiplexing (WDM) systems and other areas requiring broad wavelength coverage. The spatial separation of the quantum wells/dots also contributes to better thermal stability and lower lasing thresholds [156], [157]. This separation helps to reduce the impact of nonradiative recombination processes and minimizes self-heating effects, which are common issues in single quantum well/quantum dot lasers. Altering the compositions of the MQW/MQDs embedded in the nanowire allows for lasing at different wavelengths. This versatility has opened up new possibilities for applications in telecommunications, sensing, and medicine [6], [158], [159].

### 2.6.2 Design and Fabrication Techniques

Semiconductor nanowire lasers are essential components in various photonics applications. The two common configurations for these lasers—horizontal or vertical with respect to the substrate—present unique benefits and challenges, and the choice between them often depends on the application and available fabrication techniques.

In the more commonly used horizontal configuration of nanowires on substrates, as shown in Figure 2.14a, the end facets of the nanowire form a Fabry-Perot cavity. The large contrast between the refractive index of the air (equal to unity) and the nanowire (typically around 3.6 for GaAs) creates a highly reflective cavity. The basic working principle relies on the phenomenon of multiple-wave interference. Light entering the cavity bounces back and forth between the two mirrors, creating a series of reflections that constructively interfere when the optical path length equals an integer multiple of the light's wavelength. This constructive interference leads to very high intensity, or resonance, at specific frequencies, allowing the cavity to act as a selective filter.

This setup offers several advantages, such as a reduced lasing threshold due to the high reflectivity at both end facets and effective coupling of laser emissions to nanophotonic or plasmonic waveguides. However, there is a significant challenge: the growth substrate usually differs from the low-index substrate used in optoelectronic or photonic device fabrication. Therefore, transferring and precisely placing the nanowires on the low-index substrate can be complex. This process often requires advanced nanofabrication techniques and specialized transfer equipment, such as electron-beam or nano-imprint lithography. These are high-tech procedures that require precision and can be time-consuming and costly.

On the other hand, the vertical configuration involves growing the nanowires upright on the substrate as presented in Figure 2.14b. This setup is more compact, making it particularly suitable for integration with silicon substrates, a key requirement for on-chip photonic integration where space is at a premium. However, this arrangement has a downside: the low refractive index contrast at the nanowire/substrate interface hinders the nanowire's ability to function as a proper F-P cavity. The electromagnetic field in this configuration tends to leak into the substrate at the nanowire/substrate end facet.

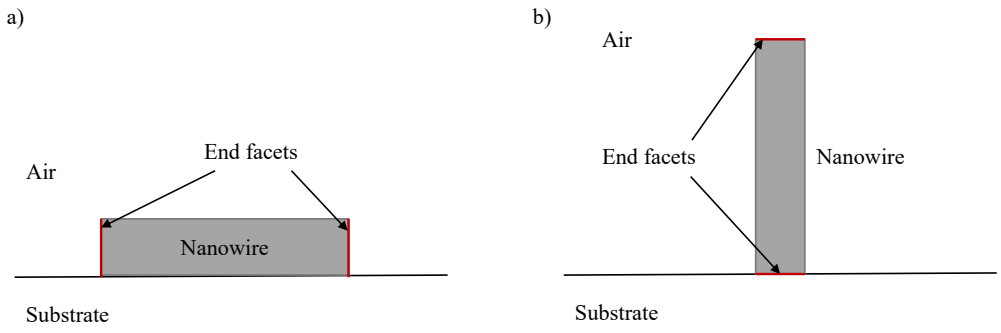


Figure 2.14: a) Horizontal and b) vertical nanowire configurations on the substrate

One method to provide optical feedback in the vertical configuration involves integrating a single nanowire into a defect within a photonic crystal cavity. In this arrangement, the nanowire

functions as the gain medium (the material that amplifies the light), while the photonic crystal provides the cavity necessary for lasing. This approach requires precise nanofabrication techniques to create the photonic crystal and accurately position the nanowire.

Researchers have grown nanowire lasers directly on silicon substrates by employing these methods [160]. This has improved performance characteristics, such as enhanced wavelength tunability ranging from 400nm to 1.5 $\mu m$ [148], decreased lasing thresholds, and increased thermal stability (maintaining performance at high temperatures). Nanowire lasers can now be used in various fields, including on-chip photonic integration, optical communications, sensing, and energy harvesting. As research progresses and new configurations and fabrication techniques are developed and optimized, we can expect further advances in the performance of nanowire lasers and their integration with different platforms. These advances will ultimately contribute to the development of next-generation photonic devices and systems, enabling faster, more efficient, and versatile optical technologies [47], [113], [161].

Fabrication of nanowire lasers involves several methods that include chemical vapor deposition (CVD), metal-organic chemical vapor deposition (MOCVD), molecular beam epitaxy (MBE), and vapor-liquid-solid (VLS) growth. These methods will be briefly discussed in the following subsections.

#### 2.6.2.1 Chemical Vapour Deposition (CVD)

Chemical Vapour Deposition (CVD) is the most widely used method for growing semiconductor nanowires. The process starts by heating a substrate in a reaction chamber to a specific temperature. Next, volatile precursors—chemicals that contribute atoms to the growing nanowire—are introduced into the chamber as vapor. These precursors react with each other or decompose on the heated substrate, resulting in nanowire growth. The growth rate, and therefore the length and thickness of the nanowire, can be controlled by adjusting parameters such as the temperature, pressure, and concentration of the precursors.

Different nanowires, including those made from silicon, germanium, and various III-V semiconductors, can be grown using this method. CVD is versatile, relatively straightforward, and compatible with existing semiconductor manufacturing processes. However, it requires a high degree of control over the reaction conditions and gas flow, making it technically challenging [162]–[167].

In CVD, the primary challenge lies in controlling the uniformity of the nanowire growth. The temperature, pressure, and gas flow rates must be precisely controlled. Additionally, the choice of precursor chemicals can greatly affect the properties of the resulting nanowires, so careful selection and handling of these precursors are necessary. Contamination is another concern, as unwanted particles in the reaction chamber can be incorporated into the growing nanowires, affecting their properties.

#### 2.6.2.2 Metal-Organic Chemical Vapor Deposition (MOCVD)

Metal-Organic Chemical Vapour Deposition (MOCVD) is a variation of CVD that uses metal-organic compounds as precursors. These compounds contain metals bonded to organic groups and can be used to deposit a wide range of semiconductors. MOCVD involves heating a substrate in a reaction chamber and introducing precursor gases like CVD.

The precursors decompose or react on the substrate, leaving a deposit forming on the nanowire.

The reaction can be enhanced by using a catalyst, which lowers the energy barrier for the reaction and allows the nanowire to grow at a lower temperature. MOCVD offers several advantages over other methods, such as the ability to grow high-quality, high-purity nanowires and the ability to control the composition and structure of the nanowires with a high degree of precision. [141], [143], [168]–[176].

While MOCVD provides greater control over the composition and structure of nanowires, it also introduces some challenges. The metal-organic precursors used in MOCVD are often quite sensitive and can decompose at room temperature or in the air, making them difficult to handle. Additionally, MOCVD processes typically require a higher temperature than CVD, which could lead to unwanted diffusion or alloying in the substrate or among different elements within the nanowires.

#### 2.6.2.3 Molecular Beam Epitaxy (MBE)

Molecular Beam Epitaxy (MBE) is another method for growing semiconductor nanowires. In MBE, beams of atoms are generated from solid or liquid sources and directed onto the growth substrate under ultra-high vacuum conditions. These atoms then react with each other to form a crystalline layer. MBE offers a high degree of control over the growth process, allowing for the fabrication of nanowires with complex structures and compositions.

This technique allows for the creation of nanowires with tailored dimensions and compositions for fabricating nanowires with embedded quantum wells and quantum dots, thus achieving quantum confinement effects. By carefully controlling the growth parameters, such as temperature and material flux, MBE can produce uniform quantum well and quantum dot structures within the nanowires [177]–[179].

It is particularly useful for growing nanowires from precursors that don't readily form volatile compounds, as required for CVD and MOCVD. MBE offers excellent control over the growth process, but it also presents its own set of challenges. The requirement for a high-vacuum environment makes MBE a complex and energy-intensive process. The process is also much slower than CVD and MOCVD, which can be a drawback for large-scale production. [180]–[184].

#### 2.6.2.4 Vapour-Liquid-Solid (VLS) Growth

Vapour-Liquid-Solid (VLS) growth is often used to grow semiconductor nanowires. In VLS, a tiny droplet of metal, often gold, is deposited on a substrate. This metal droplet acts as a catalyst. When exposed to a vapor of the desired semiconductor material, the metal droplet absorbs the vapor and forms a liquid eutectic alloy.

As more vapor is absorbed, the liquid becomes supersaturated, resulting in the precipitation of the excess as a solid nanowire that grows out of the catalyst particle. VLS growth can produce high-quality nanowires, but controlling the size and placement of the metal droplets that act as catalysts can be challenging.

These droplets often need to be deposited using techniques such as electron-beam lithography, which can be time-consuming and expensive. The choice of metal for the droplet is also critical, as different metals can influence the growth rate and properties of the nanowires. Furthermore, the metal catalyst may introduce impurities into the nanowires, affecting their optical and electrical properties [185]–[190]

One of the most significant challenges in all these methods is aligning and positioning the nanowires after growth. For many applications, the nanowires must be arranged in specific patterns or orientations, which can be difficult to achieve. Various techniques have been developed to address this, such as using electric or magnetic fields to guide the nanowires, but these add further complexity to the fabrication process. Despite these challenges, the fabrication methods for nanowire lasers have seen substantial advances over the years. Continued research and development in this field will overcome these obstacles, leading to more efficient, reliable, and cost-effective manufacturing processes for nanowire lasers.

### 2.6.3 Applications

To effectively develop semiconductor nanowire lasers, it is essential to determine their possible applications and optimize relevant performance parameters. Biological sensing has been one of the primary applications of nanowires. Their small dimensions allow for applications such as in cellular endoscopy, as Peidong Yang's group illustrated in 2011 [187].

Wu's 2018 proposal for intracellular nanowire laser applications showcased their potential in pH sensing due to the nonlinearity and sensitivity of lasers to their dielectric environment. Important factors for biological applications include small size, biologically inert materials, and visible wavelength lasing [126], [191]–[199].

Recent advances in growth techniques have sparked renewed interest in integrating nanolasers with heterogeneous substrates for on-chip photonic circuitry applications. The emergence of novel photonic architectures has increased the demand for coherent light sources in next-generation photonic computing.

Consequently, research into nanowire lasers that can be directly grown on silicon or optical waveguides has flourished. The capacity for heteroepitaxial growth with strain relief has introduced a third category of nanowire laser applications. These involve creating high-quality light sources using innovative materials like aluminum nitride or hybrid perovskites and integrating established materials such as indium gallium arsenide with more affordable substrates.

This has facilitated the development of deep-UV emitters and telecommunication-wavelength lasers. In the case of telecommunication-wavelength lasers, many research groups have focused on growing lasers on silicon or waveguides. Achieving single-mode, narrow linewidth, precise wavelength, high total power, and low-threshold operation is essential for these applications [171], [200]–[209].

In the forthcoming chapter, we will delve into the numerical approach and computational methodologies employed to explore the intricate behavior of lower-dimensional semiconductor lasers. We will start with the cavity simulations, delving into the fundamental aspects of laser cavities and their impact on device performance. Progressing further, we will delve into the intricate optical phenomena that arise within lower-dimensional gain media, shedding light on the complex interactions shaping laser behavior. Ultimately, our discussion will end with the analysis of laser rate equations, offering insight into the dynamic processes governing the operation of these sophisticated laser systems.

## 2.7 Laser Rate Equations

Laser rate equations are two interconnected differential equations that describe the interactions between photons and carriers within a semiconductor laser. By solving the laser rate equations we will be able to obtain the change in both carriers and photons with time along with the relationship between the input pump power versus the laser output power. In this section, we will investigate different forms of laser rate equations and their limitations. At the end, we will present the laser rate equations that we believe are best suited for lower-dimensional semiconductor lasers.

Different forms of laser rate equations exist in the literature to describe the behavior of semiconductor lasers. Starting with the bulk semiconductor laser[89] and nanopillars [47] to the lower dimensional semiconductor lasers such as multiple quantum well/dots embedded inside the nanowires[6], [117], [140].

The rate equations used by [6] to describe a quantum dots nanowire laser are

$$\frac{dN}{dt} = \sigma p(t) - \Gamma A_{tot} N - \frac{N}{\tau_{nr}} - A_{cavity} S(N - N_{tr}), \tag{2.52}$$

$$\frac{dS}{dt} = \Gamma A_{cavity} S(N - N_{tr}) + \beta A_{tot} N - \frac{S}{\tau_p}. \tag{2.53}$$

and the rate equations used by [117] for investigating a plasmonic nanowire laser are

$$\frac{dN}{dt} = \sigma p(t) - A_{tot} N - \frac{N}{\tau_{nr}} - \Gamma A_{cavity} S(N - N_{tr}), \tag{2.54}$$

$$\frac{dS}{dt} = \Gamma A_{cavity} S(N - N_{tr}) + \beta A_{tot} N - \frac{S}{\tau_p}, \tag{2.55}$$

in which $N$ is the number of carriers, $S$ is the number of photons, $\tau_n r$ is the non-radiative lifetime, $N_{tr}$ is the transparency carrier density, and $\sigma$ is the pump efficiency. The overall carrier decay rate, $A_{tot}$, is assumed to be approximately equal to the sum of $A_{cavity}$ and $A_0$ as

$$A_{tot} = A_{cavity} + A_0 \tag{2.56}$$

The equations above tend to describe the modification of spontaneous emission rates due to the presence of the cavity using the Purcell factor as a separate parameter in the rate equations. However, by comparing them in addressing the effect of the Purcell factor, we encounter a few challenges.

First, $A_0$ represents the rate of carrier decay into free space. $A_{cavity}$ denotes the rate of carrier decay into the cavity mode, and it's calculated as the product of the Purcell factor, $F$, and $A_0$. However, there is no information on how the Purcell factor is calculated.

Second, the use of confinement factor $\Gamma$ is completely inconsistent. In Equations 2.52-53, the confinement factor is used in the total carrier decay rate term ($\Gamma A_{tot} N$) while Equations 2.54-55 uses the confinement factor in the term describing the stimulated emission ($\Gamma A_{cavity} S(N - N_{tr})$).

In order to come up with our own rate equations that are suitable for quantum well nanowire lasers, we go through individual optical processes within the laser and present a theoretical term to describe it. First, we start with the pump. Since in the lower dimensional semiconductor

lasers, we are dealing with the cavities in the micro/nanometer regime, it is very challenging to attach the electrodes to achieve electrical pumping. Therefore most of these lasers are pumped optically. The incident pump power is presented as $P$, and the energy of a pump photon is $\hbar\omega$. Since the spot size of the pump laser is usually larger than the laser being pumped, all of the pump power is not able to interact with the carriers. Therefore, we introduce a term $\eta$ to represent the pump efficiency. Finally, since we want to write the rate equations in terms of per unit volume, we divide the term describing the pump by $V$ which represents the volume of the gain medium inside the cavity. All of this creates the first term of the rate equations ($\eta P/hvV$) which describes the rate of carriers being excited to the conduction band per unit time per unit volume.

In the next step, we will describe the spontaneous emission rate. As mentioned in section 2.2.4, the spontaneous emissions usually are emitted with different wavelengths and in different directions. The total spontaneous emission rate is obtained by the carrier density divided by the spontaneous emission lifetime ($N/\tau_{sp}$). A fraction of these spontaneous emissions are able to couple with the lasing mode of the cavity while some of them are emitted into the free space. Therefore, we can write the rate of spontaneous emissions into the lasing mode as $\beta N/\tau_{sp}$ and the rate of the spontaneous emissions that don't couple into the lasing mode as $(1-\beta)N/\tau_{sp}$. It is obvious that the sum of these two terms should be equal to the total spontaneous emission rate.

As mentioned in section 2.4.8, non-radiative processes are referred to as different processes that do not result in a photon emission. The rate of non-radiative emissions obtained using the non-radiative emission lifetime ($\tau_{nr}$) which is the average time it takes for a carrier to decay due to each of the non-radiative recombination processes. Auger recombination is one of the non-radiative processes which is more dominant compared to the others. If one is able to estimate the carrier decay rate due to the Auger recombination process, we can present the process in separate terms as $CN^3$ [47].

The stimulated emission term is obtained from the gain model. The gain model is developed from the gain spectrum of the material which will be extensively investigated in Chapter 4. The gain model describes the behavior of the gain medium as a function of carrier density ($g(N)$). However, one important factor to be considered here is that in the case of lower dimensional semiconductor lasers, the gain medium only exists in a small fraction within the cavity. Therefore, not all the electromagnetic field inside the cavity is able to interact with the gain medium. Therefore, we introduced the parameter ($\Gamma$) to take this into account.

The same processes will appear in the rate equation for the rate of change in the number of photons. However, the term photon lifetime ($\tau_p$) is added to this rate equation in order to consider the rate of the photons escaping the cavity.

Using all the information mentioned above, we propose our modified laser rate equations as

$$\frac{dN}{dt} = \frac{\eta P}{hvV} - (\frac{1-\beta}{\tau_{sp}} + \frac{\beta}{\tau_{sp}})N - \frac{N}{\tau_{nr}} - \Gamma g \frac{S}{V}, \tag{2.57}$$

$$\frac{dS}{dt} = \Gamma g S + \frac{\beta N V}{\tau_{sp}} - \frac{S}{\tau_p}, \tag{2.58}$$

where $N$ is the carrier density, and $S$ is the number of photons inside the cavity. The parameter $\eta$ is the fraction of pump power that is able to interact with the carriers, $hv$ is the energy of the

pump photon, $V$ is the volume of the active region, $\tau_{sp}$ is the spontaneous emission lifetime, $\beta$ is the spontaneous emission factor, $\tau_{nr}$ is the non-radiative recombination lifetime, $g$ is the active medium's gain, and $\tau_p$ is the photon lifetime.

The confinement factor in Equations 2.57 and 2.58 is calculated from three-dimensional simulations of the electromagnetic field in the cavity using Equation 2.47. The confinement factor here shows how much of the electric field can interact with the gain medium and depends on the location where the gain medium is placed within the cavity. A detailed discussion of the calculations of the confinement factor using 3D electromagnetic field simulations is presented in section 4.2.3.2

Diffractive effects occur when light encounters obstacles or apertures. When light encounters such obstacles, it bends, spreads, and creates intricate light patterns which is called diffraction. Diffractive behavior is influenced by the material properties of the cavity and surrounding medium. Therefore, variations in refractive index, absorption coefficients, and dispersion properties of materials should be taken into account.

Moreover, the interaction between the laser cavity and surrounding structures or interfaces can impact diffractive effects. Interfaces between nanowires, nanopillars, and substrates can introduce scattering or phase changes, leading to additional diffractive phenomena. These effects are particularly pronounced in sub-wavelength structures such as nanowires and nanopillars, where the dimensions of the structures are in the order of the wavelength of light, and diffraction patterns can significantly influence the behavior of the light.

In our laser model and simulations, we use three-dimensional eigenfrequency analysis to find the resonant modes and the electromagnetic field patterns within the laser cavity. This analysis takes into account the change of refractive index across the gain medium, cavity, and substrate, as well as the surrounding environment (air).

Additionally, our FEM simulations take some diffractive effects into account due to the hexagonal shape of the nanowire and nanopillar cavities. The hexagonal geometry introduces diffraction phenomena at each side, influencing the propagation and distribution of light within the cavity.

However, in our simulations, we make some simplifying assumptions as we assume uniformity in the cavity and the gain medium, neglecting impurities and irregularities that might exist at the interfaces between the nanowire or nanopillar and the gain medium and the substrates. Consequently, our results may not fully capture the diffraction effects that might arise from waves encountering obstacles or discontinuities within the structure. This simplification allows us to focus on the fundamental behavior of the light in the laser cavity under idealized conditions.

In Chapter 4, we will explain how we intend to employ the finite element method to simulate the laser's resonant cavity. The optical characteristics. We will also present an extremely detailed examination of the gain medium, aiming to accurately capture its response when subjected to pumping in Chapter 3.

# Chapter 3

# Formalism of Emission and Absorption Processes in Semiconductor Nanowires

## 3.1 Introduction

This chapter presents the formulation we have developed for modeling the dynamics of optical processes in a quantum well nanowire laser. Our formalism represents a significant advancement in describing the absorption, gain, and spontaneous emissions within quantum well nanowire lasers. We start with a detailed examination of the absorption, gain, and spontaneous emissions taking place within a bulk semiconductor. Subsequently, we modify the equations that were initially developed for bulk semiconductors to make them applicable to quantum wells. Our formalism offers a comprehensive and step-by-step discussion and derivations of the rates of the optical processes. This level of detail provides a deeper understanding of the underlying mechanisms governing the behavior of quantum well nanowire lasers, which was previously lacking in the literature.

Our approach follows the derivations given in [57], departing from his calculations in section 3.3, where we consider the photonic density of states in a nanowire. This model goes beyond merely accounting for how quantum confinement affects absorption, gain, and stimulated emission rates; we also consider the influence of the cavity. Unlike conventional approaches that only account for free-space spontaneous emission, neglecting the cavity effect by assuming the free-space photonic density of states and Purcell factor equal to unity, our formalism incorporates both the nanowire and free-space photonic density of states in the calculation, leading to higher rates of spontaneous emissions.

A key novelty of our formalism lies in deriving the equations to calculate the spontaneous emission factor ($\beta$) and the Purcell factor ($F_B$). Unlike existing literature, which often treats these parameters as constants and estimates them by fitting the experimental data into the simulations, our formalism demonstrates how these factors depend on material composition and cavity geometry as well as carrier density and temperature. This insight provides a deeper understanding of the relationship between these crucial parameters and enables more precise predictions of laser performance.

Moreover, our formalism enables us to incorporate a dynamic spontaneous emission into laser rate equation analysis. This approach sheds light on how the coupling of spontaneous emissions to the lasing mode changes over time during laser operation. By capturing this temporal aspect,

our formalism provides a more comprehensive understanding of the dynamics of quantum well nanowire lasers and opens avenues for optimizing their performance in practical applications.

An interesting element of our formulation is that we do not fit the experimental data in our simulations to calculate $\beta$. We obtain the output number of photons by solving the laser rate equations using $\beta$ and the gain that we develop in this chapter. Our formalism provides an easy method to calculate $\beta$ directly from material and cavity parameters, which will help to predict laser performance.

## 3.2 Absorption, Gain, and Spontaneous Emission Spectrum in a Bulk Semiconductor

In a semiconductor, interactions between incident photons and electrons in the conduction band, as well as holes in the valence band, can occur through three distinct mechanisms: absorption, spontaneous emission, and stimulated emission. To obtain the rates of these optical processes, we begin our analysis by considering transitions between discrete energy levels $E_1$ and $E_2$, as depicted in Figure 3.1.

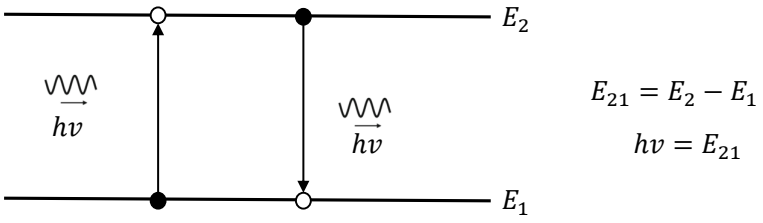


Figure 3.1: Absorption and emission of a photon between energy levels $E_1$ and $E_2$. The energy of the photon is equal to the energy difference between the two levels $hv = E_2 - E_1$.

The rate of absorption from energy level $E_1$ to the energy level $E_2$ depends on

1. The probability of a state at energy $E_1$ being occupied which we denote as $(f_1)$
2. The probability of a state at energy $E_2$ being empty which we denote as $(1 - f_2)$
3. The number of photons per unit volume per unit energy at the transition frequency $v_{21} = E_{21}/h$

where $E_{21} = E_2 - E_1$, $h$ is the Planck's constant, and $f_1$ and $f_2$ are the Fermi functions introduced in Equations 2.13-2.14.

We show the number of photons per unit volume per unit energy at $E_{21}$ with $P(E_{21})$. The parameter $P(E_{21})$ is related to the Photonic Density of States (PDOS) as

$$P(E_{21}) = N_{ph}(E_{21})n_{ph} \tag{3.1}$$

where $n_{ph}$ is the average number of existing photons at thermal equilibrium, and $N_{ph}(E_{21})$ is the photonic density of states per unit volume.

According to Boson statistics $n_{ph}$ is [57]

$$n_{ph} = \frac{1}{e^{hv/k_BT} - 1} \tag{3.2}$$

where $k_B$ is the Boltzmann's constant, and $T$ is the temperature.

We now follow the argument due to Einstein in which the rate of absorption from level 1 to level 2 per unit volume can be written as

$$R_{12}^{abs} = B_{12}P(E_{12})f_1(1 - f_2) \tag{3.3}$$

where $B_{12}$ is the Einstein B coefficient and describes the rate of the absorption [57]. We will determine the B coefficient in section 3.2.2.

Similarly, the rate of stimulated and spontaneous emission per unit volume are then

$$R_{21}^{stim} = B_{21}P(E_{21})f_2(1 - f_1) \tag{3.4}$$

and

$$R_{21}^{spon} = A_{21}f_2(1 - f_1) \tag{3.5}$$

where $B_{21}$, and $A_{21}$ are the Einstein B and A coefficients describing the rates of stimulated and spontaneous emissions [57]. Since the photons emitted via the spontaneous emissions are independent of any influence from the existing photons, $P(E_{21})$ does not appear in Equation 3.5.

At thermal equilibrium, the absorption rate equals the sum of the rates of spontaneous and stimulated emission. Therefore we have

$$R_{12}^{abs} = R_{21}^{stim} + R_{21}^{spon} \tag{3.6}$$

Using Equations 3.3-3.5, we rewrite Equation 3.6 as

$$B_{12}P(E_{12})f_1(1 - f_2) = B_{21}P(E_{21})f_2(1 - f_1) + A_{21}f_2(1 - f_1) \tag{3.7}$$

If we rewrite Equation 3.7 to find $A_{21}$, we obtain

$$A_{21} = [B_{12}\frac{f_1(1 - f_2)}{f_2(1 - f_1)} - B_{21}]P(E_{21}) \tag{3.8}$$

We now use Fermi-Dirac statistics for the electrons at energy level $E_2$ and the holes at energy level $E_1$ as

$$f_1(E_1) = \frac{1}{1 + e^{(E_1 - E_f)/k_BT}} \tag{3.9}$$

$$f_2(E_2) = \frac{1}{1 + e^{(E_2 - E_f)/k_BT}} \tag{3.10}$$

where $E_f$ is the quasi-Fermi level and $k_BT$ is the Boltzmann energy. We then have

$$\frac{f_1(1 - f_2)}{f_2(1 - f_1)} = \frac{e^{(E_2 - E_f)/k_BT}}{e^{(E_1 - E_f)/k_BT}} \tag{3.11}$$

Equation 3.11 can be simplified to

$$\frac{f_1(1 - f_2)}{f_2(1 - f_1)} = e^{(E_2 - E_1)/k_BT} \tag{3.12}$$

By substituting Equation 3.12 into Equation 3.8, we obtain

$$A_{21} = (B_{12}e^{(E_2-E_1)/k_BT} - B_{21})P(E_{21}) \tag{3.13}$$

Using Equation 4.1-4.2, we can rewrite $P(E_{21})$ as

$$P(E_{21}) = N_{ph}(E_{21})\frac{1}{e^{(E_2-E_1)/k_BT} - 1} \tag{3.14}$$

where we replaced the $hv$ in Equation 3.2 by $E_{21} = E_2 - E_1$.

From Equations 3.13 and 3.14, we get

$$P(E_{21}) = \frac{A_{21}}{B_{12}e^{E_{21}/K_BT} - B_{21}} \tag{3.15}$$

The only way this can be true for all values of $T$ is when

$$B_{12} = B_{21} \tag{3.16}$$

and

$$\frac{A_{21}}{B_{21}} = N_{ph}(E_{21}) \tag{3.17}$$

Equations 3.16-3.17 describe the relationship between the rates of absorption, stimulated, and spontaneous emissions within a semiconductor. Equation 3.17 helps us to write the rate of spontaneous emission in terms of $B_{21}$ and the photonic density of states ($N_{ph}(E_{21})$). Therefore, we can simplify the equations and compare the rate of spontaneous emissions with the absorption and stimulated emission. In the next section, we will obtain the rates of optical processes within the semiconductor using Equations 3.16-3.17.

### 3.2.1 Absorption, Stimulated, and Spontaneous Emission Rates

The absorption rate per unit volume is given by Equation 3.3. The net absorption independent of spontaneous emission is

$$R_{12}^{abs-net} = R_{12}^{abs} - R_{21}^{stim} \tag{3.18}$$

By using Equations 3.3, and 3.4 we have

$$R_{12}^{abs-net} = B_{21}P(E_{21})(f_1 - f_2) \tag{3.19}$$

From Equation 3.1, we can rewrite the net absorption rate as

$$R_{12}^{abs-net} = B_{21}N_{ph}(E_{21})(f_1 - f_2)n_{ph} \tag{3.20}$$

In a semiconductor material, we have a continuous electronic density of states (DOS) in both the conduction and valence bands which we have shown with the light and dark gray colors in Figure 3.2. Also, carriers are able to interact with the photons within a specific range of energies. Therefore, by integrating the net absorption in Equation 3.20 over all the possible energies that are able to interact with the carriers, the net absorption per unit volume is defined as

$$R_{12}^{abs-net} = \int_0^\infty B_{21}N_{ph}(E_{21})(f_1 - f_2)\delta(E_{21} - E)n_{ph}dE \tag{3.21}$$

Where the delta function only accounts for the transitions with energies equal to $E_{21}$. The

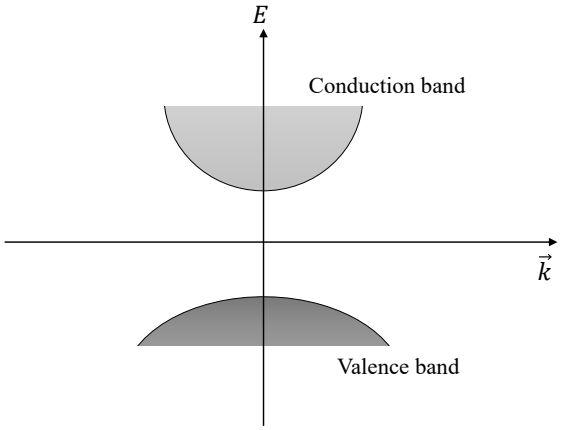


Figure 3.2: Continuous electronic density of states in the conduction band (light gray color) and in the valence band (dark grey color) in a bulk semiconductor.

spontaneous emission rate per unit volume for a discrete state is given by Equation 3.5. Using Equation 3.17, we can rewrite Equation 3.5 as

$$R_{21}^{spon} = N_{ph} B_{21}(E_{21}) f_2(1 - f_1) \tag{3.22}$$

Similar to the net absorption, by integrating over the energies that carriers can interact with, we can obtain the spontaneous emission rate as

$$R_{21}^{spon} = \int_0^\infty B_{21} N_{ph}(E_{21}) f_2(1 - f_1) \delta(E_{21} - E) dE \tag{3.23}$$

The rate of stimulated emission is obtained by assuming that the stimulated emission rate is equal to the net absorption rate when spontaneous emission is neglected. Therefore, we can write the rate of stimulated emission using Equation 3.21. However, one should keep in mind that stimulated emission occurs from $E_2$ to $E_1$, so the term $(f_1 - f_2)$ in Equation 3.21 will be replaced by the term $(f_2 - f_1)$. The rate of stimulated emission per unit volume is given as

$$R_{21}^{stim} = \int_0^\infty B_{21} N_{ph}(E_{21})(f_2 - f_1) \delta(E_{21} - E) n_{ph} dE \tag{3.24}$$

Now that we have derived the net absorption, spontaneous, and stimulated emission rates by considering all the possible energies with which the carriers are able to interact, in the next section we will consider the continuous electronic states within the conduction and valence band to derive the total rates of the optical processes.

#### 3.2.1.1 Absorption Rate in $\vec{k}$ Space

We introduce the rate of one single absorption from energy level $E_1$ to energy level $E_2$ per unit volume as

$$r_{12}^{abs,single} = B_{12} N_{ph}(E_{12})(f_1 - f_2) \delta(E_{12} - E) \tag{3.25}$$

Equation 3.25 shows the absorption rate between two discrete energy levels, $E_1$ and $E_2$, from an incident photon with energy $E$. The delta function accounts for the transitions only with energy equal to $E_{12} = |E_1 - E_2|$ as discussed in Equation 9.2.26b in [57].

The delta function ensures that energy is conserved precisely during the transition. However, in practical scenarios, energy levels are not perfectly discrete due to various broadening mechanisms, such as thermal vibrations, impurities, and other interactions within the material. These mechanisms cause the energy levels to have a finite linewidth, leading to a broadening of the spectral lines. As a result, the delta function, which represents an idealized scenario of exact energy conservation, is replaced by a Lorentzian function in practice.

Using Equation 3.25, the net absorption rate in Equation 3.21, can be rewritten as

$$R_{12}^{abs-net} = \int_0^\infty r_{12}^{abs,single} n_{ph} dE \tag{3.26}$$

From Figure 3.2 we can see that in a bulk semiconductor, there is a continuous spectrum of states in both the conduction and valence bands, presented with light and dark gray colors, where a single electron can absorb energy and move from the valence band into the conduction band.

By scanning over all of these continuous electronic states in the conduction and valence bands with wavevectors $\vec{k_a}$ and $\vec{k_b}$ for $r_{12}^{abs,single}$ as shown in Figure 3.3, we obtain the net absorption rate per unit volume per unit energy as

$$r_{net}^{abs}(E) = 2 \sum_{\vec{k_a}} \sum_{\vec{k_b}} r_{ab}^{abs,single}(E) \tag{3.27}$$

where we have added 2 to account for electron spin degeneracy.

Using Equation 3.25 in Equation 3.27, we get

$$r_{net}^{abs}(E) = 2 \sum_{\vec{k_a}} \sum_{\vec{k_b}} N_{ph} B_{ab} (f_b - f_a) \delta(E_b - E_a - E) \tag{3.28}$$

where $B_{12}$ is replaced by $B_{ab}$ to account for the rate of transition from the conduction band with wavevector $\vec{k_a}$ into the valence band with wavevector $\vec{k_b}$ instead of discrete energy levels of 1 and 2. $f_a$ and $f_b$ are the fermi functions describing the probability of electronic states in the band structure with wavevectors $\vec{k_a}$ and $\vec{k_b}$ being occupied.

Since E which is the energy at which carriers can interact with photons does not depend on $\vec{k_a}$ or $\vec{k_b}$, we can take $N_{ph}(E)$ out of the sum in Equation 3.28

$$r_{net}^{abs}(E) = 2N_{ph}(E) \sum_{\vec{k_a}} \sum_{\vec{k_a}} B_{ab} (f_b - f_a) \delta(E_b - E_a - E) \tag{3.29}$$

As mentioned before, electrons within the semiconductor are capable of interacting with photons within a spectral range of energies. The absorption spectrum within $\Delta E$ is defined as

$$\alpha \cdot \Delta E = \frac{number\ of\ photons\ absorbed/volume/s}{number\ of\ photons\ injected/area/s} \tag{3.30}$$

where $\alpha$ is the absorption coefficient.

The numerator in Equation 3.30 is the number of photons absorbed per unit volume per unit time in the spectral width, $\Delta E$, and it is obtained as

$$number\ of\ photons\ absorbed/volume/s = n_{ph} r_{abs}^{net}(E) \Delta E \tag{3.31}$$

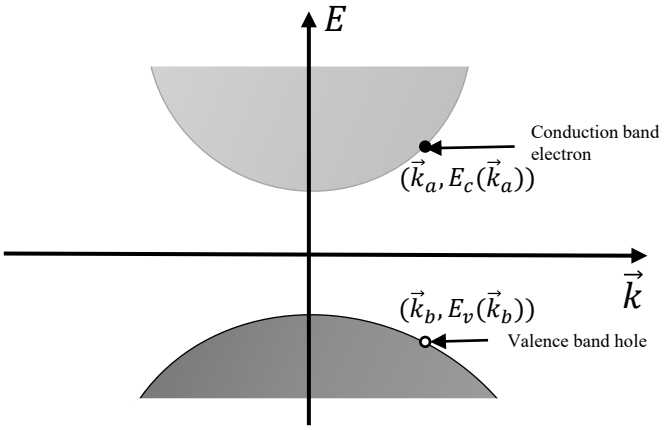


Figure 3.3: Conduction and valence band structures in $\vec{k}$ space.

The denominator of Equation 3.30 is the number of carriers injected per unit area per unit time and it is obtained as

$$number\ of\ photons\ injected/area/s = P(E)\frac{c}{n} \tag{3.32}$$

where $P(E)$ which is the number of photons per unit volume per unit energy at the energy $E$.

So, we write Equation 3.30 as

$$\alpha \cdot \Delta E = \frac{n_{ph} r_{abs}^{net}(E)\Delta E}{P(E)\frac{c}{n}} \tag{3.33}$$

Using Equation 3.1 we get

$$\alpha \cdot \Delta E = \frac{n_{ph} r_{abs}^{net}(E)\Delta E}{N_{ph} n_{ph}(c/n)} \tag{3.34}$$

and therefore, the absorption spectrum per unit volume per unit energy is

$$\alpha(E) = 2\frac{n}{c}\sum_{\vec{k_a}}\sum_{\vec{k_b}} B_{ab}(f_b - f_a)\delta(E_b - E_a - E) \tag{3.35}$$

Equation 3.35, describes the rate of absorption when not only all the electronic states within the conduction and valence bands are taken into account but also, the spectral range of frequencies in which the electrons can interact with incident photons are considered. Now that we have calculated the absorption rate, we will look into the spontaneous emission rate.

#### 3.2.1.2 Spontaneous Emission Rate in $\vec{k}$ Space

Similar to the absorption, in this section we are going to obtain the rate of spontaneous emission by taking all the electronic states in the conduction and valence band into account. The spontaneous emission rate per unit volume for a discrete state is given by Equation 3.23 when all the energies that carriers are able to interact with are considered.

Now we define the rate of a single spontaneous emission from energy level $E_2$ into the energy level $E_1$ per unit volume as

$$r_{21}^{spon,single} = N_{ph} B_{21}(E_{21}) f_2(1 - f_1)\delta(E_{21} - E) \tag{3.36}$$

If we rewrite Equation 3.23 in terms of a single spontaneous emission in Equation 3.36, we get

$$R_{21}^{spon} = \int_0^\infty r_{21}^{spon,single}(E)dE \tag{3.37}$$

A single spontaneous emission with energy ($E$) can occur from any of the continuous electronic states in the conduction and valence bands. Therefore, we integrate over all the electronic states to obtain the spontaneous emission rate of a single spontaneous emission $r_{21}^{spon,single}$ as

$$r^{spon}(E) = 2\sum_{\vec{k_a}}\sum_{\vec{k_b}} r_{ab}^{spon,single}(E) \tag{3.38}$$

Using Equation 3.36 we get

$$r^{spon}(E) = 2\sum_{\vec{k_a}}\sum_{\vec{k_b}} N_{ph}B_{ab}f_a(1-f_b)\delta(E_a - E_b - E) \tag{3.39}$$

Now that we obtained the spontaneous emission rate over the electronic states, we will investigate $B_{ab}$ in the following subsection.

### 3.2.2 Einstein B Coefficient

The parameter $B_{ab}$ describes the stimulated emission rate from an electron with wavevector $\vec{k_a}$ in the conduction band to a hole in the valence band with wavevector $\vec{k_b}$. $B_{ab}$ is given in [57] as

$$B_{ab} = \frac{2\pi}{\hbar}|<a| - \frac{eA_0}{2m_0}\hat{e}\cdot\vec{p}|b>|^2 \tag{3.40}$$

where $a$ is the initial state of the carrier, $b$ is the final state of the carrier, $A_0$ is the electromagnetic vector potential amplitude, $m_0$ is the free mass of an electron, $\hat{e}$ is the electric field polarization, and $\vec{p}$ is the dipole operator between the electron and hole.

This expression does not take the conservation of momentum into account. As discussed in section 2.2.4, we apply the conservation of momentum which states that the wavevector of the carrier before and after transition should be almost equal to each other ($\vec{k_a} \approx \vec{k_b}$). Therefore we get

$$B_{ab} = \frac{2\pi}{\hbar}|<a| - \frac{eA_0}{2m_0}\hat{e}\cdot\vec{p}|b>|^2\delta_{\vec{k_a},\vec{k_b}} \tag{3.41}$$

Equation 3.41 can be rewritten as

$$B_{ab} = \frac{2\pi}{\hbar}\frac{e^2A_0^2}{4m_0^2}|\hat{e}\cdot<a|\vec{p}|b>|^2\delta_{\vec{k_a},\vec{k_b}} \tag{3.42}$$

If we define the momentum matrix element as the rate of electron and hole recombination between electronic states with wave vectors $\vec{k_a}$ and $\vec{k_b}$ as

$$\vec{p}_{ab} =< a|\vec{p}|b> \tag{3.43}$$

Then we have

$$|\hat{e}\cdot<a|\vec{p}|b>|^2 = |\hat{e}\cdot\vec{p}_{ab}|^2 \tag{3.44}$$

$B_{ab}$ in Equation 3.42 becomes

$$B_{ab} = \frac{\pi}{\hbar}\frac{e^2 A_0^2}{4m_0^2}|\hat{e}\cdot\vec{p_{ab}}|^2\delta_{\vec{k_a},\vec{k_b}} \tag{3.45}$$

where the $A_0$ is the electromagnetic vector potential arising from a single photon in a volume $V_0$, which we think of as some volume contained within the active region, as shown in Figure 3.4

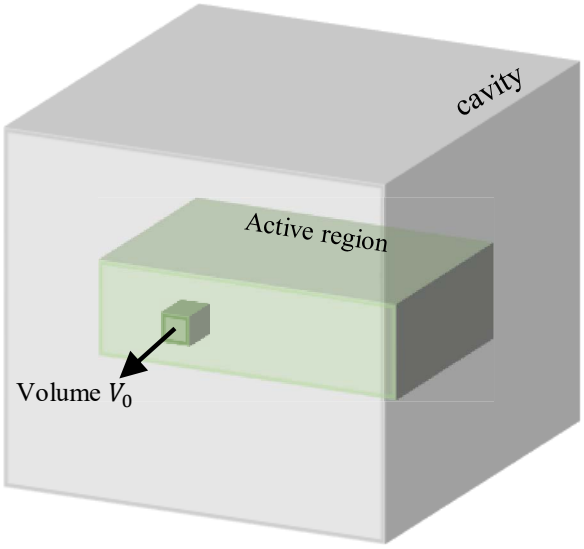


Figure 3.4: Schematic image of the volume of the cavity, active region, and volume $V_0$

Expression for $A_0$ can be derived by considering the energy arising from a single photon in a box of volume $V$ as

$$A_0^2 = \frac{2\hbar}{n^2\epsilon_0\omega}\frac{1}{V} \tag{3.46}$$

where $V$ is the volume of the active region.

By substituting $A_0$ in Equation 3.45 we get

$$B_{ab} = \frac{\pi}{\hbar}\frac{e^2}{2m_0^2}\frac{2\hbar}{n^2\epsilon_0\omega}\frac{1}{V}|\hat{e}\cdot\vec{p_{ab}}|^2\delta_{\vec{k_a},\vec{k_b}} \tag{3.47}$$

Equation 3.47 simplifies to

$$B_{ab} = \frac{\pi e^2}{m_0^2 c\epsilon_0 n\omega}\frac{c}{n}\frac{1}{V}|\hat{e}\cdot\vec{p_{ab}}|^2\delta_{\vec{k_a},\vec{k_b}} \tag{3.48}$$

We then define $C_0$ as

$$C_0 = \frac{\pi e^2}{nc\epsilon_0 m_0^2\omega} \tag{3.49}$$

where $e$ is the electron charge, $\epsilon_0$ is the vacuum permittivity, $m_0$ is the free mass of the electron, and $\hbar$ represents the reduced Planck's constant.

We can also rewrite $C_0$ in terms of energy by substituting $\omega$ with $E/\hbar$ as

$$C_0 = \frac{\pi e^2}{nc\epsilon_0 m_0^2 (E/\hbar)} \tag{3.50}$$

Substituting $C_0$ in Equation 3.48 gives us

$$B_{ab} = C_0 \frac{c}{n} \frac{1}{V} |\hat{e} \cdot \vec{p_{ab}}|^2 \delta_{\vec{k_a},\vec{k_b}} \tag{3.51}$$

Now that we have obtained the coefficient $B_{ab}$, we can continue the derivations of the spontaneous emission rate in Equation 3.39. By substituting Equation 3.51 in 3.39, we get

$$r^{spon}(E) = 2N_{ph} C_0(E) \frac{c}{n} \frac{1}{V} \sum_{\vec{k_a}} \sum_{\vec{k_b}} |\hat{e} \cdot \vec{p_{ab}}|^2 \delta_{\vec{k_a},\vec{k_b}} f_b(1 - f_a) \delta(E_b - E_a - E) \tag{3.52}$$

We introduce $E_{cv}$ as the energy difference between the conduction band and the valence band at $\vec{k_a}$ which is presented in Figure 3.5. $E_c(\vec{k_a})$ and $E_v(\vec{k_b})$ represent the energy of the conduction and valence bands, respectively. Also by taking advantage of the fact that the transition of an electron from the conduction band into a hole in the valence band can take place when $\vec{k_a} = \vec{k_b}$, we can write $E_{cv}(\vec{k})$ as

$$E_{cv}(\vec{k_a}) = (E_a - E_b)|_{\vec{k_a}=\vec{k_b}} = E_c(\vec{k_a}) - E_v(\vec{k_b}). \tag{3.53}$$

Also, we define the interband momentum matrix element as

$$\vec{p}_{cv} = \vec{p}_{ab}(\vec{k_a}, \vec{k_b})|_{\vec{k_a}=\vec{k_b}} \tag{3.54}$$

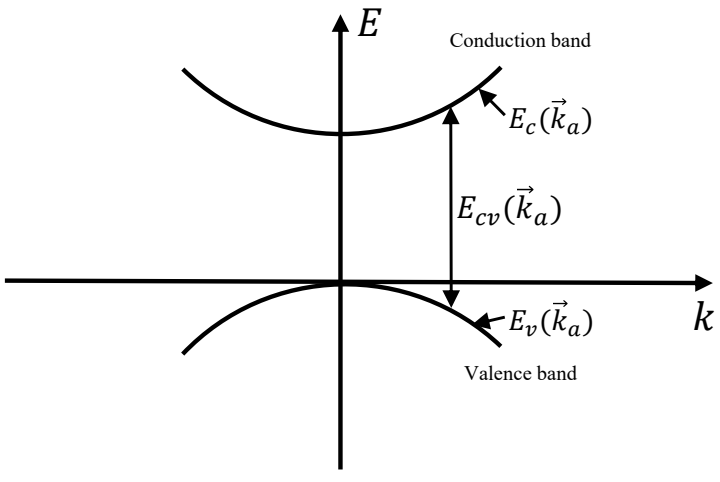


Figure 3.5: Schematic image of the difference in the energy of the conduction and valence band $E_{cv}$with respect to the wavevector $\vec{k}$

.

The Fermi-functions of the conduction and the valence band are defined as

$$f_c = f_b(\vec{k_a}) = \frac{1}{1 + e^{(E_c(\vec{k_a}) - E_f)/K_B T}} \tag{3.55}$$

$$f_v = f_a(\vec{k_a}) = \frac{1}{1 + e^{(E_v(\vec{k_a}) - E_f)/K_B T}} \tag{3.56}$$

We can rewrite the spontaneous emission rate in Equation 3.52 in terms of $E_{cv}$ in Equation 3.51, $\vec{p} - cv$ in Equation 3.52, and the Fermi functions in Equations 3.55-3.56 as

$$r^{spon}(E) = 2N_{ph}(E)C_0(E)\frac{c}{n}\frac{1}{V}\sum_{\vec{k_a}} |\hat{e} \cdot \vec{p_{ab}}|^2 f_c(1 - f_v)\delta(E_{cv} - E) \tag{3.57}$$

So far we derived the spontaneous emission rate from all the electronic states in k-space with energy $E$. For a more accurate description of the optical processes, we will add the intra-band transitions which refer to the transitions within the conduction or valence bands that provide the carriers into the band edge before the inter-band transition as shown in Figure 3.6. Intra-band transitions represent the scattering relaxations that result in the linewidth broadening. Therefore, when scattering is included, the delta function is replaced by a Lorentzian as [57]

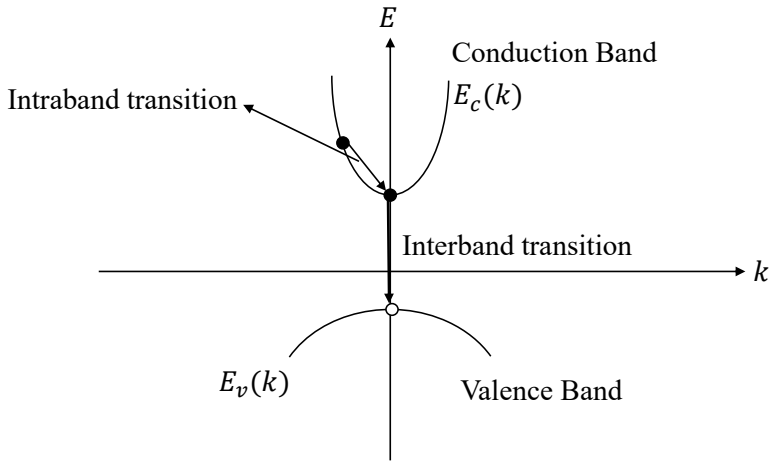


Figure 3.6: Intra-band transition in the conduction band of a semiconductor

.

$$\delta(E_{cv} - E) \Rightarrow \frac{\gamma/2\pi}{(E_{cv} - E)^2 + (\gamma/2)^2} = L(E_{cv} - E) \tag{3.58}$$

where $\gamma$ is related to the intraband scattering lifetime ($\tau_{in}$) as

$$\gamma = \frac{2\hbar}{\tau_{in}} \tag{3.59}$$

by substituting Equation 3.58 in Equation 3.57, we get

$$r^{spon}(E) = 2N_{ph}(E)C_0(E)\frac{c}{n}\frac{1}{V}\sum_{\vec{k_a}} |\hat{e} \cdot \vec{p_{ab}}|^2 f_c(1 - f_v)L(E_{cv} - E) \tag{3.60}$$

Equation 3.60 gives us the rate of spontaneous emissions by taking a sum over all the possible electronic states in the conduction and valence bands. However, since in a bulk semiconductor we are dealing with the continuum of electronic states in the conduction and valence bands, we

can replace the sum with an integral. If we assume that all three sides of the active region are equal to $L$, we can replace the sum with integral as

$$\frac{1}{V}\sum_{\vec{k_a}} = \frac{1}{L^3}\sum_{\vec{k_a}} \tag{3.61}$$

Equation 3.61 can be rewritten as

$$\frac{1}{L^3}\sum_{\vec{k}_a} = \frac{1}{(2\pi)^3}\sum_{\vec{k}_a}(\frac{2\pi}{L})^3 \tag{3.62}$$

for a bulk semiconductor with the length $L$ on three sides, we should have standing waves between the extremes. Therefore, the wavevectors in the x,y, and z directions are

$$\Delta k_x = \frac{2\pi}{L} \tag{3.63}$$

$$\Delta k_y = \frac{2\pi}{L} \tag{3.64}$$

$$\Delta k_z = \frac{2\pi}{L} \tag{3.65}$$

Using Equations 3.63-3.65, we rewrite Equation 3.62 as

$$\frac{1}{(2\pi)^3}\sum_{\vec{k}_a}(\frac{2\pi}{L})^3 = \frac{1}{(2\pi)^3}\sum_{\vec{k}_a}\Delta k \tag{3.66}$$

Finally, we can replace the sum in Equation 3.66 with three integrals in all directions as

$$\frac{1}{(2\pi)^3}\sum_{\vec{k}_a}\Delta k = \frac{1}{(2\pi)^3}\int\int\int d\vec{k} \tag{3.67}$$

By replacing the sum with the integral in Equation 3.60, the spontaneous emission rate is written as

$$r^{spon}(E) = 2N_{ph}(E)C_0(E)\frac{c}{n}\frac{1}{V}\frac{1}{(2\pi)^3}\int_0^\infty |\hat{e}\cdot\vec{p_{cv}}|^2 f_c(1-f_v)L(E_{cv}-E)d\vec{k} \tag{3.68}$$

We seek to write all the optical process rates in terms of the energy rather than the wavevector. Therefore, in the following section, we will investigate how to replace $\vec{k}$ with the energy of the conduction and valence bands.

### 3.2.3 Electronic DOS and Computation of Absorption, Gain, and Spontaneous Emission in a Bulk Semiconductor

As mentioned above, we want everything in the integral of Equation 3.68 to depend on energy rather than wavevector, so in this section, we would like to change variables from $\vec{k}$ to $E_{cv}$. If we assume that the bottom of the conduction band is at $E_g$ and the top of the valence band sits at zero, we can write

$$E_c(k) = E_g + \frac{\hbar^2}{2m_e^*}k^2 \tag{3.69}$$

$$E_v(k) = -\frac{\hbar^2}{2m_h^*}k^2 \tag{3.70}$$

where $m_e^*$ is the effective mass of the electron in the conduction band, and $m_h^*$ is the effective mass of holes in the valence band.

Using Equations 3.69 and 3.70 in Equation 3.53 gives us

$$E_{cv}(k) = E_g + (\frac{\hbar^2}{2m_e^*} + \frac{\hbar^2}{2m_h^*})k^2 \tag{3.71}$$

We show the $m_r^*$ as the reduced mass of the electron which is obtained as

$$\frac{1}{m_r^*} = \frac{1}{m_e^*} + \frac{1}{m_h^*} \tag{3.72}$$

By substituting Equation 3.72 in Equation 3.71, we rewrite $E_{cv}$ as

$$E_{cv}(k) = E_g + \frac{\hbar^2}{2m_r^*}k^2 \tag{3.73}$$

In a 3D geometry, we can write $d\vec{k}$ in spherical coordinates as

$$\int\int\int d\vec{k} = \int_0^{2\pi}\int_0^{\pi}\int_0^{\infty} k^2 d\theta_k d\phi_k dk \tag{3.74}$$

By assuming all the values for $d\theta_k$ and $d\phi_k$, Equation 3.74 becomes

$$\int_0^{2\pi}\int_0^{\pi}\int_0^{\infty} k^2 d\theta_k d\phi_k dk = 4\pi\int_0^{\infty} k^2 dk \tag{3.75}$$

In a bulk semiconductor, we are dealing with a 3D geometry. However, this step will be different in the 2D geometry of the quantum wells.

From 3.73, we obtain $k$ as

$$k = \sqrt{\frac{2m_r^*}{\hbar^2}(E_{cv} - E_g)} \tag{3.76}$$

Differentiating Equation 3.73 gives us

$$dE_{cv} = \frac{\hbar^2}{m_r^*}\sqrt{\frac{2m_r^*}{\hbar^2}(E_{cv} - E_g)}dk \tag{3.77}$$

By substituting Equation 3.76 in Equation 3.77, we get

$$dE_{cv} = \frac{\hbar^2}{m_r^*}kdk \tag{3.78}$$

Therefore,

$$k^2 dk = (\frac{2m_r^*}{\hbar^2}(E_{cv} - E_g))\frac{1}{\frac{\hbar^2}{m_r^*}\sqrt{\frac{2m_r^*}{\hbar^2}(E_{cv} - E_g)}}dE_{cv} \tag{3.79}$$

Equation 3.79 is simplified as

$$k^2 dk = \frac{1}{2}(\frac{2m_r^*}{\hbar^2})^{3/2}\sqrt{(E_{cv} - E_g)}dE_{cv} \tag{3.80}$$

We introduce $\rho_r(E_{cv})$ as the 3D joint density of electronic states (DOS)

$$\rho_r(E_{cv}) = \frac{1}{2\pi^2}(\frac{2m_r^*}{\hbar^2})^{3/2}\sqrt{(E_{cv} - E_g)} \tag{3.81}$$

Using DOS in Equation 3.80, we get

$$k^2 dk = \pi^2 \rho_r(E_{cv}) \tag{3.82}$$

Hence by applying Equations 3.77 and 3.82 to Equation 3.68, the spontaneous emission spectrum becomes

$$r^{spon}(E) = N_{ph}(E)C_0(E)\frac{c}{n}\int_{E_g}^{\infty} \rho_r(E_{cv})|\hat{e}\cdot\vec{p_{cv}}|^2 f_c(1-f_v)L(E_{cv}-E)dE_{cv} \tag{3.83}$$

Now that we can calculate the rate of spontaneous emission by considering all the electronic states, we go back to Equation 3.37 and include all the considerations of all the photon energies to obtain the total spontaneous emission rate as

$$R_{spon}^{total} = \int_0^{\infty} dE \int_{E_g}^{\infty} N_{ph}(E)C_0(E)\frac{c}{n}\rho_r(E_{cv})|\hat{e}\cdot\vec{p}_{cv}|^2 f_c(1-f_v)\frac{\gamma/2\pi}{(E_{cv}-E)^2+(\gamma/2)^2}dE_{cv} \tag{3.84}$$

Equation 3.84 gives us the total spontaneous emission rate within a bulk semiconductor. This includes spontaneous emissions with all the possible frequencies and electronic states. However, some of these spontaneous emissions couple to the lasing mode of the cavity, while some can either couple to the other existing cavity modes or they will be emitted into the free space. From the total spontaneous emission rate, we will be able to calculate $\beta$ and the Purcell factor in a laser system.

To compute the total absorption, we continue from Equation 3.35 by substituting $B_{ab}$ in Equation 3.51. Therefore, the absorption rate per unit volume is given as

$$\alpha(E) = 2\frac{n}{c}\sum_{\vec{k_a}}\sum_{\vec{k_b}} C_0\frac{c}{n}\frac{1}{V}|\hat{e}\cdot\vec{p_{ab}}|^2\delta_{\vec{k_a},\vec{k_b}}(f_a - f_b)\delta(E_b - E_a - E) \tag{3.85}$$

for a direct transition where $k_a = k_b$, we have

$$\alpha(E) = 2C_0\frac{1}{V}\sum_{\vec{k_a}}|\hat{e}\cdot\vec{p_{cv}}|^2(f_v - f_c)L(E_{cv}-E) \tag{3.86}$$

where we replace the delta function with the Lorentzian. We now assume the 3D space to replace the sum over the wavevectors with the integral over all the electronic states following Equations 3.63-3.67 and Equations 3.77-3.81. We obtain

$$\frac{1}{V}\sum_{\vec{k_a}} \rightarrow \frac{1}{2}\int_{E_g}^{\infty}\rho_r(E_{cv})dE_{cv} \tag{3.87}$$

By using Equation 3.87 in Equation 3.86, we rewrite the absorption rate as

$$\alpha(E) = C_0\int_{E_g}^{\infty}\rho_r(E_{cv})|\hat{e}\cdot\vec{p_{cv}}|^2(f_v - f_c)L(E_{cv}-E)dE_{cv} \tag{3.88}$$

The parameter $\alpha$ describes the rate of electrons absorbing the incident energy and moving from the valence band into the conduction band. Gain is the reverse of this process where the same electrons will lose their energy by emitting a photon and drop back to the valence band. Therefore, we can write that the gain as

$$g(E) = -\alpha(E) = C_0 \int_{E_g}^{\infty} \rho_r(E_{cv}) |\hat{e} \cdot \vec{p_{cv}}|^2 (f_c - f_v) L(E_{cv} - E) dE_{cv} \tag{3.89}$$

Now that we learned and fully understand how the optical processes occur within a bulk semiconductor inside a cavity we also derived the total rate of absorption, gain, and spontaneous emission rates, in the next section we will modify these equations to describe the behavior of a single quantum well inside a cavity. Please note that we will discuss the photonic density of states $N_{ph}(E)$ in more detail in Chapter 5.

## 3.3 Optical Processes within a Quantum-well Inside the Nanowire

In this section, we will discuss the optical processes within a quantum well when it is placed inside an optical cavity as shown in Figure 3.7. Equations 3.1-3.60 discuss the processes in a general form. Therefore they will hold true for both bulk and quantum well semiconductors. As we move from bulk to quantum well structure, instead of having continuous energy states in the conduction and valence bands, we will have discrete energy levels. This will introduce changes in the electronic density of states, Fermi functions, and wavevectors.

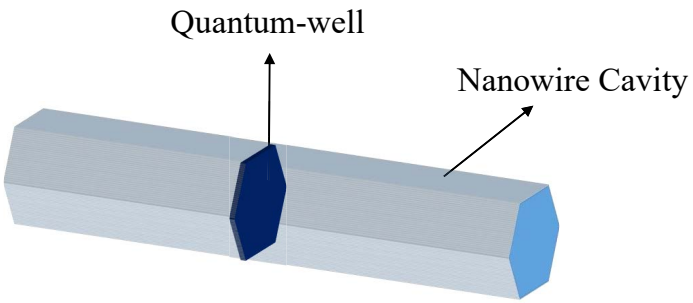


Figure 3.7: Schematic image of a quantum well inside an optical cavity

.

The confined thickness of the quantum well will apply some restrictions on how much the wavevectors are able to expand. Due to the very small length of the active region, let's say in the z-direction, the wavevector $\vec{k}$ is only capable of expanding along the x and y-directions while remaining constant in the z-direction as shown in Figure 3.8. Equation 3.67 replaces the sum of the wavevectors with integral over the 3D bulk active medium to include all the possible electronic states. However, this replacement of the sum with integral for the 2D quantum well

gains medium is obtained as

$$\frac{1}{V}\sum_{\vec{k}_a} = \frac{1}{L_z L^2}\sum_{\vec{k}_a} \tag{3.90}$$

Equation 3.90 can be rewritten as

$$\frac{1}{L_z L^2}\sum_{\vec{k}_a} = \frac{1}{L_z(2\pi)^2}\sum_{\vec{k}_a}(\frac{2\pi}{L})^2 \tag{3.91}$$

The term $(2\pi/L)^2$ is Equation 3.91 can be replaced by $\Delta k_t$ as

$$\frac{1}{L_z(2\pi)^2}\sum_{\vec{k}_a}(\frac{2\pi}{L})^2 = \frac{1}{L_z(2\pi)^2}\sum_{\vec{k}_a}\Delta k_t \tag{3.92}$$

where $k_t$ denotes the transverse wavevector in the x and y directions, $L_z$ is the thickness of the quantum well, and $L$ is the length of the active region in the x and y directions.

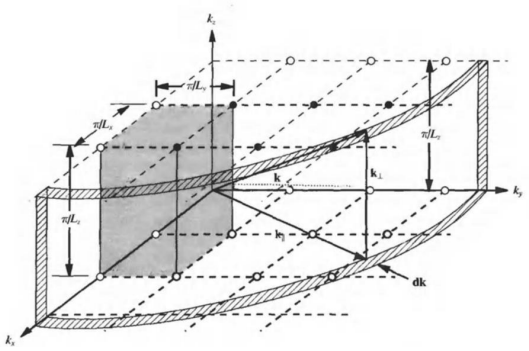


Figure 3.8: Allowed momentum vectors in a quantum well semiconductor. The solid dots represent the allowed states. Reprinted from [34].

The sum in Equation 3.92 is replaced by integrals in two directions as

$$\frac{1}{L_z(2\pi)^2}\sum_{\vec{k}_a}\Delta k_t \rightarrow \frac{1}{L_z(2\pi)^2}\int\int d\vec{k}_t \tag{3.93}$$

By replacing the sum with the integral in Equation 3.60, the spontaneous emission rate is written as

$$r^{spon}(E) = 2N_{ph}(E)C_0(E)\frac{c}{n}\frac{1}{L_z(2\pi)^2}\int\int dk_t|\hat{e}\cdot\vec{p_{ab}}|^2 f_c(1-f_v)L(E_{cv}-E) \tag{3.94}$$

Now, as mentioned in section 2.3, in a quantum well the continuous electronic states collapse into the discrete energy levels due to the quantum confinement effect. Two discrete energy levels in the conduction and valence band in a quantum well are presented in Figure 3.9. It can be seen in Figure 3.9 that the first energy level of the conduction in a quantum well lies above the bandgap energy $E_g$.

Similarly, the top of the first energy level in the valence band lies below zero. This means that the prohibited bandgap in the quantum well is larger than what it would be in the bulk form.

Since in a quantum well we have discrete energy bands, photon emission from the conduction band into the valence band also can occur via certain energies corresponding to the difference between the two specific bands. In Figure 3.9, for two energy levels in the conduction and valence bands, four types of transition can occur which we show as $E_{cvnm}$. The subscripts $n$ and $m$ correspond to the number of energy levels in the conduction and valence band in which the transition is happening. For example, we show the energy of a transition from the second energy level in the conduction band to the first energy level of the valence band as $E_{cv21}$.

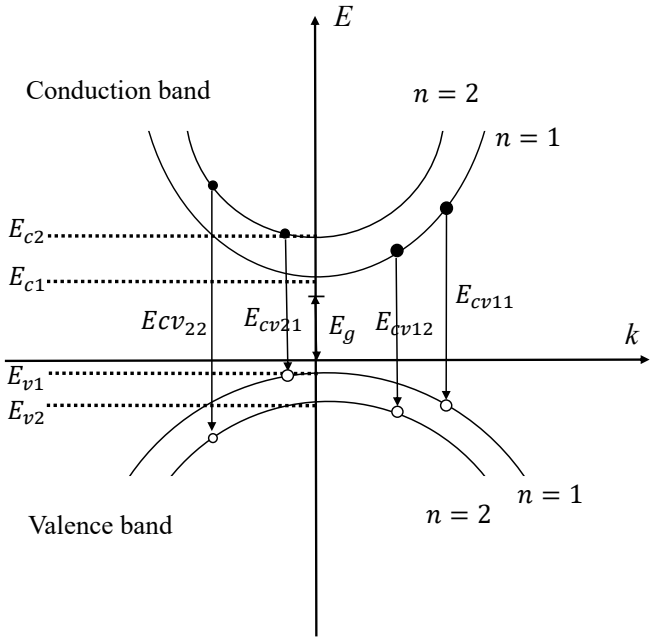


Figure 3.9: Two discrete energy levels of the conduction band and the valence band in a quantum well structure.

Similar to the approach we took in the bulk semiconductor, we seek to write Equation 3.94 in terms of $E_{cv}$ instead of the transverse wavevector.

We can write the energy in the conduction and valence bands for discrete energy levels of the quantum well as

$$E_c(k_t) = E_{cn} + \frac{\hbar^2}{2m_e^*}k_t^2 \tag{3.95}$$

$$E_v(k_t) = E_{vm} - \frac{\hbar^2}{2m_h^*}k_t^2 \tag{3.96}$$

where $E_{cn}$ and $E_{vm}$ are the bottom and top of the $n^{th}$ discrete energy level in the conduction and the top of the $m^{th}$ energy level in the valence band of the quantum well, respectively. The parameter $k_t$ represents the transverse wavevector.

By using Equations 3.95 and 3.96 in Equation 3.53, we get

$$E_{cv}(k_t) = E_{cn} + \frac{\hbar^2}{2m_e^*}k_t^2 - E_{vm} + \frac{\hbar^2}{2m_h^*}k_t^2 \tag{3.97}$$

Substituting Equation 3.72 in Equation 3.97 we get

$$E_{cv}(k_t) = E_{cn} - E_{vm} + \frac{\hbar^2}{2m_r^*}k_t^2, \tag{3.98}$$

where $m_r^*$ is the reduced mass of the carriers.

By rearranging Equation 3.98 we write the wavevector $k_t$ according to the energy $E_{cv}$ as

$$k_t^2 = \frac{2m_r^*}{\hbar^2}(E_{cv} - E_{cn} + E_{vn}) \tag{3.99}$$

In 2D geometry we have

$$\int\int d\vec{k_t} = \int_0^{2\pi}\int_0^{\infty} k_t dk_t = 2\pi\int_{E_g}^{\infty} k_t dk_t \tag{3.100}$$

We can rewrite the rate of the spontaneous emission in Equation 3.94 as

$$r^{spon}(E) = 2N_{ph}(E)C_0(E)\frac{c}{n}\frac{1}{(2\pi)^2 L_z}\int_{E_g}^{\infty} 2\pi|\hat{e}\cdot\vec{p_{cv}}|^2 f_c(1-f_v)L(E_{cv}-E)k_t dk_t \tag{3.101}$$

If we write $k_t dk_t$ in terms of $E_{cv}$ using Equation 3.99, we can obtain the spontaneous emission rate as

$$r^{spon}(E) = N_{ph}(E)C_0(E)\frac{c}{n}\sum_{n,m}\frac{m_r^*}{\pi L_z\hbar^2}\int_{E_g}^{\infty}|\hat{e}\cdot\vec{p_{cv}}|^2 f_c(1-f_v)L(E_{cv}-E)dE_{cv} \tag{3.102}$$

Now we introduce $\rho_r^{2D}$ which is the electronic density of states in a quantum well with the thickness of $L_z$ as

$$\rho_r^{2D} = \frac{m_r^*}{\pi L_z\hbar^2} \tag{3.103}$$

Therefore Equation 3.102 is obtained as

$$r^{spon}(E) = N_{ph}(E)C_0(E)\frac{c}{n}\sum_{n,m}\rho_r^{2D}\hbar^2\int_{E_g}^{\infty}|\hat{e}\cdot\vec{p_{cv}}|^2 f_c(1-f_v)L(E_{cv}-E)dE_{cv} \tag{3.104}$$

From Equation 3.103, it can be seen that the density of states in a quantum well is energy-independent. The discrete electronic density of states in the quantum well results in a step-like form of the density of states. The independence of the DOS to energy allows manipulation of the electronic properties and tuning of the emission wavelength by altering the thickness of the quantum wells. Figure 3.10 presents a comparison between the continuous density of states in a bulk semiconductor and this step-like density of states in a quantum well.

Similar to the spontaneous emission rate, by substituting Equation 3.103 and taking a sum over all the discrete energy levels in the conduction and valence bands the absorption in Equation 3.88 becomes

$$\alpha(E) = C_0(E)\rho_r^{2D}\sum_{n,m}\int_{E_g}^{\infty}|\hat{e}\cdot\vec{p_{cv}}|^2(f_v-f_c)L(E_{cv}-E)dE_{cv} \tag{3.105}$$

The gain is obtained from the negative of the absorption in Equation 3.105 as

$$g(E) = C_0(E)\rho_r^{2D}\sum_{n,m}\int_{E_g}^{\infty}|\hat{e}\cdot\vec{p_{cv}}|^2(f_c-f_v)L(E_{cv}-E)dE_{cv} \tag{3.106}$$

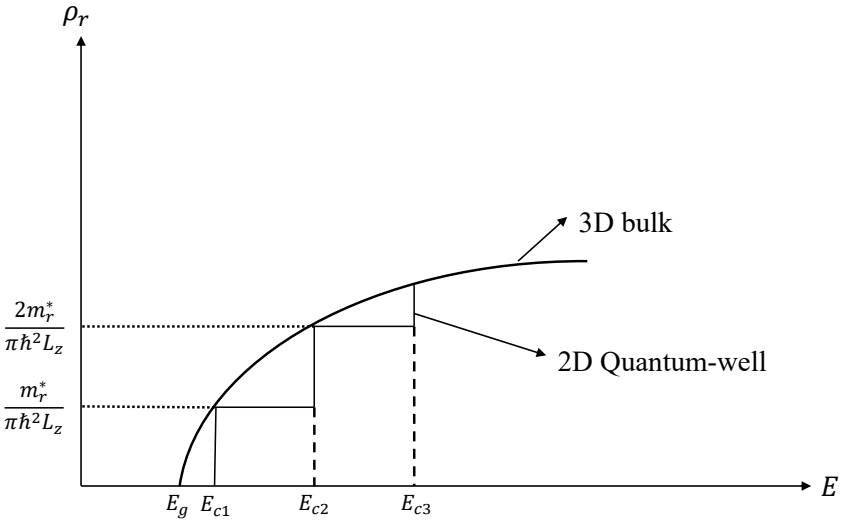


Figure 3.10: Comparison between the electronic density of states $\rho_r$ in a bulk semiconductor with a quantum well.

where,

$$f_c(Ecv) = \frac{1}{1 + e^{(Ecn + \frac{m_r^*}{m_e^*}(E_{cv} - E_{cn} + E_{vn}) - F_c)/K_B T}} \tag{3.107}$$

and

$$f_v(Ecv) = \frac{1}{1 + e^{(Evn - \frac{m_r^*}{m_h^*}(E_{cv} - E_{cn} + E_{vn}) - F_v)/K_B T}} \tag{3.108}$$

represent the Fermi functions of the quantum well in the conduction and valence bands respectively.

From Figure 2.6, we can see that when the system is at thermal equilibrium, the quasi-Fermi levels lie in the middle of the band gap $F_c = F_v = E_f$. However, achieving a population inversion requires exciting the electrons into the higher energy states. Once the electrons are excited into the conduction band, the quasi-Fermi levels are pushed further into the band structures.

$F_c$ rises above the middle of the band gap, and $F_v$ falls below it. The quasi-Fermi levels are not fixed and can be influenced by the pump power. As we introduce more pumping energy, more carriers will be excited in the system.

Available carrier densities (number of carriers per unit volume) directly influence the position of the quasi-Fermi levels. If more electrons are available to move into the conduction band, $F_c$ will be at a higher energy level. Conversely, if fewer electrons are available, $F_c$ will be lower. The same applies to $F_v$ but in relation to the number of holes.

As we discussed before, The electronic density of states (DOS) determines the number of states filled by the carriers. If we consider that the laser operates at low temperatures, the Fermi functions can be considered step functions. In this case, the number of carriers in the conduction band assuming all of the states between $E_{cn}$ and $F_c$ are filled is given as [34]

$$N_e = \int_{E_{cn}}^{F_c} \rho_e(E) dE \tag{3.109}$$

Therefore, for a given electron density $N_e$, the quasi-Fermi level $F_c$ can be easily calculated. The quasi-Fermi-level $F_c$ and $F_v$ are obtained as

$$F_c = E_{cn} + \frac{N_e}{\rho_e}, \tag{3.110}$$

$$F_v = E_{vn} - (\frac{N_h}{\rho_h}). \tag{3.111}$$

where $\rho_e$ and $\rho_h$ are the density of electrons in the conduction band and the density of holes in the valence band, respectively. We will discuss about the quasi-Fermi levels more in Chapter 5.

Using the quasi-Fermi levels in Equations 3.110-3.111, we solve the gain spectrum equation in 4.106 which enables us to generate multiple gain spectra for various carrier densities.

### 3.3.1 Spontaneous Emission Lifetime

In bulk semiconductor materials, the spontaneous emission lifetime is typically governed by the material's intrinsic properties. However, as the dimensions of the semiconductor shrink to the nanoscale, the spontaneous emission lifetime typically decreases. This is primarily attributed to the influence of quantum confinement effects. Also, when such lower dimensional gain media is placed inside the cavity, the spontaneous emission lifetime decreases even more due to the Purcell effect.

We calculate the spontaneous emission lifetime of a quantum well inside a nanowire laser from integrating over energies in the spontaneous emission rate of Equation 3.104 as

$$\frac{1}{\tau_{sp}} = R_{spon}(E) = \int_0^\infty dE \int_{E_g}^\infty N_{ph}(E) C_0(E) \frac{c}{n} \rho_r^{2D} |\hat{e} \cdot \vec{p_{cv}}|^2 f_c(1 - f_v) L(E_{cv} - E) dE_{cv} \tag{3.112}$$

Figure 3.11 represents the terms $f_c(1 - f_v)$, and $\rho_r$ in $R_{spon}$. For simplicity, if we consider that $\rho_r f_c(1 - f_v)$ varies sufficiently quickly near a value $E_0$, then we can assume that

$$\int_{E_g}^\infty \rho_r f_c(1 - f_v) dE_{cv} = N_c \tag{3.113}$$

where $N_c$ is the total number of carriers per unit volume that can be matched with a hole.

Therefore the spontaneous emission lifetime can be simplified to

$$\frac{1}{\tau_{sp}} = \int_0^\infty N_{ph}(E) C_0(E) \frac{c}{n} |\hat{e} \cdot \vec{p_{cv}}|^2 \frac{\gamma/2}{(E_0 - E)^2 + (\gamma/2)^2} dE, \tag{3.114}$$

where $\gamma$ is the FWHM of the spontaneous emission spectra, $N_{ph}$ is the photonic density of states, $E_0$ is the energy of the emitted photon, $|\hat{e} \cdot p_{cv}|^2$ is the momentum matrix element, and $n$ is the refractive index of the active medium.

The density of photonic states $N_{ph}$ is a fundamental concept in our calculations that plays a crucial role in understanding the behavior of light inside the nanowire cavity. The $N_{ph}$ describes the number of available optical states per unit volume per unit frequency within the nanowire that can be occupied by the photons.

In a three-dimensional (3D) free space, the density of photonic states is given by

$$N_{ph}^{fs}(E) = \frac{8\pi n^3 E^2}{h^3 c^3} \tag{3.115}$$

The photonic density of states $N_{ph}$ inside an optical cavity undergoes significant modifications compared to the density of states in free space. An optical cavity confines and traps light within its end facets, leading to forming standing waves and discrete resonant modes, resulting in a modified $N_{ph}$ that strongly influences light-matter interactions, emission properties, and device performance. We compute $N_{ph}$ in Chapter 5.

### 3.3.2 Purcell Factor

Inside an optical cavity, the $N_{ph}$ consists of a series of spectra each corresponding to a resonant mode of the cavity. These modes are linked to the geometry and optical properties of the cavity, such as its size, shape, and refractive index. Each resonant mode has its own characteristics such as frequency, and quality factor.

When a quantum well, is placed within the cavity, its spontaneous emission rate is strongly influenced by the $N_{ph}$ at the emission wavelength. The enhanced $N_{ph}$ inside the cavity increases the probability of spontaneous emission into the resonant modes, leading to accelerated spontaneous emission decay rates.

This phenomenon, known as the Purcell effect enables efficient coupling of spontaneous emissions to the cavity mode. We calculate the Purcell factor as the ratio of the total spontaneous emission rate within the nanowire to the total spontaneous emission rate into the free space as

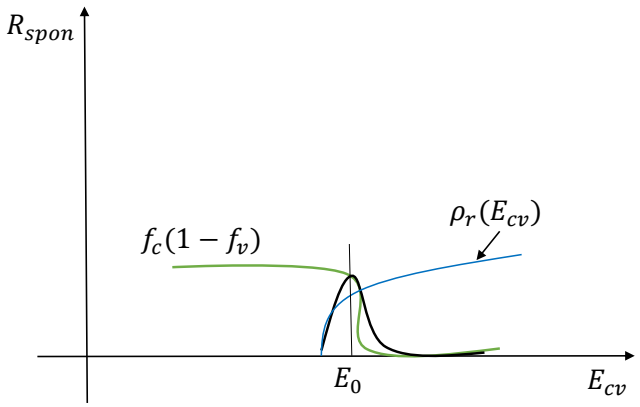


Figure 3.11: $R_{spon}$ in Equation 3.112 as a function of $E_{cv}$. The term $\rho_r$ is shown with a blue color, and $f_c(1-f_v)$ is shown with a green color near a value $E_0$.

$$F_p = \frac{\int_0^\infty dE \int_{E_g}^\infty N_{ph}(E) C_0(E) \frac{c}{n} \rho_r^{2D} |\hat{e} \cdot \vec{p_{cv}}|^2 f_c(1-f_v) L(E_{cv}-E) dE_{cv}}{\int_0^\infty dE \int_{E_g}^\infty N_{ph}^{fs}(E) C_0(E) \frac{c}{n} \rho_r^{2D} |\hat{e} \cdot \vec{p_{cv}}|^2 f_c(1-f_v) L(E_{cv}-E) dE_{cv}}, \tag{3.116}$$

where $N_{ph}$ is the photonic density of states within the cavity, calculated as

$$N_{ph} = N_{ph}^{c}(E) + N_{ph}^{fs}(E), \tag{3.117}$$

where $N_{ph}^{c}$ represents the photonic density of states of the modes of the nanowire cavity while $N_{ph}^{fs}$ is the free space density of photonic states.

### 3.3.3 Spontaneous Emission Factor

The photonic density of states inside an optical cavity can be further engineered by tailoring the cavity design and optical properties. Controlling $N_{ph}$ enables the optimization of cavity performance for specific applications.

Incorporating the parameter $N_{ph}$ in the calculations not only allows for the estimation of the spontaneous emission lifetime inside the nanowire but also provides valuable insights into the calculations of the spontaneous emission factor $\beta$ of the laser.

By considering $N_{ph}$, it becomes possible to assess the rate of spontaneous emission into the lasing mode of the cavity relative to the total rate of spontaneous emission into all modes of the cavity as well as into free space. We calculate $\beta$ from the spontaneous emission rate.

Using Equation 3.112, we derive $\beta$ as

$$\beta = \frac{R^j_{spon}}{R^{total}_{spon}} = \frac{\int_0^\infty dE \int_{E_g}^\infty N^j_{ph}(E) C_0(E) \frac{c}{n} |\hat{e} \cdot p_{cv}|^2 \rho_r(E_{cv}) f_c(1-f_v) \frac{\gamma/2}{(E_{cv}-E)^2+(\gamma/2)^2} dE_{cv}}{(\Sigma_i \int_0^\infty dE \int_{E_g}^\infty N^i_{ph}(E) C_0(E) \frac{c}{n} |\hat{e} \cdot p_{cv}|^2 \rho_r(E_{cv}) f_c)(1-f_v) \frac{\gamma/2}{(E_{cv}-E)^2+(\gamma/2)^2} dE_{cv} + \int_0^\infty dE \int_{E_g}^\infty N^{fs}_{ph}(E) C_0(E) \frac{c}{n} |\hat{e} \cdot p_{cv}|^2 \rho_r(E_{cv}) f_c(1-f_v) \frac{\gamma/2}{(E_{cv}-E)^2+(\gamma/2)^2} dE_{cv})} \tag{3.118}$$

Understanding the spontaneous emission factor $\beta$ is crucial for optimizing the performance of lasers. A high value of $\beta$ indicates efficient light emission within the nanowire, where a large fraction of spontaneous emission is directed into the desired lasing mode. This leads to improved laser efficiency, lower threshold currents, and higher output power. Conversely, a low value of $\beta$ suggests inefficient emission, with a significant portion of the spontaneous emission dissipating into other modes or escaping into free space. This knowledge helps guide design choices and allows for optimizing nanowire parameters to achieve higher $\beta$ values and improved device performance.

Now that we know how all of the parameters in the laser rate equations are calculated, we will apply our laser model to simulate some of the laser structures in the literature for validation and benchmarking.

## 3.4 Validation

To validate our incorporation of the photonic density of states (PDOS) with practical examples, we investigate [210], which includes PDOS in the calculations of gain and spontaneous emission rates, considering both homogeneous and inhomogeneous broadening effects in different nanopillar lasers. The PDOS per unit angular frequency ($\rho(\omega)$) is calculated using

$$\rho(\omega) = \frac{2}{\pi \Delta\omega_{cav}} \tag{3.119}$$

for a narrow emitter and broad cavity, and

$$\rho(\omega_{cav}) \approx \delta(\omega - \omega_{cav}) \tag{3.120}$$

for a broad emitter and narrow cavity, where $\Delta\omega_{cav}$ is the cavity linewidth. The paper specifies that the quality factor $Q$ is 235, and it operates at a wavelength of $1.55\mu m$, which corresponds

to the angular frequency of

$$\omega_{cav} \approx 1.216 \times 10^{15} rad/s \tag{3.121}$$

Thus, the cavity linewidth $\Delta\omega_{cav}$is approximately $5.17 \times 10^{12} rad/s$.

The photonic density of states (PDOS) is then

$$\rho(\omega) \approx 1.231 \times 10^{-13} (rad/s)^{-1} \tag{3.122}$$

To compare this with our calculations for the photonic density of states in the nanopillar reported in [57], we convert these values from angular frequency to energy (J). Therefore, the photonic density of states per unit of energy is

$$\rho(E) = 1.166 \times 10^{21} (J)^{-1} \tag{3.123}$$

Also, in our derivation, we have used the photonic density of states per unit energy per unit volume. So, here we divide this with the effective volumes reported in the paper for two different nanopillars:

For $V_{eff} = 0.3\mu m^3$:

$$\rho(E) \approx 2.332 \times 10^{39} (J.m^3)^{-1} \tag{3.124}$$

For $V_{eff} = 0.0025\mu m^3$:

$$\rho(E) \approx 4.664 \times 10^{41} (J.m^3)^{-1} \tag{3.125}$$

Comparing these values with our photonic density of states in Figure 5.4, ranging from $0.1 \times 10^{40} - 2.75 \times 10^{40} (J.m^3)^{-1}$ we can see that they are in the same range and comparable to each other.

Similar to [210], [211] also discusses the photonic density of states for infinitely extended nanowire arrays in gain and spontaneous emission rate calculations using theoretical and computational methods. Maxwell's equations are solved using the Finite Element Method (FEM) to determine the local density of photon states (LDOS) within nanowire arrays, considering different line widths. They also plot the spectral PLDOS, normalized to the LDOS of free space, ranging from 0.4-2. [212] calculates PDOS by Finite Element Method (FEM). The PLDOS is computed for various heights within the unit cell. Due to the C4 symmetry of the unit cell, the x-PLDOS and y-PLDOS are identical upon rotation by 90 degrees and $\log_{10}$LDOS is plotted ranging from -1-3.

In the next step, in order to validate the calculations of the gain model developments, we simulate the $In_{0.15}Ga_{0.85}As$ nanopillar laser with a GaAs shell reported in [47], and shown in Figure 3.12. We compare the obtained results with the ones reported in the paper to validate our model.

The gain model is usually obtained by plotting the maximum of each gain spectra versus its corresponding carrier density. The gain model forms the stimulated emission term in laser rate equations. Linear and logarithmic gain models are two distinct approaches to modeling the behavior of the active medium under the pump.

The laser output is directly proportional to the input in the case of the linear gain model. In other words, if you double the input, the output also doubles. This is useful in systems where a direct and proportional relationship is expected between input and output.

On the other hand, a logarithmic gain model describes a situation where an incremental change in the input leads to a proportional change in the output on a logarithmic scale. This is often

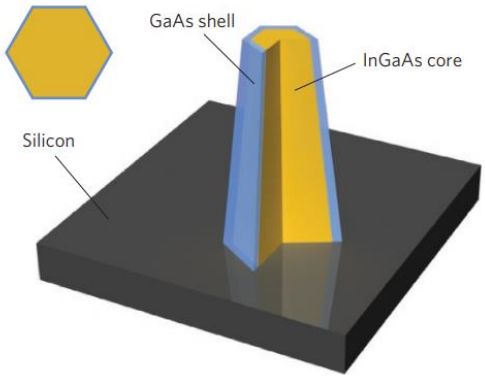


Figure 3.12: Schematic image of the $In_{0.15}Ga_{0.85}As$ nanopillar with a GaAs shell. Reprinted from [47].

found in systems where the output changes exponentially with input. The common form of the linear and logarithmic gain models is illustrated as [34]

$$g(N) = g_0(N - N_{tr}) \tag{3.126}$$

$$g(N) = g_0 ln(\frac{N + N_s}{N_{tr} + N_s}), \tag{3.127}$$

where $N_{tr}$ is the transparency carrier density, $g_0$ is the parameter representing the absorption in the gain medium, and $N_s$ is the parameter added to avoid the situation in which $ln(\frac{N+N_s}{N_{tr}+N_s})$ is equal to unity.

Table 3.1: Material characteristics of $In_{0.15}Ga_{0.85}As$ [47]

| **Paramater** | **Value** |
|---|---|
| $m_e^*$ | $0.062m_0$ kg [57] |
| $m_h^*$ | $0.5m_0$ kg [57] |
| $E_p((\hat{e} \cdot p_{c,v})^2 = \frac{m_0 E_p}{3})$ | $25.18ev$ [47] |
| $E_g$ | $1.306ev$ [57] |
| $\tau_{in}$ | $40fs$ [47] |
| $n$ | 3.7[57] |
| $T$ | $4K$ |

Using the material parameters tabulated in Table 3.1, and the band diagram presented in Figure 3.13, we solve Equation 3.89 for different carrier densities, as presented in Figure 3.14. By comparing our obtained results with the gain spectrums reported in [47], we can observe that the results almost match each other, which validates our numerical approach to calculate the gain spectrum of the material.

The gain spectrum is ultimately influenced by the confinement factor $\Gamma$ during the laser operation. This influence is illustrated by the term $\Gamma g(N)$ in the laser rate equations 2.57 and 2.58. The confinement factor  indicates how much of the electromagnetic field is confined within a specified volume, such as the cavity formed by the nanopillar. It is important to note that

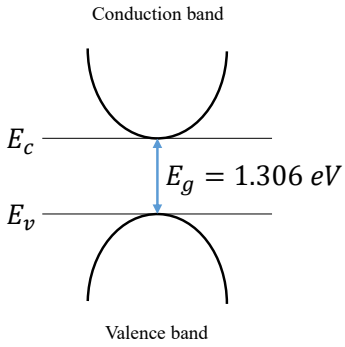


Figure 3.13: Energy band diagram of $In_{0.15}Ga_{0.85}As$ nanopillar

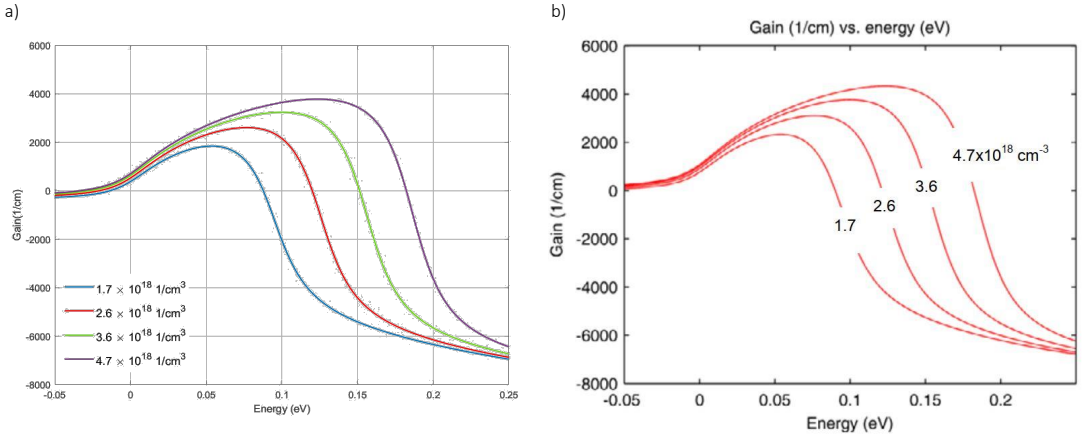


Figure 3.14: Gain spectra for various carrier densities using material parameters in Table 3.1. a) Gain spectrum obtained from our calculations, and b) The gain spectrum reported in [47]. The gain spectrum is represented in relation to the energy from the band edge.

$\Gamma$ and $g(N)$ are two distinct quantities: $g(N)$ represents the material gain, depending on the carrier density $N$ and intrinsic properties of the gain medium, while $\Gamma$ is a factor indicating the degree of field confinement. While $\Gamma$ affects the overall gain, it does not alter the material gain $g(N)$ itself. Instead, $\Gamma$ and $g(N)$ combine to give the overall gain $\Gamma g(N)$ experienced by the laser.

It is also essential to distinguish between the confinement and overlap factors. Confinement factor $\Gamma$ indicates how much of the electromagnetic field is confined in the cavity volume, while the overlap factor represents the portion of the electromagnetic field overlapping with the gain medium. In the bulk $In_{0.15}Ga_{0.85}As$ nanopillar laser, where the gain medium also serves as the cavity, the confinement factor and overlap factor are equal to each other, both having a value of unity. However, within a quantum well nanowire laser, since the nanowire volume is larger than the quantum wells volume, the Nanowire's confinement factor is not equal to the overlap factor. Therefore, in Chapter 5, for the quantum well nanowire laser, we will use the value of the overlap factor of 0.0341 for $\Gamma$.

In Figure 3.14, we plot the gain spectrum $g(N)$, the material gain, without the effect of the confinement factor $\Gamma$. The impact of $\Gamma$ will be applied later when solving the laser rate equations. In the context of quantum well nanowire lasers, where the gain medium occupies only a small portion of the cavity, the location of the quantum wells inside the nanowire becomes critically important. Failure to place them where the electromagnetic field is maximized may result in laser underperformance, as the maximum gain achievable may not be attained.

The gain spectra plot lets us calculate the maximum gains versus their corresponding carrier densities and develop the gain model. The logarithmic gain model for $In_{0.15}Ga_{0.85}As$ nanopillar is obtained, as shown in Figure 3.15. When we compare the results we obtained with the gain model mentioned in [47], we find that they are identical, which validates our numerical method used in calculating the gain model. Both the gain spectra and the logarithmic gain model, which is derived from our formalism, are very close to the results reported by Chen in [47]. This means that our model is able to accurately capture the behavior of the optical processes within a semiconductor.

Moreover, the maximum of the gain spectrums is between 1.306-1.456 eV, indicating that the maximum gain frequency coincides with the laser emission frequency. Therefore, our calculations confirm that this $In_{0.15}Ga_{0.85}As$ nanopillar laser benefits from the maximum gain.

## 3.5 Conclusion

In this chapter, we started by presenting a detailed discussion of the intricate optical processes taking place within a bulk semiconductor laser and we derived the equations describing absorption, gain, and spontaneous emission processes from the first principles. By introducing the photonic density of states in the calculations, we were able to capture the influence of the nanowire cavity on the rates of these optical processes.

Then we adapted the conventional semiconductor laser equations to describe the optical processes within a quantum well embedded inside a nanowire cavity. These modifications enable us to accurately calculate the gain and the spontaneous emission process. We also developed the equations to calculate the spontaneous emission factor and the Purcell factor in quantum well nanowire lasers. This theoretical foundation is essential for advancing our understanding of the quantum well laser's behavior and performance.

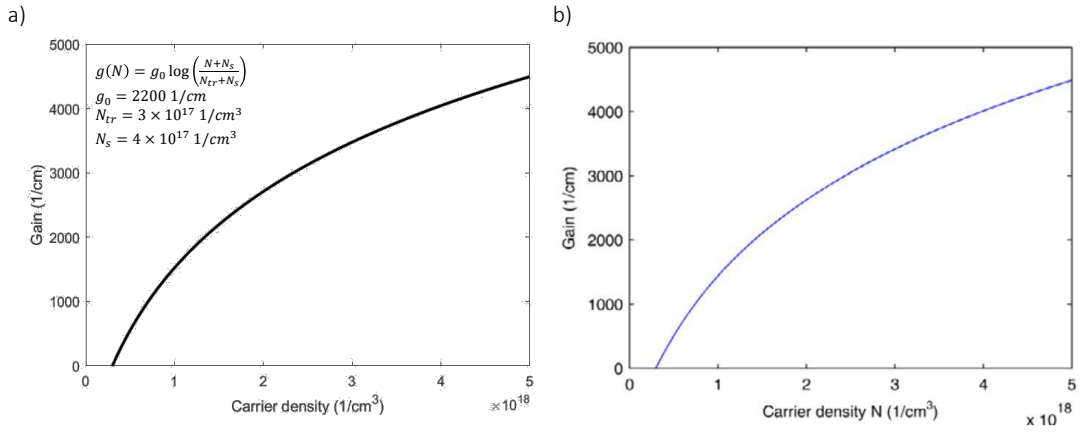


Figure 3.15: Logarithmic material gain model. a) the Gain model obtained from our calculations, and b) The gain model reported in [47].

To validate our theoretical framework for calculating the spontaneous emission factor in quantum well nanowire lasers, we can rely on both theoretical approaches and experimental data. Firstly, we can refer to relevant literature, such as [210] and [213], which investigate the spontaneous emission factor in nanopillar and quantum-dot nanocavity lasers, respectively. These studies derived equations similar to those in our theoretical framework, providing initial validation of our approach.

Secondly, comparing our simulation results with the calculations in [47] for optical processes within the $In_{0.15}Ga_{0.85}As$ nanopillar laser, allows for direct validation. By recreating the gain spectrum of the $In_{0.15}Ga_{0.85}As$ nanopillar using our formalism and comparing our simulation results with the results reported by Chen, we establish a benchmark for our theoretical framework.

Thirdly, by recreating the gain spectrum of the In0.15Ga0.85As nanopillar using our formalism and comparing our simulation results with the results reported by Chen, we establish a benchmark for our theoretical framework. Also, as discussed in Chapter 5, the peak of the spontaneous emission factor (0.0098) obtained from simulations closely aligns with the estimated value of 0.01 for $\beta$, derived from fitting the experimental data. This serves as strong evidence supporting the accuracy of our theoretical framework.

Furthermore, analyzing the L-L curve plot obtained from solving laser rate equations with $\beta$ as a function of carrier density offers another checkpoint for verification. As the simulated L-L curve plot aligns well with the experimental data presented in Chen's paper [47], it further confirms the reliability of our theoretical framework. This consistency between simulation predictions and experimental observations validates the derived equations and their ability to accurately capture the behavior of quantum well nanowire lasers.

# Chapter 4

# Computational Methods

## 4.1 Introduction

Our laser model consists of three main steps, namely cavity simulations, gain analysis, and solving the laser rate equations.

For the cavity simulation, we will discuss the Finite Element Method (FEM) in section 4.2.1. Then we will discuss how to implement FEM to simulate a nanowire laser cavity and obtain its eigenfrequencies along with the cavity-related parameters. We perform both two-dimensional (2D) and three-dimensional (3D) cavity simulations, each offering a unique understanding of the behavior of the nanowire laser. The 2D simulations in section 4.2.1 will be used to study the transverse modes of the cavity, and their corresponding effective mode indices. We will also use the 3D simulations to accurately visualize the longitudinal modes of the nanowire. Using 3D simulations also enables us to calculate the cavity-related parameters such as confinement factor ($\Gamma$), cavity quality factor ($Q$), and photon lifetime ($\tau_p$).

For solving the laser rate equations, we will discuss the fourth-order Runge-kutta numerical method in section 4.3. Also, We validate our choices of computational and numerical methods by comparing our simulation results with the experimental data.

## 4.2 Cavity Simulations

In the cavity simulations, our objective is to obtain the longitudinal and transverse modes of the nanowire laser. Once we have identified these modes, we will seek to calculate the parameters that are used in the laser rate equations.

Longitudinal modes are standing waves along the optical axis of the laser and they determine the frequencies at which the laser can oscillate, while transverse modes describe the intensity distribution of the laser beam's cross-section. To simulate the nanowire cavity, we will employ Finite Element Method (FEM) in COMSOL Multiphysics to solve Maxwell's equations which describe the electric field behavior within the lasers.

### 4.2.1 Finite Element Method (FEM)

Finite Element Method (FEM) was first established in the 1950s to assist in aircraft design and analysis [214], [215]. Its versatility, multifaceted approach, and adaptability have collectively

positioned it as an invaluable tool with countless applications. This capability has expanded FEM's usage beyond aircraft design into fields such as structural engineering, heat transfer, and fluid dynamics [215]. Its reach now extends beyond these spheres, making contributions in the optics and photonics sectors [216]–[220].

The finite-element method primarily consists of the following steps:

1. Breaking down the structure of interest into smaller elements or domains.
2. Describing the unknown solution (such as a field) with an interpolation function using values at the vertices or nodes of these elements.
3. Combining the equations for each element to create global matrix equations.
4. Solving the overall system of equations.

The core concept behind FEM is to break down a problem into smaller elements reducing the overall complexity into more digestible sections as shown in Figure 4.1. Discretization, a critical component of FEM, involves dividing the problem area into a set of simpler elements. The choice of element shape, size, and quantity depends on the problem's complexity level.

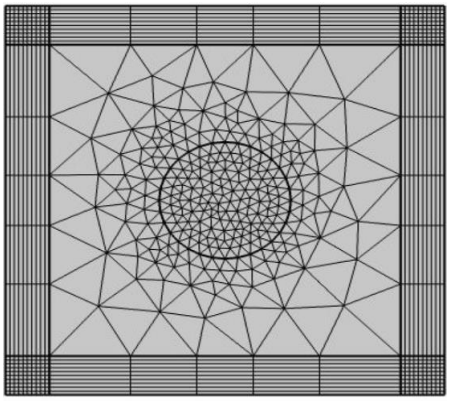

Figure 4.1: Schematic image of the transverse cross-section of a circular nanowire representing the discretization of the problem domain into smaller elements and domains in FEM.

In two-dimensional simulations, the most basic geometric unit used is the triangle as shown in Figure 4.2. However, more complex shapes such as triangles with curved sides and four-sided polygons can also be used. The same principle applies to three-dimensional problems. For three-dimensional problems, the basic finite element is the tetrahedron, with straight or curved sides as shown in Figure 4.3.

Complex geometry, varying material properties, and sophisticated boundary conditions often necessitate smaller elements, or specifically designed shapes to capture the problem's complexities accurately by taking into account that any intersection between two elements should be at an edge or a vertex and each element should contain only one homogeneous medium. Usually, the size of the individual element is not a crucial factor. However, in the domains where there are substantial field variations, a large number of smaller elements should be allocated.

In the FEM, an interpolation function, often a polynomial, is used to solve the desired equation to estimate an unknown field $\phi$. At any given node within an element, the interpolation function estimates the value of the unknown field. The field value is represented as $\phi_i$, where

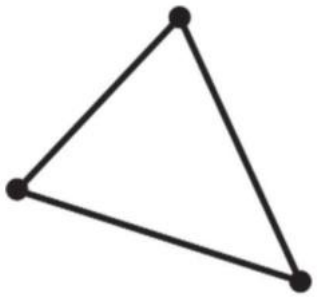

Figure 4.2: Triangle element shape used in two-dimensional problems in FEM. Reprinted from [221].

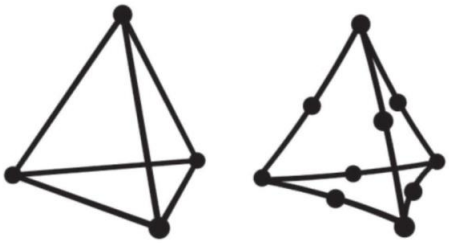

Figure 4.3: Tetrahedron element shapes with straight and curved sides used in three-dimensional problems in FEM. Reprinted from [221].

'$i$' corresponds to each node within the element. It's worth noting that different interpolation functions may be employed for each element. The unknown field in an element is defined as

$$\phi^e = \sum_{i=1}^{m} N_i \phi_i, \tag{4.1}$$

where $m$ is the total number of nodes within an element, $N_i$ is the interpolation function, and $\phi_i$ is the field at node i.

In our FEM simulation, the unknown field is the electromagnetic field ($\vec{E}$). Since the electric field is continuous across elements, the interpolation function has to be continuous as well. Also, the electric field is differentiable, therefore the interpolation function should be differentiable as well.

The degree of the polynomial, be it linear, quadratic, cubic, etc., usually corresponds with the approximation's accuracy. Higher degrees allow for capturing more complex behaviors with higher accuracy. The interpolation function needs to maintain continuity within the element. This continuity ensures that we can estimate the unknown field at any location within the element. Additionally, if adjacent elements share a node, the field will be continuous at the boundary as well. One can choose the different shapes and sizes for the elements to match the shape of the problem area. These elements collectively create a mesh, which can be a mix of small and big elements to make calculations faster and more efficient. This means using finer elements where precision is needed and larger elements in other areas.

The interpolation functions conform to the mathematical rules for each small part of a larger problem. We solve these smaller parts one by one and then combine their solutions to obtain the overall solution. The most efficient approach is to create a global matrix from all the equations that encompass all these smaller parts. This approach ensures that the solution works well within each part and smoothly connects them.

In the next step, the equations describing the field within each element (such as Equation 4.1) are assembled into a global matrix, which captures the interactions and constraints between all elements and nodes within the entire domain. The global matrix system will have a degree that is equal to or multiple times the number of nodes in the domain, which is expressed as follows [221]:

$$[A] \cdot [x] = [b] \tag{4.2}$$

where $[A]$ is the global matrix, $[x]$ is the vector of unknown field, and $[b]$ is the source vector.

Every line in the global matrix satisfies the requirements dictated by Maxwell's equations and the suitable boundary conditions. With effective techniques for solving these sets of equations and the computational power of modern computers, one can apply FEM to solve challenging problems without requiring a significant budget. In the following sections, we will present a detailed step-by-step approach to implementing FEM to obtain the transverse and longitudinal modes of a circular nanowire.

### 4.2.2 Two-dimensional Simulations

The first step in the design of a nanowire laser is two-dimensional simulations which provide insights into the transverse modes of the cavity and their corresponding effective mode indexes. By examining the relation between the nanowire's diameter and the effective mode index, designers can determine the number of guided modes and select the optimal nanowire diameter.

This knowledge facilitates the decision-making process in choosing between a single-mode or multi-mode laser configuration.

In two-dimensional simulations, we treat the nanowire as a waveguide. Also, we assume that the length of the waveguide goes to infinity. In 2D mode analysis, we solve the Helmholtz equation, which describes the mode propagation in the structure to determine the effective mode index ($n_{eff}$) of waveguide structures as

$$\nabla^2 E + {k_0}^2 n^2 E = \beta^2 E \tag{4.3}$$

Where $\nabla^2$ represents the Laplacian operator defined as $\nabla^2 = \frac{\partial^2}{\partial x^2} + \frac{\partial^2}{\partial y^2}$, $E$ is the electric field of the guided mode, $k_0$ is the free-space wavenumber given, $n$ is the refractive index of the waveguide material, and $\beta$ is the propagation constant of the mode. By solving this equation in COMSOL we can find $n_{eff}$, which is related to the propagation constant $\beta$ and the free-space wavenumber $k_0$ as

$$n_{eff} = \frac{k_0}{\beta} \tag{4.4}$$

In the following, we will use a 300nm circular GaAs nanowire laser surrounded by air which is shown in Figure 4.4 as an example. The refractive index of the GaAs nanowire is assumed to be 3.6 at 959nm, while the refractive index of the air is equal to unity. Figure 4.5 presents the simulation setup that we use to model the nanowire. Perfectly Matched Layers (PML) serve as absorbing boundary conditions to effectively dampen outgoing waves, preventing artificial reflections in the problems involving open domains or unbounded structures. In the frequency domain, the PML introduces a complex-valued coordinate transformation to the designated area, effectively ensuring absorption while maintaining a specific wave impedance, thereby eliminating reflections at the interface.

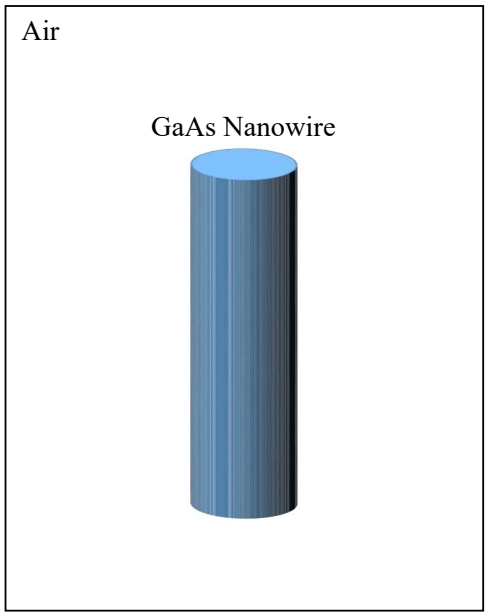


Figure 4.4: Schematic image of a 300nm circular GaAs nanowire laser surrounded by air.

As illustrated in Figure 4.5, we employ Perfectly Matched Layers (PML) at the edges of the simulation window in order to absorb the outgoing electromagnetic waves efficiently, preventing field reflections. The purpose of the PML is to simulate a domain with infinite cross-section. There are three important numerical choices that might change the outcomes of the simulations if they are not chosen wisely. First is the thickness of the PML, second is the distance of the PML from the nanowire, and third is the number of elements in the mesh. If these three parameters are not chosen properly, one might notice some variation in the results. Therefore we will perform convergence tests to make sure that our numerical choices are chosen in a way that the desired simulation accuracy is achieved.

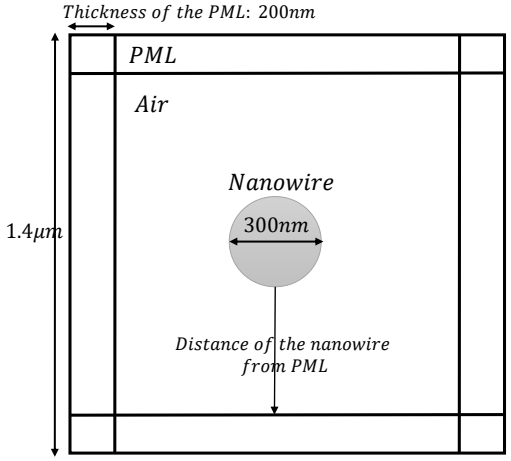


Figure 4.5: Schematic image of the transverse cross-section of the 300nm diameter circular GaAs nanowire surrounded by air in 2D simulation set-ups.

In the first step, we perform the convergence test for the $HE_{11}$ mode on the thickness of the PML. In the convergence test, we plot the variation in the effective mode index versus different thicknesses of the PML. The $n_{eff}$ describes the propagation speed of an optical mode within the nanowire, compared to the speed of light in a vacuum. In the two-dimensional transverse simulations, the effect of the length of the nanowire is neglected and the nanowire is treated similarly to a waveguide. In Figure 4.6, we can see that after a certain optimum point, there is no noticeable change in the value of the $n_{eff}$. When the thickness of the PML is larger than 160nm, the change in the $n_{eff}$ is less than 1%. Therefore, we consider this value optimal for achieving the desired accuracy and we select a PML width of 200nm throughout the simulations.

During the second step, we keep the PML thickness constant at 200nm and we change the distance between the PML layer and the nanowire, examining the impact of distance on $n_{eff}$ for the $HE_{11}$ mode. From Figure 4.7, it is clear that for distances larger than 350nm, the change in $n_{eff}$ is negligible. Therefore, we chose the value of 500nm for the distance from PML in the rest of the simulations.

The size of the elements in the simulations significantly influences the precision and computational efficiency of the simulated outputs. Figure 4.8a presents the 2D simulation domain with a mesh consisting of 770 elements while Figure 4.8b presents a mesh with 4232 elements. In the convergence test on the number of mesh elements, we set the PML thickness at 200nm and the distance from PML at 500nm, while changing the number of elements in the mode analysis.

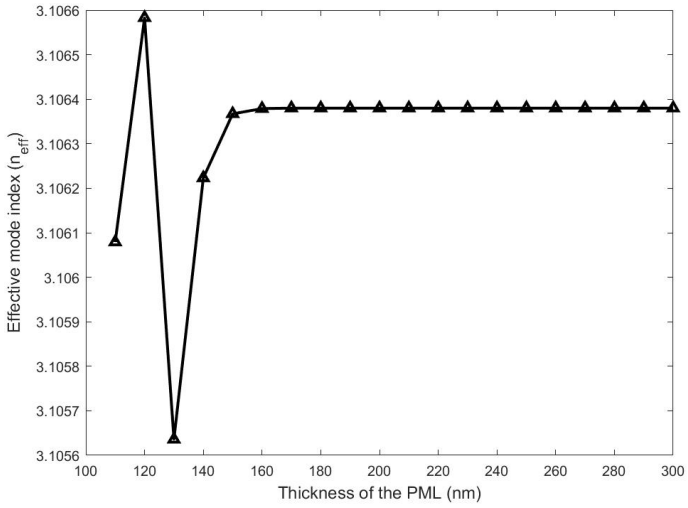


Figure 4.6: Evaluating $n_{eff}$ against PML thickness to identify the most suitable PML thickness in 2D nanowire simulations.

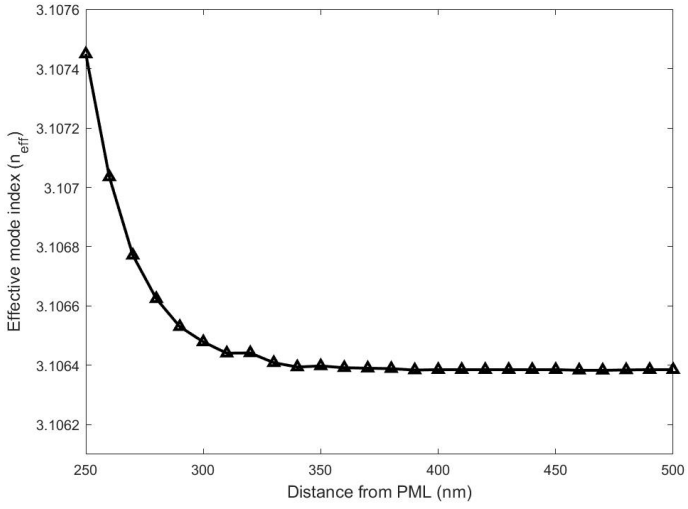


Figure 4.7: Evaluating $n_{eff}$ against the distance of the nanowire from PML to identify the most suitable distance of the PML from the nanowire in the simulations.

As discussed in section 4.2.1, as the number of mesh elements increases, the mesh is finer and the simulation is more capable of adequately sampling the field under investigation.

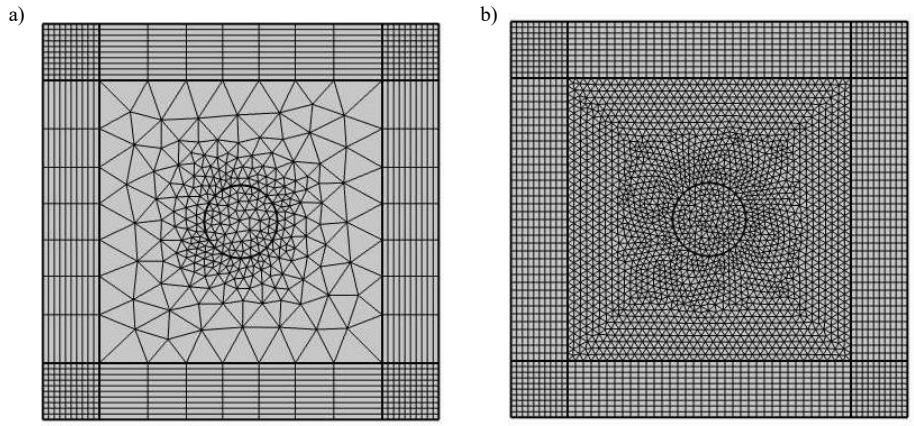


Figure 4.8: Impact of the size of the elements on the mesh in 2D simulations. a) presents the mesh with 770 elements, b) presents the mesh with 4232 elements.

Figure 4.9 portrays the convergence test plot, demonstrating the relationship between the number of mesh elements and the value of $n_{eff}$ for the $HE_{11}$ mode. The convergence plot indicates that, at the optimum number of 1000 elements the variation in $n_{eff}$ becomes negligibly small, signaling the convergence in accuracy.

By using the optimum values of PML thickness, distance from PML, and the number of mesh elements, we obtain a series of modes characterized by distinct field profiles and corresponding values of $n_{eff}$. In the following section, we will delve into the distinctive patterns of electromagnetic field distribution across the nanowire structure associated with each of these modes.

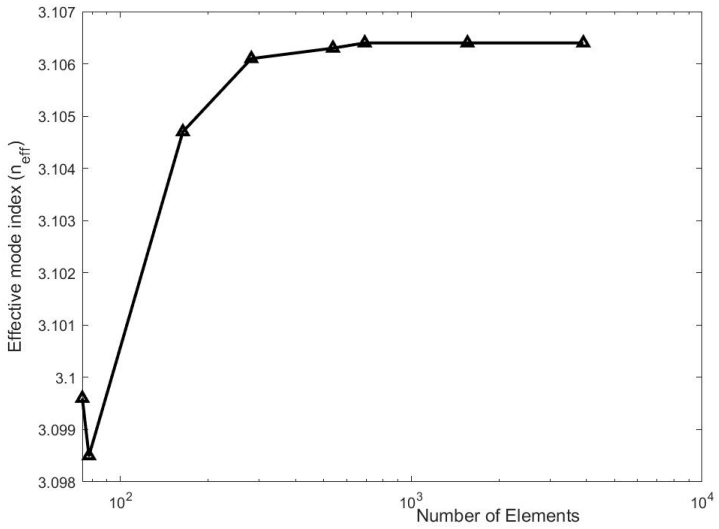


Figure 4.9: Comparing the number of elements with $n_{eff}$ to identify the ideal mesh size in the simulations.

#### 4.2.2.1 Field Distributions in Transverse Modes of the Cavity

The modes of the cavity are categorized into four types: Transverse Electric (TE), Transverse Magnetic (TM), Hybrid Electric (HE), and Hybrid Magnetic (EH) modes. The six different transverse modes in the circular GaAs nanowire of Figure 4.5 are presented in Figure 4.10. We also show the direction of the electric field with the black arrows, which assists in the mode classification. We discuss different mode classifications in the following:

When the electric field component parallel to the direction of propagation is zero, the mode is referred to as the Transverse Electric (TE) mode. The intensity of the electric field for the $TE_{01}$ mode in a circular GaAs nanowire is presented in Figure 4.10a. Conversely, Transverse Magnetic (TM) modes manifest where the magnetic field is entirely transverse, with the magnetic field component parallel to the propagation direction equal to zero. The intensity field distribution of the $TM_{01}$ mode is presented in Figure 4.10b.

Meanwhile, Hybrid modes are more intricate, having both the electric and magnetic field components parallel to the propagation direction. These modes are referred to as hybrid modes because neither the electric nor the magnetic field is entirely transverse. Hybrid Electric (HE) modes exist when the electric field is stronger than the magnetic field. Likewise, Hybrid Magnetic (EH) modes encompass electric and magnetic field components in the propagation direction, while the magnetic field is more dominant than the electric field. The $HE_{11a}$ and $HE_{11b}$ modes are the fundamental modes of the circular nanowire with the largest values of the effective mode index. Figure 4.10 presents the first eight guided modes of the circular GaAs nanowire surrounded by air at an operation wavelength of 959nm.

Hybrid modes are frequently encountered in confined cavities or irregular or asymmetric waveguides where the waveguide's geometric structure prevents the existence of either TE or TM modes. If we assume that the length of the nanowire is along the z-direction, we can summarise the mode classification as

- TE modes: $E_z = 0, H_z \neq 0$
- TM modes: $H_z = 0, E_z \neq 0$
- HE modes: $E_z > H_z$
- EH modes: $H_z > E_z$

Moreover, the modes are assigned with two different numbers for classification. The first number signifies half of the number of changes occurring in the field in the azimuthal direction, while the second number denotes the number of maximum field intensities when going from the center of the nanowire to the edge or corner. As an example, consider the mode $TE_{01}$, as illustrated in Figure 4.10a. In this case, there are no variations in field intensity along the azimuthal direction, thus the first number is zero. However, when moving from the center of the nanowire toward the edge, we once cross a maximum field intensity. Consequently, this mode is classified as $TE_{01}$. The subscript $a$ and $b$ in the mode classification defines the direction of the polarization. When the mode is polarised along the x-direction it is classified as $a$. Similarly, if it is polarised along the y-direction it is classified as $b$.

#### 4.2.2.2 Diameter versus Effective mode index

After obtaining the transverse modes of the cavity, we change the nanowire's diameter and plot the effective mode index versus the diameter, to identify the region where the nanowire will

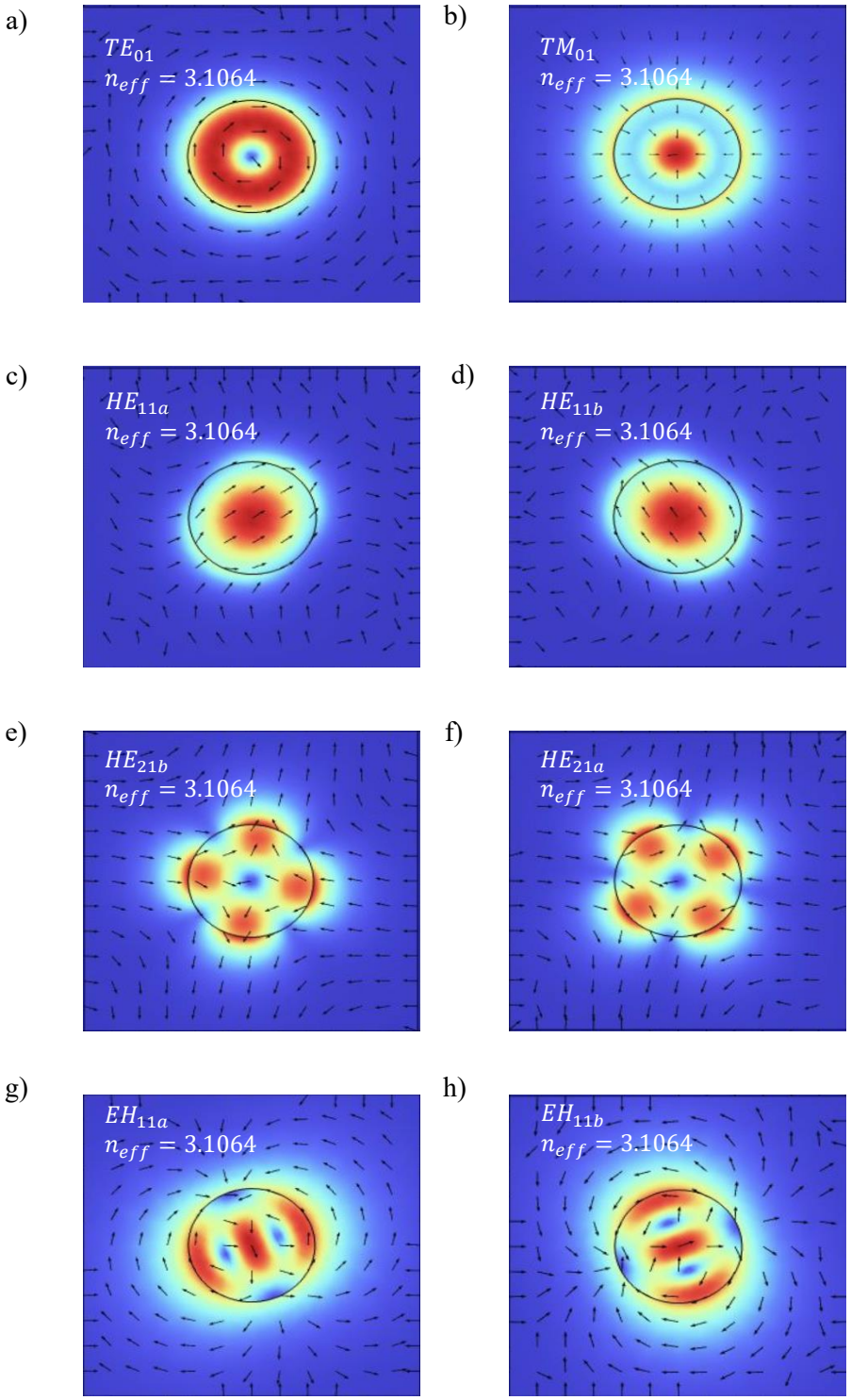


Figure 4.10: Electric field intensity of different transverse modes in the 300nm GaAs nanowire presenting a) $TE_{01}$, b) $TM_{01}$, c) $HE_{11a}$, d) $HE_{11b}$, e) $HE_{21a}$, f) $HE_{21b}$, g) $EH_{11a}$, h) $EH_{11b}$ modes. The direction of the Electric field is presented with black arrows for each mode.

operate as a single-mode laser.

It is shown in Figure 4.11 that as we increase the diameter of the nanowire, more transverse modes emerge. The fundamental transverse mode, $HE_{11}$, possesses the largest effective mode index. It is shown that for nanowires with diameters less than 200nm, the nanowire cavity only supports $HE_{11}$ modes. At the diameters larger than 200nm the cavity will support the mode $TE_{01}$ as well. As the diameter of the nanowire increases, the number of modes within the nanowire increases. If the nanowire cavity supports multiple modes, identifying which one of these modes will lase is of great importance. In the following section, we will explain how 2D simulations can be used to predict the lasing mode.

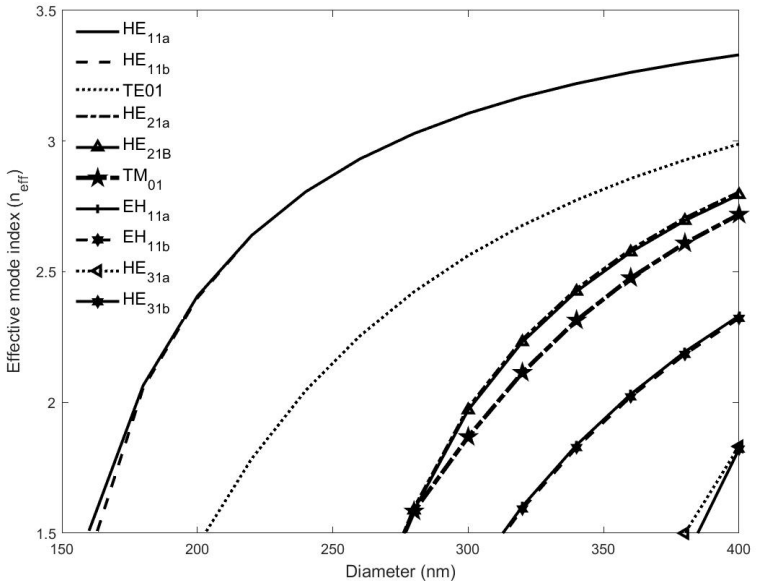


Figure 4.11: Effective mode index versus the nanowire diameter to identify the precise nanowire diameter conducive for single-mode operation.

#### 4.2.2.3 Predicting the Lasing Mode

When the diameter of a laser is large enough that it supports more than one mode, identifying which mode is the lasing mode might be quite challenging. This becomes more evident when the number of guided modes is large. Two-dimensional simulations may also be utilized as an analytical tool for predicting the lasing mode of nanowire lasers when multiple transverse modes are guided. To obtain the lasing mode, we change the operating frequency in our simulations and obtain the effective mode index of each transverse mode. Then we solve

$$2Ln_{eff} = N\lambda, \tag{4.5}$$

where $L$ corresponds to the length of the cavity, $n_{eff}$ is the effective mode index, $N$ denotes the integer number of half wavelengths, and $\lambda$ designates the wavelength. The modes which have the integer number of half wavelengths along the length of the nanowire can oscillate.

Usually, the oscillating modes within the nanowire are obtained from the 3D eigenfrequency analysis. However, solving Equation 4.5 gives us a rough prediction of the wavelengths in which each transverse mode might lase. This possible lasing wavelengths for different modes is obtained from the intersections as shown in Figure 4.12.

For a nanowire with a diameter of 250nm, and length of $2\mu m$, the prospective lasing modes can be identified at the points of intersection between the plots for each mode presented as solid colored lines and the plots indicating the integer multiple of the half wavelength, depicted by dotted black lines in Figure 4.12. From this plot, we learn that the nanowire can only lase with $HE_{11}$ mode at three distinct wavelengths of 775nm, 815nm, and 845nm. while the same nanowire will lase with $TE_{01}$ mode at 760nm, 790nm, and 827nm.

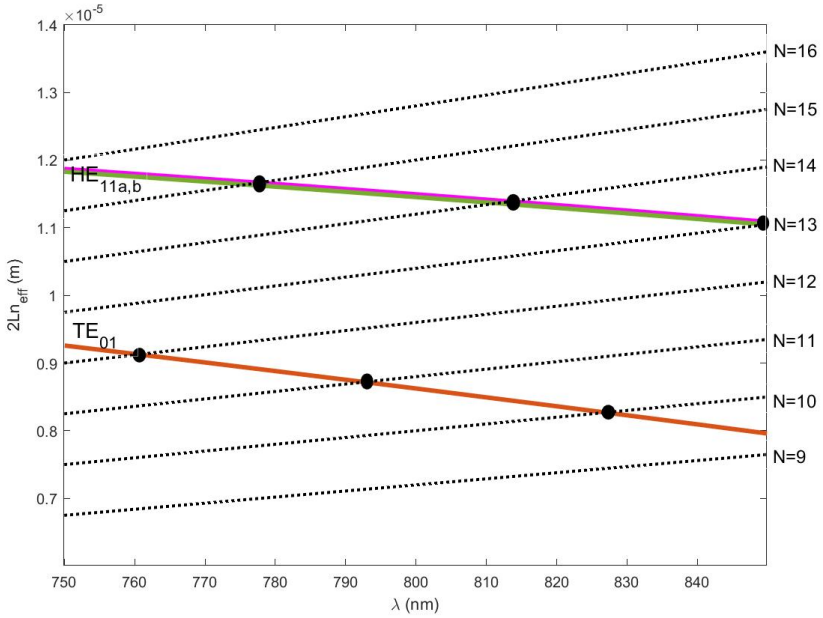


Figure 4.12: Plot of $2Ln_{eff}$ versus $N\lambda$, showing the intersections of the dotted black lines with colored lines to identify the lasing mode of a 250nm diameter and $2\mu m$ length GaAs nanowire laser.

### 4.2.3 Three-dimensional Simulations

After identifying the guided transverse modes of the nanowire and their effective mode indices a three-dimensional (3D) simulation setup is used to identify the longitudinal modes of the nanowire and calculate its optical properties. Longitudinal modes determine the resonant frequencies of the nanowire and present the electric and magnetic field distributions across its length. Moreover, 3D simulations are valuable in providing an accurate estimation for cavity-related parameters such as cavity quality factor ($Q$), confinement factor ($\Gamma$), and modal volume ($V_m$).

The wave equation for electromagnetic eigenfrequency analysis in three dimensions (3D) is based on Maxwell's equations. In the frequency domain, the wave equation is a fundamental equation that is solved to determine the resonant frequencies as

$$\nabla \times (\nabla \times \vec{E}) = \omega^2 \mu \epsilon \vec{E} \tag{4.6}$$

where $E$ is the electric field, $\omega$ is the angular frequency, $\epsilon_r$ is the relative permittivity, and $\mu$ is the relative permeability.

The wave equation describes the behavior of electric and magnetic fields in the structure. These equations are solved alongside appropriate boundary conditions and material properties, allowing the software to find solutions in the form of eigenfrequencies.

A big difference between 2D and 3D simulations is that the number of mesh elements in the 3D environment is significantly higher than in the 2D environment. Therefore, 3D simulations demand more memory space for storing detailed mesh data and it extends the duration of the simulation. It is of utmost importance to obtain an appropriate balance between accuracy and computational resource considerations in order to ensure efficient and effective simulations.

Our simulation setup in the 3D environment is shown in Figure 4.13 for the same 300nm diameter nanowire surrounded by the air used in the previous section with the GaAs nanowire having the refractive index of 3.6 at 959nm. The refractive index of the air around the nanowire is unity.

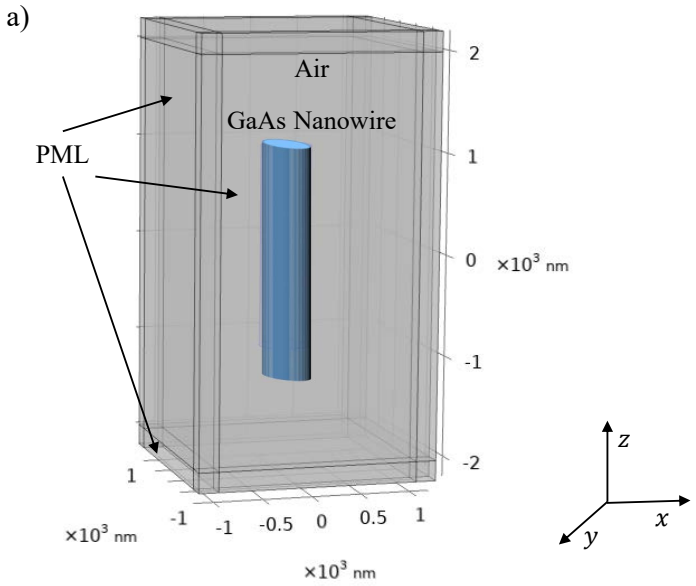


Figure 4.13: Schematic for simulation set-ups of a 300nm diameter and $2\mu m$ length circular GaAs nanowire in the rectangular 3D environment.

#### 4.2.3.1 Convergence tests, and Benchmarking

Similar to the 2D environment, the convergence tests check the independence of the simulation results from the numerical choices, such as how thick the Perfectly Matched Layers (PML) are, the distance of the nanowire from the PML, and how many mesh elements to be used. With these checks, we can feel more confident that our simulations are accurate. The convergence tests on the thickness of the PML, distance from the PML, and the number of mesh elements for the $HE_{11a}$ mode with the resonant frequency of 381.2THz are presented in Figures 4.14-4.16.

When we shift from two-dimensional (2D) to three-dimensional (3D) simulation environments using the Finite Element Method (FEM), there's a significant change in the number of mesh elements required to accurately model the nanocavity. In 2D simulations, we typically work with mesh elements around 1000, as shown in Figure 4.9. However, when we move to the more complex 3D environment, the number of mesh elements increases significantly due to the additional dimension. In 3D simulations, the mesh can grow to include 50000 elements, or even more, as depicted in Figure 4.16. The number of mesh elements is chosen based on the convergence tests, as discussed in sections 4.2.2 and 4.2.3.1. This increase in the number of

mesh elements becomes necessary to accurately capture the details and spatial complexities of the three-dimensional laser structure.

The increased number of mesh elements enhances the accuracy of the simulation by providing a finer resolution of the spatial distribution of the electromagnetic fields within the nanocavity. However, this improvement in accuracy comes at the cost of increased computational demands. Specifically, the time required to run the simulation increases substantially when transitioning from 2D to 3D. While our 2D simulations with 1000 mesh elements take around 5 minutes to compute, the 3D simulations with 50000 mesh elements take around one hour to run.

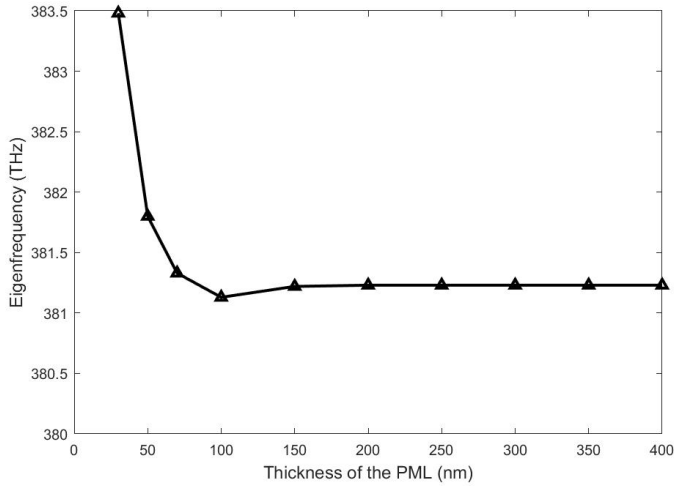


Figure 4.14: Convergence tests focusing on the numerical selections of the Perfectly Matched Layer (PML) thickness in the 3D simulations.

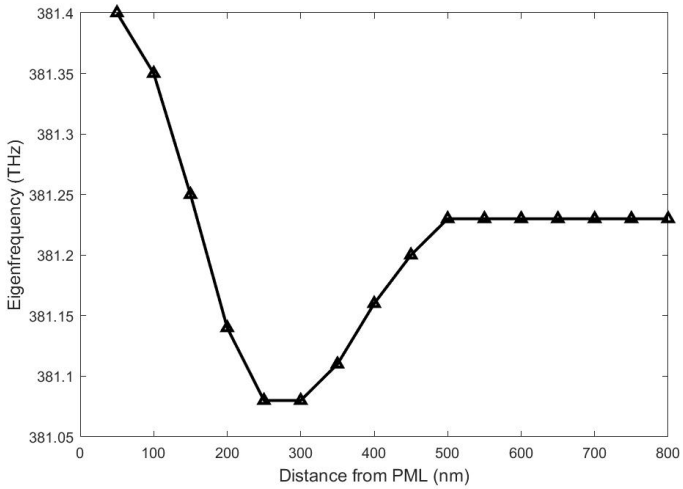


Figure 4.15: Convergence tests focusing on the numerical selections of the distance of the nanowire from the PML in the 3D simulations.

From Figures 4.14-4.16, we choose the distance from PML in the 3D simulations equal to 500nm. The thickness of the PML is chosen to be 200nm, with a number of elements close to the 50000. All of the converged values are chosen in a way that the change in the eigenfrequency values is less than 1% and the desired accuracy is achieved.

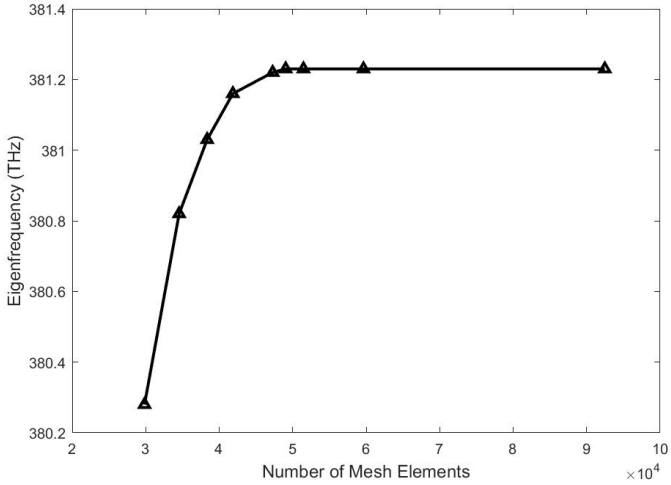


Figure 4.16: Convergence tests focusing on the numerical selections of the number of mesh elements in the 3D simulations.

#### 4.2.3.2 Longitudinal Modes and Cavity-Related Parameters

Eigenfrequency analysis in the frequency domain is used to identify the longitudinal modes of the nanowire. Figure 4.17 illustrates four of these longitudinal modes along with their corresponding resonant frequencies and electric field distributions along the length of the nanowire. The complex eigenfrequencies are directly associated with the field which attenuates within the PML. The quality factor of the cavity is also tied to these complex eigenfrequencies: a small imaginary part in the eigenfrequency suggests low loss whereas a larger imaginary part of eigenfrequency values indicates higher losses.

It is important to note that the 3D eigenfrequency analysis will give all the possible solutions for the resonant modes. Nevertheless, although some of these modes can create a standing wave along the length of the nanowire, they may not be the guided modes in the nanowire laser due to their small $n_{eff}$. Crossing out of such modes is possible due to the assistance of the 2D simulation results. When $n_{eff}$ is greater than the refractive index of the surrounding medium (here equal to unity for air), the mode is assumed to be guided. However, when the nanowire is placed on a substrate, guided modes are the ones with $n_{eff}$ larger than the refractive index of the substrate.

For each of the resonant cavity modes, by considering the position of the gain medium inside the nanowire, we are able to calculate the confinement factor $\Gamma$, Quality factor $Q$, and the photon lifetime $\tau_p$, respectively as

$$\Gamma = \frac{\int\int\int_{Gain-medium} ||\vec{E}||^2 dxdydz}{\int\int\int_{All-Domains} ||\vec{E}||^2 dxdydz}, \tag{4.7}$$

$$Q = \frac{Re(Eigenfrequency)}{2 \times Im(Eigenfrequency)}. \tag{4.8}$$

$$\tau_p = \frac{Q}{2\pi f} \tag{4.9}$$

where $\tau_p$ is the photon lifetime, and $f$ is the resonant frequency.

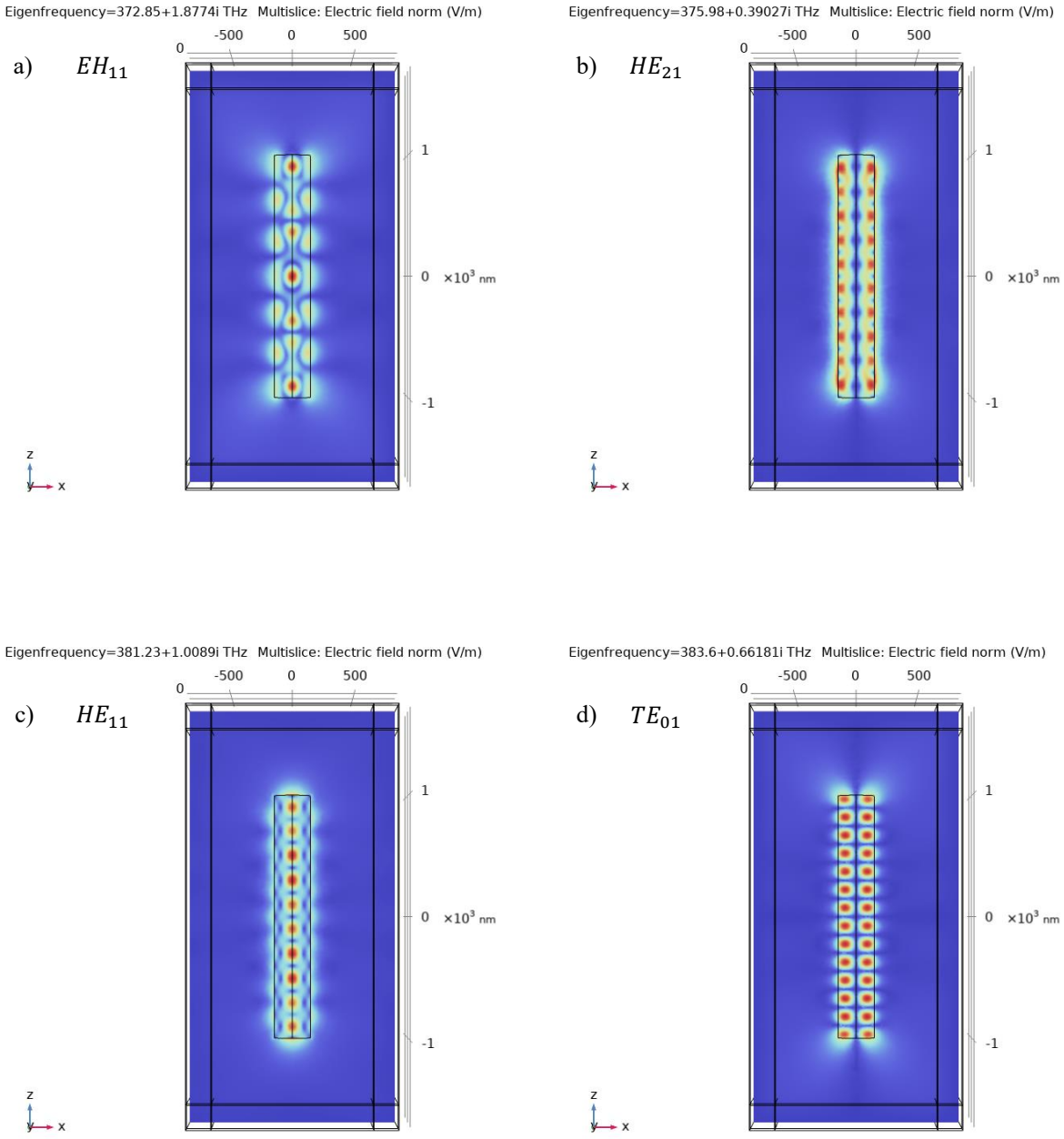


Figure 4.17: 3D simulation results of the 300nm diameter, and 2$\mu m$ long GaAs nanowire laser to obtain including resonant frequency and field intensity of a) $EH_{11}$, b) $HE_{21}$, $HE_{11}$, and $TE_{01}$ modes.

Given that the electric field profile is different for each mode, we will observe different values for $\Gamma$ and $Q$. These parameters will be used as the inputs for laser rate equations analysis.

To ensure the precision of the results of our simulations using FEM in COMSOL Multiphysics software, we compare our findings using with existing simulation results in the literature, such as Chen's work [47]. For instance, in Chapter 5, we replicate the study on an $In_{0.15}Ga_{0.85}As$ nanopillar laser and find $TM_{61}$ resonant mode around 921nm. This is consistent with the results obtained by Chen through FDTD simulations. This agreement between different simulation techniques, such as FDTD and FEM further validates the accuracy of the approach.

Additionally, we can verify our COMSOL simulation results with experimental data to build more confidence in the results. In Chapter 5, we also model the $In_{0.2}Ga_{0.8}As$ nanowire laser, identifying the $HE_{11b}$ mode as the lasing mode at 959nm, which agrees with the experimental measurements reported in [7]. Matching simulation results with experimental data provides a direct comparison between theoretical predictions and real-world observations.

Moreover, consistency between 2D and 3D simulations in identifying guided modes within the nanocavities and conducting convergence tests in sections 4.2.2 and 4.2.3 across different dimensions ensures that the results remain stable and are not overly influenced by numerical choices. In our 2D simulations, convergence tests were conducted to evaluate the effective mode index ($n_{eff}$) against the PML thickness, the distance of the PML from the Nanowire, and the number of elements in the mesh, as shown in Figures 4.6 through 4.8. From the analysis of the plots, we can see that after reaching specific points—200nm for PML thickness, 500nm for the distance of the nanowire from PML, and 1000 mesh elements—the variation in ($n_{eff}$) becomes negligible, indicating that these parameters are optimal for achieving accurate simulations. These optimized settings allowed for the consistent identification of distinct field profiles and their corresponding values across different modes.

Similarly, in our 3D simulations, convergence tests are done on the same parameters, as illustrated in Figures 4.14 through 4.16. Based on the Figures, we determined that the optimal settings for the 3D simulations are a distance of PML from the nanowire of 500nm and PML thickness of 200nm, with approximately 50,000 mesh elements. These tests ensure that for the chosen range of values of the simulation parameters, the effective mode indices and the resonant frequencies are converged and do not change by more than 1%, indicating that the results are robust and not significantly affected by the numerical choices made.

Conducting these convergence tests in both 2D and 3D simulations is crucial for validating the accuracy and stability of our COMSOL simulations. By systematically ensuring that our simulation parameters are converged, we can be confident that our simulations accurately reflect the physical phenomena being modeled. This process ensures that our findings are reliable and can be trusted for further analysis and applications.

## 4.3 Runge-Kutta Implementation

The purpose of this section is to numerically solve the laser rate equations to obtain the behavior of the carrier density and photons with time. This enables us to plot the L-L curve, which determines the relation between the laser output versus the input power. From the L-L curves, we predict the laser threshold and the spontaneous emission coupling efficiency.

The laser rate equations are

$$\frac{dN}{dt} = \frac{\eta P}{h\upsilon V} - (\frac{1-\beta}{\tau_{sp}} + \frac{\beta}{\tau_{sp}})N - \frac{N}{\tau_{nr}} - \Gamma g \frac{S}{V}, \tag{4.10}$$

$$\frac{dS}{dt} = \Gamma g S + \frac{\beta N V}{\tau_{sp}} - \frac{S}{\tau_p}, \tag{4.11}$$

The fourth-order Runge-Kutta method is a numerical technique for solving ordinary differential equations [222]. Here we present the general form of the fourth-order Runge-Kutta method:

If for an unknown function $y$ that is time dependent the differential equation is given as

$$\frac{dy}{dt} = f(t, y), \tag{4.12}$$

where

$$y(t_0) = y_0 \tag{4.13}$$

we can obtain the next value of y from the previous value of y for a step size $h$ on time as

$$k_1 = hf(t_0, y_0), \tag{4.14}$$

$$k_2 = hf(t_0 + \frac{h}{2}, y_0 + \frac{k_1}{2}), \tag{4.15}$$

$$k_3 = hf(t_0 + \frac{h}{2}, y_0 + \frac{k_2}{2}), \tag{4.16}$$

$$k_4 = hf(t_0 + h, y_0 + k_3), \tag{4.17}$$

By calculating the coefficients $k_1 - k_4$, we can obtain the value of $y(t_1)$ as

$$y(t_1) = y(t_0) + \frac{1}{6}(k_1 + 2k_2 + 2k_3 + k_4). \tag{4.18}$$

When applying the Runge-Kutta method to solve the laser rate equations, we use two separate sets of Runge-Kutta equations. One set will be dedicated to the differential equation related to carrier density ($N$), while the other set will address the differential equation for the number of photons ($S$). Therefore we can write the rate equations as

$$\frac{dN}{dt} = f_1(t, N, S), \tag{4.19}$$

$$f_1(t, N, S) = \frac{\eta P}{h\upsilon V} - (\frac{1-\beta}{\tau_{sp}} + \frac{\beta}{\tau_{sp}})N - \frac{N}{\tau_{nr}} - \Gamma g \frac{S}{V}, \tag{4.20}$$

$$\frac{dS}{dt} = f_2(t, N, S), \tag{4.21}$$

$$f_2(t, N, S) = \Gamma g S + \frac{\beta N V}{\tau_{sp}} - \frac{S}{\tau_p}. \tag{4.22}$$

where $N$ is the carrier density, and $S$ is the number of photons inside the cavity. The parameter $\eta$ is the fraction of pump power that is able to interact with the carriers, $h\upsilon$ is the energy of the pump photon, $V$ is the volume of the active region, $\tau_{sp}$ is the spontaneous emission lifetime,

$\beta$ is the spontaneous emission factor, $\tau_{nr}$ is the non-radiative recombination lifetime, $g$ is the active medium's gain, and $\tau_p$ is the photon lifetime.

There are six steps in solving the rate equations that are listed below. The coefficients $K_1 - K_4$ belong to the differential equation in 4.20, while the coefficients $L_1 - L_4$ are for the differential equation 4.22. For a starting point of $t(i)$, $N(i)$, and $S(i)$ we have

$$K_1 = f_1(t(i), N(i), S(i)), \tag{4.23}$$

$$L_1 = f_2(t(i), N(i), S(i)), \tag{4.24}$$

$$K_2 = f_1(t(i) + \frac{h}{2}, N(i) + \frac{hK_1}{2}, S(i) + \frac{hL_1}{2}), \tag{4.25}$$

$$L_2 = f_2(t(i) + \frac{h}{2}, N(i) + \frac{hK_1}{2}, S(i) + \frac{hL_1}{2}), \tag{4.26}$$

$$K_3 = f_1(t(i) + \frac{h}{2}, N(i) + \frac{hK_2}{2}, S(i) + \frac{hL_2}{2}), \tag{4.27}$$

$$L_3 = f_2(t(i) + \frac{h}{2}, N(i) + \frac{hK_2}{2}, S(i) + \frac{hL_2}{2}), \tag{4.28}$$

$$K_4 = f_1(t(i) + h, N(i) + hK_3, S(i) + hL_3), \tag{4.29}$$

$$L_4 = f_2(t(i) + h, N(i) + hK_3, S(i) + hL_3), \tag{4.30}$$

Coefficient $K$ and $L$ are defined as

$$K = \frac{h}{6}(K_1 + 2K_2 + 2K_3 + K_4) \tag{4.31}$$

and

$$L = \frac{h}{6}(L_1 + 2L_2 + 2L_3 + L_4) \tag{4.32}$$

Therefore the next step in the time which is presented with $t(i+1)$ is obtained from Equation 4.33. Also, $N(i+1)$, and $S(i+1)$ are the carrier density and the number of photons at $t(i+1)$ and are calculated using Equations 4.34 and 4.35.

$$t(i+1) = t(i) + h, \tag{4.33}$$

$$N(i+1) = N(i) + K, \tag{4.34}$$

$$S(i+1) = S(i) + L. \tag{4.35}$$

In the following section, we will solve different rate equations using the Runge-Kutta method to validate our approach. Also, we will investigate the different outcomes from solving the laser rate equations and investigate the impact of different parameters such as the quality factor on the threshold and the spontaneous emission coupling efficiency.

### 4.3.1 Solving Laser Rate Equations for Different Semiconductor Micro and Nano-cavity Lasers

Solving the laser rate equation gives us the number of the carriers and the photons with time. By plotting the input power versus the output power of the laser, we will be able to obtain the L-L curve. The L-L curve will give us the value of the threshold pump power and the spontaneous emission coupling efficiency. In the next section, we will simulate e bulk GaAs microcavity laser to investigate behavior of the the carrier density and number of photons with time. Also, we will plot the L-L curves to obtain the threshold.

#### 4.3.1.1 GaAs Microcavity Semiconductor Laser

In order to validate our choice of the numerical method, first, we solve Equations 4.10-4.11, using the fourth-order Runge-Kutta method with values tabulated in Table 4.1 for the microcavity semiconductor laser in [89] which is presented in Figure 4.18. After solving Equations 4.10-4.11, we plot the number of photons versus time as presented in Figure 4.19.

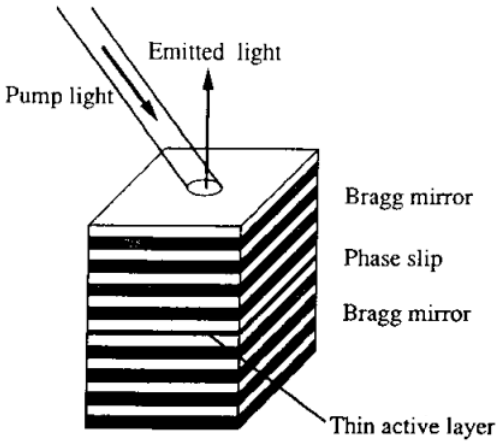


Figure 4.18: Schematic image of the microcavity laser. Reprinted from [89].

Table 4.1: Laser Rate Equation Parameters [46]

| **Paramater** | **Value** |
|---|---|
| $\gamma$ | |
| $\tau_{sp}$ | $1ns$ |
| $\tau_{nr}$ | $0.01ns$ |
| $N_{tr}$ | |
| $V$ | $10^{-15}cm^3$ |
| $\lambda$ | $1\mu m$ |

From Figure 4.19 we can see that when the number of photons inside the cavity is less than unity, the losses outweigh the gain. At this point, the laser operates below the laser threshold, indicating that spontaneous emission is the dominant process. However, the losses and the gain balance out as the number of photons inside the cavity approaches unity. Upon crossing the threshold energy within the laser cavity builds up significantly, with stimulated emission becoming the dominant process. This results in a rapid spike and subsequent oscillations in the photon response, which is shown in Figure 4.19, signaling the threshold.

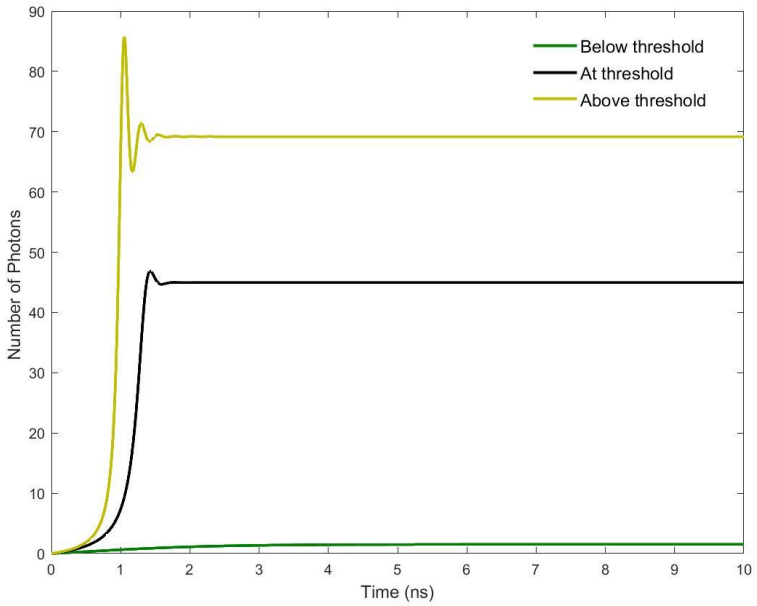


Figure 4.19: Change in the number of photons with time below, at, and above the threshold.

This sudden change signifies the transition from the sub-threshold to the supra-threshold regime. Gradually, the system stabilizes as the laser operation evolves toward a steady-state condition.

The rate equations 4.10-4.11 are fundamental to understanding the dynamics of a laser system, particularly in describing the temporal evolution of carrier density N and photon density S. These equations can be used to determine the lifetime or excitation timescale with respect to Figure 4.19. The key factor in this context is the laser's net gain, $\Gamma g$, which dictates how quickly the photon density $S$ increases once the threshold is crossed. When $\Gamma g$ exceeds the photon decay rate $(1/\tau_p)$, the number of photons rapidly increases, marking the onset of lasing and resulting in a sharp slope in Figure 4.19. This slope reflects the rapid rise in photon density and indicates the excitation timescale.

After solving the laser rate equations, the injected current can be plotted against the number of photons inside the laser cavity to create the laser's L-L curve. In Figure 4.20a, we present the L-L curve that was obtained from the numerical solution Equations 4.10-4.11 using the fourth-order Runge-Kutta method for values of $\beta$ changing from $10^{-5} - 10^{0}$.

Figure 4.20 shows a clear relationship between $\beta$ and the laser's performance. As $\beta$ increases, both the threshold current and the height of the kink in the L-L curve decrease significantly. Reducing the threshold current and kink height with increasing $\beta$ implies that more spontaneous emissions are coupling into the lasing mode. This increase in the coupling enhances the stimulation process, thereby reducing both the threshold current required for lasing and the height of the kink which ultimately leads to a more efficient lasing process.

By comparing our simulation results with the data presented in Figure 4.20b, we establish that our simulated results match the reported values in [46]. This comparison serves as a validation of the numerical method we have employed, as well as the accuracy of our assumptions and models incorporated in the laser rate equations. In order to validate our laser model for smaller semiconductor laser structures, in the next section, we simulate the nanopillar laser reported

in [47] to investigate the laser behavior.

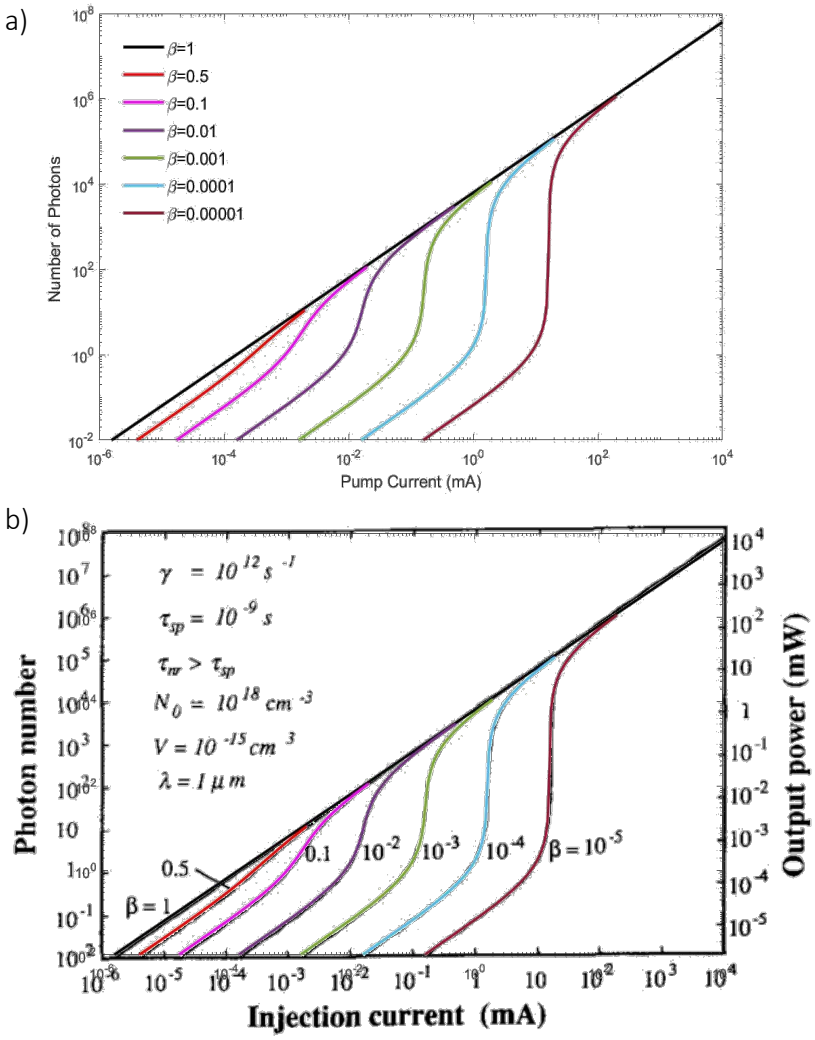


Figure 4.20: The Light-Light (L-L) curve for a semiconductor laser. a) The curve obtained from our numerical simulation using the Runge-Kutta method to solve the laser rate equations. b) The L-L curve as reported in the study by Bjork et al. (1991) [46]. Comparison between the simulation results and the reported data to check the validity and accuracy of our numerical approach for solving the laser rate equations.

After validating our numerical method using the GaAs microcavity laser with DBR cavity in [89], we simulate a nanopillar $In_{0.15}Ga_{0.85}As$ laser where it is much smaller than the one in [89] in size and its shape is much closer to a nanowire laser.

#### 4.3.1.2 $In_{0.15}Ga_{0.85}As$ nanopillar Semiconductor Laser

In this step, by employing the parameters tabulated in Table 4.2, we solve laser rates of Equations 4.10-4.11 and investigate the nanopillar laser shown in Figure 4.21 which is reported in [47]. By plotting the carrier and photon density with time, the gain-switching effect can be visualized as the jump in the value of both carrier and photon densities below and after the threshold.

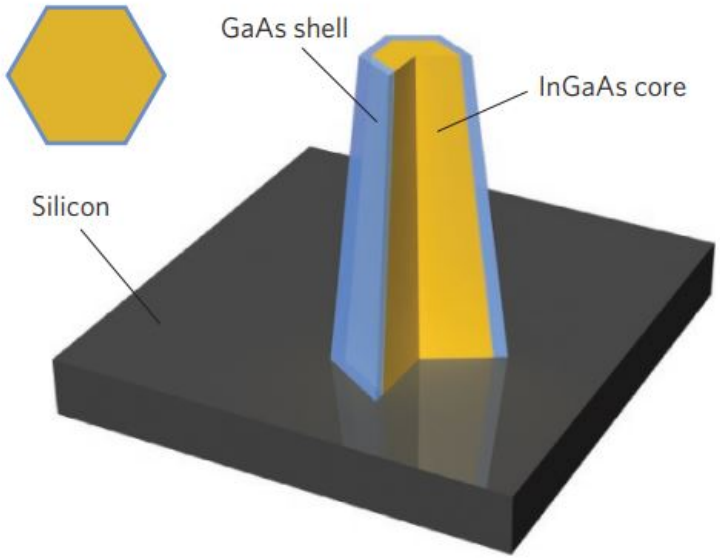


Figure 4.21: Schematic image of the $In_{0.15}Ga_{0.85}As$ nanopillar grown vertically on the silicon substrate. Reprinted from [47]

In Figures 4.22a and 4.22b, the temporal response of carrier and photon densities is depicted below the threshold, at the threshold, and above the threshold. The distinction between the response below the threshold (where the system behaves linearly) and above the threshold (where the nonlinear effect becomes noticeable) is particularly noteworthy.

An additional aspect apparent in the figure is the phenomenon of gain switching, a crucial element in the operation of lasers. Gain switching arises from the dynamic interplay between the carrier and photon densities and signifies a shift in the gain state due to population inversion. The number of carrier and photon densities versus time in Figure 4.22 reveals that a marked jump in the photon density becomes apparent when the laser crosses the threshold. This sharp increase can be seen as a reflection of the stimulated emission process, which greatly amplifies the number of photons within the laser cavity.

Table 4.2: Laser Rate Equation Parameters [47]

| **Parameter** | **Value** |
|---|---|
| $A$ | $1.43\times10^{8}s^{-1}$ |
| $\tau_{sp}$ | 4 ns |
| $C$ | $3.5\ \times10^{-30}cm^{6}.s$ |
| $n_g$ | 4.2 |
| $\Gamma$ | 1 |
| $N_s$ | $4\times10^{17}cm^{-3}$ |
| $g_0$ | 2200 $cm^{-1}$ |
| $N_{tr}$ | $3\times10^{17}cm^{-3}$ |
| $V$ | $6\ \times10^{-13}cm^{3}$ |
| $\eta$ | 2.5% |

After solving the rate equations, we investigate the effect of changing the quality factors, as demonstrated in Figure 4.23. The Q-factor measures the energy losses in the cavity. A higher Q-factor corresponds to lower losses, meaning the energy is stored better in the system over

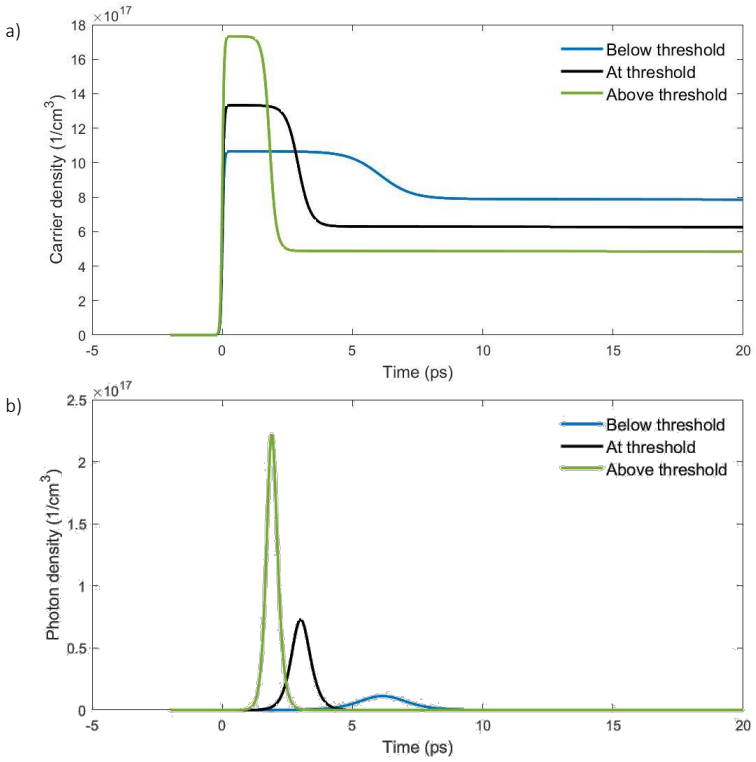


Figure 4.22: The change of the a) carrier and b) photon densities with time below the threshold, at the threshold, and above the threshold.

time. It is evident from the plots that as the quality factor increases, photon lifetime increases as well. Therefore, higher values of the quality factor are desirable.

Consequently, a longer photon lifetime, triggered by a higher quality factor, implies minimizing losses within the cavity. This phenomenon can be interpreted as the cavity becoming increasingly efficient at retaining and building up energy. This effect directly influences the interaction between carriers and photons within the active medium. When cavity losses are reduced and photon lifetime increases, the light within the cavity has more opportunities to interact with the active medium. This promotes the critical lasing process of stimulated emission.

The laser threshold tends to decrease as the quality factor increases. This is because the efficient energy buildup in the cavity, due to reduced losses and increased photon lifetime, enables the necessary condition of population inversion to be achieved more easily. Hence, less pump power is needed to achieve lasing.

## 4.4 Conclusion

In this chapter, we have embarked on the exploration of the various stages involved in accurately modeling a laser. We started by introducing the FEM as an approach for simulating the laser cavity, which enables the determination of parameters associated with the cavity. Then we discussed the step-by-step approach to implementing FEM in the 2D and 3D simulation environment to determine the transverse and longitudinal modes of the nanowire. We also presented the equations for calculating the nanowire optical properties such as the confinement factor, and quality factor.

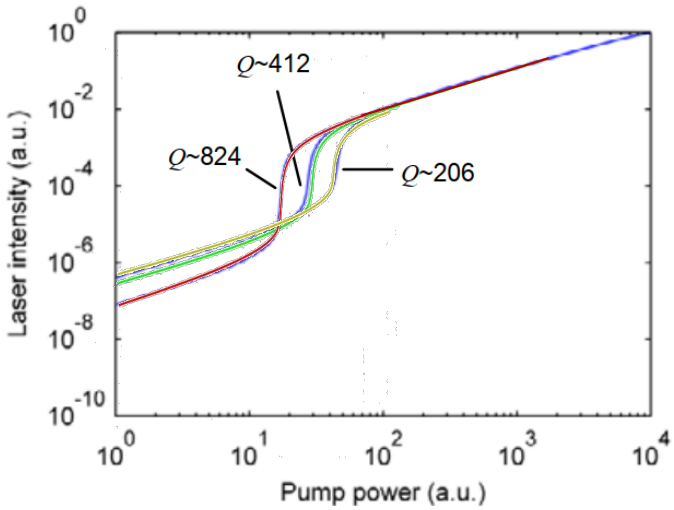


Figure 4.23: The L-L curve obtained for different values of quality factors with a) our numerical simulations, and b) data reported in [47].

Finally, we discussed the fourth-order Runge-Kutta method as our numerical choice of method to solve the laser rate equations. We also validated and benchmarked our theoretical model and simulation results by analyzing different laser structures in [47], [89] and comparing the simulation results with the outcomes reported in these papers.

# Chapter 5

# Lasing Dynamics and Characteristic Parameters of Nanopillar and Quantum-well Nanowire Lasers

## 5.1 Introduction

In this chapter, first, we will present an application of our formalism by simulating the behavior of an $In_{0.15}Ga_{0.85}As$ nanopillar laser, which belongs to the category of bulk semiconductor microcavity lasers as reported in [47]. Once we examine the laser characteristics and validate our simulation results through comparison with experimental data, we will move from the study of bulk nanopillar lasers to quantum well nanowire lasers. This provides us with a deeper understanding of how laser properties change from bulk to quantum wells.

In the next step, we will implement the formalism we developed for quantum well nanowire lasers into action. Building on the concepts discussed in Chapters 3 and 4. Our focus is to model the ten $In_{0.2}Ga_{0.8}As/GaAs$ quantum wells nanowire laser, which is reported in [7]. To accomplish this, we will utilize both full three-dimensional (3D) and two-dimensional (2D) simulations of the nanowire to gain a comprehensive understanding of how the nanowire's geometry affects its optical properties.

Within this context, we will apply the theoretical framework introduced in Chapter 3 to explore how absorption, gain, and spontaneous emissions take place within the 19nm thick quantum wells when placed inside the nanowire. Furthermore, we will integrate the results obtained from the nanowire simulations and the optical processes within the quantum wells to solve the laser rate equations. We will then compare our results with previous models used to solve these equations and validate our findings by cross-referencing them with experimental data. This investigation will enhance our understanding of the nanowire laser's performance and demonstrate the accuracy of our theoretical framework.

## 5.2 $In_{0.15}Ga_{0.85}As$ Nanopillar Laser

In order to validate our formalism and our laser model in different types of lasers, in this section we are going to simulate the $In_{0.15}Ga_{0.85}$ nanopillar laser reported in [47]. This $In_{0.15}Ga_{0.85}$ nanopillar laser is a bulk microcavity semiconductor laser. The gain spectrum simulations for

this nanopillar laser are obtained using our formalism in section 3.4 using the bulk electronic density of states in Equation 3.81. Also, we discussed solving the laser rate equations to obtain the threshold of this nanopillar laser using $\beta = 0.01$ which is obtained by fitting the experimental data to the simulations in section 4.3.1.2. In this section, we will implement the Finite Element Method in order to simulate the electromagnetic field within the nanopillar. Figure 5.1 presents a schematic image of the nanopillar laser. A hexagonal 330nm nanopillar laser with a height of $3\mu m$ is grown vertically on the silicon substrate.

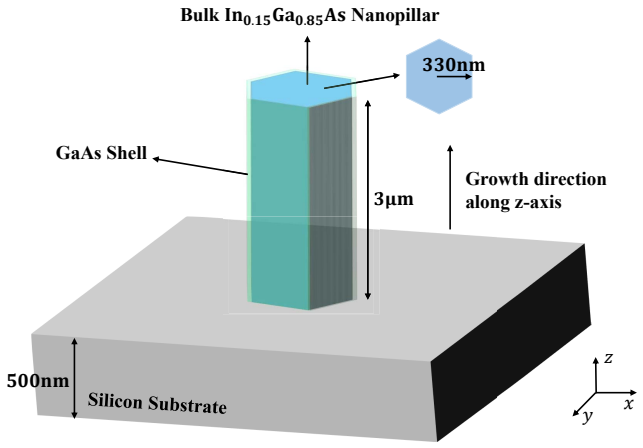


Figure 5.1: Schematic image of the $In_{0.15}Ga_{0.85}As$ nanopillar grown vertically on the silicon substrate.

### 5.2.1 Nanopillar Electromagnetic Field Simulations

We use the Finite Element Method to simulate the electromagnetic field within the nanopillar using a similar approach discussed in section 4.2.3. Using the 3D nanopillar simulation setup in Figure 5.2 with a PML thickness of 200nm, distance from PML equal to 500nm, and 72822 mesh elements, we perform the eigenfrequency analysis in the frequency domain to obtain the electromagnetic field within the nanopillar.

The 3D eigenfrequency analysis of the nanopillar laser gives us the resonant modes of the nanopillar listed in Table 5.1. The experimental data in [47], reports the emission frequency of the laser at 325 THz. Using the 3D eigenfrequency analysis, we observe that around the emission frequency, $TM_{61}$ with the frequency at 324.54 THz has the highest quality factor equal to 4779. Therefore, we predict that this mode is most likely the lasing mode of the nanopillar. This agrees with the results reported in [47]. One can see the electric field intensity profile of the $TM_{61}$ mode in Figure 5.3. In the follwing section, we will use the results of our 3D nanopillar simulations and the resonant modes listed in Table 5.1 to obtain the photonic density of states.

### 5.2.2 Photonic Density of States (PDOS) of the $In_{0.15}Ga_{0.85}$ Nanopillar Laser

The photonic density of states within the nanopillar determines the number of available states at particular energies that photons can couple with them, per unit volume.

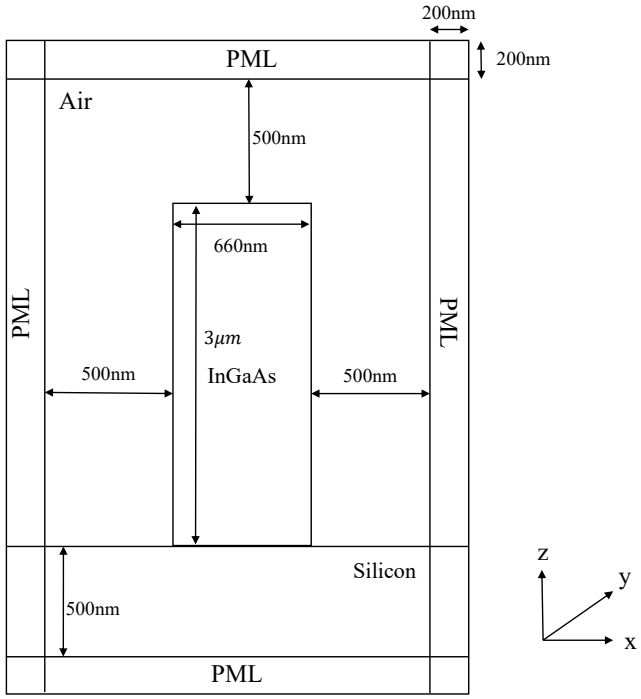


Figure 5.2: Schematic image of the cross-section from the 3D simulation setup in xy-plane for the $In_{0.15}Ga_{0.85}As$ nanopillar grown vertically on the silicon substrate.

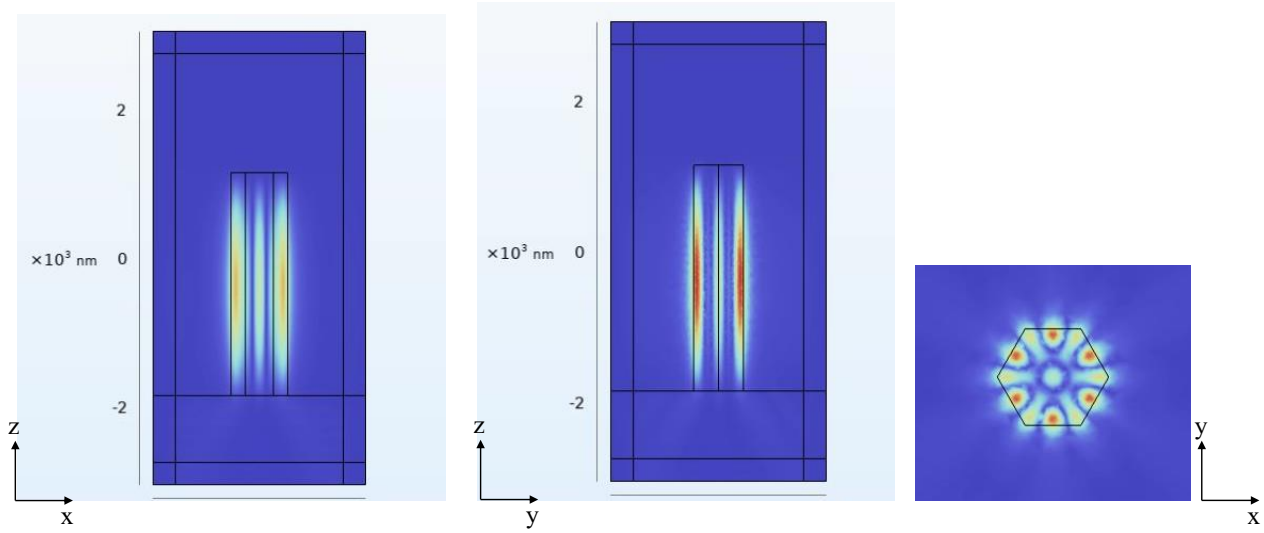


Figure 5.3: Electric field intensity of the $TM_{61}$ mode within the $In_{0.15}Ga_{0.85}As$ nanopillar.

Table 5.1: Resonant modes of the nanowire obtained from 3D eigenfrequency simulations

| Modes | Frequency (THz) | Quality factor |
|---|---|---|
| $TE_{49a}$ | 323.14 THz | 64.34 |
| $TE_{49b}$ | 323.16 THz | 63.88 |
| $TE_{61a}$ | 323.27 THz | 2962.3 |
| $TE_{61b}$ | 323.27 THz | 2964.7 |
| $TE_{49a}$ | 323.81 THz | 69.19 |
| $TE_{49b}$ | 323.81 THz | 69.25 |
| $TE_{25a}$ | 324.02 THz | 51.46 |
| $TE_{25b}$ | 323.02 THz | 53.75 |
| $TE_{52a}$ | 324.55 THz | 1148.0 |
| $TE_{52b}$ | 324.55 THz | 1148.7 |
| $TM_{61}$ | 324.62 THz | 4779.9 |
| $TE_{37}$ | 324.67 THz | 135.40 |
| $TE_{01}$ | 324.96 THz | 70.69 |
| $TM_{62}$ | 325.27 THz | 2708.3 |
| $TM_{63}$ | 326.37 THz | 1512.3 |
| $TE_{63a}$ | 326.53 THz | 640.94 |
| $TE_{63b}$ | 326.53 THz | 641.12 |
| $TE_{18a}$ | 326.96 THz | 99.80 |
| $TE_{18b}$ | 326.96 THz | 99.82 |
| $TE_{61}$ | 327.32 THz | 9842.2 |
| $TM_{64}$ | 327.92 THz | 921.14 |
| $TE_{62}$ | 327.97 THz | 4005.8 |
| $TE_{38a}$ | 328.38 THz | 96.58 |
| $TE_{38b}$ | 329.05 THz | 174.15 |
| $TE_{63}$ | 329.06 THz | 1975.5 |

We use the spectrum of the twenty modes listed in Table 5.1 to obtain the nanopillar PDOS ($N_{ph}^{NP}$) in Figure 5.4. The spectrum for each mode is given by a Lorentzian function which is related to the linewidth of the modes within the nanopillar as

$$N_{ph}^{NP}(E) = \sum_{j=1}^{m} \frac{1}{V} \frac{\gamma_j/2\pi}{(E - E_j)^2 + (\gamma_j/2)^2} \tag{5.1}$$

where $E_j$ is the central energy of the $j^{th}$ resonant mode of the nanopillar, $V$ is the volume of the nanopillar, $m$ is the number of resonant modes within the nanopillar, and $\gamma$ is the linewidth of each mode of the nanopillar. The linewidth of each mode is obtained as

$$\gamma_j = \frac{E_j}{Q_j} \tag{5.2}$$

where $Q_j$ is the quality factor of each mode.

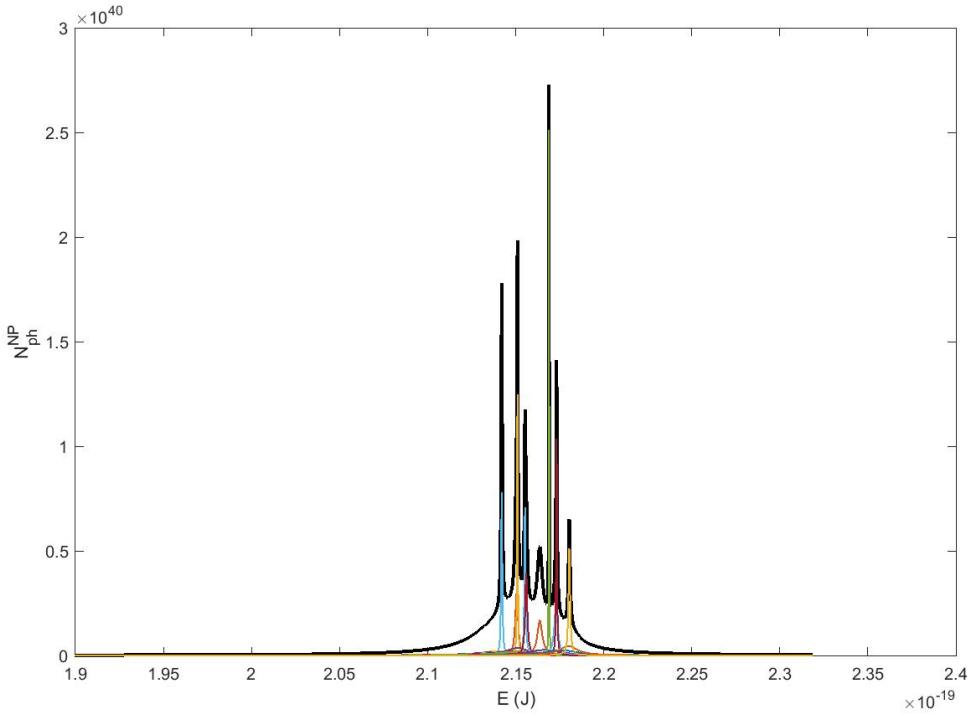


Figure 5.4: Spectra of the twenty modes of the nanopillar listed in Table 5.1 around laser emission energy(colored lines) and the nanopillar photonic density of states represented with black color.

The photonic density of states ($N_{ph}$) is obtained from the sum of the free space PDOS and the spectra of the resonant modes within the nanopillar as

$$N_{ph} = N_{ph}^{fs} + N_{ph}^{NP} \tag{5.3}$$

The free space PDOS is given as [57]

$$N_{ph}^{fs} = \frac{8\pi n^3 E^2}{h^3 c^3}, \tag{5.4}$$

where $n$ is the refractive index of the gain medium, $h$ is Planck's constant, and $c$ is the speed of light.

From Equation 5.3 we know that the total PDOS is obtained from the sum of the nanopillar PDOS and the free space PDOS. Figure 5.5 presents free space PDOS with a blue line, and the total PDOS with a black line. In the following section, we will use the PDOS to obtain the spontaneous emission rate and calculate $\beta$.

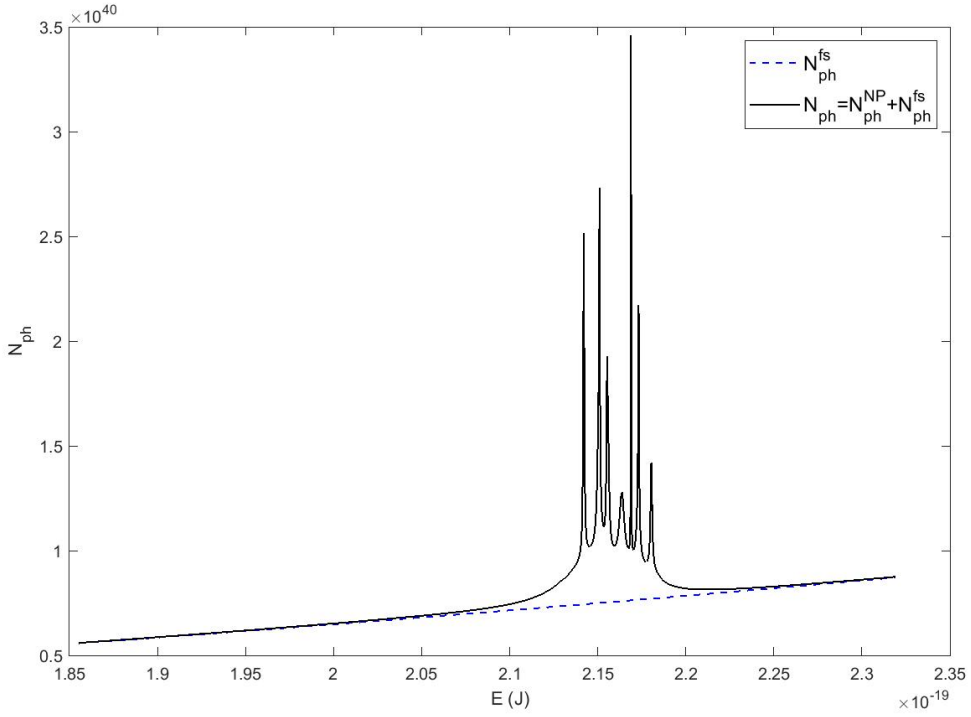


Figure 5.5: $N_{ph}^{fs}$ (blue dotted line) PDOS and $N_{ph}$ (black line) in the nanopillar.

### 5.2.3 Spontaneous Emission Factor $\beta$ in the $In_{0.15}Ga_{0.85}$ Nanopillar Laser

By using the $In_{0.15}Ga_{0.85}As$ material characteristics in Table 3.1, and photonic density of states simulation results in section 5.2.2, we solve Equation 3.118 to calculate the spontaneous emission factor ($\beta$). The spontaneous emission factor for the $In_{0.15}Ga_{0.85}As$ nanopillar lasers is presented in Figure 5.6.

From Figure 5.6 we can see that for low carrier densities, $\beta$ remains almost constant at a value of 0.0028. When the carrier density is larger than $1 \times 10^{22} m^{-3}$, $\beta$ gradually increases. However, when the carrier density is between $1 \times 10^{23} - 1 \times 10^{24} m^{-3}$, $\beta$ dramatically rises and reaches to 0.0092. For large carrier densities, $\beta$ decreases to around 0.001.

For carrier densities close to the intrinsic carrier density $\beta$ almost remains constant. As the carrier density increases, we will have an increase in the $\beta$ for carrier densities between the transparency carrier density and the threshold. After that, by increasing the carrier densities, the spontaneous emission factor will decrease and the photons emitted from the spontaneous emission process, will either couple to other nanowire modes or most likely emitted into free

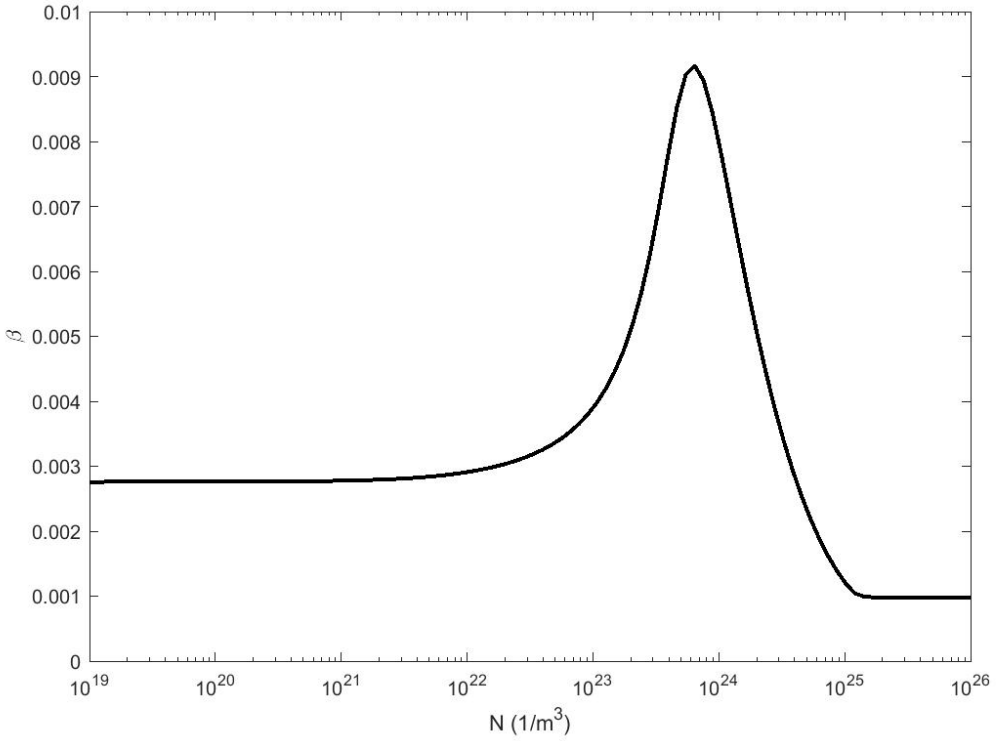


Figure 5.6: $\beta$ versus carrier density for the $In_{0.15}Ga_{0.85}As$ nanopillar laser.

space. The spontaneous emission rate into the free space is more dominant compared to the spontaneous emission rate into the other modes of the nanowire.

Spontaneous emission factor is treated as a fitting parameter in [47] and it is reported as a constant value equal to 0.01. Comparing the value of $\beta$ with the $\beta$ obtained from our formalism, our formalism predicts that $\beta$ changes with carrier density and presents a mechanism to calculate it. we can see that the maximum of our $\beta$ reaches 0.0098 which is very close to the fitted value which validates our formalism for bulk semiconductors. In the following section, we will use the gain model that we developed in Section 3.4 and $\beta$ obtained in this section to solve the laser rate equations to obtain the laser threshold and compare the simulation results with the experimental data to further validate our model for bulk semiconductor lasers.

### 5.2.4 Laser Rate Equation Analysis

In this section, we will use the gain model that we obtained from our formalism and presented in Figure 3.15 to solve the laser rate Equations 3.35-3.36 and we compare the results with experimental data to validate our laser model. One of the advantages of our model is that we don't use the logarithmic fitting function in the form of Equation 3.120. We directly use the gain model from our formalism in the laser rate equations. We solve the laser rate equations using the parameter in Table 4.2 except for the parameters $g_0$, $N_{tr}$, and $N_s$ as they are related to the gain fitting function. Figure 5.7 presents the L-L curve of the nanopillar laser for $Q = 206$. Here we first plotted the L-L curve using our formalism for gain and $\beta$. This plot is shown with the red line in Figure 5.7. Then, we plotted the L-L curve using $\beta = 0.01$ to study how the L-L curve is different when $\beta$ is a constant value. This plot is shown with the black line. Finally, to validate our laser model we compare our simulation results with the L-L curve plot

for $Q = 206$ reported in the [47]. This plot is presented with the blue line.

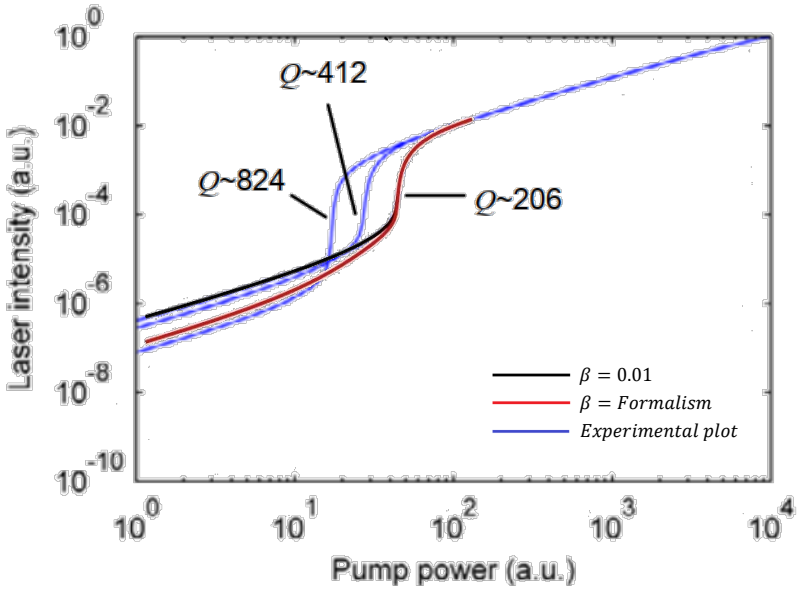


Figure 5.7: L-L Curve plots for $In_{0.15}Ga_{0.85}As$ nanopillar laser for $Q = 206$ obtained for a) $\beta = 0.01$ (black line), b) $\beta$ and gain from our formalism (red line), and the experimental plot (blue line)

Figure 5.7 shows that below the threshold, the L-L curve obtained from our formalism has smaller values compared to the scenario when $\beta = 0.01$. This is explained using the Figure 5.47. Low pump powers are not able to excite a high carrier density into the conduction band. Therefore, for low pump powers, the $\beta$ from our formalism is 0.0028. However, as the pump power increases, $\beta$ increases as well, and for the values near the threshold ($N = 1 \times 10^{23} - 1 \times 10^{24} m^{-3}$) the red and black plots get closer to each other. From Figure 5.6 we can see that for all of the carrier densities, $\beta$ from our formalism is always less than 0.01. That's why the red plot is below the black plot where the changes in $\beta$ with carrier density are neglected. For large pump powers, the stimulated emission dominates laser emission. From Figure 5.7 we notice that for $Q = 206$, our formalism is also able to predict the laser threshold accurately which further validates our gain model.

Similar arguments can be used to describe the laser behavior for $Q = 412$ in Figure 5.8. The same behavior is also observed when we use $Q = 412$. The L-L curve plot from our formalism has smaller values below the threshold when the spontaneous emission process is dominant. By comparing Figure 5.7 and 5.8 we can see that as the quality factor increases, the nanopillar threshold decreases while the height of the kink in the L-L curves increases.

The simulation of the $In_{0.15}Ga_{0.85}As$ nanopillar laser enabled us to validate both our theoretical framework and the accuracy of our laser model, particularly in the context of bulk nanocavity lasers. Having established the foundation, the subsequent section of our study extends and builds upon our understanding of bulk laser behavior and move from the study of bulk nanocavity lasers to the quantum well nanowire lasers. This helps us to gain a deeper understanding of how laser properties evolve and how the laser's behavior transforms when we move from bulk nanopillar laser to quantum well nanowires.

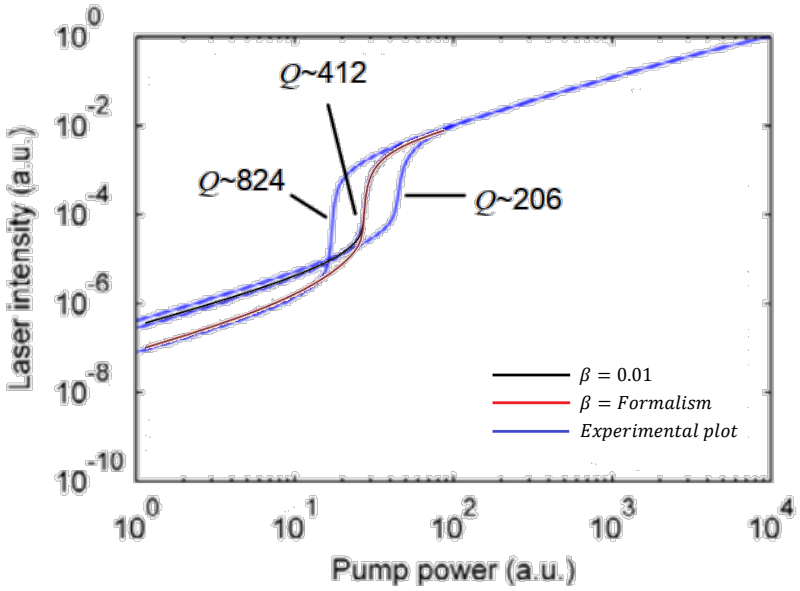


Figure 5.8: L-L Curve plots for $In_{0.15}Ga_{0.85}As$ nanopillar laser for $Q = 412$ obtained for a) $\beta = 0.01$ (black line), b) $\beta$ and gain from our formalism (red line), and the experimental plot (blue line)

This transition from conventional bulk semiconductor lasers to quantum well (QW) nanowire lasers leads to key changes in laser characteristics that support the wider use of QW nanowire lasers. These key changes are summarized as follows:

**Quantum Confinement Effects:** Bulk semiconductor Lasers operate in a three-dimensional structure with a large gain medium in terms of volume; carriers can move freely within the bulk gain medium with a continuous parabolic electronic density of states, while in QW nanowire laser, the small thickness of the QWs, carriers can move in two directions, and we have confinement in one direction. This leads to discrete energy levels and a step-like electronic density of states. The quantum confinement effect causes a higher probability of recombination at these levels and more efficient population inversion at lower thresholds, making the lasing process more efficient compared to bulk lasers, where the carriers are distributed over a broader range of energy states [223].

**Enhanced Material Gain:** This increase in the gain occurs because the quantum confinement in QW nanowire lasers leads to discrete energy levels and the step-like electronic density of states, which result in a higher probability of electron-hole recombination at specific energies, thereby increasing the material gain. In the gain spectrum of the material, where the x-axis represents energy and the y-axis represents gain, this quantum confinement effect results in a sharper and higher peak compared to bulk lasers. Also, the gain model of the material is obtained by plotting the maximum of the gain spectrum at different carrier densities. Since the peak height in the gain spectrum of a QW laser is higher than that of a bulk nanowire laser, this results in a larger gain model. For example, the peak of the gain spectrum in a GaAs nanowire laser reached $2000cm^{-1}$, while the maximum of the gain spectrum in a GaAs/AlGaAs multiple QW nanowire laser is around $3700cm^{-1}$ [149], illustrating the superior gain characteristics due to the enhanced electron-hole recombination efficiency in QW nanowire lasers.

**Larger spontaneous emission factor:** In bulk semiconductor lasers, the spontaneous emission coupling factor ($\beta$) is relatively low because the active region is large, and spontaneous emission occurs in all directions. However, the quantum confinement effect in the quantum wells combined with the optical confinement in the nanowire ensures efficient interaction between the gain medium and optical modes, which directs a larger proportion of spontaneous emission into the lasing mode, resulting in a higher $\beta$ factor. For example, in the GaAs nanowire laser in [149], the spontaneous emission factor is 0.015, while in the multiple GaAa/AlGaAs nanowire laser $\beta$ is 0.03.

**Reduced threshold pump power:** The reduction in threshold pump power is directly linked to the step-like density of states resulting from quantum confinement. The efficient population inversion in QW nanowire lasers reduces the number of carriers required to achieve lasing, thus lowering the threshold pump power [223]. In contrast, nanowire lasers without QWs have continuous energy states similar to the bulk, and require a higher pump power to achieve the same level of population inversion, resulting in a higher threshold current. For instance, the threshold pump power of the GaAs nanowire laser is reported as $177\mu Jcm^{-2}$ per pulse, while the threshold pump power of the GaAs/AlGaAs multiple QW nanowire laser is around $110\mu Jcm^{-2}$ per pulse [149].

**Non-radiative Recombination rates:** QW nanowire lasers exhibit lower non-radiative recombination rates due to the enhanced carrier confinement and their nanoscale dimensions. Localized electrons and holes in discrete energy states reduce the probability of non-radiative recombinations. For instance, in the nanowire lasers discussed in [149], the GaAs nanowire without quantum wells exhibits a non-radiative lifetime of 0.44ns, whereas the GaAs/AlGaAs quantum well nanowire laser shows a longer non-radiative lifetime of 5ns. This longer non-radiative lifetime in the QW nanowire laser results in a reduced rate of non-radiative recombination.

**Wavelength tunability:** In bulk semiconductor lasers, the emission wavelength is mainly determined by the bandgap of the gain medium, which is a fixed property of the material. This means the laser can only emit at wavelengths close to this bandgap energy. In contrast, QW nanowire lasers offer a remarkable degree of wavelength tunability by altering the thickness of the QWs. Changing the QW thickness modifies the energy levels of the confined carriers, as shown in Figure 5.38, effectively shifting the emission wavelength. Thinner QWs result in higher energy transitions (shorter wavelengths), while thicker wells have lower energy transitions (longer wavelengths). This design flexibility allows the QW nanowire lasers to produce a wide range of emission wavelengths, enhancing the versatility and functionality of these lasers across different applications. For example, in [158], it is shown that by adjusting the number and thickness of InGaN/GaN QWs in GaN nanowires, the lasing emission could be tuned across a broad spectrum from 365 to 494 nm.

**Temperature sensivitty:** Increases in temperature lead to a broadening of energy states, which can destabilize the lasing process by shifting the emission wavelength and reducing gain [224]. However, in QW nanowire lasers, the discrete energy levels remain relatively stable with temperature changes, maintaining the efficiency of the lasing process even at elevated temperatures. This stability is crucial for applications requiring consistent performance over a wide temperature range. III-V QW nanowire lasers featuring quantum-confined active regions have been developed in [140], [159], offering improved temperature stability compared to their bulk counterparts.

## 5.3 Ten $In_{0.2}Ga_{0.8}As$/GaAs Quantum-well Nanowire Laser

Figure 5.9 provides a visual representation of the ten $In_{0.2}Ga_{0.8}As$/GaAs quantum well nanowire laser studied in [7]. A single $2.2\mu m$ height hexagonal GaAs nanowire with 200nm diameter is grown vertically on a $SiO_2$(285nm)/Si substrate with growth direction along the z-axis. Ten 19nm thick $In_{0.2}Ga_{0.8}As$/GaAs quantum wells (shown with green color) are embedded inside the nanowire. Quantum wells are located at $1.2\mu m$ from the bottom of the nanowire. However, the nanowire is peeled off from the substrate and placed horizontally on the substrate for lasing measurements.

We will apply our laser model to simulate the nanowire laser laid horizontally on the Silica substrate, as shown in Figure 5.9 in three main steps:

1. Classical simulations of the electromagnetic field within the nanowire
2. Analysis of absorption, gain, and spontaneous emission dynamics
3. Laser rate equation analysis

In the following sections, we will explore each of these steps in detail, starting with the electromagnetic field simulations inside the nanowire.

## 5.4 Nanowire Electromagnetic Field Simulations

In the field simulations section, we implement Finite Element Method (FEM) in COMSOL Multiphysics software to model the nanowire as discussed in section 4.2. Our objectives are to obtain the transverse and longitudinal modes of the nanowire and identify the lasing mode. Then we will calculate optical parameters such as the quality factor, confinement factor, and the photonic density of states. We first start with the two-dimensional nanowire simulations.

### 5.4.1 Two-dimensional Simulations

The objective of the two-dimensional simulations is to obtain the transverse modes of the cavity and calculate their corresponding effective mode indices. Here, we assume that both the length of the nanowire and the substrate are infinitely large. With this assumption, we can treat the nanowire as a waveguide. The two-dimensional simulation setup is presented in Figure 5.10. This configuration is obtained by taking a transverse cross-section from the middle of the nanowire laser lying on the substrate when the quantum wells are excluded. We choose the refractive index of the GaAs nanowire, $SiO_2$(285nm)/Si substrate, and air to be equal to 3.6, 1.45, and unity, respectively.

Perfectly Matched Layers (PML) are placed at the boundaries of our simulation setup to simulate the air surrounding the nanowire as a domain with an infinite cross-section. Their function is to absorb any outgoing electromagnetic waves efficiently, preventing field reflections.

#### 5.4.1.1 Convergence Tests for 2D Simulations

By performing the convergence test following the procedures outlined in Chapter 4, we can use the results depicted in Figure 5.11 to choose an appropriate PML thickness in our simulations. This figure represents the convergence test on how the thickness of the PML affects $n_{eff}$. Our

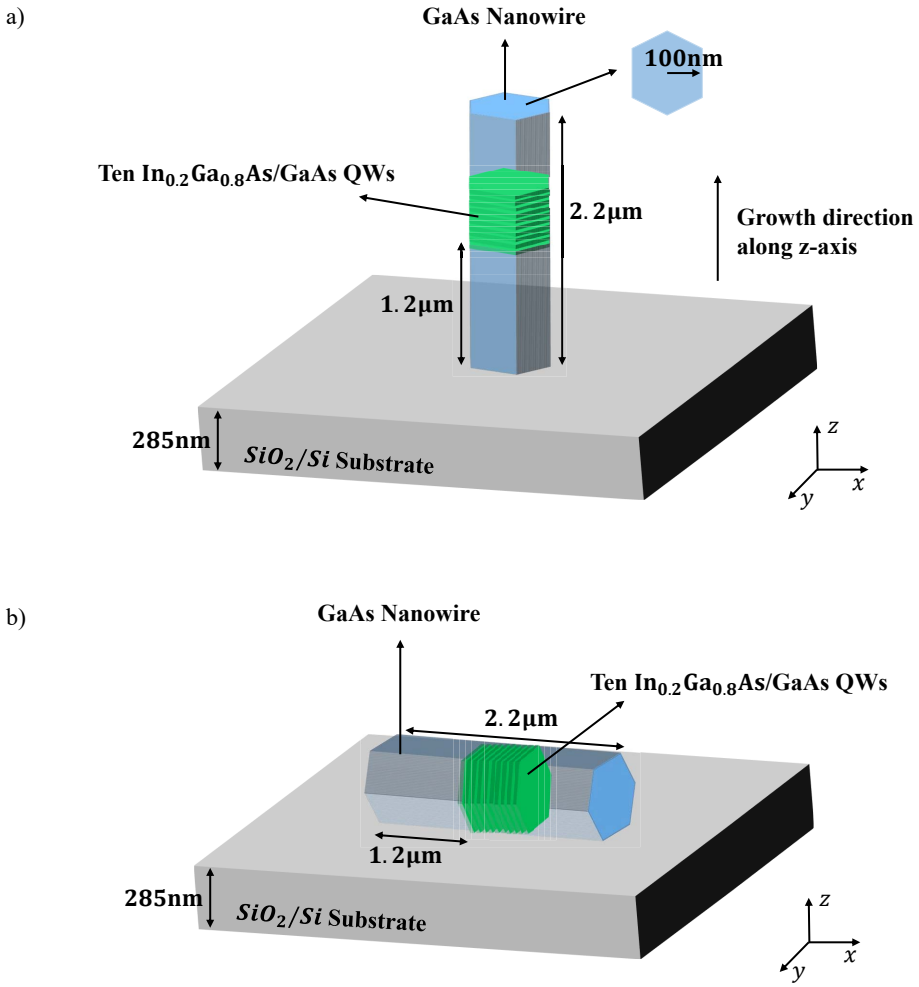


Figure 5.9: Schematic image of a hexagonal GaAs nanowire studied in [7], with the height of 2.2 and 200 $nm$ diameter a) grown vertically on a $SiO_2$(285 nm)/Si substrate, b) laid horizontally for lasing measurements. Ten $In_{0.2}Ga_{0.8}As$/GaAs quantum wells are embedded inside the nanowire as presented with a green color.

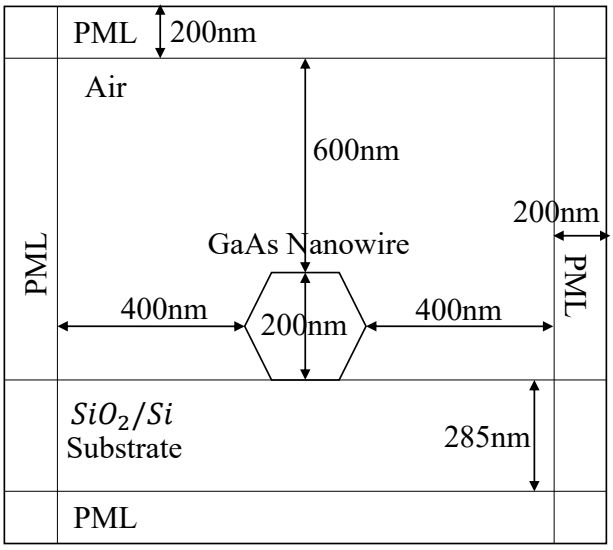


Figure 5.10: Schematic representation of the transverse cross-section of the 200nm hexagonal GaAs nanowire lying on the $SiO_2$(285nm)/Si substrate.

simulation results indicate that when the PML thickness exceeds 150nm, the changes in the $n_{eff}$ is less than 1%. We chose a PML thickness of 200nm in the two-dimensional simulations.

Similarly, the convergence test on the distance of the nanowire from PML in Figure 5.12 reveals that the value of the $n_{eff}$ will be converged when the distance of the nanowire from PML is larger than 300nm. We chose the distance of 400nm in the 2D simulations.

The last convergence test involves determining the optimal number of mesh elements. Figure 5.13 represents the change in the $n_{eff}$ with the number of elements within the mesh. As demonstrated in Figure 5.13, once the number of mesh elements surpasses 3000, the variation in $n_{eff}$ remains below the 1%. Consequently, we have selected the number 3274 as the suitable number of elements for our mesh.

#### 5.4.1.2 Guided Transverse Modes of the Nanowire

Once we ensured that our simulation results had converged, we plot $n_{eff}$ against the nanowire diameter to determine the number of guided transverse modes. We consider guided modes for the GaAs nanowire lying on the $SiO_2$(285nm)/Si substrate are the modes with $n_{eff}$ larger than the substrate (1.45).

In Figure 5.14, we increase the nanowire's diameter from 150nm to 400nm and plot the corresponding $n_{eff}$ values for each mode. When the GaAs nanowire has a diameter between 160nm and 240nm, only the $HE_{11a}$ and $HE_{11b}$ modes are guided within the nanowire. These modes are the fundamental modes of the hexagonal nanowire. However, as we increase the nanowire's diameter to 240nm, $TE_{01}$ mode also appears. When the nanowire's diameter increases even more, higher-order modes will be guided within the nanowire.

As illustrated in Figure 5.14, for diameters less than 240nm, the nanowire operates as a single-mode cavity. Lasers with single-mode cavities offer significant advantages as they efficiently

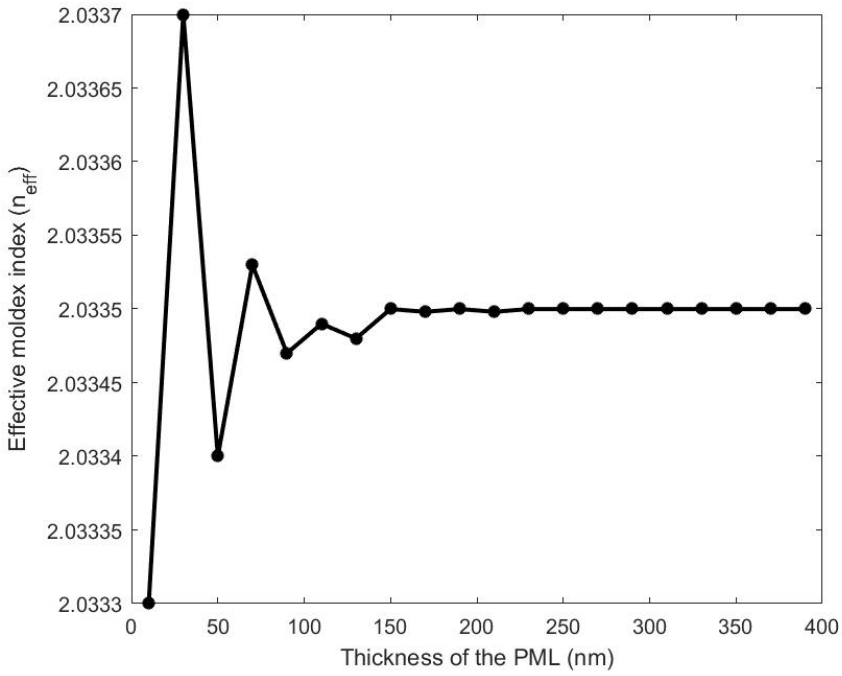


Figure 5.11: Evaluating $n_{eff}$ against the thickness of the PML to identify the appropriate PML thickness in the simulations.

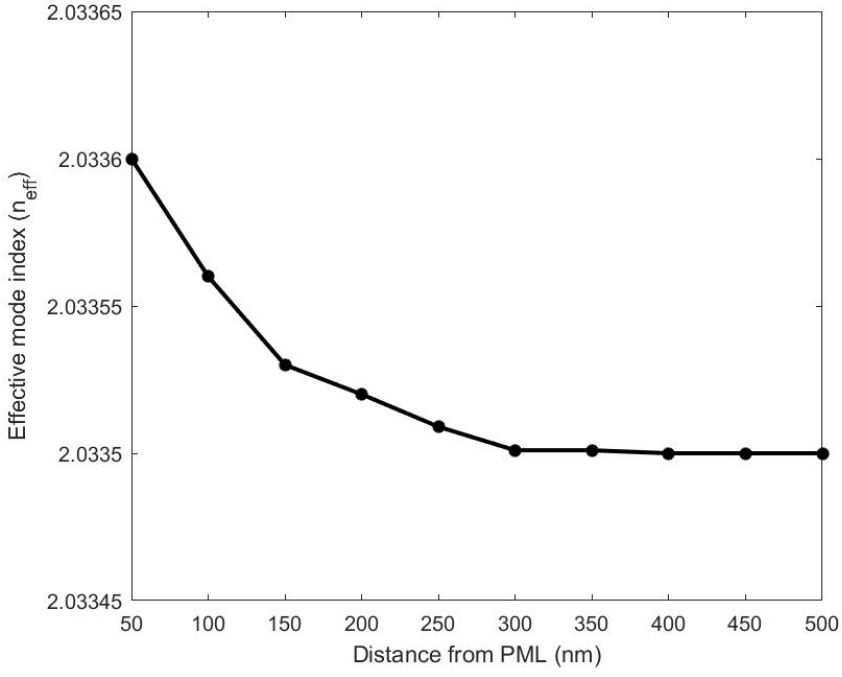


Figure 5.12: Evaluating $n_{eff}$ against the distance of the nanowire from PML to identify the appropriate distance of the nanowire from PML in the simulations.

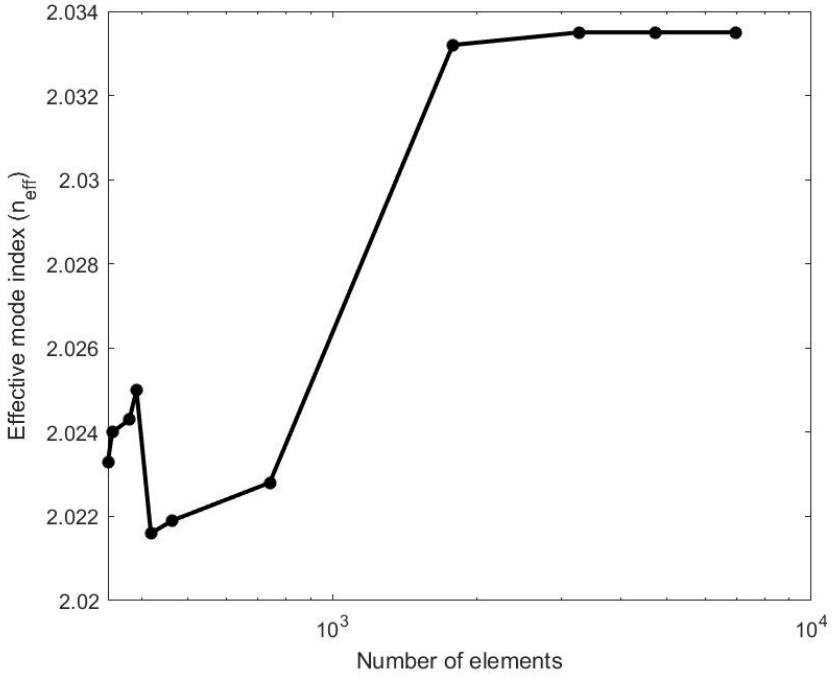


Figure 5.13: Evaluating $n_{eff}$ against the number of mesh elements to identify the appropriate number of mesh elements in the simulations.

channel all emitted photons into a single-lasing mode. Such lasers exhibit lower thresholds and higher spontaneous emission coupling efficiencies compared to multi-mode lasers. When multiple modes coexist within the laser, operational efficiency decreases as energy disperses among several resonant modes.

Since the GaAs nanowire that we investigate in this chapter has a diameter of 200nm, only the $HE_{11a}$ and $HE_{11b}$ modes with $n_{eff}$ equal to 2.0335 and 1.9546, respectively will be guided. It's worth mentioning that as the nanowire's diameter increases, although higher-order modes appear within the nanowire, their corresponding $n_{eff}$ values consistently remain lower than the fundamental modes ($HE_{11a}$ and $HE_{11b}$). The field intensity profile of the modes $HE_{11a}$ and $HE_{11b}$ is presented in Figure 5.15. We have shown the direction of the electric field field with the red arrows. When the electric field is polarised along the z-axis, we classify the modes as $HE_{11a}$, and when it is polarized along the y-axis, we have the mode $HE_{11b}$.

In the next subsection, we will perform three-dimensional nanowire simulations to identify the lasing mode of the nanowire, and field distribution along the length of the nanowire. We will also calculate the cavity-related parameters.

### 5.4.2 Three-dimensional Simulations

In the two-dimensional simulations, we neglected the length of the nanowire and the substrate in order to obtain the guided transverse modes of the nanowire. However, the length of the nanowire is one of the most important factors in laser operation which determines the emission frequency and nanowire's spectral characteristics. A longer nanowire supports a wider range of modes, each corresponding to a different wavelength, while a shorter cavity has fewer longitudinal modes. If the length of the nanowire is very small, it might not be able to support

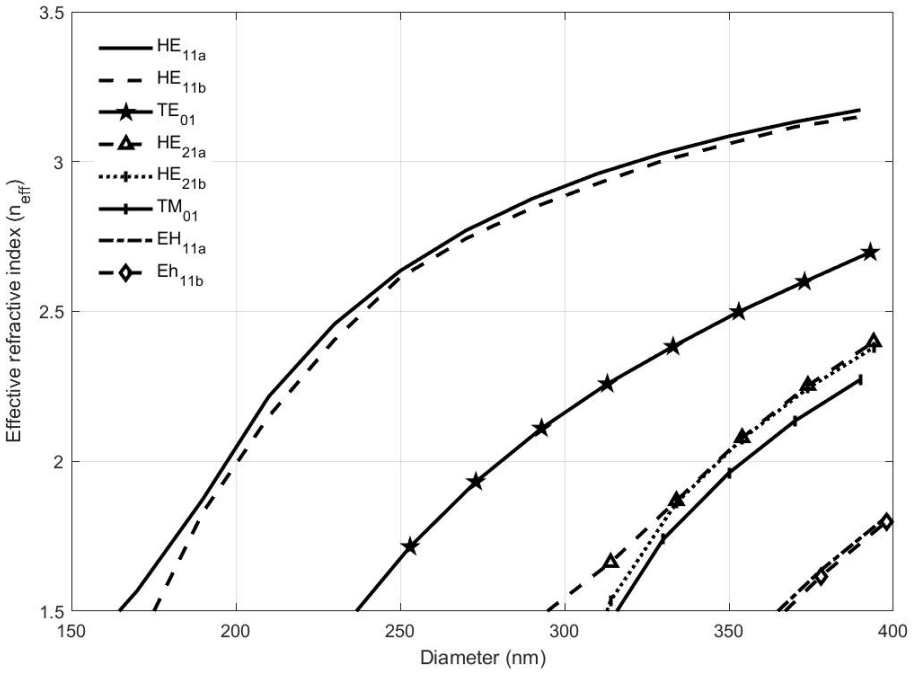


Figure 5.14: $n_{eff}$ versus the diameter of the nanowire to determine the number of guided transverse modes in the nanowire.

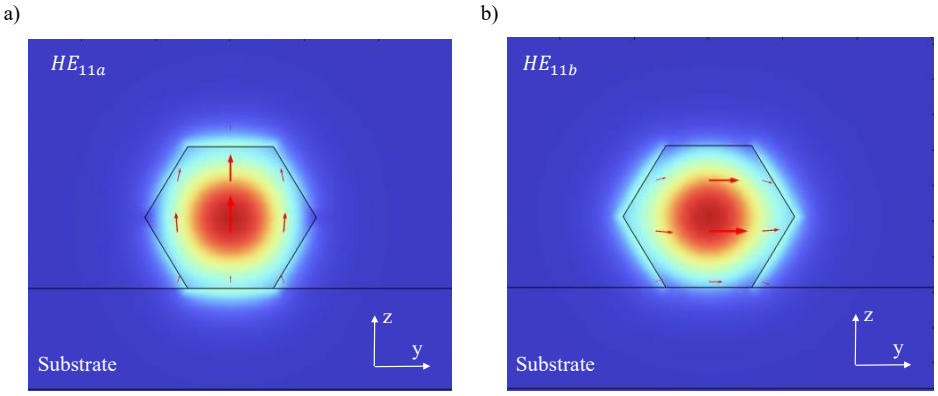


Figure 5.15: Electric field intensity distribution of the $HE_{11a}$ and $HE_{11b}$ modes. The polarization of the electric field is shown by red arrows. $HE_{11a}$ is polarised along the z-axis while $HE_{11b}$ is polarised along the y-axis.

any resonant mode. Therefore in this section, we will add another dimension to our previous simulations which represents the length of the nanowire.

Three-dimensional simulations give us the resonant frequencies of the nanowire. Using 3D simulations, we seek to determine which one of the transverse guided modes is the lasing mode. Also, 3D simulations enable us to accurately calculate the confinement factor and the quality factor for each resonant mode within the nanowire.

The 3D simulation environment is presented in Figure 5.16. A cross-section in the xz plane of Figure 5.16 is presented in Figure 5.17 to show a better view of the 3D simulation setups. We used to perform eigenfrequency analysis to obtain the resonant modes of the nanowire. We use Finite Element Method (FEM) to perform eigenfrequency analysis to obtain the resonant modes of the nanowire.

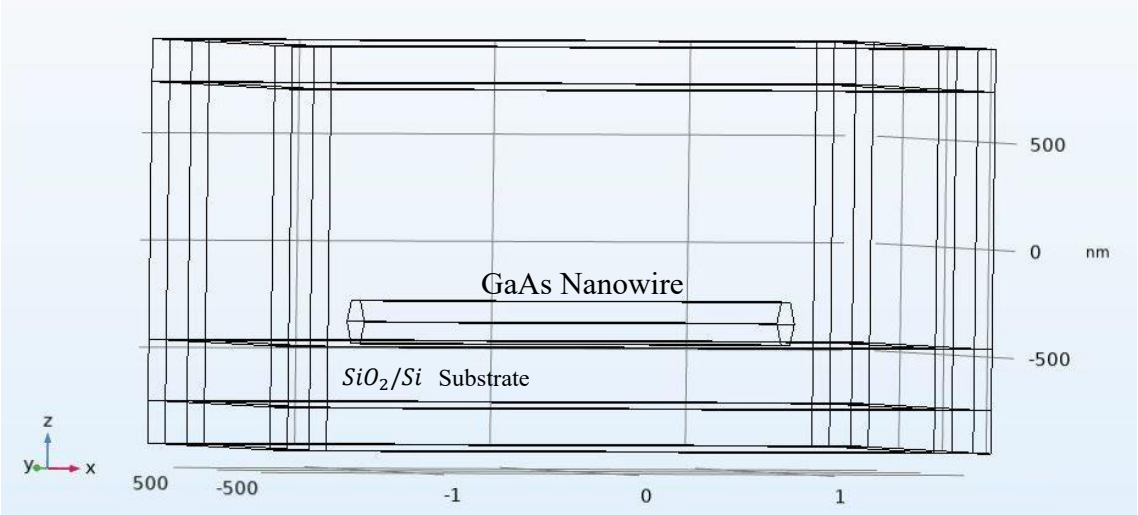


Figure 5.16: Three-dimensional simulation setup of the 200nm diameter hexagonal GaAs nanowire with the length of 2.2$\mu m$ lying down on a $SiO_2$(285nm)/Si substrate.

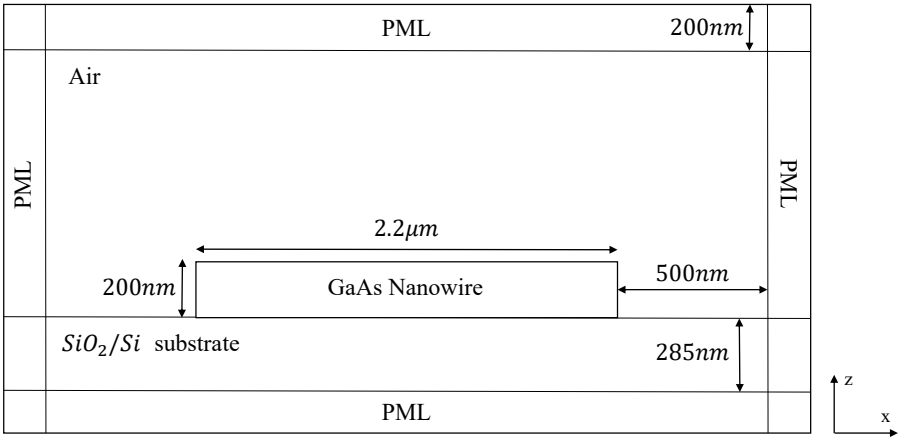


Figure 5.17: Schematic image of the 3D simulation setup for 2.2$\mu m$ GaAs nanowire with 200nm diameter lying on the $SiO_2$(285 $nm$)/Si substrate.

#### 5.4.2.1 Convergence Tests for 3D Simulations

Just as we performed convergence tests for the 2D simulations, we will apply similar tests to the three-dimensional simulations. This involves convergence tests on the thickness of the PML, the distance between the nanowire and the PML, and the number of mesh elements to ensure that our selection of simulation parameters is well-considered. When the variation in eigenfrequency is below 1%, we consider the simulation parameters as converged.

Figure 5.18 presents the convergence test on the thickness of the PML. From Figure 5.19, we choose the value of 200nm for the PML thickness in the 3D simulations. From the convergence test on the distance of the nanowire from the PML in Figure 5.20, we can see that to achieve the desired accuracy in the 3D simulations distances larger than 450nm are required. We chose 500nm for the distance of the nanowire from the PML in our 3D simulations.

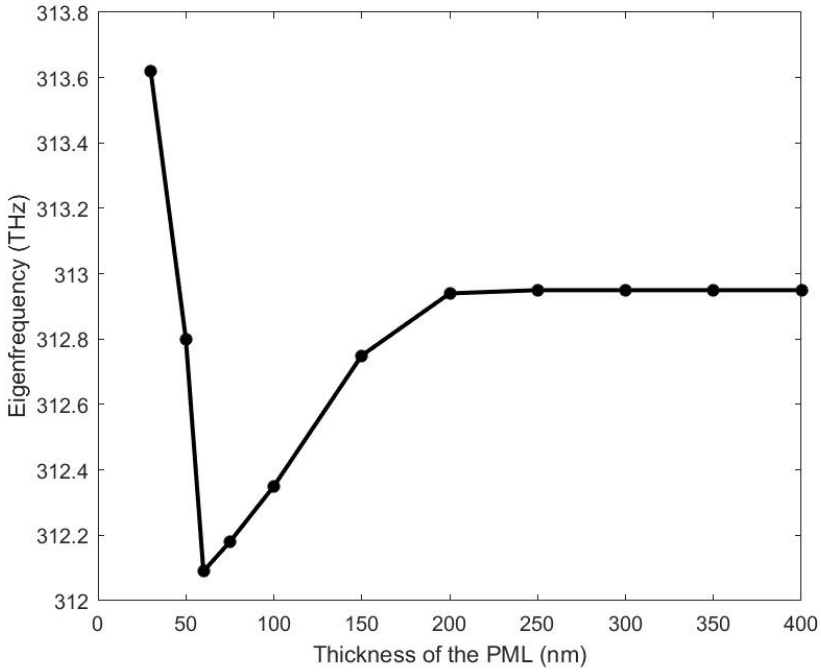


Figure 5.18: Thickness of the PML against eqigenfrequency of the $HE_{11b}$ mode to identify the suitable PML thickness in 3D simulations.

One of the significant differences between the 2D and 3D simulations is the number of mesh elements. In 3D simulations, due to the additional dimension, the number of mesh elements is substantially larger compared to their 2D environment. Therefore, potentially longer simulation times are needed when transitioning from 2D to 3D simulations. From Figure 5.20, we can see that any number of mesh elements larger than 31000 should be enough for accurate eigenfrequency results. We chose 35000 elements for the mesh in our 3D simulations.

#### 5.4.2.2 Resonant Modes of the Nanowire

Eigenfrequency analysis in the frequency domain results in a set of solutions representing the resonant modes that can exist within the nanowire laser. We present the list of eigenfrequencies obtained from our 3D simulations in Table 5.2. These modes are characterized by having an integer number of half wavelengths along the length of the nanowire. Figure 5.21 represents a

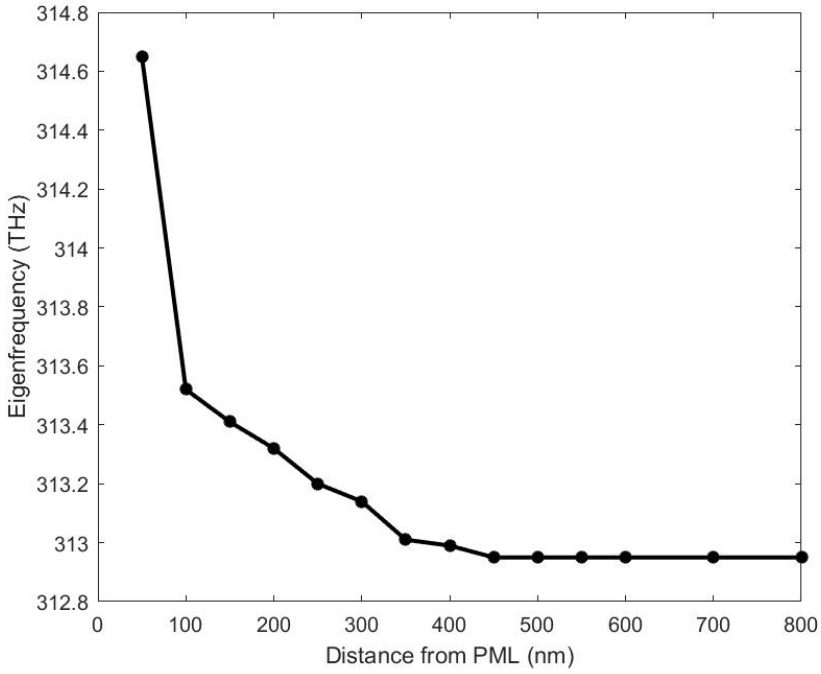


Figure 5.19: Distance of the nanowire from PML against eqigenfrequency of the $HE_{11b}$ mode to identify the suitable distance in 3D simulations.

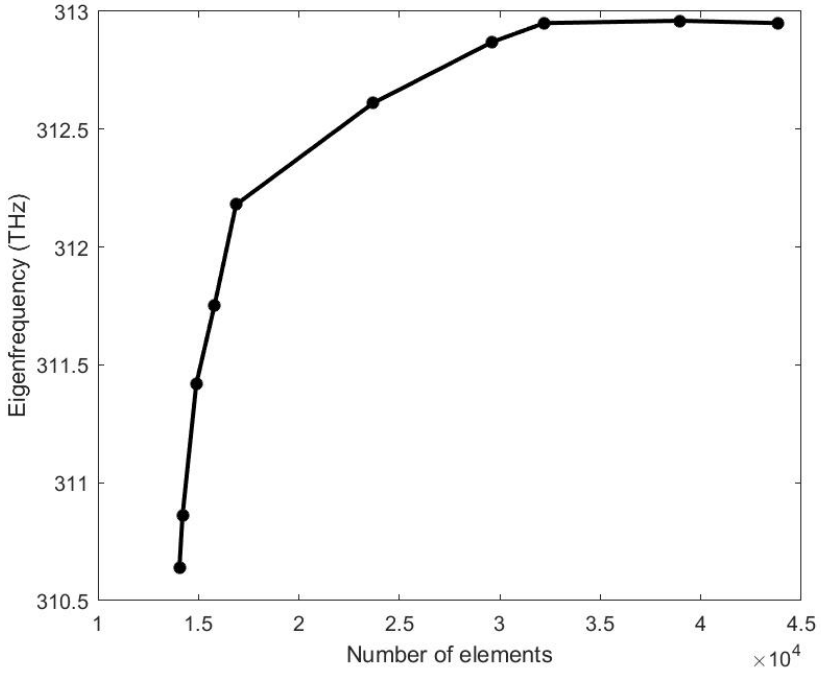


Figure 5.20: The number of mesh elements against eqigenfrequency of the $HE_{11b}$ mode to identify the suitable number of mesh elements in 3D simulations.

Table 5.2: Resonant modes of the nanowire obtained from 3D eigenfrequency simulations

| Modes | Frequency (THz) | Quality factor |
|---|---|---|
| $HE_{11a}$ | 267.73 THz | 13.556 |
| $HE_{11b}$ | 276.7 THz | 15.993 |
| $HE_{11a}$ | 282.09 THz | 26.122 |
| $TM_{01}$ | 288.32 THz | 5.49 |
| $HE_{11b}$ | 289.04 THz | 29.803 |
| $TE_{01}$ | 291.38 THz | 5.0267 |
| $HE_{11a}$ | 295.49 THz | 39.171 |
| $TE_{01}$ | 295.87 THz | 5.61 |
| $TE_{01}$ | 298.89 THz | 6.47 |
| $HE_{11b}$ | 301.10 THz | 45.221 |
| $TE_{01}$ | 306.11 THz | 9.34 |
| $HE_{11a}$ | 308.34 THz | 59.432 |
| $HE_{11b}$ | 312.94 THz | 99.559 |
| $TE_{01}$ | 316.69 THz | 14.61 |
| $HE_{11a}$ | 321.17 THz | 81.321 |
| $TM_{01}$ | 323.35 THz | 5.27 |
| $HE_{11b}$ | 325.06 THz | 73.459 |
| $TE_{01}$ | 329.48 THz | 24.20 |
| $HE_{11a}$ | 334.29 THz | 69.615 |
| $HE_{11b}$ | 337.59 THz | 83.122 |
| $TE_{01}$ | 342.77 THz | 38.23 |
| $HE_{11a}$ | 347.66 THz | 75.586 |
| $HE_{11b}$ | 350.49 THz | 89.856 |
| $HE_{11a}$ | 361.43 THz | 83.539 |
| $HE_{11b}$ | 363.83 THz | 95.485 |
| $HE_{11a}$ | 375.61 THz | 84.236 |
| $HE_{11b}$ | 377.61 THz | 98.014 |
| $HE_{11a}$ | 389.97 THz | 84.790 |
| $HE_{11b}$ | 391.78 THz | 98.980 |

cross-section in the xz-plane in the 3D simulations of the nanowire cavity at y=0, in which the x-axis aligns with the nanowire optical axis, for four distinct eigenfrequency solutions, around 312THz, derived from our 3D simulations. From Table 5.1 and Figure 5.21a-d, we can see that $TE_{01}$ mode is among the modes appearing in the 3D simulation results. The electric field intensity distributions of the $TE_{01}$ modes in Figure 5.21a and Figure 5.21d shows us that most of the field is leaking into the air and the substrate. This agrees with the two-dimensional simulations which we obtained $n_{eff}$ of around 1.32 for the $TE_{01}$ mode. As discussed before, since $n_{eff}$ is smaller than the refractive index of the substrate (1.45), this mode is not guided. The loss in the nanowire structure is directly related to the imaginary part of the eigenfrequency. A larger value of the imaginary part in the eigenfrequency means that the loss is high as well. This confirms the 2D results as well indicating that this nanowire is not able to support higher-order modes due to the large losses.

From the band diagram of the $In_{0.2}Ga_{0.8}As/GaAs$ quantum well in Figure 5.24 which we will

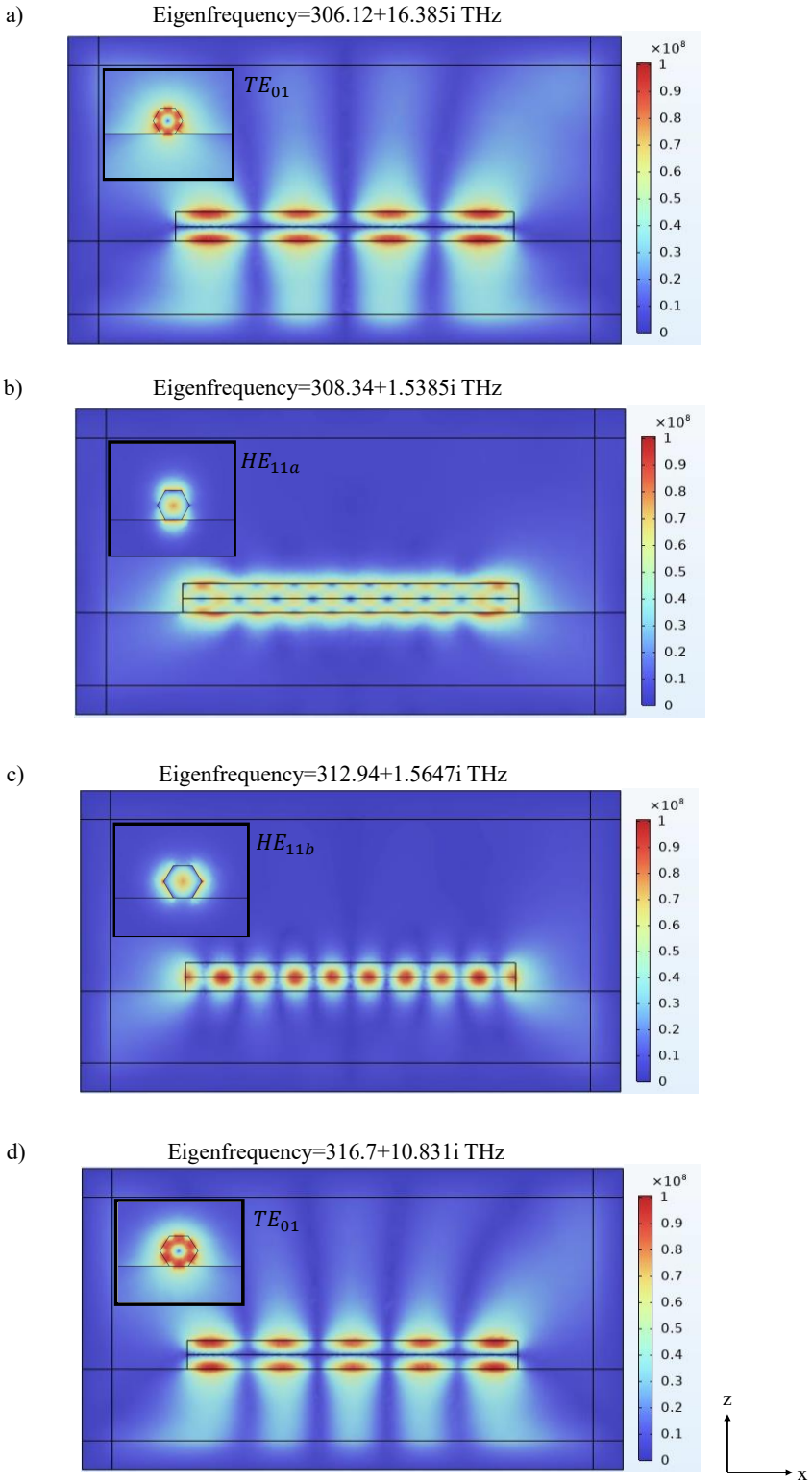


Figure 5.21: Four resonant mode as the solutions from our 3D Eiegenfrequency analysis for a) $TE_{01}$, $HE_{11b}$, $HE_{11a}$, and $TE_{01}$ modes. The inset figures represent the field in the transverse cross-section of the nanowire for each mode. Although $TE_{01}$ appears in the results, it is not considered a guided mode due to its large losses.

discuss in section 5.5, we can see that the photons emitted from the ground state transitions have a frequency between 304THz and 319THz. Using the list of all the eigenfrequency solutions in Table 5.2, we can see that these photons can couple to either the $HE_{11a}$ mode with resonant frequency of 308.34THz or the $HE_{11b}$ mode at 312.94THz. The quality factor for the $HE_{11a}$ mode is 59.432 while the quality factor of the $HE_{11b}$ is 99.559. The mode with the higher quality factor has a better chance to lase. Therefore, from the 3D eigenfrequency simulations, we predict the $HE_{11b}$ mode as the lasing mode of the $In_{0.2}Ga_{0.8}As/GaAs$ nanowire laser. The experimental data in [7] states that the lasing mode is the $HE_{11b}$ at the emission frequency of 312THz. This agrees with our 3D simulation results where we identified the $HE_{11b}$ resonant mode at 312.94THz as the lasing mode of the quantum wells nanowire. Therefore, in the following sections, we will consider the $HE_{11b}$ mode of Figure 5.21c as the lasing mode of the nanowire with its unique optical properties calculated in subsection 5.4.2.3.

#### 5.4.2.3 Quality factor ($Q$) and the Confinement factor ($\Gamma$)

The quality factor for each mode of the nanowire is calculated from

$$Q = \frac{real(Eigenfrequency)}{2Imaginary(Eigenfrequency)} \tag{5.5}$$

the Quality factor for the $HE_{11b}$ is obtained as 99.559 from the 3D simulations. The quality factor is used to calculate the photon lifetime $\tau_p$ in the laser rate equations.

The confinement factor determines how much of the field is concentrated within the gain medium. In order to calculate $\Gamma$, we integrate the field in all directions within the gain medium and divide it by the integration of the field in all domains as

$$\Gamma = \frac{\int_{Gain \quad medium} ||\vec{E}||^2 dV}{\int_{All \quad domains} ||\vec{E}||^2 dV} \tag{5.6}$$

We calculate the confinement factor of the $HE_{11b}$ mode is near 0.0341. Confinement factor will be used in the laser rate equations which we will discuss in section 5.6.

#### 5.4.2.4 Calculating the Photonic Density of States (PDOS) of the Nanowire

The PDOS given by $N_{ph}(E)$ in nanowires determines the number of photon states available at a particular energy, per unit volume. It characterizes the spectral distribution of photons within the nanowire. The PDOS depends on the nanowire geometry, composition, and spectral linewidth of the resonant modes. Considering the PDOS in the analysis of the absorption, gain, and spontaneous emission dynamics enables us to incorporate the effect of the nanowire cavity on the carrier-photon interaction within the quantum wells. The photonic density of states in a nanowire is different from free space PDOS and the PDOS for a semiconductor bulk material.

The free space photonic density of states describes the number of states that are available in the absence of any material medium (i.e., in vacuum or free space). The bulk PDOS refers to the distribution of the photonic states within a bulk semiconductor material. It accounts for the fact that in such semiconductors, the number of photonic states is different from that in free space due to the material's properties. The nanowire PDOS describes the number of available photonic density of states within the nanowire which is specific to the nanowire geometry and the dimensions.

The photonic density of states ($N_{ph}(E)$) consists of the sum of the free space photonic density of states ($N_{ph}^{fs}$), and the photonic density of states within the nanowire ($N_{ph}^{NW}$) as

$$N_{ph}(E) = N_{ph}^{fs} + N_{ph}^{NW}. \tag{5.7}$$

PDOS of the nanowire is obtained from the spectrum of each mode of the nanowire cavity. The spectrum for each mode is defined by a Lorentzian function which is related to the linewidth of the modes within the nanowire using Equation 5.1.

Using the 3D nanowire simulations, the spectra of the twenty modes of the nanowire cavity around the emission energy ($E = 2.0736 \times 10^{-19}$) are obtained from the values in Table 5.2. The spectra for the cavity modes are shown with the colored solid lines in Figure 5.22. The $N_{ph}^{NW}$ is obtained from the sum of the colored spectra, which is shown as the black spectra in Figure 5.23.

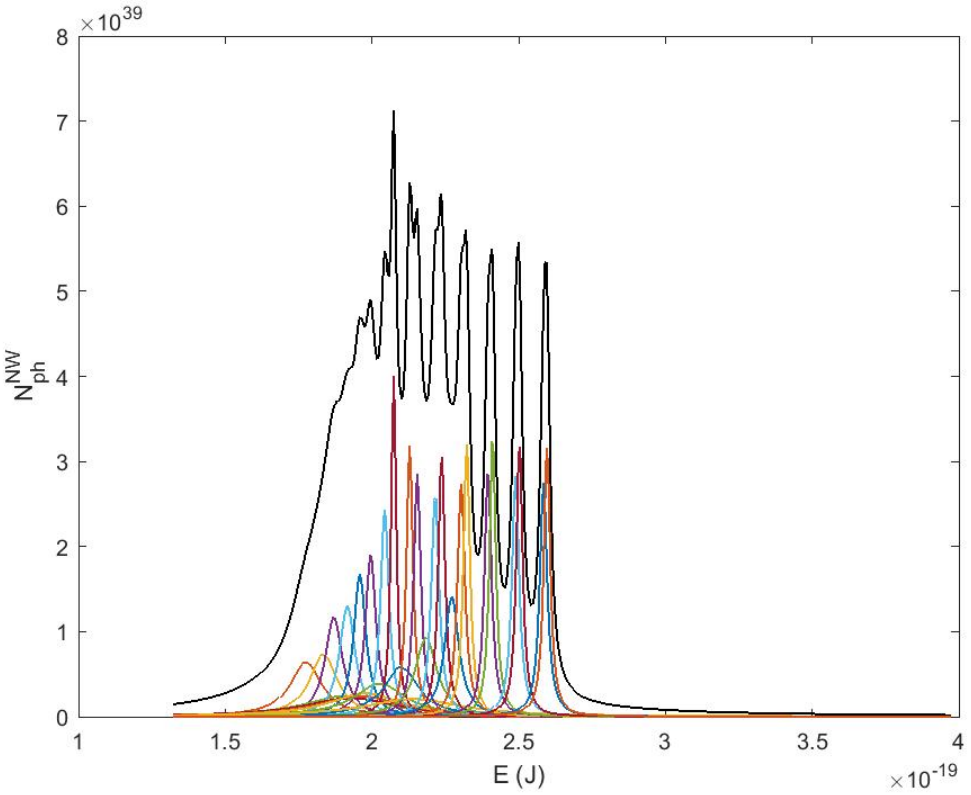


Figure 5.22: Spectra of the twenty-eight modes of the nanowire around emission energy (colored lines) and the nanowire photonic density of states represented with the black color.

However, as mentioned above, this total photonic density of states is the sum of the nanowire photonic density of states and the free space photonic density of states. The free space PDOS is shown with a solid green line, the nanowire PDOS is shown with a solid blue line, and the total PDOS for the nanowire is represented with a solid black line in Figure 5.23.

The $N_{ph}(E)$ captures the effect of the nanowire cavity on the carrier-photon interaction dynamics where a photon within a nanowire laser is capable of either being emitted to free space or coupling into one of the resonant modes of the nanowire cavity. Considering the total PDOS in analyzing the dynamics of the absorption, gain, and spontaneous emission results in a higher

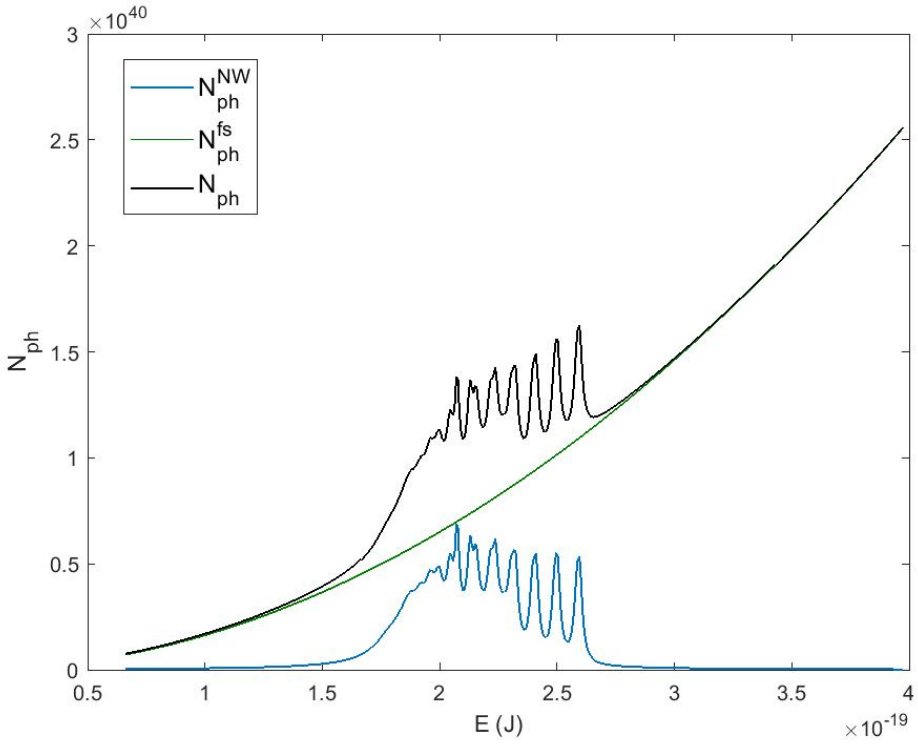


Figure 5.23: Photnic density of states of the modes of the GaAs nanowire (solid green line), free space (dashed blue line), and the total photonic density of states (solid back line)

rate of carrier-photon interactions compared to the scenario where only the free space PDOS is assumed. One of the most important advantages of our model is the full examination of the PDOS in comparison to the previous models where only the free space PDOS is considered [57], [89].

## 5.5 Analysis of Absorption, Gain, and Spontaneous Emission Dynamics

In this section, we will examine the dynamics associated with absorption, gain, and spontaneous emission processes within the 19nm $In_{0.2}Ga_{0.8}As/GaAs$ quantum wells acting as the gain medium. We will use the material parameters reported in [47], [57] and the photonic density of states obtained in the nanowire simulations section 5.4.2.4.

This analysis will provide insights into how these processes take place within the laser and enable us to estimate the spontaneous emission coupling efficiency and the Purcell factor. Furthermore, we develop a gain model of the $In_{0.2}Ga_{0.8}As/GaAs$ quantum wells, which will be used later in the laser rate equations analysis. The gain model describes how the active medium will act under the pump. The gain model will also help us to identify at which wavelength the gain is maximized. If the frequency in which the gain is at its maximum coincides with the lasing frequency, the maximum number of photon emissions can be achieved.

The first step in the analysis of the dynamics of absorption, gain, and spontaneous emissions, is to obtain the band diagram of the quantum wells. Using the material characteristics of $In_{0.2}Ga_{0.8}As$ tabulated in Table 5.3, the energy band diagram of the QW is plotted in Figure

5.24. The bandgap of the $In_{0.2}Ga_{0.8}As$ at 5K is equal to 1.2380ev [57]. We define all the energies with respect to the top of the valence band so that the top of the valence band lies at the energy level equal to zero and the bottom of the conduction band is located at the energy level equal to the bandgap ($E_g$). In this case, we calculated the first three energy levels of the conduction and valence bands as

$$E_{c1} = E_c + \frac{[\hbar(\frac{\pi}{L_z})]^2}{2m_e^*} = 1.2557ev, \tag{5.8}$$

$$E_{v1} = E_v - \frac{[\hbar(\frac{\pi}{L_z})]^2}{2m_h^*} = -0.0028ev. \tag{5.9}$$

$$E_{c2} = E_c + \frac{[\hbar(\frac{2\pi}{L_z})]^2}{2m_e^*} = 1.3086ev, \tag{5.10}$$

$$E_{v2} = E_v - \frac{[\hbar(\frac{2\pi}{L_z})]^2}{2m_h^*} = -0.0113ev. \tag{5.11}$$

$$E_{c3} = E_c + \frac{[\hbar(\frac{3\pi}{L_z})]^2}{2m_e^*} = 1.3969ev, \tag{5.12}$$

$$E_{v3} = E_v - \frac{[\hbar(\frac{3\pi}{L_z})]^2}{2m_h^*} = -0.0253ev. \tag{5.13}$$

where $L_z$ is the thickness of the quantum wells, $m_e^*$ is the effective mass of electrons in the conduction band, $m_h^*$ is the effective mass of the holes in the valence band, and $\hbar$ is the reduced Planck's constant. The material characteristics of the $In_{0.2}Ga_{0.8}As$ are given in Table 5.3. $E_c$ and $E_v$ are obtained by assuming that the top of the valence band ($E_v$) sits at the zero energy level and the bottom of the conduction band ($E_c$) sits at the energy level equal to the $E_g$ in the bulk form.

The fourth energy level of the conduction band is

$$E_{c4} = E_c + \frac{[\hbar(\frac{4\pi}{L_z})]^2}{2m_e^*} = 1.5205ev, \tag{5.14}$$

However, as shown in Figure 5.24, this energy level is larger than the bandgap of the GaAs barriers ($1.519ev$). Therefore only three energy levels can exist within the $In_{0.2}Ga_{0.8}As$/GaAs quantum well. In the next step, by using the band diagram of Figure 5.24, we will investigate the gain spectrum analysis of a single quantum well inside a nanowire cavity.

Table 5.3: Material characteristics of $In_{0.2}Ga_{0.8}As$ [47], [57]

| **Parameter** | **Value** |
|---|---|
| $m_e^*$ | $0.059m_0$ kg [57] |
| $m_h^*$ | $0.370m_0$ kg [57] |
| $E_p((\hat{e} \cdot p_{c,v})^2 = \frac{m_0 E_p}{3})$ | $25.18ev$ [47] |
| $E_g$ | $1.2380ev$ [57] |
| $\tau_{in}$ | $40fs$ [47] |
| $n$ | 3.6[57] |
| $T$ | $5K$ |

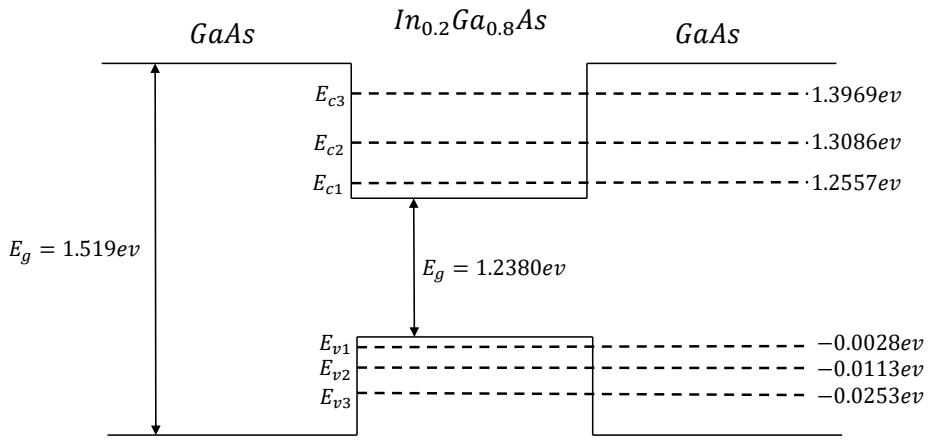


Figure 5.24: Energy band diagram of a single $In_{0.2}Ga_{0.8}As/GaAs$ quantum well with a thickness of 19nm with three energy levels in the conduction and the valence bands.

### 5.5.1 Dynamics of the Absorption, and Gain in a single $In_{0.2}Ga_{0.8}As/GaAs$ Quantum-well

The objective of this section is to calculate the gain spectrum, and the spontaneous emission rate using the outcomes of the nanowire simulations along with the material parameters in the literature. By solving the gain equation in 5.16, we will obtain the gain spectrum of a single 19nm $In_{0.2}Ga_{0.8}AS/GaAs$ quantum well. The joint density of states in Equation 5.16 will present the effect of the quantization in the quantum well. Moreover, by calculating the total spontaneous emission rates for a quantum well within a nanowire cavity, we will be able to perform a comprehensive analysis of the dynamics of the spontaneous emissions and calculate the spontaneous emission coupling efficiency in the nanowire laser.

A detailed discussion on the formulation of the absorption and gain processes within a quantum well is presented in Chapter 3. We obtain the absorption and the gain spectrum in Equations 3.105-3.106 as

$$\alpha(E) = \sum_{n,m} C_0(E)\rho_r^{2D} \int_{E_g}^{\infty} |\hat{e} \cdot \vec{p_{cv}}|^2 (f_v - f_c) L(E_{cv} - E) dE_{cv}, \tag{5.15}$$

and

$$g(E) = -\alpha(E) = \sum_{n,m} C_0(E)\rho_r^{2D} \int_{E_g}^{\infty} |\hat{e} \cdot \vec{p_{cv}}|^2 (f_c - f_v) L(E_{cv} - E) dE_{cv}, \tag{5.16}$$

where $|\hat{e} \cdot \vec{p_{cv}}|^2$ is the momentum matrix element, $E_{cv}$ is the energy difference of the conduction and the valence band, $\rho_r^{2D}$ is the joint electronic density of states in the quantum well, $f_c$, and $f_v$ are the Fermi functions. The parameter $C_0$ is a constant coefficient which is given as

$$C_0 = \frac{\pi e^2}{nc\epsilon_0 m_0^2 (E/\hbar)}. \tag{5.17}$$

The joint electronic density of states in a quantum well with the thickness of $L_z$ is

$$\rho_r^{2D} = \frac{m_r^*}{\pi L_z \hbar^2}. \tag{5.18}$$

Finally, the Fermi functions in a quantum well are

$$f_c(E_{cv}) = \frac{1}{1 + e^{(E_{cn} + \frac{m_r^*}{m_e^*}(E_{cv} - E_{cn} + E_{vn}) - F_c)/k_B T}}, \tag{5.19}$$

and

$$f_v(E_{cv}) = \frac{1}{1 + e^{(E_{vm} - \frac{m_r^*}{m_h^*}(E_{cv} - E_{cn} + E_{vm}) - F_v)/k_B T}}, \tag{5.20}$$

where $E_{cn}$ represents the minimum energy level of the $n^{th}$ band in the conduction band and $E_{vm}$ is the maximum of energy level of the $m^{th}$ band in the valence band. The quasi-Fermi levels of the conduction and valence bands are $F_c$ and $F_v$, respectively. When the laser is under the pump, the electrons within the valence band absorb the energy of the incident photons and are excited into the conduction band. As more and more carriers are excited into the conduction band, the quasi-Fermi levels $F_c$ and $F_v$ are pushed up in the conduction band and down in the valence band.

As shown in the band diagram of the $In_{0.2}Ga_{0.8}AS/GaAs$ quantum well in Figure 5.24, based on the number of carriers excited into the conduction band, $F_c$ can have any value between $1.2557ev$ and $1.480ev$. Similarly, $F_v$ can have any value between $-0.0028ev$ and $-0.0386ev$. The upper bound of the $F_c$ and the lower bound of $F_v$ are calculated when the transition energy is equal to the bandgap of the GaAs ($1.519ev$).

Figure 5.25 represents the electronic density of states and the energy levels in the conduction and valence bands in the quantum well. An example of the quasi-Fermi levels in the conduction and in the valence bands is presented with green dashed and dotted lines. If we assume that $F_c$ is somewhere between $E_{c1}$ and $E_{c2}$, carriers will fill all the electronic states in the first energy level of the conduction band. When all the electronic states within the first energy level are occupied, carriers will start to fill out the electronic states in the second energy level. A similar process is true for the holes in the valence band. In quantum well nanowire lasers, the emitted photons are from the transition between the first energy levels in the conduction and valence bands.

The carrier density in the first energy level of the conduction band in a quantum well is calculated as [57]

$$N = \int_{E_{c1}}^{Fc} \rho_{e1} f_c(E_{cv}) dE_{cv} \tag{5.21}$$

where $\rho_{e1}$ is the density of electrons in the first energy level of the conduction band which is given as

$$\rho_{e1} = \frac{m_e^*}{\pi \hbar^2 L_z} \tag{5.22}$$

By using Equation 5.21, we can solve the gain spectrum in Equation 5.16 for different carrier densities. In order to solve Equation 5.16, we should calculate the momentum matrix element $|\hat{e} \cdot \vec{p}_{cv}|$ of the transitions. The momentum matrix element in a bulk semiconductor doesn't depend on the polarization of the field ($\hat{e}$). The momentum matrix element for bulk semiconductors is given by Chuang in [57] as

$$|\hat{x} \cdot \vec{p}_{cv}| = |\hat{y} \cdot \vec{p}_{cv}| = |\hat{z} \cdot \vec{p}_{cv}| = M_b^2 = \frac{m_0 E_p}{6} \tag{5.23}$$

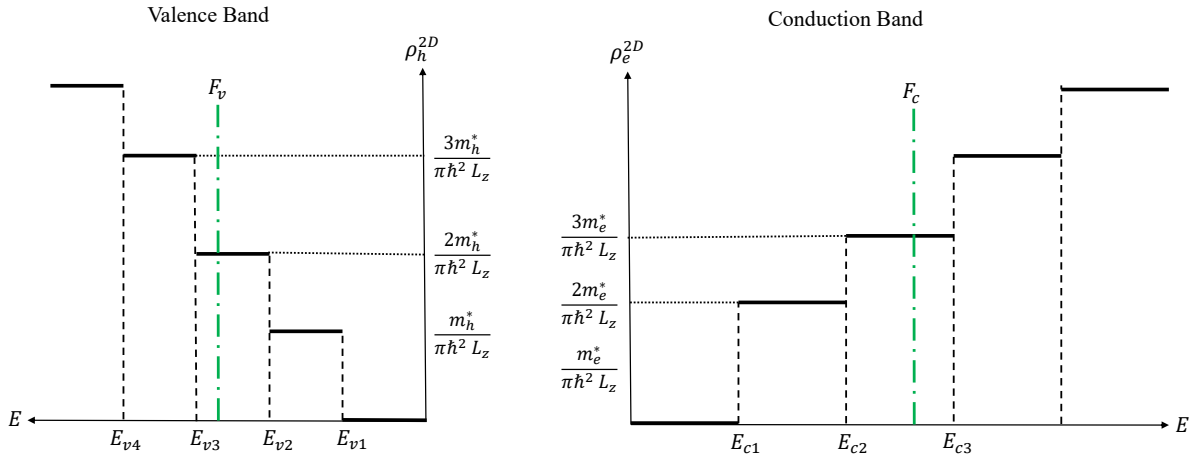


Figure 5.25: Electronic density of states for the electron in the conduction band ($\rho_e^{2D}$) and the holes in the valence band ($\rho_h^{2D}$) with three discrete energy levels in a quantum well.

However, in a quantum well, the momentum matrix element depends on the polarization of the field. In a general form, when the thickness of the quantum well is along the z-direction, a TE field is polarized along the x or y-directions. Momentum matrix element $|\hat{e} \cdot \vec{p}_{cv}|$ is given as [57]

$$\begin{aligned} < |\hat{e} \cdot M_{c-hh}| > &= \frac{3}{4}(1 + cos^2\theta)M_b^2 \\ < |\hat{e} \cdot M_{c-lh}| > &= (\frac{5}{4} - \frac{3}{4}cos^2\theta)M_b^2 \end{aligned} \tag{5.24}$$

where $M_{c-hh}$ and $M_{c-lh}$ represent the momentum matrix element for transitions from the conduction band into the heavy-holes and light-holes, respectively. A TM field is polarized along the z-direction and $|\hat{e} \cdot \vec{p}_{cv}|$ is obtained as [57]

$$\begin{aligned} < |\hat{e} \cdot M_{c-hh}| > &= \frac{3}{2}sin^2\theta M_b^2 \\ < |\hat{e} \cdot M_{c-lh}| > &= \frac{1}{2}(1 + cos^2\theta)M_b^2 \end{aligned} \tag{5.25}$$

The conservation rule dictates that for transitions from the conduction band into both heavy and light holes, we have

$$< |\hat{e} \cdot M_{c-hh}| > + < |\hat{e} \cdot M_{c-lh}| >= 2M_b^2 \tag{5.26}$$

In the electromagnetic field simulations presented in Figure 5.15, for our ten, $In_{0.2}Ga_{0.8}As/GaAs$ quantum well nanowire laser, the $HE_{11b}$ lasing mode is polarized along the y-direction perpendicular to the optical axis of the nanowire. Therefore, we are dealing with a situation similar to the TE polarized field in Equation 5.24. We calculate the momentum matrix element as

$$< |\hat{y} \cdot M_{c-hh}| > + < |\hat{y} \cdot M_{c-lh}| >= 2M_b^2 \tag{5.27}$$

Using the momentum matrix element in Equation 5.27, we solve Equation 5.16 to plot the gain spectrum. Figure 5.27 presents the gain spectra of the $In_{0.2}Ga_{0.8}AS/GaAs$ quantum well when the carrier density is between $N = 10^{19}m^{-3}$, and $N = 10 \times 10^{25}m^{-3}$. From Figure 5.27, we can see that when the carrier density is around the intrinsic carrier density $N = 10^{19}m^{-3}$, the gain spectrum has negative values. This means that in this case, the quantum well will absorb the incident light. Therefore, instead of gain, we will have absorption. As more carriers are excited into the conduction band, the gain spectrum will rise to the positive values.

In order to obtain the full gain term in the laser rate equations, we plot the maximum of each gain spectrum in Figure 5.26 versus their corresponding carrier density to obtain the gain model in Figure 5.27. The peak of the gain spectra in Figure 5.26 is very close to the energy of the emitted photons from the laser supporting our assumption that the photons emitted from the first energy levels are most likely to couple to the lasing mode while the photons emitted from the higher energy levels will either couple to the resonant modes of the nanowire with higher oscillation energy or they will be lost into the free space.

By comparing the gain spectrum of the bulk $In_{0.15}Ga_{0.85}As$ in Figure 3.14, with the gain spectrum of the $In_{0.2}Ga_{0.8}AS/GaAs$ quantum well in Figure 5.26, we can see that the bulk gain spectrum is broader. This means that the carriers and photons are able to interact in a broad range of frequencies. On the other hand, we have a narrower gain spectrum in the quantum wells, where only specific energy transitions are allowed.

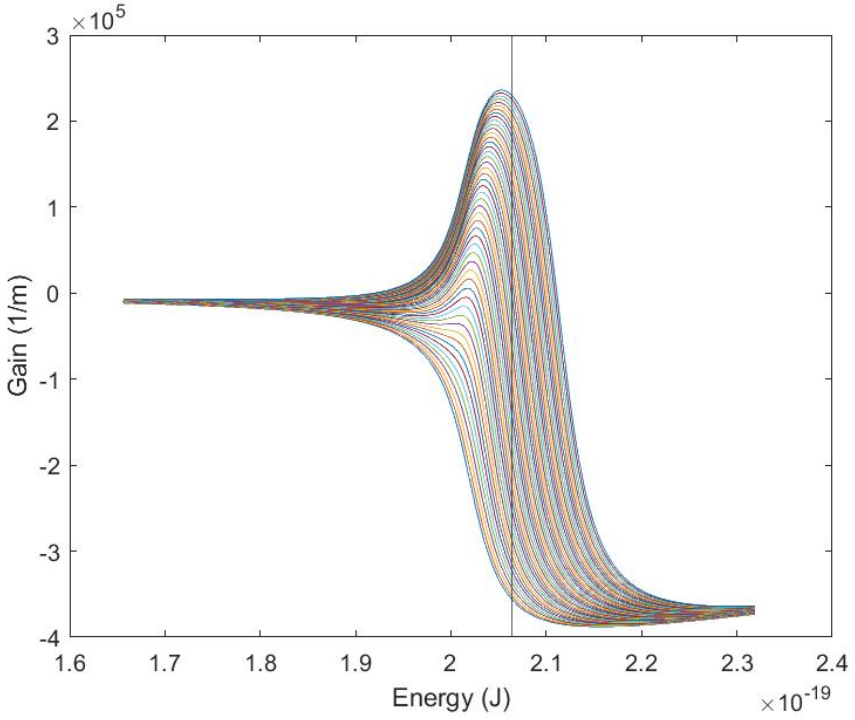


Figure 5.26: Gain spectrum of the 19nm $In_{0.2}Ga_{0.8}As/GaAs$ quantum well when only the transition between the first energy levels is considered.

Each line in the gain spectra plot in Figure 5.26, corresponds to a specific carrier density. If we plot the maximum of each gain spectrum versus the carrier density, we can develop the logarithmic gain model which creates the stimulated emission term in the laser rate equations. In the previous models [47], the logarithmic gain model of Figure 5.27 is fitted in Equation 5.28

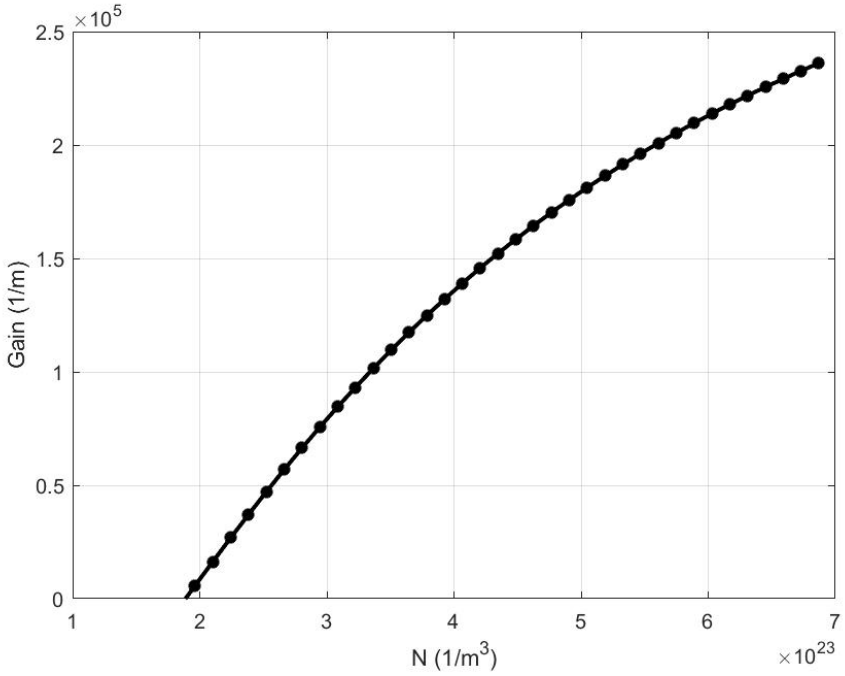


Figure 5.27: Gain model of the 19nm $In_{0.2}Ga_{0.8}As/GaAs$ quantum well when only the transition between the first energy levels is considered.

to build the logarithmic gain model.

$$g(N) = g_0 ln(\frac{N + N_s}{N_s + N_{tr}})F \tag{5.28}$$

Fitting equations, while a common practice in laser analysis and modeling, is not always the ideal approach. The logarithmic gain model in bulk semiconductors can be fitted to Equation 5.28 with good accuracy. However, as the thickness of the quantum wells decreases, the arc in the logarithmic gain model of Figure 5.27 tends to become less apparent and the gain changes almost linearly by increasing the carrier density. Therefore, Equation 5.28 will not serve as an ideal form to present the gain in ultra-thin quantum wells and this will decrease the accuracy of the results. However, since we will not use any fitting parameters in the gain model, our simulation results will not suffer from gain model fitting challenges. In section 5.6, we will use the gain model that we developed from our formulations to solve the laser rate equations and to obtain the L-L curves.

#### 5.5.1.1 Spontaneous Emission Rate, and the Spontaneous Emission Lifetime

In this section, our objective is to calculate the spontaneous emission spectrum of the 19nm $In_{0.2}Ga_{0.8}AS/GaAs$ nanowire when it is placed inside the nanowire. We will also calculate the spontaneous emission lifetime $\tau_{sp}$ which will be used in the laser rate equations. In the last step of this section, we obtain the total spontaneous emission rates. Obtaining the total spontaneous emission rates enables us to investigate $\beta$ and the Purcell factor in the ten-quantum well nanowire laser.

When the quantum wells are placed inside a nanowire, the total spontaneous emission rate is increased compared to the scenario in which quantum wells are investigated in free space. This is due to the Purcell factor. In section 3.2.3, we obtained the total spontaneous emission rate

of a quantum well within the nanowire in Equation 3.84 as

$$R_{spon} = \int_0^\infty dE \int_{E_g}^\infty N_{ph}(E) C_0(E) \frac{c}{n} \rho_r^{2D} |\hat{e} \cdot \vec{p_{cv}}|^2 f_c(1 - f_v) L(E_{cv} - E) dE_{cv} \tag{5.29}$$

The spontaneous emission spectrum of the quantum well is

$$r_{spon}(E) = N_{ph}(E) C_0(E) \frac{c}{n} \rho_r^{2D} \int_{E_g}^\infty |\hat{e} \cdot \vec{p_{cv}}|^2 f_c(1 - f_v) L(E_{cv} - E) dE_{cv} \tag{5.30}$$

Figure 5.28 shows the normalized spontaneous emission spectrum of the $In_{0.2}Ga_{0.8}AS/GaAs$ quantum well within the nanowire for the carrier density of $N = 3 \times 10^{24} m^{-3}$. To compare our proposed model with the previous ones which only consider $N_{ph}^{fs}$, we also present the normalized spontaneous emission spectrum with free space PDOS. By comparing the two spontaneous emission spectrums in Figure 5.28, we can see that the spontaneous emission rate is significantly higher for all transition energies.

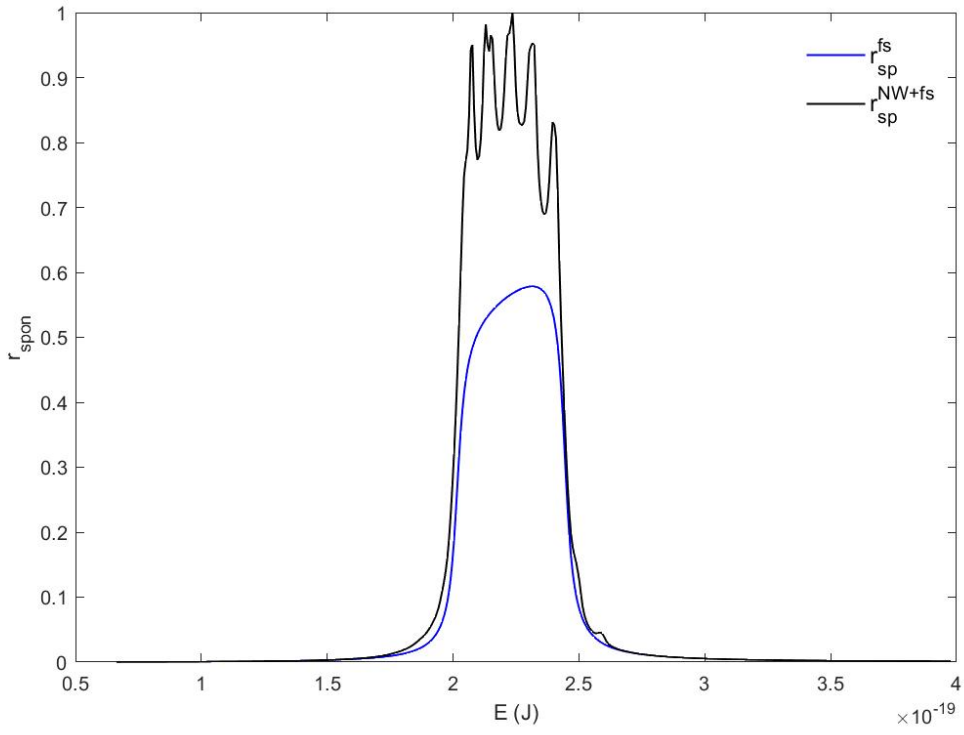


Figure 5.28: Spontaneous emission spectrum obtained from solving Equation 5.30 with the total PDOS (solid black line) and the free space PDOS (solid blue line) for the $In_{0.2}Ga_{0.8}As/GaAs$ quantum well inside the nanowire.

We calculate the spontaneous emission lifetime of around 0.2ns using

$$\frac{1}{\tau_{sp}} = \int_0^\infty N_{ph}(E) C_0(E) \frac{c}{n} |\hat{e} \cdot \vec{p_{cv}}|^2 \frac{\gamma/2}{(E_0 - E)^2 + (\gamma/2)^2} dE \approx 0.2ns, \tag{5.31}$$

where $N_{ph}$ is the photonic density of states, $E_0$ is the energy of the emitted photon, $|\hat{e} \cdot p_{cv}|^2$ is the momentum matrix element, and $n$ is the refractive index of the active medium. $\gamma$ is

the FWHM of the spontaneous emission spectra, and it is related to the intraband transition lifetime as discussed in Equations 3.59. $E_0$ is the emission energy and it is obtained as

$$E_0 = h = 2.0737 \times 10^{-19} J \tag{5.32}$$

where $h$ is Planck's constant and $f$ is the resonant frequency of the lasing mode.

#### 5.5.1.2 Spontaneous Emission Factor

The spontaneous emission factor is the ratio of the rate of spontaneous emissions into the lasing mode to the total spontaneous emission rates. In section 3.3.4, we derived the mathematical equation to calculate the spontaneous emission factor in a quantum well inside the nanowire as

$$\begin{aligned}\beta = \frac{R^j_{spon}}{R^{total}_{spon}} = \frac{\int_0^\infty dE \int_{E_g}^\infty N^j_{ph}(E) C_0(E) \frac{c}{n} |\hat{e} \cdot p_{cv}|^2 \rho_r(E_{cv}) f_c(1-f_v) \frac{\gamma/2}{(E_{cv}-E)^2+(\gamma/2)^2} dE_{cv}}{(\Sigma_i \int_0^\infty dE \int_{E_g}^\infty N^i_{ph}(E) C_0(E) \frac{c}{n} |\hat{e} \cdot p_{cv}|^2 \rho_r(E_{cv}) f_c)(1-f_v) \frac{\gamma/2}{(E_{cv}-E)^2+(\gamma/2)^2} dE_{cv}} \\ + \int_0^\infty dE \int_{E_g}^\infty N^{fs}_{ph}(E) C_0(E) \frac{c}{n} |\hat{e} \cdot p_{cv}|^2 \rho_r(E_{cv}) f_c(1-f_v) \frac{\gamma/2}{(E_{cv}-E)^2+(\gamma/2)^2} dE_{cv})\end{aligned} \tag{5.33}$$

If we take a close look at Equation 5.33, we can see that the denominators contain integrals over the free space spontaneous emission spectrum and the spontaneous emission spectrum obtained with the nanowire PDOS. The spontaneous emission spectrum of the free space is obtained by using free space PDOS in Equation 5.30, while the nanowire spontaneous emission spectrum is obtained when we use the nanowire PDOS in Equation 5.30. Therefore, $\beta$ can be calculated by taking the area under the curve for $r^{fs}_{spon}$, $r^{NW}_{spon}$, and $r^j_{spon}$ which represent the spontaneous emission rate into the free space, into all modes of the cavity, and then into the lasing mode.

Figure 5.29 represents the spontaneous emission spectrum of the free space, nanowire, and lasing mode, respectively for different carrier densities. The area under the red curve is divided by the sum of the areas under the black and the blue curves in Figure 5.29 gives us the spontaneous emission factor $\beta$. However, in our investigations, we noticed that $\beta$ changes by increasing the carrier density. This means that the rate of spontaneous emissions changes with the carrier density.

To investigate how the spontaneous emission factor depends on the carrier density we plot the $\beta$ against $N$ as shown in Figure 5.30. When the carrier density is close to the intrinsic carrier density, $\beta = 0.0379$. However, as the carrier density increases, the spontaneous emission increases until it reaches a maximum of 0.0746, and then $\beta$ starts to decrease for carrier densities larger than $6.13 \times 10^{23}(m^{-3})$.

The decrease in $\beta$ for high carrier densities can be traced back to the spontaneous emission spectra in Figure 5.29, where the spontaneous emission spectrum broadens with increasing carrier density. However, the change in the spontaneous emission spectrum of the lasing mode ($r^j_{spon}$) is very small compared to the change in the free space and nanowire spontaneous emission spectrums ($r^{fs}_{spon}$ and $r^{NW}_{spon}$). This signifies that above the threshold, most spontaneous emissions fade into the free space, and the majority of the remaining ones couple into the non-lasing optical modes of the nanowire. Consequently, the number of spontaneous emissions contributing to the lasing mode decreases compared to lower carrier densities, where fewer modes are involved. This indicates that for higher carrier densities, the spontaneous emissions are more likely to either couple to the other modes of the nanowire or be emitted into free space.

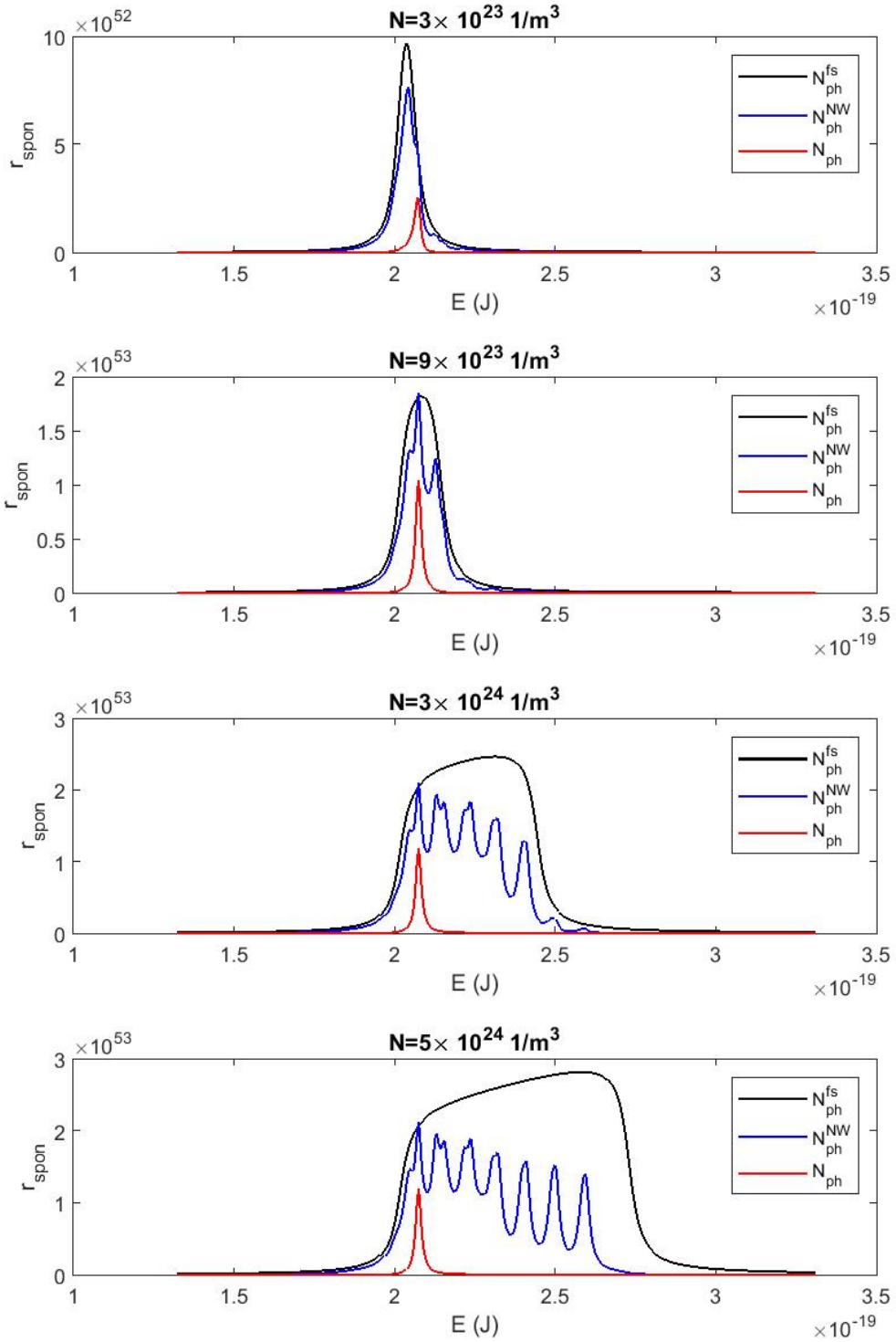


Figure 5.29: Spontaneous emission spectrum obtained from solving Equation 5.30 with the free space PDOS (solid black line), the nanowire PDOS (solid blue line), and the lasing mode PDOS (solid red line) for different carrier densities.

Given the definition of the spontaneous emission factor $\beta$, which is the ratio of the area under the spontaneous emission spectrum for the lasing mode to the sum of the areas under the spectra for the free space and nanowire modes, this spectral redistribution becomes critical. At higher carrier densities, the area under the spontaneous emission spectrum for the lasing mode does not increase as much as the total area under the spectra for the free space and nanowire modes. This disproportionate increase in the denominator of the $\beta$ equation leads to a sharp decrease in $\beta$ at $N > 10^{24}m^{-3}$.

From Figure 5.29 we saw that the spontaneous emission spectrum broadens as the carrier density increases. This results in the decrees in the $\beta$ in Figure 5.30 due to the fact that with increasing the number of carriers, the transitions occur with higher energy levels. The spontaneous emissions with higher energies shift the spontaneous emission spectrums to the right indicating the existence of the spontaneous emissions that are spread in a larger energy spectrum.

Additionally, once the threshold is crossed, stimulated emissions begin to dominate the lasing process. Stimulated emission depletes the carrier population more efficiently, reducing the availability of carriers for spontaneous emission into the lasing mode.

Thus, the sharp drop in $\beta$ for $N > 10^{24}m^{-3}$ is primarily due to the increased spectral broadening of the free space and nanowire modes, which diverts more spontaneous emissions away from the lasing mode. This effect, combined with the dominance of stimulated emissions at high carrier densities, results in a reduced fraction of spontaneous emissions contributing to the lasing mode, leading to the observed decrease in $\beta$.

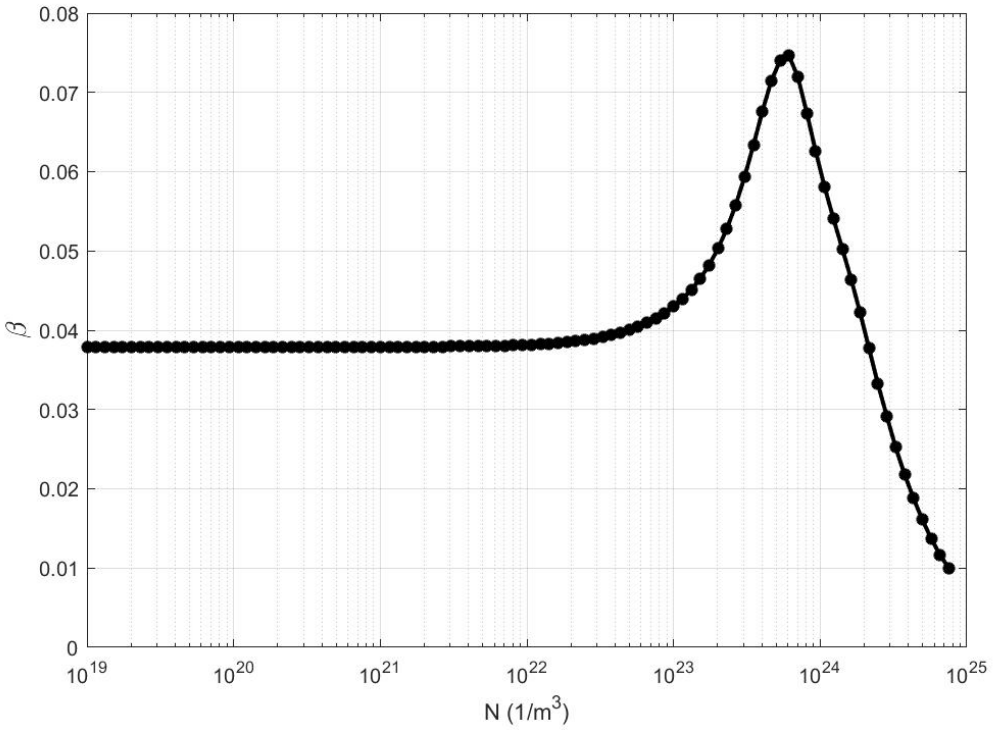


Figure 5.30: Spontaneous emission factor $\beta$ versus carrier density $N$ for three energy levels in $In_{0.2}Ga_{0.8}As/GaAs$ quantum well nanowire.

In the previous laser models, Yamamoto proposed a mathematical approach to estimate $\beta$ in

the bulk semiconductor lasers [89] in Equation 2.50 as

$$\beta = \frac{\lambda^4}{4\pi^2 V \Delta\lambda \epsilon^{3/2}} \tag{5.34}$$

Moreover, even for the bulk semiconductor lasers, he assumes the free space photonic density of states in the $\beta$ calculations. The outcome of the equation proposed by Yamamoto is only able to predict the value of the spontaneous emission at low carrier densities as a constant value. However, our proposed theoretical approach not only considers the quantum confinement effect in the quantum wells but also includes the effect of the nanowire cavity on the spontaneous emission rates. Moreover, our simulations reveal the pulsed shape of the spontaneous emission factor with respect to the carrier density which we report for the first time in the quantum well nanowire laser analysis.

Comparing the value of $\beta$, which is obtained from our calculations, with the value of $\beta$ which is obtained by fitting the experimental data, we notice that for the low carrier densities (below $10^{23}m^{-3}$) spontaneous emission factor in the quantum well nanowire laser is close to 0.04 which is larger than the typical spontaneous emission factor in the bulk microcavity semiconductor lasers in which $\beta$ is close to 0.01 [47].

Understanding the change in the spontaneous emission factor ($\beta$) with carrier density and time is helpful in developing high-performance quantum well nanowire lasers. Given that both transparency and threshold carrier density are determined by the quantum well thickness, understanding the dependency of $\beta$ on carrier density offers invaluable guidance in determining the optimum QW thickness. For example, from Figure 5.41, we can determine the optimum QW thickness of 11.8nm for the 200nm diameter nanowire with 2.2µm length. This insight enables researchers to strategically adjust the quantum well thickness to achieve maximum spontaneous emission coupling efficiency.

Also, the calculations in Section 5.5 offer insights into determining the discrete energy levels across various quantum well thicknesses, enabling the design of lasers with targeted wavelength outputs and high spontaneous emission coupling efficiency.

The investigations in Chapter 5 also provide insights into how $\beta$ changes with operating temperature, offering valuable data for predicting spontaneous emission coupling efficiency under different thermal conditions. For example, in Figure 5.50, we demonstrate that when the QW nanowire laser operates at a low temperature of 5K, the maximum spontaneous emission coupling efficiency is around 0.07. However, as the operating temperature increases to 300K, $\beta$ decreases to approximately 0.056. This decrease indicates that higher temperatures reduce the efficiency of spontaneous emission coupling, likely due to increased non-radiative recombination. By understanding this temperature dependence, laser designs can be optimized to minimize performance losses at higher operating temperatures.

Moreover, the choice of pump mechanism and pump power is also important in this context. By carefully selecting the pumping mechanism and adjusting the pump power, the laser can operate at an optimal carrier density where $\beta$ is at its peak. For example, by using Figure 5.40, we can see that the pump power should be able to excite $10^{23}$-$10^{24}$ $m^{-3}$ carrier densities to ensure that the maximum number of spontaneous emissions are directed into the lasing mode, which consequently leads to a lower threshold.

Furthermore, understanding the temporal dynamics of $\beta$, as shown in Figures 5.34 and 5.35, enables the design of lasers with faster modulation speeds under pulsed operation. By analyzing

the transient responses, designers can optimize the laser structure to achieve faster modulation speeds, which is essential for high-speed data transmission and communication applications.

#### 5.5.1.3 Purcell Factor

As discussed in section 3.3.2, the Purcell factor determines how much the spontaneous emission lifetime is decreased when the quantum well is placed within the nanowire, and it is crucial in laser design, particularly in lower-dimensional nanolasers, where optimizing light emission efficiency is of great importance. Adjusting and optimizing the Purcell factor enables us to control how the electromagnetic field within the laser cavity and the gain medium interact. Maximizing this factor in nanolasers leads to higher spontaneous emission rates and shorter spontaneous emission lifetimes, which is achieved by adjusting nanowire geometry and material composition [225].

Changing the nanowire's geometry, both in diameter and length, affects the photonic density of states and, consequently, the total spontaneous emission rates in Equation 5.35. Therefore. by optimizing the Purcell factor, we can maximize the number of spontaneous emissions coupling into the lasing mode. This yields lower threshold lasers with a larger spontaneous emission factor ($\beta$), which leads to the reduced height of the kink in the L-L curves plot. However, common nanowire lasers often overlook this optimization potential, treating the Purcell factor as a constant, usually set to unity, as observed by [6], [117].

Moreover, the Purcell factor also impacts the 3dB direct modulation bandwidth of the nanowire lasers, impacting the laser's overall efficiency [226] and optimization of this factor is essential for achieving peak modulation responses, which enhances the operational dynamics of nanowire lasers across various applications ranging from telecommunications to medical devices.

Understanding the dependency of the Purcell factor on carrier density helps to improve the design of more efficient quantum well nanowire lasers by adjusting both nanowire structure and carrier injection mechanisms to maximize spontaneous emission rates within the nanowire cavity. Manipulating the carrier density injection enables the nanowire laser to operate at carrier densities in the range where the Purcell factor is maximized. This control enhances laser efficiency and reduces threshold currents and higher spontaneous emission coupling efficiency, making quantum well nanowire lasers more suitable for integration into photonics and optical communication systems. Furthermore, leveraging the Purcell factor's dependency on carrier density improves the quantum efficiency of these lasers, resulting in increased output power and decreased energy consumption.

We calculate the Purcell factor ($F_p$) from the ratio of the total spontaneous emission rate within the nanowire to the total spontaneous emission rate into free space as

$$F_p = \frac{\int_0^\infty dE \int_{E_g}^\infty N_{ph}(E) C_0(E) \frac{c}{n} \rho_r^{2D} |\hat{e} \cdot \vec{p_{cv}}|^2 f_c(1-f_v) L(E_{cv}-E) dE_{cv}}{\int_0^\infty dE \int_{E_g}^\infty N_{ph}^{fs}(E) C_0(E) \frac{c}{n} \rho_r^{2D} |\hat{e} \cdot \vec{p_{cv}}|^2 f_c(1-f_v) L(E_{cv}-E) dE_{cv}}, \tag{5.35}$$

Similar to the $\beta$, the Purcell factor changes with carrier density. Figure 5.31 presents the change in the Purcell factor ($F_p$) with the increase in the carrier density.

To explain the behavior of the Purcell factor we again go back to Figure 5.29. The Purcell factor is the ratio of the area under the sum of the black and blue curves to the area under the black curve. For low carrier densities, $F_p$ is close to 1.4505. Except for the small peak of the Purcell factor at carrier density near $N = 6.13 \times 10^{23} m^{-3}$, the value of 1.4505 is among the highest

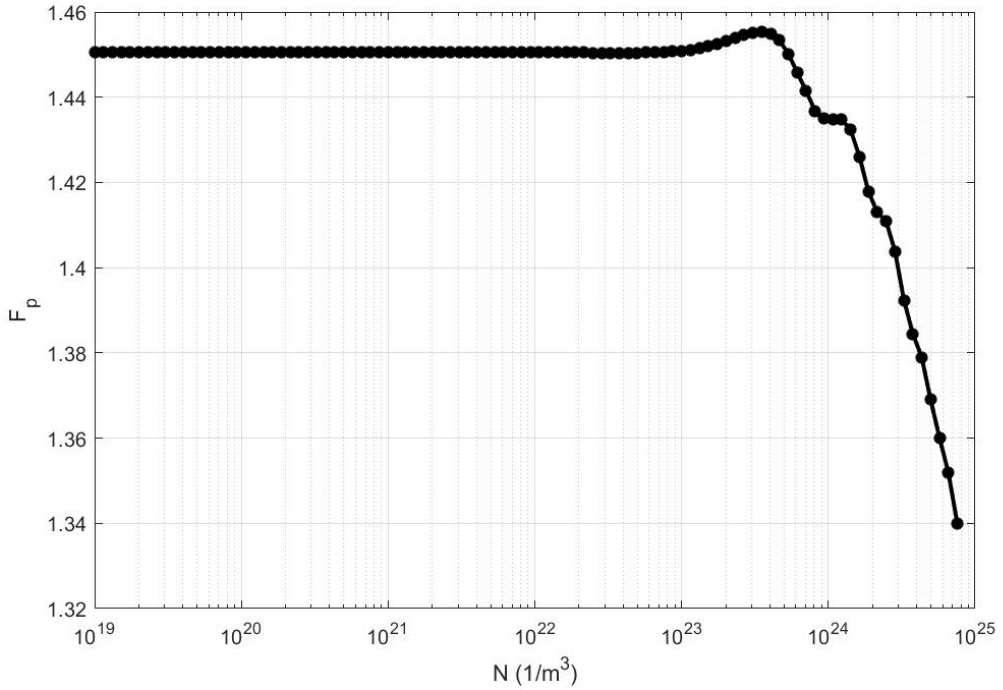


Figure 5.31: Purcell factor ($F$) versus carrier density $N$ for three energy levels in $In_{0.2}Ga_{0.8}As/GaAs$ quantum well nanowire.

values of $F_p$. This is due to the fact that when the carrier densities are low, the spontaneous emission spectrum is narrow. Therefore, the total spontaneous emission rate divided by the spontaneous emission rate in free space is large.

Although both the black and blue spectra change by increasing the carrier density, the change in the free space spontaneous emission spectrum $r_{spon}^{fs}$ is more than the amount of change in the nanowire spontaneous emission spectrum ($r_{spon}^{NW}$). As the number of carriers increases, the broadening of the free space spontaneous emission spectrum is quite large compared to the nanowire spontaneous emission spectrum. Therefore, the change in the numerator of Equation 5.35 gets smaller and smaller, and the Purcell factor decreases. From Figure 5.31, we can see that the decrease in the Purcell factor by increasing the carrier density is not linear. When the spontaneous emission is at its maximum, this means the laser is experiencing the shortest spontaneous emission lifetime achievable for the lasing mode. We should keep in mind that since ($N_{ph}(E)$) in the numerator of Equation 5.35 includes ($N_{ph}^{fs}$), the Purcell factor is always larger than the unity.

In the next step of our laser model, by using the results obtained from nanowire simulations and the examinations of the behaviors of gain and spontaneous emissions, we will solve the laser rate equations to obtain the nanowire laser characteristics such as the threshold and the coupling efficiency.

## 5.6 Laser Rate Equation Analysis

In the final step of our laser model, we will solve the laser rate equations to obtain the output number of photons per pulse versus the input pump fluence. Building upon the results acquired in the previous two steps, we will solve Equations 5.36-5.37 to predict the threshold and the

spontaneous emission coupling efficiency of the ten quantum wells nanowire laser. This analysis will yield crucial information about the laser's operation and performance.

The laser rate equations are

$$\frac{dN}{dt} = \frac{\eta P(t)}{hvV} - (\frac{1-\beta(N)}{\tau_{sp}} + \frac{\beta(N)}{\tau_{sp}})N - \frac{N}{\tau_{nr}} - \Gamma v_g m g(N)\frac{S}{V}, \tag{5.36}$$

$$\frac{dS}{dt} = \Gamma v_g m g(N)S + \frac{\beta(N)NV}{\tau_{sp}} - \frac{S}{\tau_p}, \tag{5.37}$$

where $N$ is the carrier density, and $S$ is the number of photons inside the cavity. The parameter $\eta$ is the fraction of pump power that is able to interact with the carriers, $hv$ is the energy of the pump photon, $V$ is the volume of the active region, $\tau_{sp}$ is the spontaneous emission lifetime, $\beta$ is the spontaneous emission factor, $\tau_{nr}$ is the non-radiative recombination lifetime, $g$ is the active medium's gain, $\tau_p$ is the photon lifetime, $m$ is the number of quantum wells, and $v_g$ is the group velocity. The laser is optically pumped with an 800nm pulsed laser with a pulse width of 35fs. We assume that the pump pulse has a Gaussian shape as

$$P(t) = P_0 e^{\frac{-t^2}{\Delta t^2}}, \tag{5.38}$$

where $P_0$ peak power of the pulse, and $\Delta t$ is the pulse width. The pump pulse is presented in Figure 5.32 when $P_0$=1Watt. By using the parameters Tabulated in Table 5.4, we solve

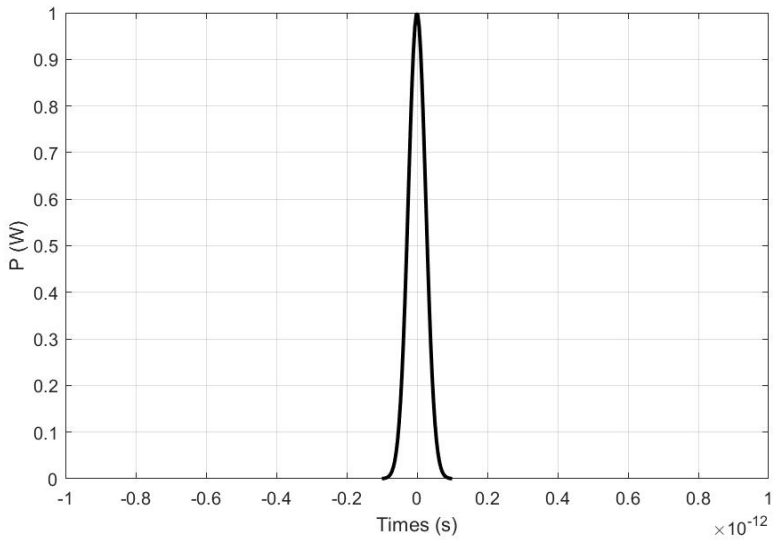


Figure 5.32: Pump pulse with the pulse width of 35fs.

the laser rate equations. First, we use the gain model that we developed in section 5.5.1 and presented in Figure 5.26 along with $\beta$ in Figure 5.30 to solve the laser rate equations using the fourth-order Runge-Kutta method.

By solving the laser rate equations with the parameters in Table 5.4 and the spontaneous emission factor which depends on the carrier density and is obtained from our theoretical calculations, we get the black plot in Figure 5.33.

In order to compare the L-L curves obtained from our formalism with the L-L curve when $\beta$ is treated as a constant value of 0.0397, we again solve the laser rate equations using $\beta = 0.0397$

Table 5.4: Laser Rate Equation Parameters

| **Parameter** | **Value** |
|---|---|
| $\eta$ | 0.0132 |
| $V$ | $6.5943 \times 10^{-21} \quad m^3$ |
| $\tau_{sp}$ | $0.2ns$ |
| $\tau_{nr}$ | $1 \times 10^{-5} \quad s$ |
| $\Gamma$ | 0.0341 |
| $\tau_p$ | $5.0877 \times 10^{-14} \quad s$ |
| $v_g$ | $8.1081 \quad m/s$ |
| $n$ | 3.7 |
| $m$ | 10 |

and plot the pump fluence versus the number of photons per pulse the blue plot in Figure 5.33. We chose the value of 0.0397 for $\beta$ to solve the laser rate equations with a constant value based on Figure 5.30 at low carrier densities near the intrinsic carrier density ($10^{193}m^{-3}$).

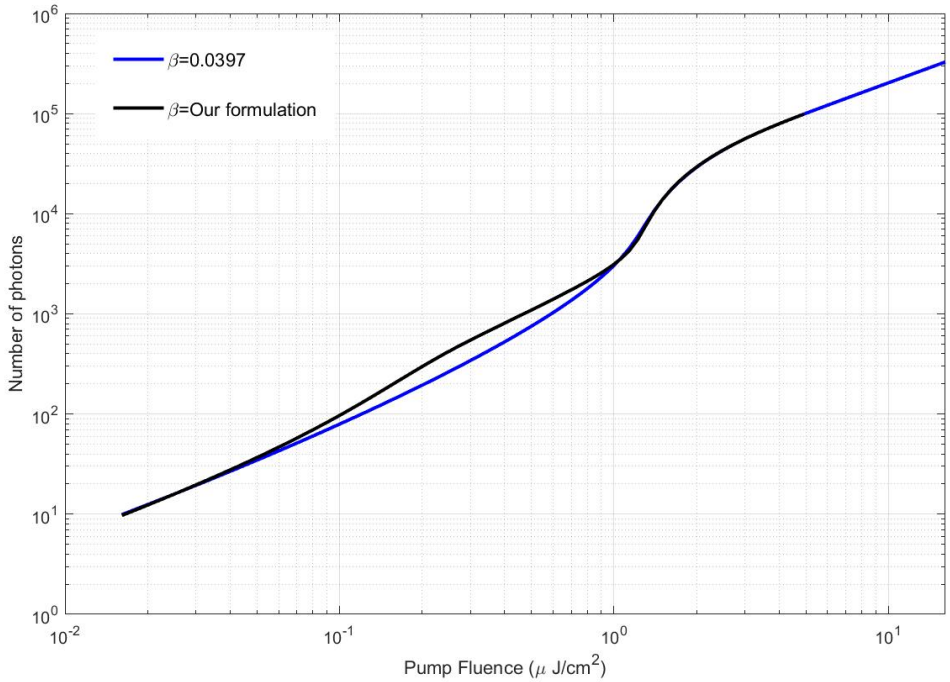


Figure 5.33: Pump Fluence versus the number of photons per pulse obtained by solving the laser rate equations.

From Figure 5.33, we can see that at low pump powers, when the pump is not strong enough to excite a large number of carriers into the conduction band, the two black and blue plots overlap. This indicates that at low carrier densities, the value of the spontaneous emission is very close to 0.0397. In order to better investigate why the L-L curve plot from our formalism has larger values compared to the scenario where $\beta$ is constant, we plot the carrier density versus time for two example points in the L-L curves. The first point is at a pump power of $0.0302\mu J/cm^2$ which is well below the threshold as presented in Figure 5.34. In the pump power as small as $0.0302\mu J/cm^2$, we can see that the peak of the carrier density in Figure 5.34, is around $9 \times 10^{22}m^{-3}$ and the number of photons per pulse is around 0.006. At the maximum

carrier density, we can see in Figure 5.22 that the value of $\beta$ is at the edge of the rising point. Figure 5.34c shows that $\beta$ starts to increase with the increase in the carrier density. Reaching the maximum of 0.0427 before dropping.

One of the most important factors that should be noticed is that due to the pulsed shape of the pump laser, the output of the nanowire laser is also in the pulsed shape. In each pulse, the carrier density rises from the intrinsic carrier density of $10^{19}1/m^3$ with time, reaches a maximum value, and then drops to the values close to the intrinsic carrier density again. Therefore, we also expect that $\beta$ also increases with the increase in the carrier density with time, reaches a maximum, and drops down to the values near 0.0397.

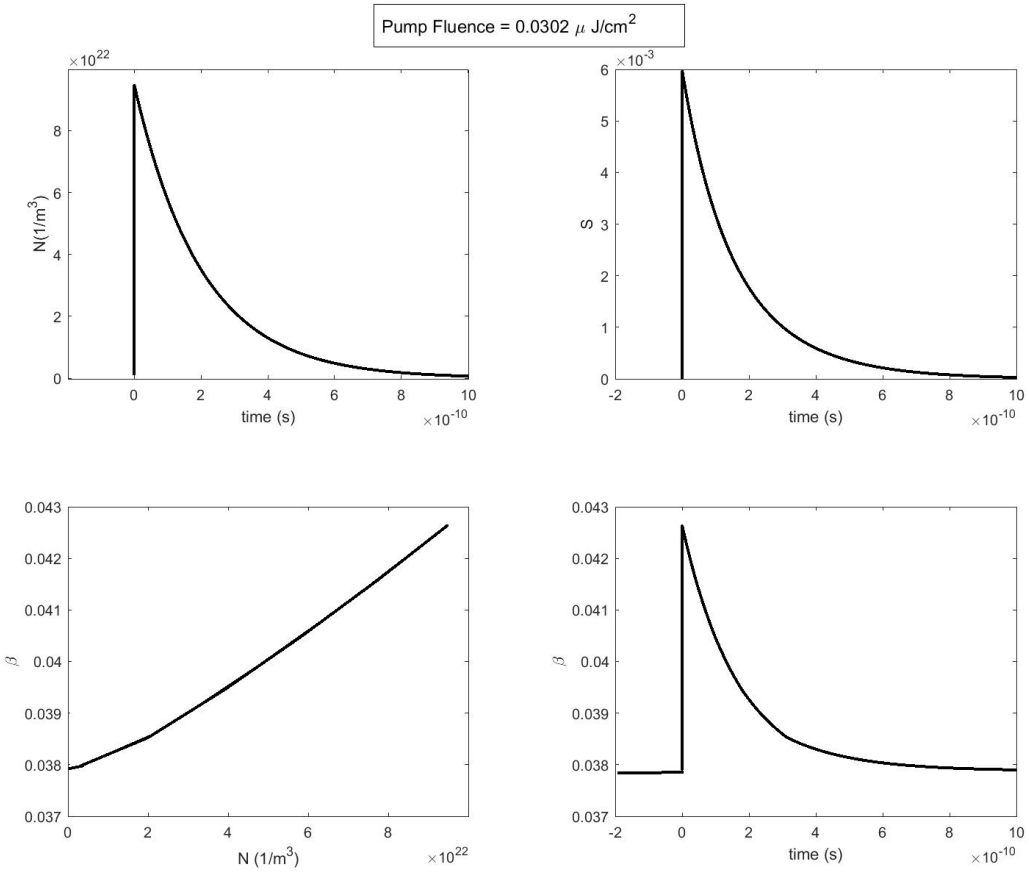


Figure 5.34: Outcomes of the laser rate equations for a) carrier density versus time, b) number of photons versus time, c) $\beta$ versus carrier density, and d) $\beta$ versus time at pump fluence=0.0302 $\mu J/cm^2$.

The second point is almost in the middle of the split between the black and the blue plots in Figure 5.33 with the pump power at $0.1219\mu J/cm^2$ as shown in Figure 5.35. We can see that the peak of the carrier density is higher at larger pump power compared to Figure 5.34. This is due to the fact that higher pump power is able to excite more carriers from the valence band into the conduction band. Higher peaks of the carrier densities will also result in an increase in the spontaneous emission coupling efficiency. When the maximum carrier density reaches around $3.8 \times 10^{23}m^{-3}$. At this carrier density, the spontaneous emission factor reaches 0.065 which is quite large compared to 0.0397, and then starts to decrease with the decrease in the carrier density.

Temporal responses of the carrier densities, number of photons per pulse, and $\beta$ in Figures 5.34 and 5.35 indicate that as the pump power increases, more spontaneous emissions couple to the lasing mode. This leads to a larger number of output photons per pulse in the black plot of the L-L curve in Figure 5.33 and results in the split between the plots for the $\beta$ as a function and $\beta$ as a constant. The split between the two lines reaches its maximum at the pump fluence of $0.15\mu J/cm^2$ which corresponds to the maximum value of $\beta$ at carrier densities around $6.13 \times 10^{23} m^{-3}$. In high pump powers, the carrier density is large, therefore from the spontaneous emission plot in Figure 5.30, we can see that the spontaneous emission coupling efficiency is at its minimum. Also, above the threshold, since the number of stimulated emissions is very large compared to the number of spontaneous emissions, the difference in the black and the blue plot in Figure 5.33 becomes negligible and the two plots once again overlap.

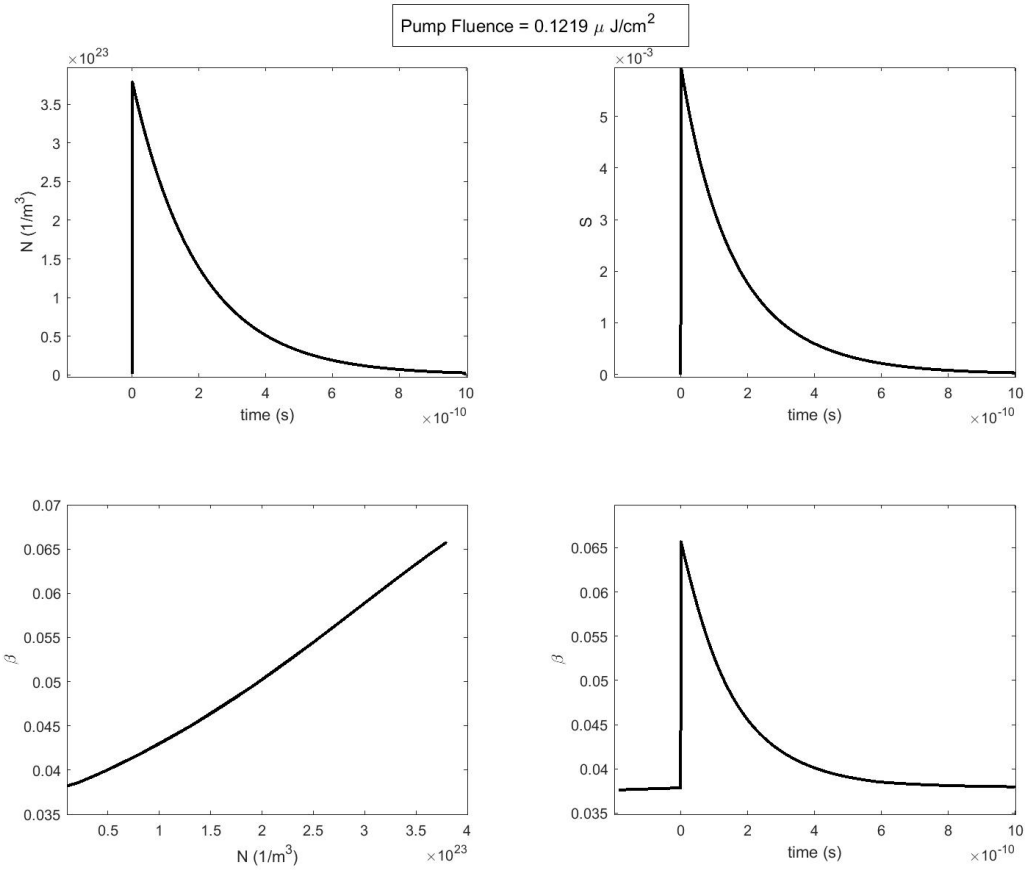


Figure 5.35: Outcomes of the laser rate equations for a) carrier density versus time, b) number of photons versus time, c) $\beta$ versus carrier density, and d) $\beta$ versus time at pump fluence=0.1219 $\mu J/cm^2$

### 5.6.1 Comparison between the Experimental Data and the Simulation Results

In this section, we compare the experimental data with our simulation results to validate our laser model. The inset of Figure 5.36 represents the experimental data reported in [7]. The experimental nanowire laser threshold is around $1.6\mu J/cm^2$. However, we obtain the threshold value of $1\mu J/cm^2$ for the nanowire laser. The gap between the simulated and experimental

threshold values for the nanowire laser can be caused by the idealized conditions assumed in the simulation.

In our simulations, we assumed that the non-radiative recombination lifetime ($\tau_{nr}$) is sufficiently long so as not to significantly impact the lasing behavior. Given that the laser was operating at a very low temperature of 5K, this assumption is quite reasonable. At such low temperatures, non-radiative processes are typically suppressed [224], and spontaneous emission dominates, making the influence of non-radiative recombination minimal.

However, although the impact of the non-radiative processes is small, incorporating it into the model leads to more realistic results. Especially when the operating temperature increases, the non-radiative recombination lifetime becomes a significant factor in lasing performance. For example, in the work by Bjork [46], it was demonstrated that when the non-radiative lifetime is approximately 100 times longer than the spontaneous emission lifetime ($\tau_{sp}$), such as $\tau_{nr}$=$10^{-9}$s and $\tau_{nr}$=$10^{-7}$s, the impact of non-radiative recombination on the laser's performance is negligible. When the non-radiative lifetime is shorter or comparable to the spontaneous emission lifetime, non-radiative recombination becomes a critical factor that must be considered.

Bjork's study further indicates that when non-radiative recombination dominates below the lasing threshold, it can significantly affect the laser's characteristics. Specifically, it can shift the threshold current from approximately it can shift the threshold current from approximately 0.001mA to 0.1mA, and the height of the kink in the L-L curve can increase to twice what it would be when non-radiative recombination is negligible.

We assumed a non-radiative lifetime of $\tau_{nr}$=$10^{-5}$ seconds, which is long enough to consider the non-radiative losses negligible compared to the $\tau_{sp}$=0.2ns in our model. However, if we were to measure the non-radiative lifetime experimentally at 5K and incorporate this experimentally determined value into our model, the simulation results would likely agree more closely with the experimental data.

Surface recombination occurs when charge carriers recombine non-radiatively at the surface of a semiconductor, often due to surface states—energy levels within the bandgap caused by disruptions like dangling bonds, defects, and impurities. This process is exacerbated by factors such as oxidation, surface roughness, and a high surface-to-volume ratio in nanostructures, which can be detrimental to the performance of optoelectronic devices like lasers [227]. For example, with a surface recombination velocity of 1000m/s, the threshold current for a quantum well laser diode in [227] was calculated to be around 1.1mA at a cavity length of 3µm. However, by reducing the surface recombination velocity to 100m/s, the threshold current significantly drops to 0.11mA under the same conditions.

The study also discusses how a lower surface recombination velocity leads to a higher spontaneous emission coupling efficiency. For instance, with a surface recombination velocity of 1000m/s, the quantum efficiency reaches about 50%. When the surface recombination velocity is reduced to 100m/s, the quantum efficiency improves significantly, reaching 74%. By performing additional experiments to accurately measure the surface recombination rate in our QW nanowire laser, we can incorporate this data into our laser rate equations to better reflect the impact of surface states on the threshold and spontaneous emission coupling efficiency.

Currently, the tolerance in our laser model is around 37%, indicating the degree of variation between the model's predictions and experimental data. To reconcile the difference between our simulation results, which calculate a laser threshold of around 1µJ/cm$^2$, and the experimental results showing a threshold of 1.6µJ/cm$^2$, considering factors like surface recombination,

non-radiative lifetimes, and defects can bring these results closer. By incorporating accurate measurements of these recombination rates and adjusting the model parameters accordingly, we can reduce this tolerance and improve the model's accuracy.

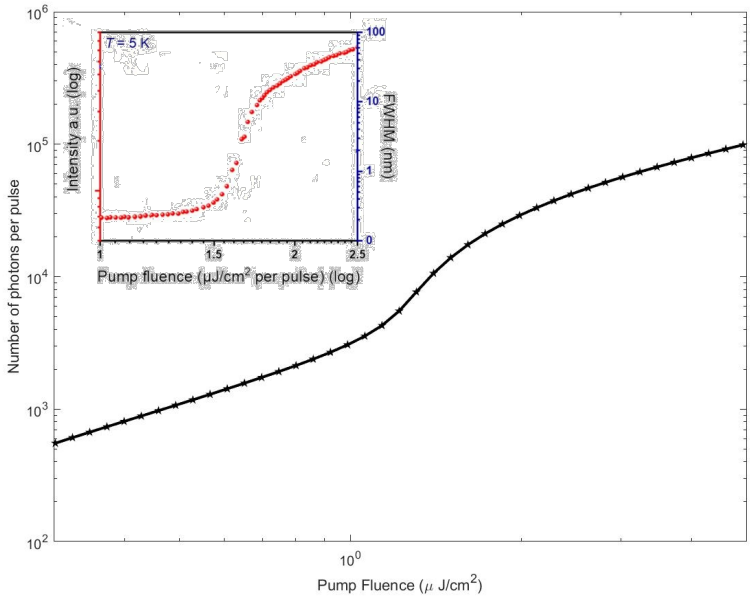


Figure 5.36: Comparing the experimental data [7] with our simulation results to validate our laser model.

In order to further investigate the behavior of the spontaneous emission factor, in the next step we will investigate the effect of the thickness of the quantum well and the temperature on the spontaneous emission coupling efficiency and the gain spectrum.

## 5.7 Spontaneous Emission Factor and Gain for Different Quantum-well Thicknesses and Temperatures

In Chapter 3, we derived the spontaneous emission rate for a quantum well nanowire laser from the first principles. Building upon the theoretical framework of Chapter 3, we implemented our theoretical approach to calculate the spontaneous emission factor for 19nm thick quantum well lasers. We also showed that $\beta$ is not a constant parameter as reported in the previous models [47], [89] and it depends on the carrier density. Now, in order to build a deeper understanding of the behavior of $\beta$ we will consider different thicknesses of the $In_{0.2}Ga_{0.8}As/GaAs$ quantum wells within the same 200nm hexagonal GaAs nanowire with the length $2.2\mu m$ which we simulated in section 5.3. It is worth mentioning that the optical properties of the nanowire cavity such as the guided modes, photonic density of states, and quality factors will remain the same as in section 5.3. The only parameter changing in the simulations is the thickness of the quantum wells.

By solving Equation 5.16 using material parameters in Table 5.3, we plot the gain spectrum for different quantum wells with thicknesses between 10nm to 30nm for a constant carrier density of $N = 1 \times 10^{24} m^{-3}$. From Figure 5.37 we can see that as the thickness of the quantum wells increases, the maximum of the gain spectra plots will decrease while the gain spectrum broadens

and shifts to the left as well. The 10nm quantum well has the sharpest and the highest peak. This is due to the discrete electronic density of states. By changing the thickness of the quantum wells the position of the first subbands will also change due to the quantum confinement effect. As you can see in Figure 5.38, for the quantum well thickness of 10nm the energy levels sit at higher energy values compared to the 15nm quantum well. Also, the photon emitted from the first energy levels in the 10nm quantum well (1.3119ev) has higher energy compared to the 15nm quantum well (1.2708ev). As the well becomes thinner, the energy difference between these subbands increases, leading to sharper transitions between energy states and emission peaks at larger energy. For example, from Figure 5.39, we can see that in thicker quantum wells, the energy levels are more closely spaced. This results in a broader range of energy levels where carriers can exist, making broader gain spectra. The shift in the transition energy is depicted by the term $f_c(E_{cv}) - f_v(E_{cv})$ in Equation 5.16. Figure 5.39 shows the shift of the transition energy to the smaller values (to the left) as the thickness of the quantum wells increases.

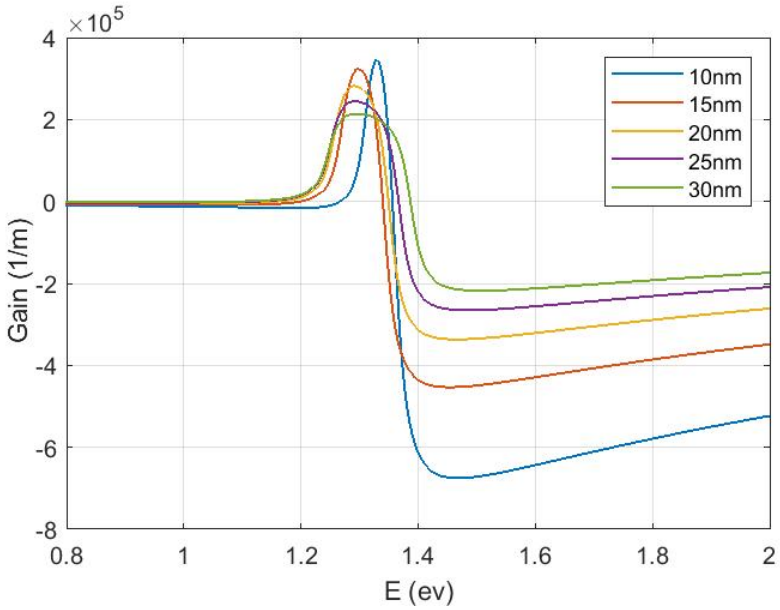


Figure 5.37: Gain spectrum for $In_{0.2}Ga_{0.8}As/GaAs$ quantum wells with thicknesses from 10nm to 30nm.

Now we will solve Equation 5.33 to obtain the spontaneous emission factor for different quantum well thicknesses. Figure 5.40 presents $\beta$ against carrier density for different quantum well thicknesses. We can see that as the thickness of the quantum well increases, $\beta$ will increase for quantum wells with a thickness between 10nm to 12nm. However, quantum wells larger than 12nm $\beta$ start to decrease, and a peak will appear. As the thickness of the quantum wells increases, we can see that we get closer to the shape of the $\beta$ in the bulk laser presented in 5.6. The interesting point out here worth mentioning is how the shape of the $\beta$ for thin quantum wells is different from the thick quantum wells and the bulk.

From Figure 5.40, we can see that there is a big jump in the plots for $\beta$ between 10nm to 12nm. In order to take a closer look at the $\beta$ for thicknesses between 10nm to 12nm, we will add more plots in that region. Figure 5.41 presents $\beta$ for quantum well thicknesses between 10-12nm. Here we can see that as the thickness of the quantum wells increases from 10nm to 12nm, the spontaneous emission factor increases until it reaches the maximum of around 0.097 when the

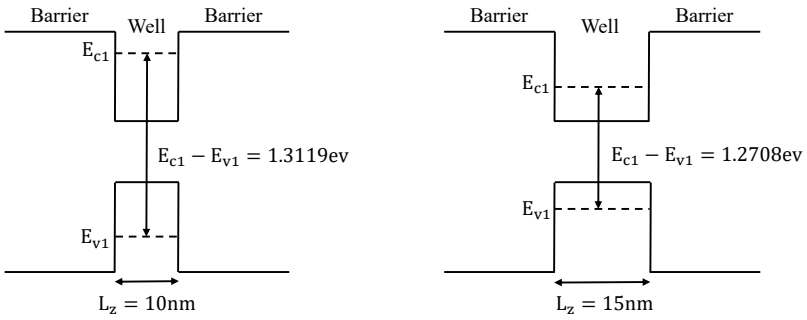


Figure 5.38: Energy band diagram in 10nm and 15nm $In_{0.2}Ga_{0.8}As/GaAs$ quantum wells.

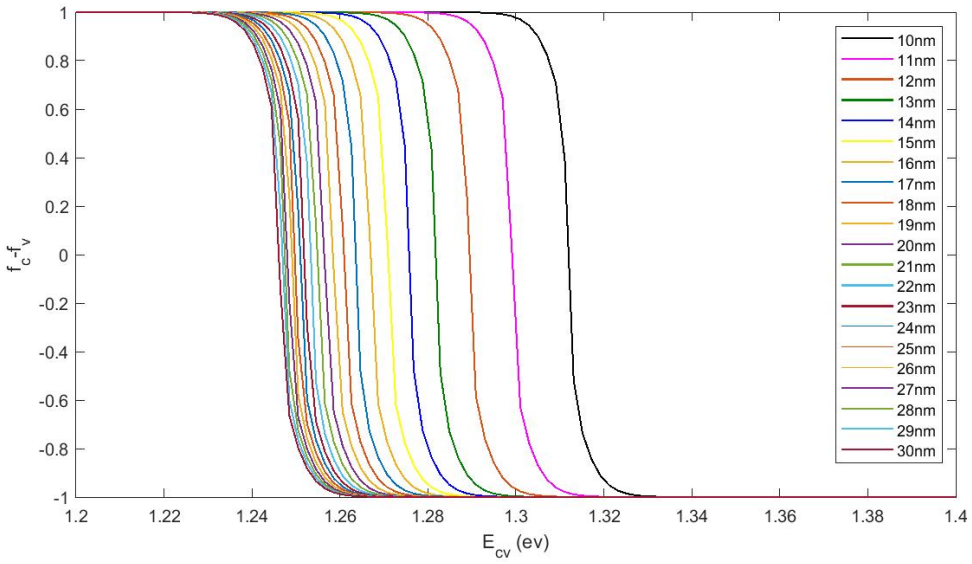


Figure 5.39: The term $(f_c - f_v)$ in Equation 5.16 for gain.

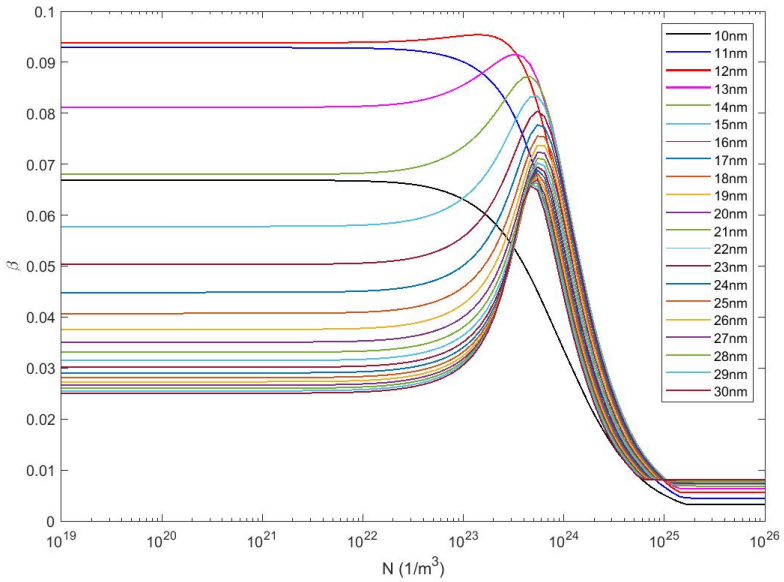


Figure 5.40: Spontaneous emission factor ($\beta$) versus carrier density for quantum well thicknesses between 10nm to 30nm.

quantum well thickness is 11.8nm. For quantum wells larger than 11.8nm, the spontaneous emission factor decreases, and with increasing the carrier density, a peak will appear. This is very useful because, from this figure, we can identify the optimum quantum well thickness of 11.8nm for this specific nanowire cavity.

To better visualize the change in $\beta$ with both carrier density and the quantum well thickness, we use a 3D plot with carrier density along the x-axis, quantum well thickness along the y-axis, and $\beta$ along the z-axis. Figures 5.42-5.43 both present the 3D representations of the spontaneous emission factor. The only difference in the plots is the linear and logarithmic scaling in the carrier density. We can see that the maximum beta is achieved when the thickness of the quantum well is around 11.8nm at carrier densities between $1 \times 10^{23} - 1 \times 10^{24} m^{-3}$.

We also show the top view of the 3D Figures 5.42-5.43 with carrier density and thickness of the quantum wells in the x and y axis, respectively while $\beta$ is presented with different colors in Figure 5.44. The blue color spectrum shows the small values of $\beta$ while the orange and yellow colors show the large values of $\beta$. We can see that beta for quantum well thicknesses between 10nm-14nm has the highest values when carrier density is between $1 \times 10^{23} - 1 \times 10^{24} m^{-3}$. The maximum $\beta$ is achieved at the thickness of 11.8nm.

The effect of quantum well thickness on $\beta$ can be explained in the spontaneous emission spectrum for different thicknesses of quantum wells at specific carrier densities. Figures 5.45-5.47 present the spontaneous emission spectrum for quantum well thicknesses of 10nm, 11.8nm, and 19nm at different carrier densities. From Figure 5.45, we can see that when the quantum well thickness is at 10nm, the spontaneous emission spectra are very narrow and sharp for both the free space and the nanowire modes. Also, we can see that the lasing mode is well-located within the spectrum. Therefore, a larger ratio of the spontaneous emission is capable of coupling to the lasing mode. However, as the carrier density increases, the free space and the nanowire mode spectra broaden which results in a decrease in the $\beta$ for larger carrier density values. between $1 \times 10^{24} - 1 \times 10^{25} m^{-3}$ we have the largest amount of change in the spontaneous

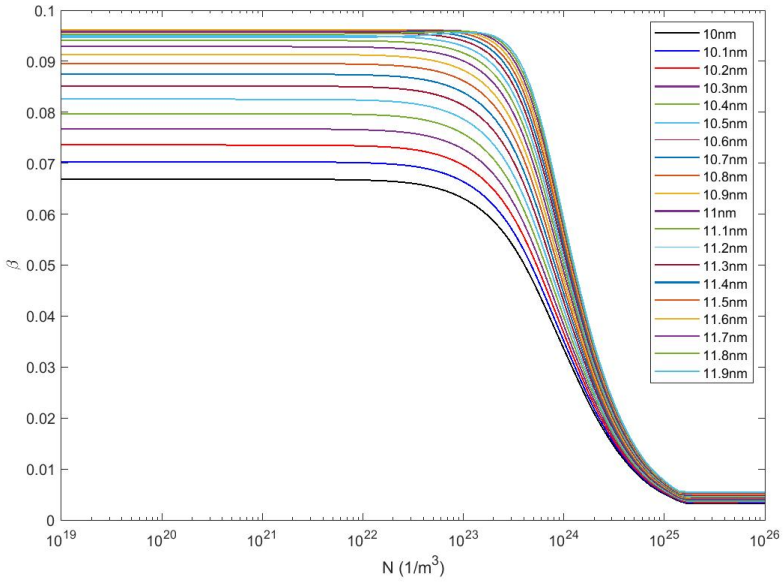


Figure 5.41: Spontaneous emission factor ($\beta$) versus carrier density for quantum well thicknesses between 10nm to 12nm.

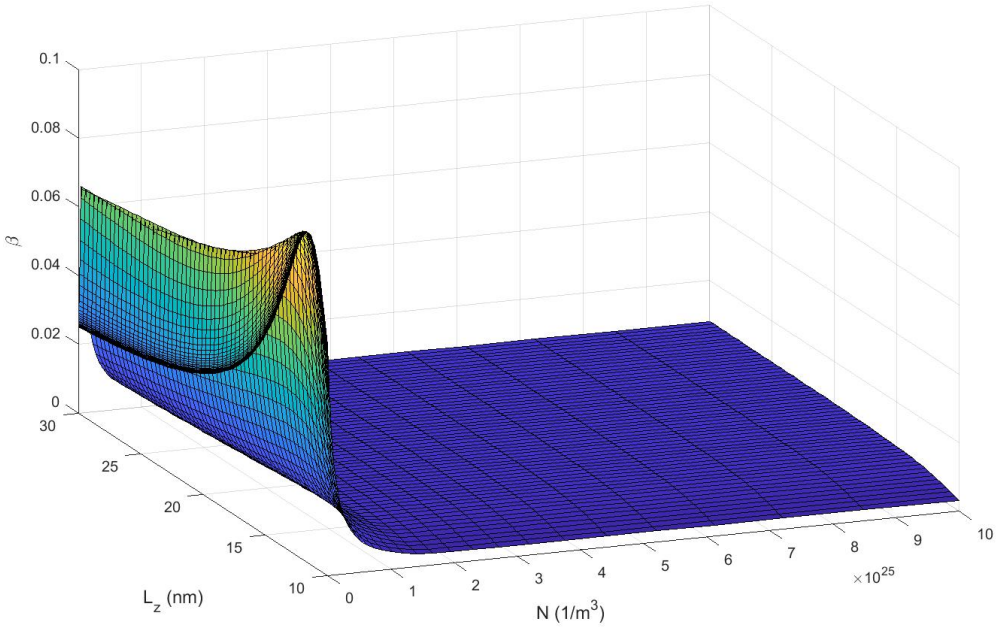


Figure 5.42: Spontaneous emission factor ($\beta$) versus carrier density (linear scale), and quantum well thicknesses.

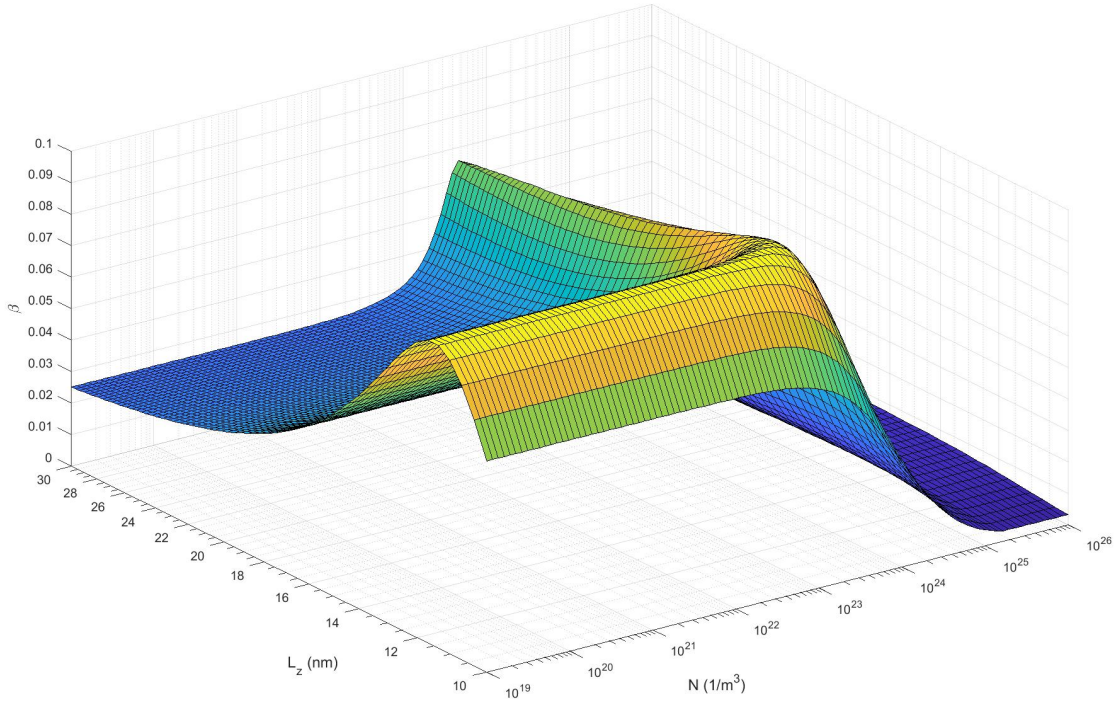


Figure 5.43: Spontaneous emission factor ($\beta$) versus carrier density (logarithmic scale), and quantum well thicknesses.

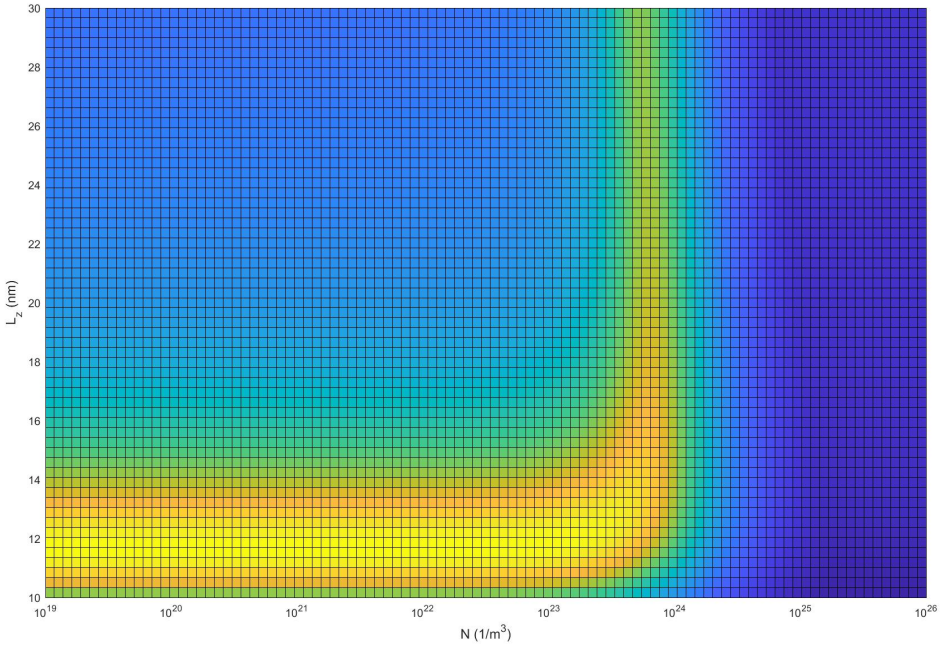


Figure 5.44: Spontaneous emission factor ($\beta$) versus carrier density (logarithmic scale), and quantum well thicknesses from the top view of Figure 5.44.

emission spectra. Similar behavior is observed for the 11.08 and 19nm thick quantum wells in Figure 5.46-5.47.

It is worth mentioning that in 19nm thick quantum well, at low carrier densities the spontaneous emission spectrum of the lasing mode is very small. This means that at low carrier densities, the spontaneous emission spectrum of the lasing mode is not completely located within the spontaneous emission spectra of the free space (black plot), and nanowire modes (blue plot). However, as the carrier density increases, due to the broadening of the spontaneous emission spectra, the lasing mode spectrum falls within the black and red plots at carrier density around $1 \times 10^{24}$. This means that more and more spontaneous emissions are coupling to the lasing mode and this results in the peak in the spontaneous emission spectrum versus carrier density in Figure 5.40.

After investigating the effect of the quantum well thickness on the gain and $\beta$, in the following, we will investigate the effect of the temperature. In order to obtain the effect of the temperature on the gain, we plot the gain spectrum of the 19nm thick $In_{0.2}Ga_{0.8}As/GaAs$ quantum well for different temperatures ranging from 5K to 300K for carrier density of $1 \times 10^{24}$ in Figure 5.48.

Here we can see that by increasing the temperature, the peak of the gain spectrum of the 19nm thick quantum well decreases. That's due to the fact that as the temperature increases the Fermi functions is smoother. In Equation 5.16 we can see that the gain depends on the Fermi functions with the term $f_c - f_v$. The decrease in the Fermi functions will therefore result in the decrease of the peak in the gain spectrum compared to low temperatures where Fermi functions almost act like step functions. Figure 5.49 presents the Fermi functions at temperatures 5K, 100K, 200K, and 300K. We can see that as the temperature increases, Fermi functions $f_c$ and $f_v$ get smoother. Therefore, at higher temperatures instead of the Fermi functions having values close to the unity for temperatures near 0K at the transition energy, they will have smaller values between 0-1.

In the next step, we solve Equation 5.33 to obtain $\beta$ with different temperatures varying from 5K to 300K for the 19nm thick $In_{0.2}Ga_{0.8}As/GaAs$ quantum well in Figure 5.50. Here we can see that as the temperature increases the spontaneous emission constantly decreases until the peak of the beta completely disappears. The smaller number of carriers means that there will be less number of spontaneous emissions which can couple to the lasing mode. Also, higher temperatures lead to increased carrier scattering and phonon-assisted processes, causing a broader energy distribution of electrons and holes within the quantum wells. Moreover, in high temperatures larger number of carriers are lost due to the non-radiative processes and this reduces the population inversion and diminishes the rate of spontaneous emission. This decrease in the spontaneous emission rate, results in a smaller probability of the spontaneous emissions coupling to the lasing mode and smaller values of $\beta$.

In this section, we investigated the effect of the quantum well thickness and the temperature on the gain and the spontaneous emission spectrum. By plotting $\beta$ versus different thicknesses of the quantum wells, we can identify the optimum quantum well thickness for a specific nanowire cavity to maximize the spontaneous emission coupling efficiency. Also, we understood how $\beta$ decreases as the temperature increases, and the peak in $\beta$ versus carrier density disappears at high temperatures.

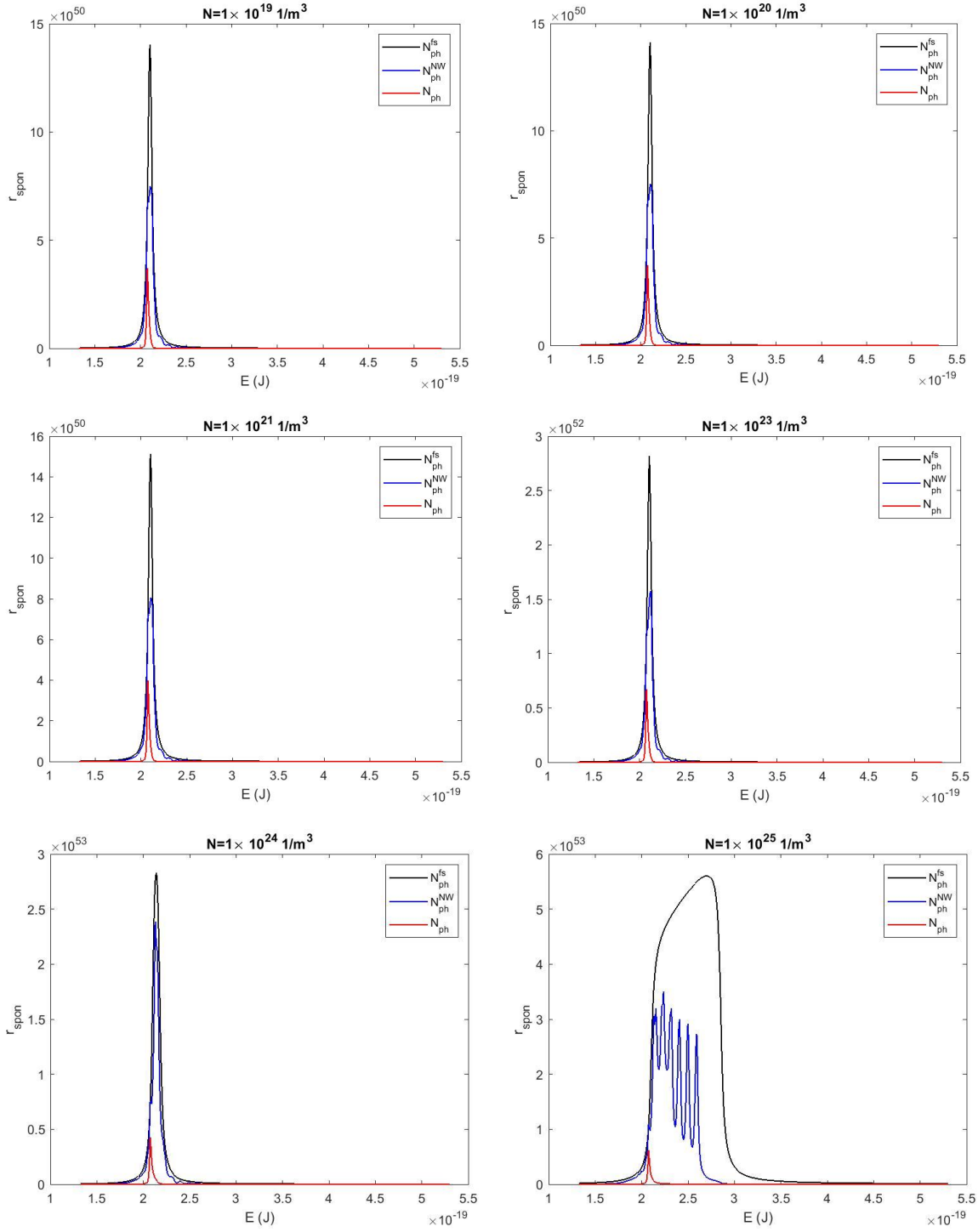


Figure 5.45: Spontaneous emission spectrum for 10nm thick $In_{0.2}Ga_{0.8}As/GaAs$ quantum well. The black plot presents the free space spontaneous emission spectrum, the blue plot shows the nanowire spontaneous emission spectrums obtained using the $N_{ph}^{NW}$, and the red plot presents the spontaneous emission of the lasing mode.

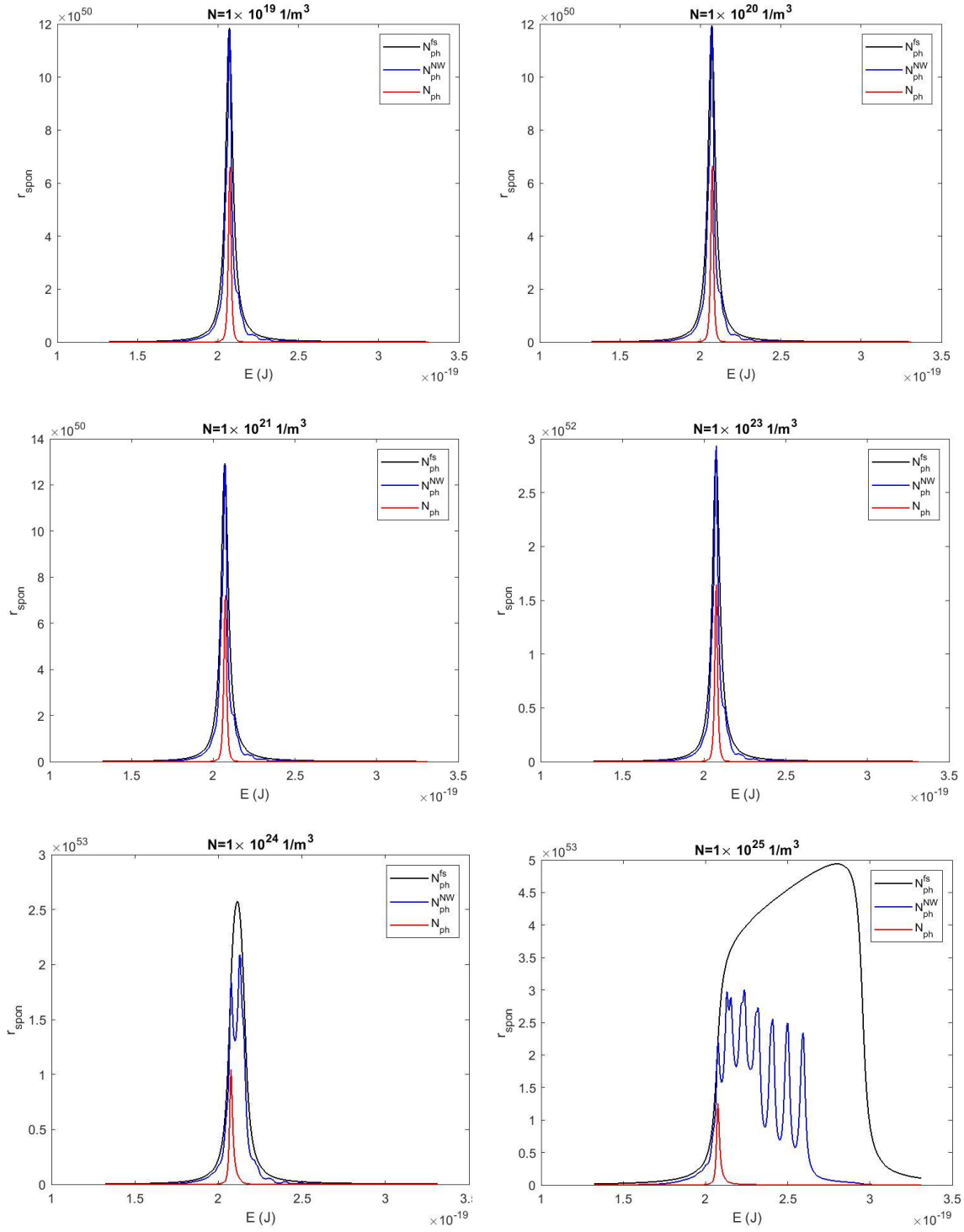


Figure 5.46: Spontaneous emission spectrum for 11.8nm thick $In_{0.2}Ga_{0.8}As/GaAs$ quantum well. The black plot presents the free space spontaneous emission spectrum, the blue plot shows the nanowire spontaneous emission spectrums obtained using the $N_{ph}^{NW}$, and the red plot presents the spontaneous emission of the lasing mode.

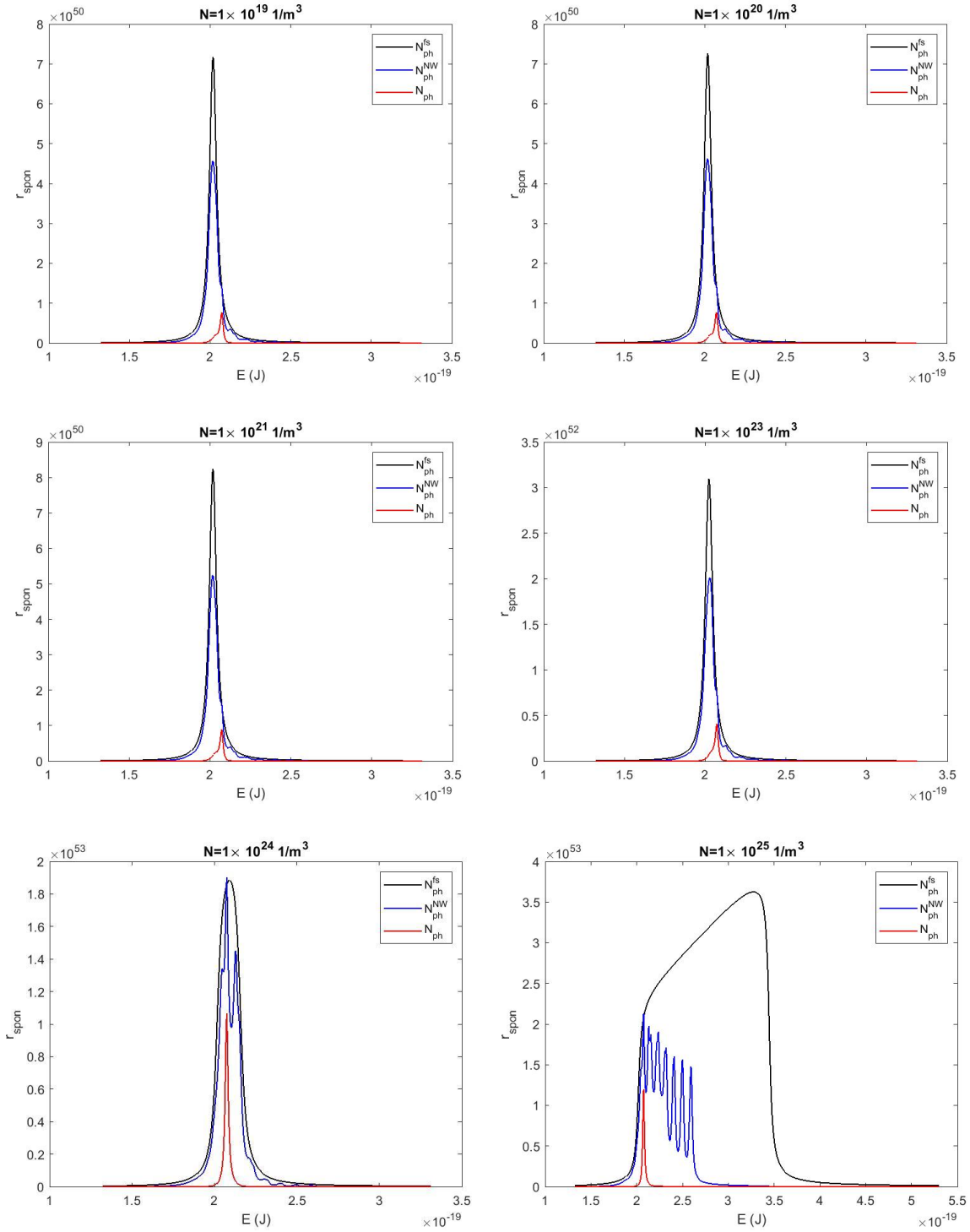


Figure 5.47: Spontaneous emission spectrum for 19nm thick $In_{0.2}Ga_{0.8}As/GaAs$ quantum well. The black plot presents the free space spontaneous emission spectrum, the blue plot shows the nanowire spontaneous emission spectrums obtained using the $N_{ph}^{NW}$, and the red plot presents the spontaneous emission of the lasing mode.

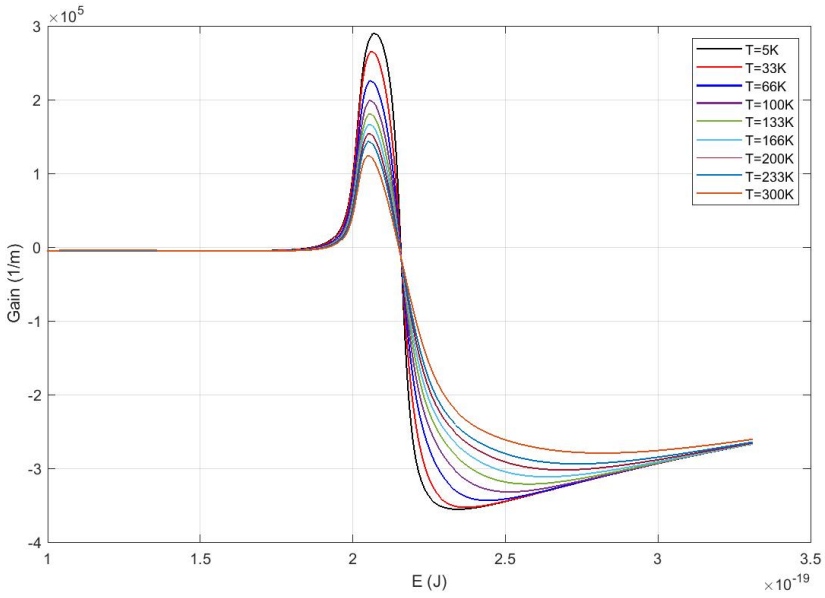


Figure 5.48: Gain spectrum of the 19nm thick $In_{0.2}Ga_{0.8}As/GaAs$ quantum well at different temperatures ranging from 5K-300K.

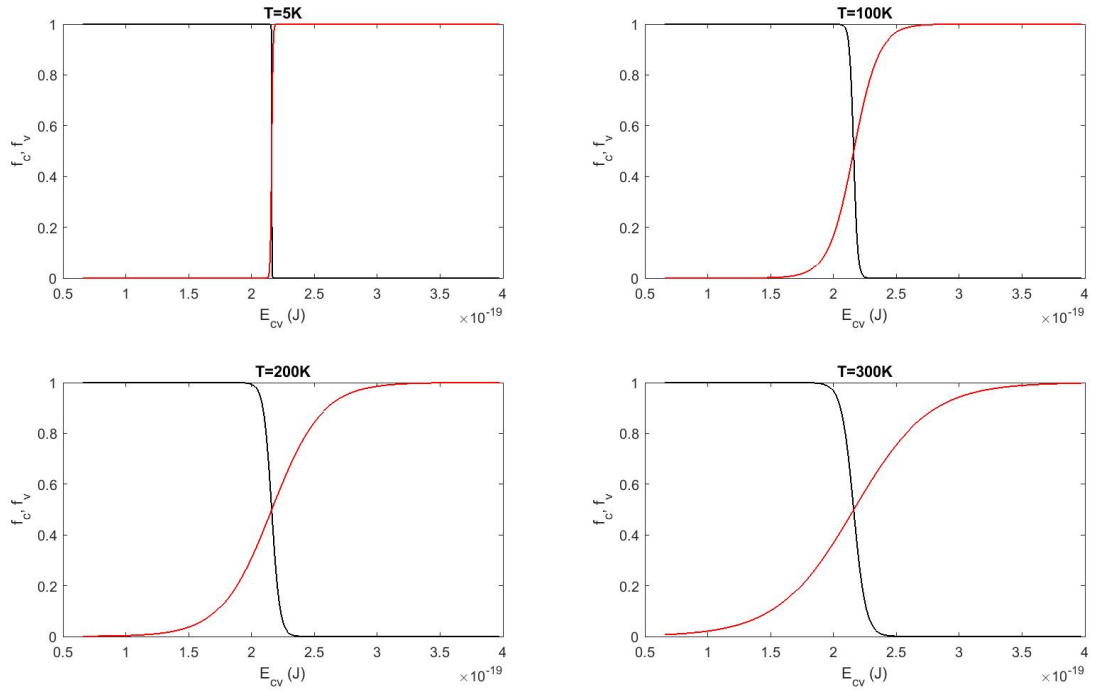


Figure 5.49: Fermi functions $f_c$ and $f_v$ at different temperatures ranging from 5K-300K.

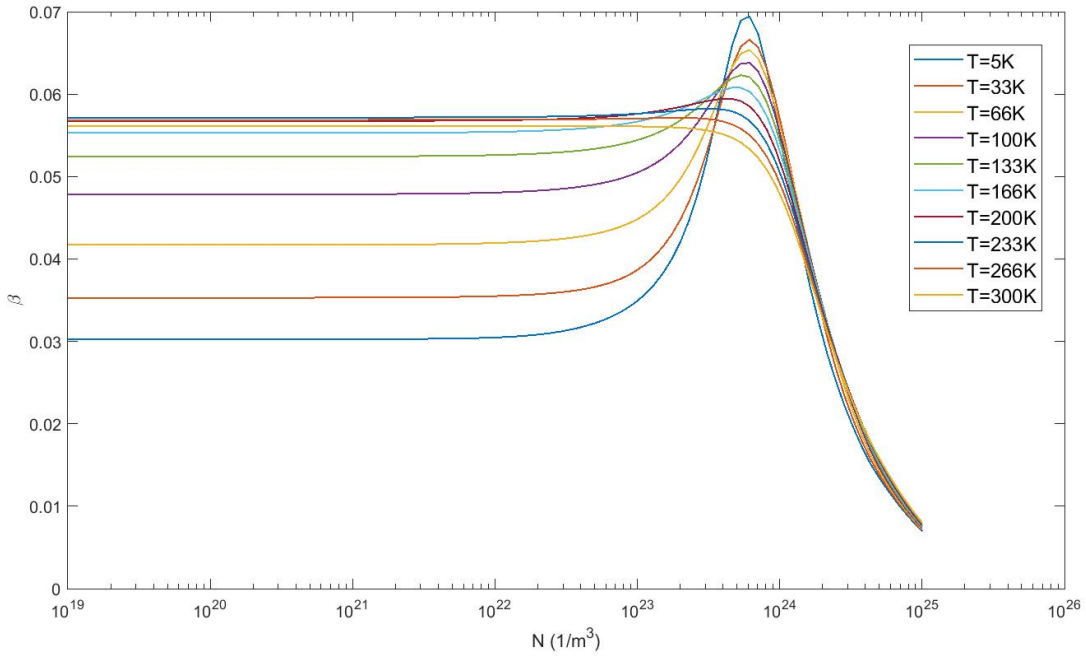


Figure 5.50: Spontaneous emission factor ($\beta$) for the 19nm thick $In_{0.2}Ga_{0.8}As/GaAs$ quantum well at different temperatures ranging from 5K-300K.

## 5.8 Bending Effects in Nanowire Lasers

Nanowire bending is also observed in [158] within MQW core/shell nanowire structures containing 13 and 26 quantum wells (QWs) and is strongly associated with the non-uniform shell coating and high indium (In) content. These structures feature a GaN core surrounded by InGaN/GaN MQW shells, as depicted in the schematic image of Figure 5.51a, with shell thickness varying significantly across different facets—approximately 65 nm on the 1101 facets and around 10 nm on the 0001 facet, as shown in Figure 5.51b. This non-uniformity induces differential strain, particularly on the thicker facets. This strain is a result of the lattice mismatch between the GaN core and the InGaN quantum wells, which in turn leads to the mechanical bending of the nanowires, as illustrated in Figure 5.51c, despite dislocation-free growth of highly uniform InGaN/GaN quantum wells.

The bending becomes more pronounced as the In content increases due to the greater lattice mismatch between the GaN core and the InGaN QWs. Interestingly, this bending does not prevent the nanowires from lasing, demonstrating effective waveguiding within the nanowire structure. Additionally, by varying the In content in the quantum wells, the emission wavelength of the optically pumped lasers can be tuned across a wide range, from 383 nm (UV region) to 478 nm (visible region). This wavelength tunability is directly related to the In composition in the quantum wells, with higher In content resulting in longer emission wavelengths.

In our 3D simulations of the quantum well nanowire laser, ten highly uniform $In_{0.2}Ga_{0.8}As/GaAs$ quantum wells within the nanowire cannot change the optical properties of the nanowire owing to the small number of QWs. Thus, we have focused solely on simulating the GaAs nanowire laser to obtain the optical properties of the nanowire cavity. However, the alternating layers of GaN and InGaN can be incorporated easily into our 3D simulation setup within the nanowire. By accurately defining the material properties specific to InGaN with varying indium content,

we could use 3D simulations to model the strain distribution along the nanowire's length and cross-section. By varying the indium content in the simulations, we can directly observe the change in the electromagnetic field distribution and the optical properties of the laser in the regions with high indium content, resulting in strain differences that lead to bending.

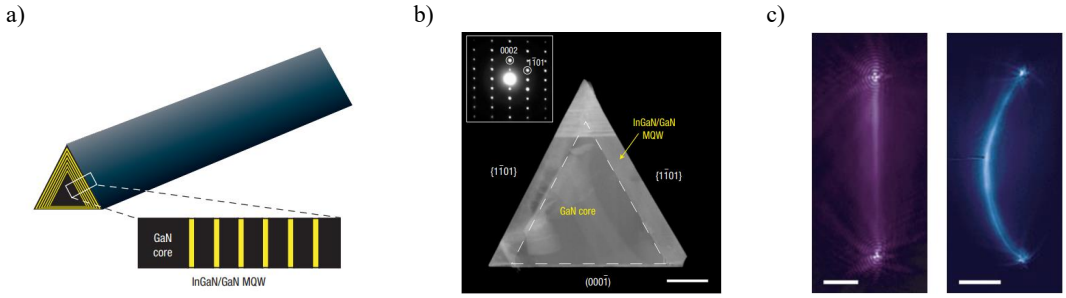


Figure 5.51: a) A schematic representation of a multi-quantum well (MQW) nanowire, along with an enlarged cross-sectional view of a nanowire facet, illustrates the InGaN/GaN MQW structure. In this depiction, the InGaN layers are shown in yellow, b)dark-field cross-sectional STEM image of a 26MQW nanowire structure, captured along the [1120] zone axis, clearly shows the core/shell interface highlighted by dashed lines. In the inset, the corresponding electron diffraction pattern is indexed for the [1120] zone axis, and c) photoluminescence images of GaN/$In_{0.05}Ga_{0.95}N$ (left) and GaN/$In_{0.23}Ga_{0.77}N$ (right) MQW nanowire structures highlight the bending effect. Reprinted from [158].

## 5.9 Conclusion

In this chapter, we presented simulation results of an $In_{0.15}Ga_{0.85}As$ nanopillar laser to validate our model for bulk semiconductors as well. By computing the gain spectrum, gain model, and the L-L curves of the bulk $In_{0.15}Ga_{0.85}As$ using material parameters, we validated our model for bulk semiconductors.

In the next step, we used our three-step laser model in order to investigate the laser properties of the ten $In_{0.2}Ga_{0.8}As$/GaAs quantum well nanowire laser. Through extensive simulations, we uncover insights into nanowire laser characteristics and how they can be optimized. One intriguing finding relates to the behavior of the spontaneous emission factor in relation to the number of carriers. At low carrier densities, $\beta$ is small. However, as the carrier density increases, to the order of $N = 1 \times 10^{23} - 1 \times 10^{24} m^{-3}$, $\beta$ increases until it reaches a maximum, and then it starts to decrease for large carrier densities. When we use $\beta$ from our formalism to solve the laser rate equations, we can see that below the threshold, when the spontaneous emission process is dominant, we observe that the difference between using different $\beta$s appears. Above the threshold, stimulated emissions take over, causing a decrease in the spontaneous emission factor.

Then we investigated the effect of the quantum well thickness and the temperature on the spontaneous emission factor and the gain. From investigations on the $\beta$ against quantum well thickness, we were able to identify the optimum quantum well thickness value to have the highest spontaneous emission coupling efficiency. We also observed that as the thickness of the quantum well increases, the peak of the gain decreases while the gain spectrum broadens,

and the peak shifts to the left. Moreover, by increasing the temperature, the peak of the gain decreases constantly. Similar behavior is also observed in $\beta$. As the temperature increases, $\beta$ decreases until, for temperatures larger than 200K, the peak in $\beta$ disappears.

It's important to elaborate on how the validation of our findings with experimental data has significantly advanced our understanding of quantum well (QW) nanowire lasers and how this can lead to the fabrication of more efficient devices.

The step-by-step formalism developed in Chapter 3 provides a detailed derivation of the optical processes within QW nanowire lasers, distinguishing their behavior from conventional bulk semiconductor lasers. This formalism, which includes the photonic density of states (PDOS) within the nanowire cavity, captures the complex interplay between absorption, gain, and spontaneous emission rates—an aspect often overlooked in existing literature. By incorporating the PDOS, our approach addresses a critical gap in current theoretical models, enabling a more comprehensive understanding of optical dynamics, as detailed in Equations 3.104-3.106, for gain and spontaneous emission rates.

The detailed computational method outlined in Chapter 4 for 2D and 3D modeling of the nanowire cavity dimensions using finite element method (FEM) provides a systematic way to design the cavity for optimal performance. For example, Figure 4.14 illustrates the region for selecting the nanowire diameter in which the cavity would guide a single mode, offering a focused beam with higher spatial coherence compared to a multimode laser. Also, Sections 4.2.2.3 and 4.2.3.2 offer guidance on how to identify the lasing mode in case of having a multimode nanowire cavity in 2D and 3D simulation setups, respectively. Moreover, discussions on the convergence tests in Figures 4.6 through 4.16 demonstrate how to choose simulation parameters and the boundary conditions to achieve reliable simulation results.

The derivation of the spontaneous emission factor ($\beta$) and the Purcell effect in Equations 3.116 and 3.118 allows for the prediction and optimization of these factors before laser fabrication. Unlike conventional approaches where $\beta$ is determined post-fabrication through fitting experimental data, our method enables its calculation based on the material parameters and the nanowire's dimensions, which is crucial for designing lasers with lower thresholds and higher spontaneous emission coupling efficiency.

For example, in Figure 5.30, we demonstrate that $\beta$ reaches a peak at around threshold carrier density before decreasing as stimulated emission processes begin to dominate. By identifying this peak, we can strategically select an optimum pump mechanism that operates at the carrier density where $\beta$ is maximized. When $\beta$ is at its maximum, the laser operates under conditions where the highest number of spontaneous emissions couple into the lasing mode. This coupling is directly linked to achieving a lower laser threshold because, below the threshold, spontaneous emission processes are dominant. Therefore, maximizing the coupling of spontaneous emissions to the lasing mode minimizes the pump power required to achieve lasing.

Furthermore, our analysis of quantum well thickness and temperature effects on $\beta$, as shown in Figures 5.42 and 5.50, demonstrates how these factors directly influence $\beta$. These insights enable the precise selection of QW thickness and operating temperature to maximize $\beta$ and improve laser performance. For instance, in Section 5.7 Figure 5.41, we identify that the optimum QW thickness for a 200nm diameter hexagonal GaAs nanowire with a length of 2.2µm is 11.8nm which provides the highest $\beta$ values. Our simulations also showed how temperature variations affect $\beta$, with lower temperatures generally resulting in higher $\beta$ due to reduced phonon interactions, as depicted in Figure 5.50.

Comparing our simulated L-L curves in Figure 5.36 with experimental data not only shows good agreement in predicting laser thresholds and the shape of the L-L curves but also demonstrates the significance of using a dynamic $\beta$, where $\beta$ depends on the carrier density in solving the laser rate equations of 5.36 and 5.37. Specifically, when comparing the L-L curves obtained using a dynamic $\beta$ to the one using a constant $\beta$ in Figure 5.33, a clear difference emerges. The maximum difference between the black and blue curves occurs around a pump power of around 0.25 $\mu J/cm^2$, corresponding to a difference of 0.0367 in $\beta$ between the two curves at this pump power. This insight underscores the importance of accounting for the dependence of $\beta$ on carrier density to achieve more accurate modeling and optimized laser performance.

# Chapter 6

# Conclusions and Future Work

In this dissertation, we presented an exploration of semiconductor lasers, with a particular focus on quantum well nanowire lasers and the development of a theoretical framework for modeling the dynamics of the optical processes in quantum well nanowire lasers. Our formulation unveiled insights into the design, simulation, and novel understanding of the spontaneous emission factor. In this concluding chapter, we will summarize the key findings and contributions of this work, discuss their implications, and outline potential directions for future research.

## 6.1 Key Reseach Results

The main contribution of this thesis is to develop the formulation to describe emission and absorption processes in semiconductor nanowires. By investigating the optical processes within a bulk semiconductor, we adapt the equations for quantum wells by considering the changes in the optical characteristics due to the quantum confinement effect in quantum wells. We then added the effect of the nanowire cavity on the absorption gain, and spontaneous emission rates when the quantum well is placed within a nanowire in Chapter 3. This thesis also proposes the theoretical equations to calculate the spontaneous emission factor and the Purcell effect for quantum well nanowire lasers.

A key element of our formulation is that we do not fit the experimental data in our simulations to calculate $\beta$. We solve the laser rate equations using $\beta$ and the gain that we develop from our formulations. Our formalism provides an easy method to calculate $\beta$ directly from material and cavity parameters which will help to predict laser performance.

The simulations of the ten $In_{0.2}Ga_{0.8}As/GaAs$ quantum well nanowire in Chapter 5 revealed that when we incorporate the photonic density of states in the equations describing the dynamics of the optical processes, higher rates for spontaneous emission is obtained compared to the literature where only free space photonic density of states is considered.

Also, the simulations based on our developed model reveal that the spontaneous emission factor is not a constant value like usually reported in the literature, and it depends on the carrier density. By plotting the carrier density versus $\beta$, we were able to report the pulse shape of the spontaneous emission against time and carrier density. The spontaneous emission factor remains constant for low carrier densities. However, as the pump power increases, $\beta$ will increase to a maximum around the threshold carrier density and the decrease again for the carrier densities

above the threshold. This behavior is not reported in the previous models of the quantum well nanowire lasers to the best of our knowledge.

We also investigated the effect of the temperature and the quantum well thickness on the gain and $\beta$. Our simulation results show that by increasing the quantum well thickness from 10nm to 11.8nm, the spontaneous emission factor increases constantly, after reaching a maximum of 0.094 for 11.8nm it starts to decrease as the carrier density increases. This finding is quite interesting because it can predict the optimum thickness of the quantum well within a nanowire to obtain the highest spontaneous emission coupling efficiency. Also, we investigated the effect of the temperature on the spontaneous emission factor. Our simulation results reveal that as temperature increases the $\beta$ gradually decreases. for temperature larger than 200K, the peak in the $\beta$ almost fades away.

Our simulations and theoretical framework effectively capture the laser dynamics, providing an understanding of the interplay between absorption, gain, and spontaneous emission rates. This thesis contributes to the fundamental understanding of MQW-nanowire lasers.

## 6.2 Future Work

In the course of this research, we have contributed to advancing our understanding of quantum well nanowire lasers, their behavior, and their potential applications. However, as with any scientific endeavor, there remain promising avenues for future exploration and innovation. In the following sections, we outline several compelling directions for future work in the field of nanowire lasers.

1. **Effect of the nanowire geometry on the spontaneous emission factor and Purcell effect**

   To investigate the effect of the nanowire geometry on the spontaneous emission factor and Purcell effect, we can change the nanowire's geometry, such as its length and diameter, which can alter the resonant modes of the nanowire along with its optical properties such as quality factor, and the confinement factor in Equations 5.5 and 5.6, respectively.

   These changes in geometry ultimately lead to the change in the photonic density of states ($N_{ph}(E)$) in the rate of optical processes occurring within the nanowire. Specifically, the modifications in the photonic density of states due to the altered geometry directly influence the spontaneous emission rates and, consequently, the spontaneous emission factor in Equation 5.33 and the Purcell factor in Equation 5.35. When the geometry of the nanowire is adjusted, the resonant modes can either enhance or inhibit the spontaneous emission, depending on how well the modes overlap with the gain medium.

   The Purcell effect relates to the decrease in the spontaneous emission lifetime within the QWs when they are placed in the nanowire cavity. The Purcell factor depends on both the quality factor of the resonant modes and their effective mode volume. Therefore, by changing the nanowire's diameter and length, the quality factor and mode volume are modified, which also changes the $N_{ph}(E)$, leading to the change in the Purcell factor. A higher quality factor and smaller mode volume typically lead to a higher Purcell factor, reducing the spontaneous emission lifetime.

   Consequently, adjusting the nanowire geometry enables us to control and optimize the photonic density of states, thereby maximizing the spontaneous emission and Purcell

factors. For future studies, exploring the dependency of both the spontaneous emission and the Purcell factors on nanowire geometry is a promising area. This research could lead to improved designs for nanowire-based photonic devices, offering better control over light-matter interactions at the nanoscale.

2. **Effect of dimensionality on the Purcell effect**

   Investigating the effect of different quantum well thicknesses on the spontaneous emission and Purcell factors represents another significant area of research. To discuss the effect of dimensionality on the Purcell effect, we can vary the thickness of QWs. Altering the QW thickness will change the electronic density of states ($\rho(E_{cv})$) in the absorption, gain, and spontaneous emission rates within the QW nanowire laser in Equations 5.16 and 5.30. The thickness of the QWs determines where the energy levels exist within the band diagram and the number of energy levels present. Thinner QWs have fewer energy levels, resulting in a narrower gain and spontaneous emission spectrum with higher peaks.

   By adjusting the thickness of the QWs, we can effectively control the energy levels, which in turn shifts the laser emission wavelength. This allows for designing QW nanowire lasers tailored to emit at specific wavelengths suitable for particular applications. For instance, fine-tuning the QW thickness can provide the necessary control in optoelectronic devices where precise wavelength emission is critical.

   As mentioned above, changing the QW thickness affects the electronic density of states and consequently influences the spontaneous emission and Purcell factors. Therefore, we can identify the optimal QW thickness for a given nanowire dimension by exploring how these factors change with varying QW thicknesses and picking the optimum value where the spontaneous emission factor is maximum. This approach enables the design of QW nanowire lasers with customized emission properties optimized for specific applications. Future studies focusing on the relationship between QW thickness and the spontaneous emission and Purcell factors will further enhance our ability to engineer nanoscale photonic devices with precise control over their optical characteristics.

3. **Implementing the quantum well nanowire model, developed in this thesis, to the more complex structures**

   The quantum well nanowire model developed in this thesis can be implemented to investigate more complex laser structures. For example, it can be applied to nanowire lasers with both radial and axial QWs, as reported in [153], where it is unclear whether lasing is achieved through the radial or axial QWs. This uncertainty challenges understanding and optimizing the lasing mechanisms within such structures.

   By employing our theoretical model, we can investigate the lasing properties of radial and axial QWs separately. This involves simulating the nanowire cavity's optical characteristics along with the absorption, gain, and spontaneous emission rates coming from either radial or axial QWs, considering the specific geometry and arrangement of the QWs. By comparing the simulation results of the L-L curves with the experimental measurements, we can identify which type of QW (radial or axial) contributes the most to the lasing process.

   The ability to differentiate the contributions of radial and axial QWs allows for a more detailed understanding of the lasing mechanisms in complex QW nanowire structures. This insight can guide the design and optimization of nanowire lasers. For instance, if the

model indicates that radial QWs contribute more significantly to lasing, future designs can focus on optimizing the radial QWs' properties, such as their thickness and composition, to achieve better lasing efficiency.

Furthermore, this approach enables the exploration of hybrid QW nanowire structures where both radial and axial QWs are engineered to work simultaneously. Understanding the individual and combined effects of these QWs on the lasing properties can develop more sophisticated and efficient nanowire lasers.

4. **Modify the mathematical framework proposed in this thesis for Quantum wire and quantum dot nanowire lasers**

   The step-by-step approach of our formalism presented in Chapter 3 comprehensively discusses how confinement in one direction (in the QWs) is incorporated into the formalism of the bulk gain medium to the QWs. This methodology serves as a foundational guide for extending the formalism to quantum wires (QWRs) and quantum dots (QDs), which exhibit confinement in two and three dimensions, respectively.

   To adapt the equations for QWRs and QDs nanowire lasers, one should also begin with the bulk equations. Similar to the approach we presented for QWs, it is necessary to consider the impacts of the constrained geometry on the wavevectors and the electronic density of states. For quantum wires, confinement in two directions leads to a series of one-dimensional subbands in the electronic density of states. Similarly, confinement in all three directions results in discrete energy levels for quantum dots. Our formalism specifically highlights where and why the confinement effects alter the equations. For example, in QWs, confinement affects the in-plane wavevectors and leads to quantized energy levels perpendicular to the well plane. For QWRs, this confinement would extend to two dimensions, affecting the wavevectors in both confined directions and resulting in a series of quantized subbands. For QDs, the complete three-dimensional confinement results in discrete energy levels, transforming the density of states into a set of delta functions.

   By clearly identifying these points of modification, our formalism paves the way for developing the mathematical framework for quantum wire and quantum dot nanowire lasers. This step-by-step approach ensures a consistent transition from bulk to low-dimensional gain media, maintaining the physical principles while addressing the unique characteristics of the change of material properties, such as gain and spontaneous emission rates when moving from bulk to quantum wires and quantum dots. By following the formalism developed in this thesis, one can effectively extend the model for quantum wire and quantum dot lasers, thereby broadening the applicability and impact of the theoretical framework.

# Bibliography


[1] L. Cao, J. S. White, J.-S. Park, J. A. Schuller, B. M. Clemens, and M. L. Brongersma, "Engineering light absorption in semiconductor nanowire devices," *Nature materials*, vol. 8, no. 8, pp. 643–647, 2009.

[2] L. Cao, P. Fan, A. P. Vasudev, *et al.*, "Semiconductor nanowire optical antenna solar absorbers," *Nano letters*, vol. 10, no. 2, pp. 439–445, 2010.

[3] S. Mokkapati, D. Saxena, H. Tan, and C. Jagadish, "Optical design of nanowire absorbers for wavelength selective photodetectors," *Scientific reports*, vol. 5, no. 1, p. 15 339, 2015.

[4] J. Claudon, J. Bleuse, N. S. Malik, *et al.*, "A highly efficient single-photon source based on a quantum dot in a photonic nanowire," *Nature Photonics*, vol. 4, no. 3, pp. 174–177, 2010.

[5] M. E. Reimer, G. Bulgarini, N. Akopian, *et al.*, "Bright single-photon sources in bottom-up tailored nanowires," *Nature communications*, vol. 3, no. 1, p. 737, 2012.

[6] J. Tatebayashi, S. Kako, J. Ho, Y. Ota, S. Iwamoto, and Y. Arakawa, "Room-temperature lasing in a single nanowire with quantum dots," *Nature Photonics*, vol. 9, no. 8, pp. 501–505, 2015.

[7] X. Zhang, R. Yi, N. Gagrani, *et al.*, "Ultralow threshold, single-mode ingaas/gaas multiquantum disk nanowire lasers," *ACS nano*, vol. 15, no. 5, pp. 9126–9133, 2021.

[8] J. Arbiol, M. De La Mata, M. Eickhoff, and A. F. i Morral, "Bandgap engineering in a nanowire: Self-assembled 0, 1 and 2d quantum structures," *Materials today*, vol. 16, no. 6, pp. 213–219, 2013.

[9] M. Fox and R. Ispasoiu, "Quantum wells, superlattices, and band-gap engineering," *Springer Handbook of Electronic and Photonic Materials*, pp. 1–1, 2017.

[10] L. Francaviglia, A. Giunto, W. Kim, *et al.*, "Anisotropic-strain-induced band gap engineering in nanowire-based quantum dots," *Nano Letters*, vol. 18, no. 4, pp. 2393–2401, 2018.

[11] M. Kurban, Y. Şimşek, and Ş. Erkoç, "III-V semiconductors bandgap engineering," in *Handbook of III-VI Semiconductor-Based Sensors and Radiation Detectors: Volume 1, Materials and Technology*, Springer, 2023, pp. 109–131.

[12] M. Ezzeldien, R. Dolia, M. Alzaid, I. H. Alsohaimi, A. M. Quraishi, and P. A. Alvi, "Tunable optical gain characteristics of AlN/GaN/InAlN quantum well heterostructure under uniaxial and biaxial pressures," *physica status solidi (b)*, vol. 260, no. 3, p. 2 200 479, 2023.

[13] S. Church, N. Patel, R. Al-Abri, *et al.*, "Holistic nanowire laser characterization as a route to optimal design," *arXiv preprint arXiv:2210.06958*, 2022.

[14] M. Moradi and M. Moradi, "The effects of temperature and electric field on the electronic and optical properties of an inas quantum dot placed at the center of a gaas nanowire," *Journal of Surface Investigation: X-ray, Synchrotron and Neutron Techniques*, vol. 16, no. 6, pp. 1237–1247, 2022.

[15] A. Einstein, "On the quantum theory of radiation physik," *Z*, vol. 18, p. 121, 1917.
[16] J. Weber, "Amplification of microwave radiation by substances not in thermal equilibrium," *Transactions of the IRE Professional Group on Electron Devices*, no. 3, pp. 1–4, 1953.
[17] J. P. Gordon, H. J. Zeiger, and C. H. Townes, "The maser—new type of microwave amplifier, frequency standard, and spectrometer," *Physical review*, vol. 99, no. 4, p. 1264, 1955.
[18] A. L. Schawlow and C. H. Townes, "Infrared and optical masers," *Physical review*, vol. 112, no. 6, p. 1940, 1958.
[19] N. Basov and A. Guenther, "History of the development of lasers at the pn lebedev physics institute, academy of sciences of the ussr," *Soviet Journal of Quantum Electronics*, vol. 15, no. 3, p. 301, 1985.
[20] N. Basov and A. Prokhorov, "About possible methods for obtaining active molecules for a molecular oscillator,", vol. 28, 1955.
[21] T. H. Maiman *et al.*, "Stimulated optical radiation in ruby," 1960.
[22] T. H. Maiman, "Stimulated optical emission in fluorescent solids. i. theoretical considerations," *Physical Review*, vol. 123, no. 4, p. 1145, 1961.
[23] T. H. Maiman, R. Hoskins, I. J. D'Haenens, C. K. Asawa, and V. Evtuhov, "Stimulated optical emission in fluorescent solids. II. spectroscopy and stimulated emission in ruby," *Physical Review*, vol. 123, no. 4, p. 1151, 1961.
[24] A. H. Rawicz, "Theodore harold maiman and the invention of laser," in *Photonics, Devices, and Systems IV*, SPIE, vol. 7138, 2008, pp. 39–46.
[25] Z. Alferov, "Heterostructures for optoelectronics: History and modern trends," *Proceedings of the IEEE*, vol. 101, no. 10, pp. 2176–2182, 2013.
[26] A. K. Maini, *Lasers and optoelectronics: fundamentals, devices and applications*. John Wiley & Sons, 2013.
[27] M. A. Parker, *Physics of optoelectronics*. CRC Press, 2018.
[28] R. de Vivie-Riedle and U. Troppmann, "Femtosecond lasers for quantum information technology," *Chemical reviews*, vol. 107, no. 11, pp. 5082–5100, 2007.
[29] G. Hüttmann, C. Yao, and E. Endl, "New concepts in laser medicine: Towards a laser surgery with cellular precision," *Medical Laser Application*, vol. 20, no. 2, pp. 135–139, 2005.
[30] L. Xinju, *Laser technology*. CRC press, 2010.
[31] R. Steiner, "New laser technology and future applications," *Medical Laser Application*, vol. 21, no. 2, pp. 131–140, 2006.
[32] I. I. Khanin, *Fundamentals of laser dynamics*. Cambridge Int Science Publishing, 2006.
[33] K. Thyagarajan and A. Ghatak, *Lasers: fundamentals and applications*. Springer Science & Business Media, 2010.
[34] J. T. Verdeyen, "Laser electronics," 1989.
[35] G. P. Agrawal and N. K. Dutta, *Semiconductor lasers*. Springer Science & Business Media, 2013.
[36] Z. Fang, H. Cai, G. Chen, and R. Qu, *Single frequency semiconductor lasers*. Springer, 2017.
[37] J. Ralston, S. Weisser, K. Eisele, *et al.*, "Low-bias-current direct modulation up to 33 Ghz in InGaAs/GaAs/AlGaAs pseudomorphic MQW ridge-waveguide lasers," *IEEE photonics technology letters*, vol. 6, no. 9, pp. 1076–1079, 1994.
[38] S. Weisser, E. Larkins, K. Czotscher, *et al.*, "Damping-limited modulation bandwidths up to 40 Ghz in undoped short-cavity In/sub 0.35/Ga/sub 0.65/As-GaAs multiple-

quantum-well lasers," *IEEE Photonics Technology Letters*, vol. 8, no. 5, pp. 608–610, 1996.
[39] X. Zhang, A. Gutierrez-Aitken, D. Klotzkin, P. Bhattacharya, C. Caneau, and R. Bhat, "0.98-/spl mu/m multiple-quantum-well tunneling injection laser with 98-ghz intrinsic modulation bandwidth," *IEEE Journal of Selected Topics in Quantum Electronics*, vol. 3, no. 2, pp. 309–314, 1997.
[40] A. K. Ghatak and K. Thyagarajan, *Optical electronics*. 1989.
[41] H. Kroemer, "A proposed class of hetero-junction injection lasers," *Proceedings of the IEEE*, vol. 51, no. 12, pp. 1782–1783, 1963.
[42] H. Kressel and H. Nelson, "Close-confinement gallium arsenide pn junction lasers with reduced optical loss at room temperature(close confinement GaAs p-n junction lasers with reduced optical loss at room temperature)," *RCA review*, vol. 30, pp. 106–113, 1969.
[43] J. L. Chilla, S. D. Butterworth, A. Zeitschel, *et al.*, "High-power optically pumped semiconductor lasers," vol. 5332, pp. 143–150, 2004.
[44] J. Chilla, Q.-Z. Shu, H. Zhou, E. Weiss, M. Reed, and L. Spinelli, "Recent advances in optically pumped semiconductor lasers," *Solid State Lasers XVI: Technology and Devices*, vol. 6451, pp. 56–65, 2007.
[45] R. Phelan Jr and R. Rediker, "Optically pumped semiconductor laser," *Applied Physics Letters*, vol. 6, no. 4, pp. 70–71, 1965.
[46] G. Bjork and Y. Yamamoto, "Analysis of semiconductor microcavity lasers using rate equations," *IEEE Journal of Quantum Electronics*, vol. 27, no. 11, pp. 2386–2396, 1991.
[47] R. Chen, T.-T. D. Tran, K. W. Ng, *et al.*, "Nanolasers grown on silicon," *Nature Photonics*, vol. 5, no. 3, pp. 170–175, 2011.
[48] R. Röder, D. Ploss, A. Kriesch, *et al.*, "Polarization features of optically pumped cds nanowire lasers," *Journal of Physics D: Applied Physics*, vol. 47, no. 39, p. 394 012, 2014.
[49] J. Wang, M. S. Gudiksen, X. Duan, Y. Cui, and C. M. Lieber, "Highly polarized photoluminescence and photodetection from single indium phosphide nanowires," *Science*, vol. 293, no. 5534, pp. 1455–1457, 2001.
[50] L. A. Coldren, S. W. Corzine, and M. L. Mashanovitch, *Diode lasers and photonic integrated circuits*. John Wiley & Sons, 2012.
[51] D. J. Klotzkin, *Introduction to semiconductor lasers for optical communications*. Springer, 2020.
[52] U. Keller, "Recent developments in compact ultrafast lasers," *nature*, vol. 424, no. 6950, pp. 831–838, 2003.
[53] A. E. Siegman, "New developments in laser resonators," in *Optical resonators*, Spie, vol. 1224, 1990, pp. 2–14.
[54] A. E. Siegman, *Lasers*. University science books, 1986.
[55] D. Marcuse, "Computer simulation of laser photon fluctuations: Theory of single-cavity laser," *IEEE Journal of Quantum Electronics*, vol. 20, no. 10, pp. 1139–1148, 1984.
[56] H. Mabuchi and A. Doherty, "Cavity quantum electrodynamics: Coherence in context," *Science*, vol. 298, no. 5597, pp. 1372–1377, 2002.
[57] S. L. Chuang, *Physics of photonic devices*. John Wiley & Sons, 2012.
[58] N. Pikhtin, S. Slipchenko, Z. Sokolova, and I. Tarasov, "Internal optical loss in semiconductor lasers," *Semiconductors*, vol. 38, pp. 360–367, 2004.
[59] B. R. Nag, *Physics of quantum well devices*. Springer Science & Business Media, 2001, vol. 7.
[60] V. Badilita, "Study of vertical coupled-cavity laser structures," EPFL, Tech. Rep., 2004.

[61] Y. Arakawa and A. Yariv, "Quantum well lasers–gain, spectra, dynamics," *IEEE journal of quantum electronics*, vol. 22, no. 9, pp. 1887–1899, 1986.
[62] K.-Y. Jeong, M.-S. Hwang, J. Kim, J.-S. Park, J. M. Lee, and H.-G. Park, "Recent progress in nanolaser technology," *Advanced Materials*, vol. 32, no. 51, p. 2 001 996, 2020.
[63] C.-Z. Ning, "Semiconductor nanolasers and the size-energy-efficiency challenge: A review," *Advanced Photonics*, vol. 1, no. 1, pp. 014 002–014 002, 2019.
[64] M. T. Hill and M. C. Gather, "Advances in small lasers," *Nature Photonics*, vol. 8, no. 12, pp. 908–918, 2014.
[65] Y. Liang, C. Li, Y.-Z. Huang, and Q. Zhang, "Plasmonic nanolasers in on-chip light sources: Prospects and challenges," *ACS nano*, vol. 14, no. 11, pp. 14 375–14 390, 2020.
[66] L. Esaki and R. Tsu, "Superlattice and negative conductivity in semiconductors, ibm res," *Note, RC-2418*, 1969.
[67] L. Esaki and R. Tsu, "Superlattice and negative differential conductivity in semiconductors," *IBM Journal of Research and Development*, vol. 14, no. 1, pp. 61–65, 1970.
[68] E. O. Odoh and A. S. Njapba, "A review of semiconductor quantum well devices," *Advances in Physics Theories and Applications*, vol. 46, pp. 26–32, 2015.
[69] T. Fujii, S. Yamakoshi, K. Nanbu, O. Wada, and S. Hiyamizu, "Very low threshold current GaAs–AlGaAs GRIN-SCH lasers grown by mbe for oeic applications," *Journal of Vacuum Science & Technology B: Microelectronics Processing and Phenomena*, vol. 2, no. 2, pp. 259–261, 1984.
[70] E. Kapon, S. Simhony, R. Bhat, and D. Hwang, "Single quantum wire semiconductor lasers," *Applied physics letters*, vol. 55, no. 26, pp. 2715–2717, 1989.
[71] M. Asada, Y. Miyamoto, and Y. Suematsu, "Theoretical gain of quantum-well wire lasers," *Japanese journal of applied physics*, vol. 24, no. 2A, p. L95, 1985.
[72] A. Yariv, "Scaling laws and minimum threshold currents for quantum-confined semiconductor lasers," *Applied physics letters*, vol. 53, no. 12, pp. 1033–1035, 1988.
[73] Y. Hasegawa, T. Egawa, T. Jimbo, and M. Umeno, "First demonstration of extremely low-threshold algaas/gaas quantum wire-like lasers grown on V-grooved GaAs/Si substrates," in *Proceedings of IEEE 14th International Semiconductor Laser Conference*, IEEE, 1994, pp. 75–76.
[74] M. Walther, E. Kapon, J. Christen, D. Hwang, and R. Bhat, "Carrier capture and quantum confinement in gaas/algaas quantum wire lasers grown on v-grooved substrates," *Applied physics letters*, vol. 60, no. 5, pp. 521–523, 1992.
[75] K. J. Vahala, J. A. Lebens, C. S. Tsai, *et al.*, "Quantum wire and quantum dot semiconductor lasers," in *Nonlinear Optical Materials and Devices for Photonic Switching*, SPIE, vol. 1216, 1990, pp. 120–129.
[76] G. B. Stringfellow, "Use of nanostructures for high brightness light-emitting diodes," *Energy Efficiency and Renewable Energy Through Nanotechnology*, pp. 803–842, 2011.
[77] Y. Arakawa and H. Sakaki, "Multidimensional quantum well laser and temperature dependence of its threshold current," *Applied physics letters*, vol. 40, no. 11, pp. 939–941, 1982.
[78] N. Kirstaedter, N. Ledentsov, M. Grundmann, *et al.*, "Low threshold, large to injection laser emission from (inga) as quantum dots," *Electronics Letters*, vol. 30, no. 17, pp. 1416–1417, 1994.
[79] R. Mirin, A. Gossard, and J. Bowers, "Room temperature lasing from InGaAs quantum dots," *Electronics Letters*, vol. 32, no. 18, pp. 1732–1734, 1996.

[80] H. Hirayama, K. Matsunaga, M. Asada, and Y. Suematsu, "Lasing action of ga0. 67in0. 33as/gainasp/inp tensile-strained quantum-box laser," *Electronics Letters*, vol. 30, no. 2, pp. 142–143, 1994.
[81] J. C. Norman, D. Jung, Z. Zhang, *et al.*, "A review of high-performance quantum dot lasers on silicon," *IEEE Journal of Quantum Electronics*, vol. 55, no. 2, pp. 1–11, 2019.
[82] D. Bimberg and U. W. Pohl, "Quantum dots: Promises and accomplishments," *Materials Today*, vol. 14, no. 9, pp. 388–397, 2011.
[83] T. Kageyama, K. Nishi, M. Yamaguchi, *et al.*, "Extremely high temperature (220 c) continuous-wave operation of 1300-nm-range quantum-dot lasers," in *The European Conference on Lasers and Electro-Optics*, Optica Publishing Group, 2011, PDA_1.
[84] H. Schmeckebier and D. Bimberg, "Quantum-dot semiconductor optical amplifiers for energy-efficient optical communication," *Green photonics and electronics*, pp. 37–74, 2017.
[85] A. Y. Liu, S. Srinivasan, J. Norman, A. C. Gossard, and J. E. Bowers, "Quantum dot lasers for silicon photonics," *Photonics Research*, vol. 3, no. 5, B1–B9, 2015.
[86] F. Grillot, J. C. Norman, J. Duan, *et al.*, "Physics and applications of quantum dot lasers for silicon photonics," *Nanophotonics*, vol. 9, no. 6, pp. 1271–1286, 2020.
[87] O. Stier, M. Grundmann, and D. Bimberg, "Electronic and optical properties of strained quantum dots modeled by 8-band k p theory," *Physical Review B*, vol. 59, no. 8, p. 5688, 1999.
[88] K. Thyagarajan and A. K. Ghatak, "Lasers: Theory and applications," 1981.
[89] Y. Yamamoto, S. Machida, and G. Björk, "Microcavity semiconductor laser with enhanced spontaneous emission," *Physical Review A*, vol. 44, no. 1, p. 657, 1991.
[90] E. M. Purcell, "Spontaneous emission probabilities at radio frequencies," *Confined Electrons and Photons: New Physics and Applications*, pp. 839–839, 1995.
[91] A. Haug, "Band-to-band auger recombination in semiconductors," *Journal of Physics and Chemistry of Solids*, vol. 49, no. 6, pp. 599–605, 1988.
[92] A. Haug, "Auger recombination in direct-gap semiconductors: Band-structure effects," *Journal of Physics C: Solid State Physics*, vol. 16, no. 21, p. 4159, 1983.
[93] T. Goudon, V. Miljanović, and C. Schmeiser, "On the shockley–read–hall model: Generation-recombination in semiconductors," *SIAM Journal on Applied Mathematics*, vol. 67, no. 4, pp. 1183–1201, 2007.
[94] A. S. Polkovnikov and G. G. Zegrya, "Auger recombination in semiconductor quantum wells," *Physical Review B*, vol. 58, no. 7, p. 4039, 1998.
[95] M. Govoni, I. Marri, and S. Ossicini, "Auger recombination in Si and GaAs semiconductors: Ab initio results," *Physical Review B*, vol. 84, no. 7, p. 075 215, 2011.
[96] A. W. Cohn, A. M. Schimpf, C. E. Gunthardt, and D. R. Gamelin, "Size-dependent trap-assisted auger recombination in semiconductor nanocrystals," *Nano letters*, vol. 13, no. 4, pp. 1810–1815, 2013.
[97] J. D. Murphy, K. Bothe, R. Krain, V. Voronkov, and R. Falster, "Parameterisation of injection-dependent lifetime measurements in semiconductors in terms of shockley-read-hall statistics: An application to oxide precipitates in silicon," *Journal of Applied Physics*, vol. 111, no. 11, p. 113 709, 2012.
[98] P. Webster, R. Carrasco, A. Newell, *et al.*, "Utility of shockley–read–hall analysis to extract defect properties from semiconductor minority carrier lifetime data," *Journal of Applied Physics*, vol. 133, no. 12, 2023.
[99] A. Yashin, "Applicability of a simplified shockley-read-hall model to semiconductors with various types of defects," *Semiconductors*, vol. 39, pp. 1285–1289, 2005.

[100] M. I. Nathan, W. P. Dumke, G. Burns, F. H. Dill Jr, and G. Lasher, "Stimulated emission of radiation from gaas p-n junctions," *Applied Physics Letters*, vol. 1, no. 3, pp. 62–64, 1962.
[101] R. N. Hall, G. E. Fenner, J. Kingsley, T. Soltys, and R. Carlson, "Coherent light emission from gaas junctions," *Physical Review Letters*, vol. 9, no. 9, p. 366, 1962.
[102] H. J. Eichler, J. Eichler, O. Lux, H. J. Eichler, J. Eichler, and O. Lux, "Semiconductor lasers," *Lasers: Basics, Advances and Applications*, pp. 165–203, 2018.
[103] J. L. Chilla, H. Zhou, E. Weiss, *et al.*, "Blue and green optically pumped semiconductor lasers for display," in *Projection Displays XI*, SPIE, vol. 5740, 2005, pp. 41–47.
[104] E. Hulicius and V. Kubeček, "Semiconductor lasers for medical applications," in *Lasers for Medical Applications*, Elsevier, 2013, pp. 222–250.
[105] C.-Z. Ning, "Semiconductor nanolasers," *physica status solidi (b)*, vol. 247, no. 4, pp. 774–788, 2010.
[106] S. F. Yu, *Analysis and design of vertical cavity surface emitting lasers*. John Wiley & Sons, 2003, vol. 7.
[107] J. Harris, T. O'sullivan, T. Sarmiento, M. Lee, and S. Vo, "Emerging applications for vertical cavity surface emitting lasers," *Semiconductor science and technology*, vol. 26, no. 1, p. 014 010, 2010.
[108] Y. Zhang, X. Zhang, K. H. Li, Y. F. Cheung, C. Feng, and H. W. Choi, "Advances in III-nitride semiconductor microdisk lasers," *physica status solidi (a)*, vol. 212, no. 5, pp. 960–973, 2015.
[109] S. Ghosh, W. Wang, F. Mendoza, *et al.*, "Enhancement of spin coherence using q-factor engineering in semiconductor microdisc lasers," *Nature materials*, vol. 5, no. 4, pp. 261–264, 2006.
[110] M. Kamp, T. Happ, S. Mahnkopf, G. Duan, S. Anand, and A. Forchel, "Semiconductor photonic crystals for optoelectronics," *Physica E: Low-dimensional Systems and Nanostructures*, vol. 21, no. 2-4, pp. 802–808, 2004.
[111] W. Zheng, "Semiconductor photonic crystal laser," *Chinese Physics B*, vol. 27, no. 11, p. 114 211, 2018.
[112] S. W. Eaton, A. Fu, A. B. Wong, C.-Z. Ning, and P. Yang, "Semiconductor nanowire lasers," *Nature reviews materials*, vol. 1, no. 6, pp. 1–11, 2016.
[113] C.-Z. Ning, "Semiconductor nanowire lasers," *Semiconductors and Semimetals*, vol. 86, pp. 455–486, 2012.
[114] C.-C. Shen, T.-C. Hsu, Y.-W. Yeh, *et al.*, "Design, modeling, and fabrication of high-speed vcsel with data rate up to 50 Gb/s," *Nanoscale research letters*, vol. 14, pp. 1–6, 2019.
[115] L. K. Van Vugt, S. Rühle, and D. Vanmaekelbergh, "Phase-correlated nondirectional laser emission from the end facets of a zno nanowire," *Nano letters*, vol. 6, no. 12, pp. 2707–2711, 2006.
[116] B. Ellis, M. A. Mayer, G. Shambat, *et al.*, "Ultralow-threshold electrically pumped quantum-dot photonic-crystal nanocavity laser," *Nature photonics*, vol. 5, no. 5, pp. 297–300, 2011.
[117] J. Ho, J. Tatebayashi, S. Sergent, C. F. Fong, S. Iwamoto, and Y. Arakawa, "Low-threshold near-infrared GaAs–AlGaAs core–shell nanowire plasmon laser," *Acs Photonics*, vol. 2, no. 1, pp. 165–171, 2015.
[118] P. Moser, J. Lott, P. Wolf, *et al.*, "56 fJ dissipated energy per bit of oxide-confined 850 nm vcsels operating at 25 gbit/s," *Electronics letters*, vol. 48, no. 20, pp. 1292–1294, 2012.

[119] P. Wolf, P. Moser, G. Larisch, H. Li, J. Lott, and D. Bimberg, "Energy efficient 40 gbit/s transmission with 850 nm vcsels at 108 fj/bit dissipated heat," *Electronics letters*, vol. 49, no. 10, pp. 666–667, 2013.
[120] D. Bimberg, A. Larsson, and A. Joel, "Faster, more frugal, greener vcsels," *Compd. Semicond*, vol. 22, pp. 34–39, 2014.
[121] S. McCall, A. Levi, R. Slusher, S. Pearton, and R. Logan, "Whispering-gallery mode microdisk lasers," *Applied physics letters*, vol. 60, no. 3, pp. 289–291, 1992.
[122] R. Slusher, A. Levi, U. Mohideen, S. McCall, S. Pearton, and R. Logan, "Threshold characteristics of semiconductor microdisk lasers," *Applied physics letters*, vol. 63, no. 10, pp. 1310–1312, 1993.
[123] M. Nomura, S. Iwamoto, K. Watanabe, *et al.*, "Room temperature continuous-wave lasing in photonic crystal nanocavity," *Optics Express*, vol. 14, no. 13, pp. 6308–6315, 2006.
[124] K. Nozaki, S. Kita, and T. Baba, "Room temperature continuous wave operation and controlled spontaneous emission in ultrasmall photonic crystal nanolaser," *Optics express*, vol. 15, no. 12, pp. 7506–7514, 2007.
[125] H.-G. Park, S.-H. Kim, S.-H. Kwon, *et al.*, "Electrically driven single-cell photonic crystal laser," *Science*, vol. 305, no. 5689, pp. 1444–1447, 2004.
[126] A. Maslov and C. Ning, "Reflection of guided modes in a semiconductor nanowire laser," *Applied physics letters*, vol. 83, no. 6, pp. 1237–1239, 2003.
[127] M. H. Huang, S. Mao, H. Feick, *et al.*, "Room-temperature ultraviolet nanowire nanolasers," *science*, vol. 292, no. 5523, pp. 1897–1899, 2001.
[128] J. C. Johnson, H. Yan, R. D. Schaller, L. H. Haber, R. J. Saykally, and P. Yang, "Single nanowire lasers," *The Journal of Physical Chemistry B*, vol. 105, no. 46, pp. 11 387–11 390, 2001.
[129] C. Couteau, A. Larrue, C. Wilhelm, and C. Soci, "Nanowire lasers," *Nanophotonics*, vol. 4, no. 1, pp. 90–107, 2015.
[130] H.-J. Choi, J. C. Johnson, R. He, *et al.*, "Self-organized gan quantum wire uv lasers," *The Journal of Physical Chemistry B*, vol. 107, no. 34, pp. 8721–8725, 2003.
[131] X. Duan, Y. Huang, R. Agarwal, and C. M. Lieber, "Single-nanowire electrically driven lasers," *Nature*, vol. 421, no. 6920, pp. 241–245, 2003.
[132] S. F. Yu, C. Yuen, S. P. Lau, W. Park, and G.-C. Yi, "Random laser action in zno nanorod arrays embedded in zno epilayers," *Applied physics letters*, vol. 84, no. 17, pp. 3241–3243, 2004.
[133] S. Gradečak, F. Qian, Y. Li, H.-G. Park, and C. M. Lieber, "Gan nanowire lasers with low lasing thresholds," *Applied Physics Letters*, vol. 87, no. 17, p. 173 111, 2005.
[134] A. Pan, R. Liu, Q. Yang, *et al.*, "Stimulated emissions in aligned CdS nanowires at room temperature," *The Journal of Physical Chemistry B*, vol. 109, no. 51, pp. 24 268–24 272, 2005.
[135] D. Vanmaekelbergh and L. K. Van Vugt, "Zno nanowire lasers," *Nanoscale*, vol. 3, no. 7, pp. 2783–2800, 2011.
[136] H.-C. Hsu, C.-Y. Wu, and W.-F. Hsieh, "Stimulated emission and lasing of random-growth oriented zno nanowires," *Journal of Applied Physics*, vol. 97, no. 6, p. 064 315, 2005.
[137] R. Agarwal, C. J. Barrelet, and C. M. Lieber, "Lasing in single cadmium sulfide nanowire optical cavities," *Nano letters*, vol. 5, no. 5, pp. 917–920, 2005.

[138] M. A. Zimmler, J. Bao, F. Capasso, S. Müller, and C. Ronning, "Laser action in nanowires: Observation of the transition from amplified spontaneous emission to laser oscillation," *Applied Physics Letters*, vol. 93, no. 5, p. 051 101, 2008.
[139] D. Saxena, S. Mokkapati, P. Parkinson, *et al.*, "Optically pumped room-temperature gaas nanowire lasers," *Nature photonics*, vol. 7, no. 12, pp. 963–968, 2013.
[140] D. Saxena, N. Jiang, X. Yuan, *et al.*, "Design and room-temperature operation of GaAs/AlGaAs multiple quantum well nanowire lasers," *Nano letters*, vol. 16, no. 8, pp. 5080–5086, 2016.
[141] H. Kim, W.-J. Lee, A. C. Farrell, *et al.*, "Monolithic ingaas nanowire array lasers on silicon-on-insulator operating at room temperature," *Nano letters*, vol. 17, no. 6, pp. 3465–3470, 2017.
[142] A. Chin, S. Vaddiraju, A. Maslov, C. Ning, M. Sunkara, and M. Meyyappan, "Near-infrared semiconductor subwavelength-wire lasers," *Applied Physics Letters*, vol. 88, no. 16, p. 163 115, 2006.
[143] B. Hua, J. Motohisa, Y. Kobayashi, S. Hara, and T. Fukui, "Single GaAs/GaAsP coaxial core- shell nanowire lasers," *Nano letters*, vol. 9, no. 1, pp. 112–116, 2009.
[144] Z. Wang, B. Tian, M. Paladugu, *et al.*, "Polytypic inp nanolaser monolithically integrated on (001) silicon," *Nano letters*, vol. 13, no. 11, pp. 5063–5069, 2013.
[145] B. Mayer, D. Rudolph, J. Schnell, *et al.*, "Lasing from individual gaas-algaas core-shell nanowires up to room temperature," *Nature communications*, vol. 4, no. 1, p. 2931, 2013.
[146] Q. Gao, D. Saxena, F. Wang, *et al.*, "Selective-area epitaxy of pure wurtzite inp nanowires: High quantum efficiency and room-temperature lasing," *Nano letters*, vol. 14, no. 9, pp. 5206–5211, 2014.
[147] Z. Liu, L. Yin, H. Ning, Z. Yang, L. Tong, and C.-Z. Ning, "Dynamical color-controllable lasing with extremely wide tuning range from red to green in a single alloy nanowire using nanoscale manipulation," *Nano letters*, vol. 13, no. 10, pp. 4945–4950, 2013.
[148] A. Pan, W. Zhou, E. S. Leong, *et al.*, "Continuous alloy-composition spatial grading and superbroad wavelength-tunable nanowire lasers on a single chip," *Nano letters*, vol. 9, no. 2, pp. 784–788, 2009.
[149] D. Saxena, "Design and characterisation of iii-v semiconductor nanowire lasers," Ph.D. dissertation, The Australian National University (Australia), 2017.
[150] C. Wang, B. Lingnau, K. Lüdge, J. Even, and F. Grillot, "Enhanced dynamic performance of quantum dot semiconductor lasers operating on the excited state," *IEEE Journal of quantum electronics*, vol. 50, no. 9, pp. 1–9, 2014.
[151] R. Yan, D. Gargas, and P. Yang, "Nanowire photonics," *Nature photonics*, vol. 3, no. 10, pp. 569–576, 2009.
[152] D. Gevaux, "Quantum wells meet nanowires," *Nature Photonics*, vol. 2, no. 10, pp. 594–594, 2008.
[153] F. Zhang, X. Zhang, Z. Li, *et al.*, "A new strategy for selective area growth of highly uniform ingaas/inp multiple quantum well nanowire arrays for optoelectronic device applications," *Advanced Functional Materials*, vol. 32, no. 3, p. 2 103 057, 2022.
[154] Y. Li, X. Yan, X. Zhang, *et al.*, "Low-threshold miniaturized core-shell gaas/ingaas nanowire/quantum-dot hybrid structure nanolasers," *Optics & Laser Technology*, vol. 152, p. 108 150, 2022.
[155] F. Koc, A. E. Kavruk, and M. Sahin, "Advanced tunability of optical properties of cds/znse/znte/cdse multi-shell quantum dot by the band edge engineering," *Physica E: Low-dimensional Systems and Nanostructures*, vol. 145, p. 115 479, 2023.

[156] Y. Lu, "Development of high-performance, cost-effective quantum dot lasers for data-centre and si photonics applications," Ph.D. dissertation, UCL (University College London), 2023.
[157] P. Schmiedeke, N. Mukhundhan, A. Thurn, *et al.*, "Heterogeneous iii-v nanowire lasers and quantum dot emitters on silicon photonic circuits," in *Integrated Photonics Research, Silicon and Nanophotonics*, Optica Publishing Group, 2022, ITu3B–4.
[158] F. Qian, Y. Li, S. Gradečak, *et al.*, "Multi-quantum-well nanowire heterostructures for wavelength-controlled lasers," *Nature materials*, vol. 7, no. 9, pp. 701–706, 2008.
[159] T. Stettner, P. Zimmermann, B. Loitsch, *et al.*, "Coaxial GaAs-AlGaAs core-multishell nanowire lasers with epitaxial gain control," *Applied Physics Letters*, vol. 108, no. 1, p. 011 108, 2016.
[160] J. Heo, W. Guo, and P. Bhattacharya, "Monolithic single gan nanowire laser with photonic crystal microcavity on silicon," *Applied Physics Letters*, vol. 98, no. 2, p. 021 110, 2011.
[161] H. Sun, F. Ren, K. W. Ng, T.-T. D. Tran, K. Li, and C. J. Chang-Hasnain, "Nanopillar lasers directly grown on silicon with heterostructure surface passivation," *Acs Nano*, vol. 8, no. 7, pp. 6833–6839, 2014.
[162] D. Wang and H. Dai, "Low-temperature synthesis of single-crystal germanium nanowires by chemical vapor deposition," *Angewandte Chemie International Edition*, vol. 41, no. 24, pp. 4783–4786, 2002.
[163] N. M. Hwang, W. S. Cheong, D. Y. Yoon, and D.-Y. Kim, "Growth of silicon nanowires by chemical vapor deposition: Approach by charged cluster model," *Journal of crystal growth*, vol. 218, no. 1, pp. 33–39, 2000.
[164] J. Ge and Y. Li, "Selective atmospheric pressure chemical vapor deposition route to cds arrays, nanowires, and nanocombs," *Advanced Functional Materials*, vol. 14, no. 2, pp. 157–162, 2004.
[165] Z. Ma, S. Chai, Q. Feng, *et al.*, "Chemical vapor deposition growth of high crystallinity Sb2Se3 nanowire with strong anisotropy for near-infrared photodetectors," *Small*, vol. 15, no. 9, p. 1 805 307, 2019.
[166] Q. Luo, R. Yuan, Y.-L. Hu, and D. Wang, "Spontaneous cvd growth of inxga1-xn/gan core/shell nanowires for photocatalytic hydrogen generation," *Applied Surface Science*, vol. 537, p. 147 930, 2021.
[167] M. Hasan, M. F. Huq, and Z. H. Mahmood, "A review on electronic and optical properties of silicon nanowire and its different growth techniques," *SpringerPlus*, vol. 2, no. 1, pp. 1–9, 2013.
[168] J. Ho, J. Tatebayashi, S. Sergent, *et al.*, "A nanowire-based plasmonic quantum dot laser," *Nano letters*, vol. 16, no. 4, pp. 2845–2850, 2016.
[169] M. A. Johar, H.-G. Song, A. Waseem, *et al.*, "Universal and scalable route to fabricate gan nanowire-based led on amorphous substrate by mocvd," *Applied Materials Today*, vol. 19, p. 100 541, 2020.
[170] S. D. Hersee, X. Sun, and X. Wang, "The controlled growth of gan nanowires," *Nano letters*, vol. 6, no. 8, pp. 1808–1811, 2006.
[171] H. Kim, W.-J. Lee, A. C. Farrell, A. Balgarkashi, and D. L. Huffaker, "Telecom-wavelength bottom-up nanobeam lasers on silicon-on-insulator," *Nano letters*, vol. 17, no. 9, pp. 5244–5250, 2017.
[172] B. Shi and K. M. Lau, "Growth of III–V semiconductors and lasers on silicon substrates by mocvd," in *Semiconductors and Semimetals*, vol. 101, Elsevier, 2019, pp. 229–282.

[173] B. O. Jung, S.-Y. Bae, Y. Kato, *et al.*, "Morphology development of gan nanowires using a pulsed-mode mocvd growth technique," *CrystEngComm*, vol. 16, no. 11, pp. 2273–2282, 2014.

[174] Y. Kim, H. J. Joyce, Q. Gao, *et al.*, "Influence of nanowire density on the shape and optical properties of ternary ingaas nanowires," *Nano letters*, vol. 6, no. 4, pp. 599–604, 2006.

[175] G. Koblmüller, B. Mayer, T. Stettner, G. Abstreiter, and J. J. Finley, "Gaas–algaas core–shell nanowire lasers on silicon: Invited review," *Semiconductor Science and Technology*, vol. 32, no. 5, p. 053 001, 2017.

[176] H.-J. Chu, T.-W. Yeh, L. Stewart, and P. D. Dapkus, "Wurtzite inp nanowire arrays grown by selective area mocvd," *physica status solidi c*, vol. 7, no. 10, pp. 2494–2497, 2010.

[177] Q. Zhang, X. Yin, and S. Zhao, "Recent progress on aluminum gallium nitride deep ultraviolet lasers by molecular beam epitaxy," *physica status solidi (RRL)–Rapid Research Letters*, vol. 15, no. 7, p. 2 100 090, 2021.

[178] M. F. Vafadar, Q. Zhang, and S. Zhao, "Direct observation of al migration enhancement by changing the al and n source relative position in the molecular beam epitaxy of AlGaN Nanowires," *Crystal Growth & Design*, 2023.

[179] S. Zhao and Z. Mi, "Recent advances on p-type III-nitride nanowires by molecular beam epitaxy," *Crystals*, vol. 7, no. 9, p. 268, 2017.

[180] Z. Mi, S. Zhao, S. Woo, *et al.*, "Molecular beam epitaxial growth and characterization of Al (Ga) n nanowire deep ultraviolet light emitting diodes and lasers," *Journal of Physics D: Applied Physics*, vol. 49, no. 36, p. 364 006, 2016.

[181] S. Zhao, R. Wang, S. Chu, and Z. Mi, "Molecular beam epitaxy of III-nitride nanowires: Emerging applications from deep-ultraviolet light emitters and micro-leds to artificial photosynthesis," *IEEE Nanotechnology Magazine*, vol. 13, no. 2, pp. 6–16, 2019.

[182] S. Zhao, S. Woo, S. Sadaf, *et al.*, "Molecular beam epitaxy growth of Al-rich AlGaN nanowires for deep ultraviolet optoelectronics," *Apl Materials*, vol. 4, no. 8, p. 086 115, 2016.

[183] S. Zhao, M. Kibria, Q. Wang, H. Nguyen, and Z. Mi, "Growth of large-scale vertically aligned GaN nanowires and their heterostructures with high uniformity on sio x by catalyst-free molecular beam epitaxy," *Nanoscale*, vol. 5, no. 12, pp. 5283–5287, 2013.

[184] Q. Wang, S. Zhao, A. Connie, *et al.*, "Optical properties of strain-free aln nanowires grown by molecular beam epitaxy on si substrates," *Applied Physics Letters*, vol. 104, no. 22, p. 223 107, 2014.

[185] A. Marcu, L. Trupina, R. Zamani, J. Arbiol, C. Grigoriu, and J. Morante, "Catalyst size limitation in vapor–liquid–solid zno nanowire growth using pulsed laser deposition," *Thin Solid Films*, vol. 520, no. 14, pp. 4626–4631, 2012.

[186] H.-J. Choi, "Vapor–liquid–solid growth of semiconductor nanowires," in *Semiconductor nanostructures for optoelectronic devices: Processing, characterization and applications*, Springer, 2011, pp. 1–36.

[187] Y. Yang, Y. Feng, and G. Yang, "Experimental evidence and physical understanding of zno vapor-liquid-solid nanowire growth," *Applied Physics A*, vol. 102, pp. 319–323, 2011.

[188] K.-K. Lew, L. Pan, E. C. Dickey, and J. M. Redwing, "Vapor–liquid–solid growth of silicon–germanium nanowires," *Advanced Materials*, vol. 15, no. 24, pp. 2073–2076, 2003.

[189] A. Klamchuen, M. Suzuki, K. Nagashima, *et al.*, "Rational concept for designing vapor–liquid–solid growth of single crystalline metal oxide nanowires," *Nano letters*, vol. 15, no. 10, pp. 6406–6412, 2015.

[190] A. Kar, J. Yang, M. Dutta, M. A. Stroscio, J. Kumari, and M. Meyyappan, "Rapid thermal annealing effects on tin oxide nanowires prepared by vapor–liquid–solid technique," *Nanotechnology*, vol. 20, no. 6, p. 065 704, 2009.

[191] S. Bhaskar, P. Das, V. Srinivasan, S. B. Bhaktha, and S. S. Ramamurthy, "Plasmonic-silver sorets and dielectric-nd2o3 nanorods for ultrasensitive photonic crystal-coupled emission," *Materials Research Bulletin*, vol. 145, p. 111 558, 2022.

[192] A. Maslov and C. Ning, "Modal gain in a semiconductor nanowire laser with anisotropic bandstructure," *IEEE journal of quantum electronics*, vol. 40, no. 10, pp. 1389–1397, 2004.

[193] A. Maslov and C.-Z. Ning, "Size reduction of a semiconductor nanowire laser by using metal coating," in *Physics and simulation of optoelectronic devices XV*, SPIE, vol. 6468, 2007, pp. 138–144.

[194] F. Patolsky, G. Zheng, and C. M. Lieber, "Nanowire sensors for medicine and the life sciences," 2006.

[195] B. He, T. J. Morrow, and C. D. Keating, "Nanowire sensors for multiplexed detection of biomolecules," *Current opinion in chemical biology*, vol. 12, no. 5, pp. 522–528, 2008.

[196] Z. Wang, S. Lee, K.-i. Koo, and K. Kim, "Nanowire-based sensors for biological and medical applications," *IEEE transactions on nanobioscience*, vol. 15, no. 3, pp. 186–199, 2016.

[197] R. Yan, J.-H. Park, Y. Choi, *et al.*, "Nanowire-based single-cell endoscopy," *Nature nanotechnology*, vol. 7, no. 3, pp. 191–196, 2012.

[198] R. Liu, R. Chen, A. T. Elthakeb, *et al.*, "High density individually addressable nanowire arrays record intracellular activity from primary rodent and human stem cell derived neurons," *Nano letters*, vol. 17, no. 5, pp. 2757–2764, 2017.

[199] X. Wu, Q. Chen, P. Xu, *et al.*, "Nanowire lasers as intracellular probes," *Nanoscale*, vol. 10, no. 20, pp. 9729–9735, 2018.

[200] I. A. Young, E. Mohammed, J. T. Liao, *et al.*, "Optical I/O technology for tera-scale computing," *IEEE Journal of solid-state circuits*, vol. 45, no. 1, pp. 235–248, 2009.

[201] C. Sun, M. T. Wade, Y. Lee, *et al.*, "Single-chip microprocessor that communicates directly using light," *Nature*, vol. 528, no. 7583, pp. 534–538, 2015.

[202] B. Mayer, L. Janker, B. Loitsch, *et al.*, "Monolithically integrated high-$\beta$ nanowire lasers on silicon," *Nano letters*, vol. 16, no. 1, pp. 152–156, 2016.

[203] F. Schuster, J. Kapraun, G. N. Malheiros-Silveira, S. Deshpande, and C. J. Chang-Hasnain, "Site-controlled growth of monolithic InGaAs/InP quantum well nanopillar lasers on silicon," *Nano letters*, vol. 17, no. 4, pp. 2697–2702, 2017.

[204] J. Bissinger, D. Ruhstorfer, T. Stettner, G. Koblmüller, and J. J. Finley, "Optimized waveguide coupling of an integrated III-V nanowire laser on silicon," *Journal of applied physics*, vol. 125, no. 24, p. 243 102, 2019.

[205] T. Stettner, T. Kostenbader, D. Ruhstorfer, *et al.*, "Direct coupling of coherent emission from site-selectively grown III–V nanowire lasers into proximal silicon waveguides," *ACS Photonics*, vol. 4, no. 10, pp. 2537–2543, 2017.

[206] E. M. Fadaly, A. Dijkstra, J. R. Suckert, *et al.*, "Direct-bandgap emission from hexagonal Ge and SiGe alloys," *Nature*, vol. 580, no. 7802, pp. 205–209, 2020.

[207] H. Kim, W.-J. Lee, T.-Y. Chang, and D. L. Huffaker, "Room-temperature ingaas nanowire array band-edge lasers on patterned silicon-on-insulator platforms," *physica status solidi (RRL)–Rapid Research Letters*, vol. 13, no. 3, p. 1 800 489, 2019.

[208] H. Kim, T.-Y. Chang, W.-J. Lee, and D. L. Huffaker, "Iii–v nanowire array telecom lasers on (001) silicon-on-insulator photonic platforms," *Applied Physics Letters*, vol. 115, no. 21, p. 213 101, 2019.

[209] A. Yokoo, M. Takiguchi, M. D. Birowosuto, *et al.*, "Subwavelength nanowire lasers on a silicon photonic crystal operating at telecom wavelengths," *Acs Photonics*, vol. 4, no. 2, pp. 355–362, 2017.

[210] B. Romeira and A. Fiore, "Purcell effect in the stimulated and spontaneous emission rates of nanoscale semiconductor lasers," *IEEE Journal of Quantum Electronics*, vol. 54, no. 2, pp. 1–12, 2018.

[211] J. Kupec, R. L. Stoop, and B. Witzigmann, "Light absorption and emission in nanowire array solar cells," *Optics express*, vol. 18, no. 26, pp. 27 589–27 605, 2010.

[212] N. Lawrence and L. Dal Negro, "Light scattering, field localization and local density of states in co-axial plasmonic nanowires," *Optics Express*, vol. 18, no. 15, pp. 16 120–16 132, 2010.

[213] N. Gregersen, T. Suhr, M. Lorke, and J. Mørk, "Quantum-dot nano-cavity lasers with purcell-enhanced stimulated emission," *Applied Physics Letters*, vol. 100, no. 13, 2012.

[214] O. C. Zienkiewicz and R. L. Taylor, *The finite element method for solid and structural mechanics*. Elsevier, 2005.

[215] J. N. Reddy and D. K. Gartling, *The finite element method in heat transfer and fluid dynamics*. CRC press, 2010.

[216] J.-M. Jin, *The finite element method in electromagnetics*. John Wiley & Sons, 2015.

[217] J.-M. Jin and D. J. Riley, *Finite element analysis of antennas and arrays*. John Wiley & Sons, 2008.

[218] P. P. Silvester and R. L. Ferrari, *Finite elements for electrical engineers*. Cambridge university press, 1996.

[219] M. Koshiba, "Nonlinear optical waveguides," *Optical Waveguide Theory by the Finite Element Method*, pp. 211–227, 1993.

[220] A. C. Polycarpou, "Introduction to the finite element method in electromagnetics," *Synthesis Lectures on Computational Electromagnetics*, vol. 1, no. 1, pp. 1–126, 2005.

[221] J. R. Cardoso, *Electromagnetics through the finite element method: A simplified approach using maxwell's equations*. Crc Press, 2016.

[222] A. Iserles, *A first course in the numerical analysis of differential equations*. Cambridge university press, 2009.

[223] L. V. Asryan, S. Luryi, and R. A. Suris, "Internal efficiency of semiconductor lasers with a quantum-confined active region," *IEEE journal of quantum electronics*, vol. 39, no. 3, pp. 404–418, 2003.

[224] D. J. Biswas, *A Beginner's Guide to Lasers and Their Applications, Part 1: Insights into Laser Science*. Springer Nature, 2023.

[225] K. J. Vahala, "Optical microcavities," *nature*, vol. 424, no. 6950, pp. 839–846, 2003.

[226] Z. A. Sattar and K. A. Shore, "Analysis of the direct modulation response of nanowire lasers," *Journal of Lightwave Technology*, vol. 33, no. 14, pp. 3028–3033, 2015.

[227] M. Ogura and H. Hsieh, "Effect of surface recombination velocity on the threshold current and differential quantum efficiency of the surface-emitting laser diode," *IEEE journal of quantum electronics*, vol. 32, no. 4, pp. 597–606, 1996.